Analysis, Design and Optimisation of Various Antenna Types Based on Equivalent Magnetic-Current Concept

by

Nghia Nguyen Trong

B. Engineering (Electrical and Electronic, Honours),
University of Adelaide, Australia, 2013

Thesis submitted for the degree of

Doctor of Philosophy

in

Electrical and Electronic Engineering,
Faculty of Engineering, Computer and Mathematical Sciences
The University of Adelaide, Australia

January, 2017

Supervisors:

Prof Christophe Fumeaux, School of Electrical & Electronic Engineering

Dr Leonard Hall, Defence Science and Technology Group

Dr Thomas Kaufmann, School of Electrical & Electronic Engineering (Feb. 2014 - Feb. 2015)

THE UNIVERSITY *of* ADELAIDE

Contents

Abstract

The field equivalence principle is a classical technique, simple to use but remarkably effective to analyse aperture antennas. For most of thin planar structures, the aperture can be approximated as perfect magnetic conductor. Thus, the field equivalence principle typically yields a well-approximated equivalent problem that is much easier to solve than the original geometry. Inspired by this principle, a wide range of novel antenna structures are proposed in this thesis. These structures are further developed, optimised and tailored for various practical applications. Three main types of antennas are investigated, including travelling-wave antennas, low-profile monopolar antennas and reconfigurable antennas, corresponding to three major parts of this dissertation.

The first part examines various realisations of travelling-wave half-mode substrate-integrated waveguide (HMSIW) antennas and their optimisations. This type of antenna is equivalent to a magnetic dipole. In this part, the core contribution is a generalised semi-analytical model to effectively analyse continuous-source travelling-wave antennas, based on which different optimisation techniques for bandwidth and radiation patterns are proposed. An optimisation procedure that includes parameter uncertainties is also demonstrated.

The second part focuses on a type of low-profile monopolar antennas that can be interpreted as magnetic-current loops using the field equivalence principle. The main contributions are different configurations of symmetrical radiating slots that act as additional magnetic-current loop sources.

The last major part covers a wide range of reconfigurable antennas targeting various applications. These includes a family of stub-loaded substrate-integrated antennas, a circular resonant cavity, and low-profile monopolar antennas that have been introduced in the second major part. These antennas not only cover three main application types of reconfigurable antennas, i.e. frequency- , polarisation-, and pattern-tunability, but also combine those in a single device. Moreover, significant improvements in performances compared to antennas available in the literature are demonstrated.

Overall, the thesis provides different frameworks to design many types of antennas. The analytical models, using the field equivalence principle as a common fundamental technique, provide not only thorough understandings on antennas' radiation mechanisms but also an effective means for rapid antenna optimisations.

Statement of Originality

I certify that this work contains no material which has been accepted for the award of any other degree or diploma in my name, in any university or other tertiary institution and, to the best of my knowledge and belief, contains no material previously published or written by another person, except where due reference has been made in the text. In addition, I certify that no part of this work will, in the future, be used in a submission in my name, for any other degree or diploma in any university or other tertiary institution without the prior approval of the University of Adelaide and where applicable, any partner institution responsible for the joint-award of this degree.

I give consent to this copy of my thesis when deposited in the University Library, being made available for loan and photocopying, subject to the provisions of the Copyright Act 1968.

I acknowledge that copyright of published works contained within this thesis resides with the copyright holder(s) of those works.

I also give permission for the digital version of my thesis to be made available on the web, via the University's digital research repository, the Library Search and also through web search engines, unless permission has been granted by the University to restrict access for a period of time.

Signed

Date

Acknowledgments

I would like to express my sincere gratitude to all people and organisations whose support, skills and encouragement are crucial to the successful completion of this thesis.

First and foremost, I would like to convey my deep gratitude to my principal supervisor, **Prof. Christophe Fumeaux** for his constant support throughout my research time at the University of Adelaide. His encouragement, constructive feedback, critical comments, travel funds and responsiveness are all essential factors that lead me throughout my candidature. He has not only inspired in me the passion for research but also helped me to balance it with social life and professional development. To me, he is a wonderful research supervisor and mentor whose advice I always trust.

Second, I would like to mention my co-supervisors, **Dr Thomas Kaufmann** and **Dr Leonard Hall**. I am thankful to have Dr Thomas Kaufmann as my lecturer in the Engineering Electromagnetic Course. He was the one who brought me to the field of electromagnetic. After working through the summer research under his excellent supervision, I gained and started to build up my research skills and experiences. I am also strongly indebted to Dr. Leonard Hall, who has offered me much useful feedback on my designs as well as advices in the professional engineering life. Thanks to him, I have also learned and appreciated the importance of the fabrication procedures.

In addition, I wish to express my gratitude to the technical staffs at the School of Electrical and Electronic Engineering Workshop, who have done excellent jobs on fabricating the devices presented in this thesis. Thanks to their guidance, I have also learned many different fabrication techniques. I would like to specially mention here Mr Alban O'Brien and Mr Pavel Simcik who have been patiently helping me fabricate multiple antenna designs until the prototypes are successful. I also thank Mr Brandon Pullen and Mr Danny Di Giacomo for their assistance on fabrication and material ordering.

My PhD research would not be possible without the assistance from the University of Adelaide and the School of Electrical and Electronic, from which I received financial support and technical instruments for my research. I would like to thank the administrative

team, Mrs Ivana Rebellato, Mrs Rose-Marie Descalzi, Ms Jodie Schluter, Ms Laura McNamara, Ms Deborah Koch and Ms Daphne Zammit who have helped me through administrative work in the most efficient way. I would also like to acknowledge the Vietnam Ministry of Education and Training who allowed me to continue my study in Australia after four year of undergraduate sponsorship.

Throughout my PhD candidature, I have received valuable help from many friends and colleagues. I would like to thank all of group members in the Applied Electromagnetic Groups, including Dr Withawat Withayachumnankul, Dr Ali Horestani, Dr Zahra Shaterian, Dr Amir Ebrahimi, Dr Cheng Zhao, Sree Pinapati, Shengjian Chen, Wendy Lee, Chengjun Zou, Jack Gao, Andrew Udina, Deshan Govender, Siti Nailah Zainarry and Ali Makatooni for their constructive feedback on my presentations as well as their willingness to help me in any occasion. I have had a great time doing research at the University thanks to their constant support and friendship. I also especially thank Lachlan James Gunn who has always been eager to help me on designing Printed Circuit Boards (PCB) despite of being extremely busy for his own thesis. I also thank Duong Nguyen and Thanh Bui, two of my Vietnamese friends in the School, who have helped me in multiple occasions and shared great times together with me.

I wish to give my deep appreciation to my dear fiancée, Ms Phuong-Tu Nguyen, who has always been by my side in any situations and supported me unconditionally. Her love, patience and continuous support has guided me through this challenging journey. Last but not least, I would like to give my endless love and appreciation to my father, my mother and my brother, who have been caring for and encouraging me infinitely.

Nghia Nguyen-Trong,
January 2017,
Adelaide

Thesis Conventions

The following conventions have been adopted in this thesis:

Typesetting

This document was compiled using LaTeX2e. TeXstudio were used as text editor interfaced to LaTeX2e. Inkscape was used to produce schematic diagrams and other drawings.

Referencing

The IEEE style has been adopted for referencing.

System of units

The units comply with the international system of units recommended in an Australian Standard: AS ISO 1000–1998 (Standards Australia Committee ME/71, Quantities, Units and Conversions 1998).

Spelling

Australian English spelling conventions have been used, as defined in the Macquarie English Dictionary (A. Delbridge (Ed.), Macquarie Library, North Ryde, NSW, Australia, 2001).

Publications

Note: Articles with an asterisk (*) are directly relevant to this thesis. Articles with a hash (#) are related to this thesis but the work was carried out before the candidature and are not part of original contributions.

Journal Articles

1. **N. Nguyen-Trong**, L. Hall, T. Kaufmann and C. Fumeaux, "Wideband Millimeter-Wave Antennas With Magnetic-Dipole Patterns Integrated in Metallic Structures," *IEEE Transactions on Antennas and Propagation*, vol. 64, no. 11, pp. 4877-4882, Nov. 2016. *

2. **N. Nguyen-Trong**; A. Piotrowski; L. Hall; C. Fumeaux, "A Frequency- and Polarization-Reconfigurable Circular Cavity Antenna," *IEEE Antennas and Wireless Propagation Letters* , 2016, in print, DOI: 10.1109/LAWP.2016.2616128. *

3. **N. Nguyen-Trong**; A. Piotrowski; T. Kaufmann and C. Fumeaux, "Low-Profile Wideband Monopolar UHF Antennas for Integration Onto Vehicles and Helmets," *IEEE Transactions on Antennas and Propagation*, vol. 64, no. 6, pp. 2562-2568, June 2016. *

4. **N. Nguyen-Trong**; L. Hall and C. Fumeaux,"A Frequency- and Pattern-Reconfigurable Center-Shorted Microstrip Antenna," *IEEE Antennas and Wireless Propagation Letters*, 2016, in print, DOI: 10.1109/LAWP.2016.2544943. *

5. **N. Nguyen-Trong**, L. Hall and C. Fumeaux, "Transmission-Line Model of Nonuniform Leaky-Wave Antennas," *IEEE Transactions on Antennas and Propagation*, vol. 64, no. 3, pp. 883-893, March 2016. *

6. A. Kouassi, **N. Nguyen-Trong**, T. Kaufmann, S. Lalléchère, P. Bonnet and C. Fumeaux, "Reliability-Aware Optimization of a Wideband Antenna," *IEEE Transactions on Antennas and Propagation*, vol. 64, no. 2, pp. 450-460, Feb. 2016. *The two first authors contributed equally to the work.* *

7. **N. Nguyen-Trong**, L. Hall and C. Fumeaux , "A Frequency- and Polarization-Reconfigurable Stub-Loaded Microstrip Patch Antenna," *IEEE Transactions on Antennas and Propagation*, vol. 63, no. 11, pp. 5235-5240, Nov. 2015. *

8. **N. Nguyen-Trong**, T. Kaufmann, L. Hall and C. Fumeaux, "Analysis and Design of a Reconfigurable Antenna Based on Half-Mode Substrate-Integrated Cavity", *IEEE Transactions on Antennas and Propagation*, vol. 63, no. 8, pp. 3345-3353, Aug. 2015. *

9. **N. Nguyen-Trong**, T. Kaufmann, L. Hall and C. Fumeaux, "Variational Analysis of Folded Substrate-Integrated Waveguides", *IEEE Microwave and Wireless Components Letters*, vol. 25, no. 6, pp. 352-354, June 2015. *

10. **N. Nguyen-Trong**, T. Kaufmann and C. Fumeaux, "A Semi-Analytical Solution of a Tapered Half-Mode Substrate-Integrated Waveguide With Application to Rapid Antenna Optimization", *IEEE Transactions on Antennas and Propagation*, vol. 62, no. 6, pp. 3189-3200, June 2014. #

11. **N. Nguyen-Trong**, T. Kaufmann, and C. Fumeaux, "A wideband omnidirectional horizontally polarized travelling-wave antenna based on Half-mode Substrate Integrated Waveguide", *IEEE Antennas and Wireless Propagation Letters*, vol. 12, pp. 682-685, 2013. **First Prize winner for the IEEE Australian Council Paper Contest for undergraduate students**. #

Conference Articles

1. **N. Nguyen-Trong**, C. Fumeaux, A. Kouassi, S. Lalléchère and P. Bonnet, "Reliability-aware optimization for the sidelobe level of leaky-wave antennas," *2016 International Conference on Electromagnetics in Advanced Applications (ICEAA)*, Cairns, Australia, 2016, pp. 708-711. *

2. **N. Nguyen-Trong**, L. T. Hall and C. Fumeaux, "Pattern synthesis with angular mask for leaky-wave antennas," *2016 17th International Symposium on Antenna Technology and Applied Electromagnetics (ANTEM)*, Montreal, QC, 2016, pp. 1-2. *

3. **N. Nguyen-Trong**, L. T. Hall and C. Fumeaux, "Impedance matching of a frequency- and pattern-reconfigurable antenna," *2016 17th International Symposium on Antenna Technology and Applied Electromagnetics (ANTEM)*, Montreal, QC, 2016, pp. 1-2. *

4. **N. Nguyen-Trong**, C. Fumeaux, S. Gupta and C. Caloz, "Pulse radiation from a leaky-wave antenna," *2016 IEEE International Symposium on Antennas and Propagation (APSURSI)*, Fajardo, 2016, pp. 87-88.

5. **N. Nguyen-Trong**, L. Hall and C. Fumeaux, "A reconfigurable quarter-wave patch antenna employing a folded loading stub," 2016 IEEE International Symposium on Antennas and Propagation (APSURSI), Fajardo, 2016, pp. 831-832. *

6. **N. Nguyen-Trong**, L. Hall and C. Fumeaux, "Reconfigurable antennas based on stub-loaded substrate-integrated circuits," *10th European Conference on Antennas and Propagation (EuCAP)*, Davos, Switzerland, 2016, pp. 1-4. *

7. **N. Nguyen-Trong**, T. Kaufmann and C. Fumeaux, "Perturbation method for near-elliptical Half-Mode cavity antennas," *10th European Conference on Antennas and Propagation (EuCAP)*, Davos, Switzerland, 2016, pp. 1-3.*

8. **N. Nguyen-Trong**, L. Hall and C. Fumeaux, "A biasing technique for varactor-loaded reconfigurable antennas," *2016 IEEE 2nd Australian Microwave Symposium (AMS)*, Adelaide, SA, 2016, pp. 23-24. *

9. **N. Nguyen-Trong**, L. Hall and C. Fumeaux, "On the tuning range of a reconfigurable half-mode substrate-integrated cavity antenna," *International Symposium on Antennas and Propagation (ISAP)*, Hobart, TAS, 2015, pp. 1-4. *

10. **N. Nguyen-Trong**, T. Kaufmann, L. Hall and C. Fumeaux, "Optimization of Leaky-Wave Antennas Based on Non-Uniform HMSIW", presented at *IEEE MTT-S International Conference on Numerical Electromagnetic and Multiphysics Modeling and Optimization (NEMO)*, 2015. **First prize winner student paper competition**. *

11. **N. Nguyen-Trong**, T. Kaufmann, L. Hall and C. Fumeaux, "Investigation of parasitic effects from feed and termination on the far-field pattern of leaky-wave antennas based on HMSIW", *Loughborough Antennas and Propagation Conference (LAPC)*, pp. 72-76, 10-11 Nov. 2014. *

12. **N. Nguyen-Trong**, T. Kaufmann and C. Fumeaux, "Near-field characteristics of a wideband travelling-wave antenna based on a tapered Half-Mode Substrate-Integrated Waveguide", *International Workshop on Antenna Technology (iWAT)* pp. 300-303, 4-6 March 2014. **Best student paper award**. #

13. **N. Nguyen-Trong**, T. Kaufmann, and C. Fumeaux, "Wideband transition from coaxial cable to Half-mode Substrate Integrated Waveguide", *Asia-Pacific Microwave Conference Proceedings (APMC)*, pp.110-112, 5-8 Nov. 2013. #

Papers Accepted or under Review

1. **N. Nguyen-Trong**, A. Piotrowski, and C. Fumeaux, "A Frequency-Reconfigurable Dual-Band Low-Profile Monopolar Antenna", submitted to *IEEE Transactions on Antennas and Propagation*, under review. *

2. **N. Nguyen-Trong**, A. Piotrowski, L. Hall, C. Fumeaux, "Concept of a Beam-Steerable Cavity-Fed Antenna with Magnetic-Dipole Coupling Elements", accepted for presentation at *11th European Conference on Antennas and Propagation (EuCAP)*, Paris, France, 2017. *

3. **N. Nguyen-Trong**, L. Hall, C. Fumeaux, "Conformal Integration of Traveling-Wave Slot Antennas in Millimeter-Wave Regime", accepted for presentation at *International Workshop on Antennas and Propagation (iWAT)*, Athens, Greek, 2017. *

4. **N. Nguyen-Trong**, L. Hall, C. Fumeaux, "Variational Analysis of Substrate-Integrated Waveguides with Longitudinal Slot", accepted for presentation at *Applied Computational Electromagnetics Society Conference* Firenze, Italy, 2017. *

List of Figures

List of Tables

Chapter 1

Introduction

THIS chapter first provides a background on the field equivalence principle and magnetic-current sources, which are used throughout this thesis as fundamental basis to analyse the radiation mechanism of various antennas. The applications of the principle are demonstrated in several practical cases with discussions on their accuracies. The motivations and aims of the thesis are then stated, followed by a description of the whole document structure, including a detailed listing of the chapters' topics and their main contributions.

1.1 Background

This section introduces the field equivalence principle and illustrates the use of magnetic-current sources to analyse aperture antennas. The technique is classical yet it is remarkably effective for the analysis of a wide range of antenna types, especially in the microwave and millimetre-wave regimes where most of the antennas radiate from one or an array of apertures – in contrast to wire antennas which are typically used in the lower radio-frequency region. Since this technique can be found in many textbooks, it is briefly summarised and adapted to the antenna types investigated in this thesis.

1.1.1 Theory of the Field Equivalence Principle

To adequately understand this principle, one should first recall the uniqueness theorem in electromagnetics. This theorem states that if the tangential components of either electric field, or magnetic field, are known over a closed surface, the field can be uniquely determined for a given source in the region inside or outside this boundary [1]. For a problem in electromagnetics, i.e. given current sources with boundary conditions and material properties, the main application of the field equivalence principle is to allow creating a new problem that is easier to solve and yields the same solution as that of the original problem in a region of interest. In this formulation, the uniqueness theorem is used to show that the solution of the new problem is unique if all conditions are satisfied.

Let us consider an actual problem: a physical source is fed to an antenna (Fig. 1.1). To solve electric and magnetic fields $(\mathbf{E}, \mathbf{H})$ at any position, one may need to solve the Maxwell's equations in the entire space with appropriate boundary conditions, such as perfect electric conductor (PEC) on the metal surface. The solution can be cumbersome and not analytically available considering that the shape of an antenna is typically complicated and the materials inside the antenna may be nonuniform. To find an alternative approach, an imaginary boundary S is introduced with an arbitrary shape to enclose the source and the antenna. This surface divides the space into two regions labelled as I and II. The boundary S should be chosen such that region II is source-free and entirely free-space. The next step is to remove the source and replace the entire region I with PEC so that the electric and magnetic field are zero everywhere in this region. It is noted that the perfect magnetic conductor (PMC) may be used alternatively but this dual-case is not considered here for

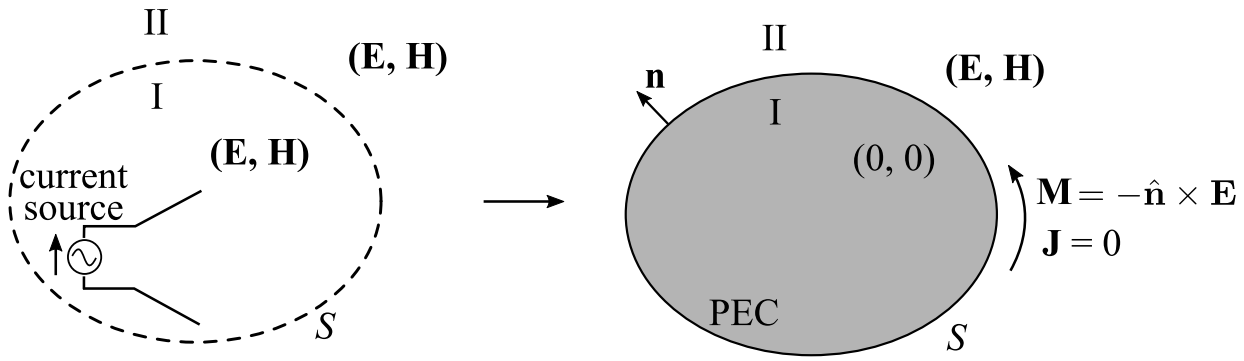

Figure 1.1. Actual and equivalent problem.

brevity. In order to still produce the field $(\mathbf{E}, \mathbf{H})$ in region II, the boundary conditions between two regions I and II have to be satisfied. This means that there exist current sources defined as $\mathbf{J}$ and $\mathbf{M}$ on the boundary S such that

$$\mathbf{M} = -\hat{\mathbf{n}} \times \mathbf{E}, \tag{1.1}$$

$$\mathbf{J} = \hat{\mathbf{n}} \times \mathbf{H}, \tag{1.2}$$

where $\hat{\mathbf{n}}$ is the normal unit vector pointing from region I to region II. Since the entire region I is PEC, the electric current $\mathbf{J}$ is "shorted" on the boundary. Thus, it becomes zero ($\mathbf{J} = 0$) and there are only magnetic current sources $\mathbf{M}$ radiating into free-space in the presence of the surface S with PEC boundary condition.

It can be noticed that the field in region II is specified by the source $\mathbf{M}$ and zero tangential electric field everywhere on the imaginary surface S. According to the uniqueness theorem, the field $(\mathbf{E}, \mathbf{H})$ are then specfied uniquely. Therefore, for region II, instead of solving for $(\mathbf{E}, \mathbf{H})$ using the original source, one can solve with the new source $\mathbf{M}$ and PEC boundary condition over the entire imaginary surface S.

1.1.2 Applications of the Field Equivalence Principle

At the first sight, the new equivalent problem might appear not easier than the original one because the radiation problem still has to be solved with a magnetic-current source and a seemingly arbitrary PEC boundary, which really depends on the shape of the antenna. Indeed, it should be noted that an exact solution can only be found readily in

the case of a current source radiating into free space without presence of any arbitrarily shaped conductor [2]. However, there are several circumstances in which the field equivalence principle can be used to give exact analytical solutions or very close approximations. This section will discuss such cases and the accuracy of these approximations.

The first example is the rectangular aperture antenna within an infinite ground plane, i.e. an infinite plane starting at the edges of the aperture (Fig. 1.2a). The electric field at the aperture $\mathbf{E}_a$ may be determined with high accuracy using a modal analysis for rectangular waveguides. For the formulation of the field equivalence principle, the surface S is chosen as the entire infinite ground plane plus the aperture (Fig. 1.2b). In this plane, the tangential electric field is known everywhere ($\mathbf{E} = \mathbf{E}_a$ in the aperture and $\mathbf{E} = 0$ on the ground plane). The uniqueness theorem implies that the field in the half free space can be determined from the equivalent source $\mathbf{M} = -\hat{\mathbf{n}} \times \mathbf{E}$ only, the tangential electric field on the boundary being zero since entire region I is PEC. Since the surface S is an infinite flat plane, using image theory, the equivalent problem now needs to double the magnetic current $\mathbf{M}$ radiating into free space. As mentioned above, this problem is simple and analytically solvable [2]. It is worth emphasising that under the infinite ground plane configuration, the analysis above is exact, i.e. no approximation has been made. In practice, the infinite ground plane can be well approximated by an electrically large metal plate.

Let us now consider the aperture antenna above but without the infinite ground plane. Since the tangential electric field is non-zero and unknown outside the aperture, the problem becomes more complicated. In this case, the rigorous treatment above cannot be used, instead, an approximation is necessary as follows [2]: the tangential field outside of the aperture is approximated to be zero and the far-field pattern should be calculated with both electric- and magnetic-current sources [equations (1.1) and (1.2)], i.e. none of them are suppressed in contrast to the previous case. This approximation has been verified with simulation and experiment data in [2] and is not further discussed here.

The next considered problem, which is the most relevant to this thesis, is an aperture antenna with a very thin profile (Fig. 1.3a). Before elaborating on the solution for this antenna, it should be noticed that if a magnetic-current source in z-direction radiates into free space, the electric field is perpendicular to any plane that contains the z-axis (thus the E-plane is xy-plane). This means that if a semi-infinite ground plane that contains the

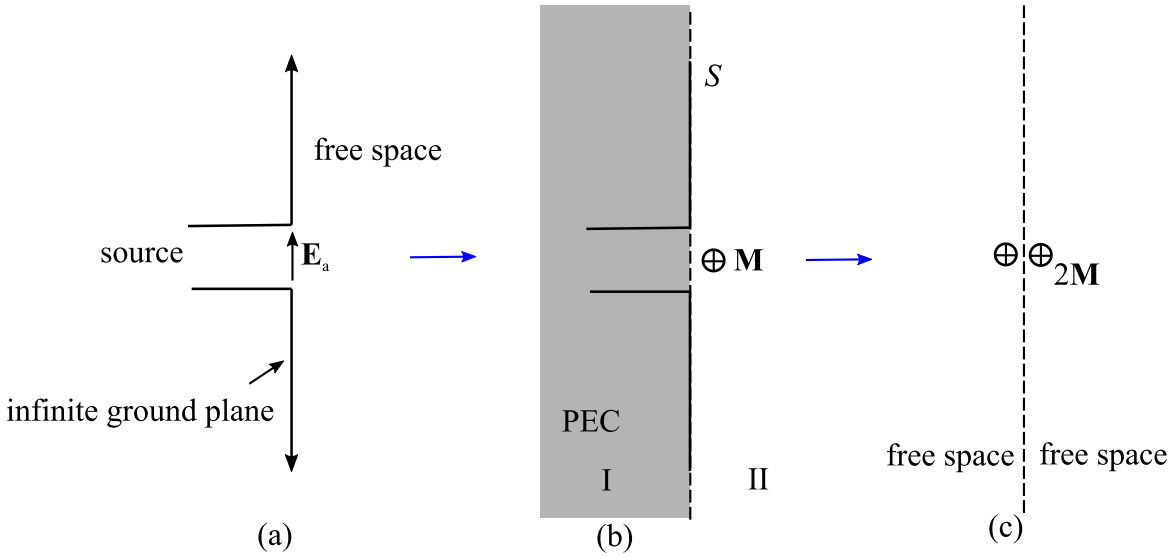

Figure 1.2. Analysis of aperture antenna. (a) Actual problem: aperture antenna with infinite ground plane radiating into half free space. (b) Equivalent problem using field equivalence principle. (c) Equivalent problem using image theory.

z-axis is introduced, this new boundary does not disturb the field distribution. Therefore, in the considered problem, the surface S can be chosen as consisting of two semi-infinite planes and the thin aperture as shown in Fig. 1.3b. Following the process presented in Section 1.1.1, the antenna is equivalent to a magnetic-current source $\mathbf{M}$ radiating in free space in the presence of these two semi-infinite PEC planes. When the antenna thickness h is very small in terms of wavelength, the problem can be further approximated as shown in Fig. 1.3c. As explained above, this semi-infinite ground plane does not affect the far-field pattern. Therefore, the antenna can just be approximated as a magnetic current radiating into free-space (Fig. 1.3d). This treatment also agrees with the second example above (aperture in free space) because when the thickness h is small, the tangential magnetic field $\mathbf{H}$ becomes negligible, resulting in close-to-zero equivalent electric current $\mathbf{J}$.

As a validation of the analysis above, Fig. 1.4 shows the simulated radiation patterns in three fundamental planes of the antenna shown in Fig. 1.3a for the length corresponding to 0.48 wavelengths in free space. It can be verified that the antenna is indeed equivalent to a magnetic dipole radiating into free-space. The results also confirm that the application of the field equivalence principle presented above is very accurate when the antenna thickness is relatively small. Since all of the antennas investigated in this thesis are planar

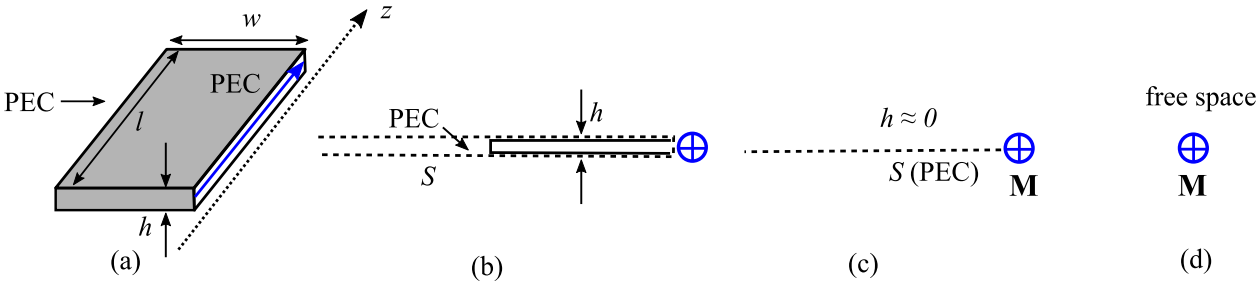

Figure 1.3. Aperture antenna with very thin profile. (a) A cavity antenna with thin aperture; (b) The cross-section with the chosen surface for applying the field equivalence principle; (c) The approximation when the thickness tends to zero; (d) The final equivalent problem.

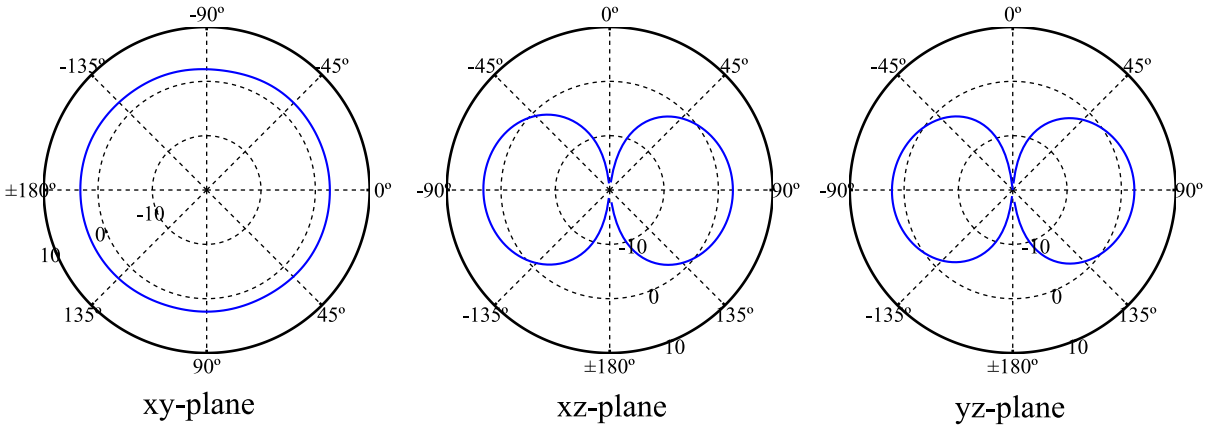

Figure 1.4. Gain pattern (dBi) of the cavity antenna with thin aperture. The antenna in Fig. 1.3a is simulated with $w = 10$ mm, $l = 20$ mm, $h = 0.787$ mm and relative permittivity $\epsilon_r = 2.2$. The resonance frequency is 7.2 GHz.

or low-profile, this treatment of the field equivalence principle will be used throughout the thesis to analyse the antennas' radiation mechanism.

1.2 Thesis Summary

This thesis aims to explore various antenna types from the magnetic-current source perspective. The field equivalence principle is demonstrated to be remarkably effective not only for an immediate understanding of the antenna radiation mechanism but also for a thorough analysis of the structure. The analytical and semi-analytical models proposed in

this thesis play an important role in the physical understanding as well as provide useful tool for rapid optimisations.

Inspired by the field equivalence principle, a wide range of novel antenna structures are also proposed. These structures are further developed and tailored for many different applications. Moreover, they are also thoroughly studied with many side effects being explored and discussed, mainly originating from knowledge gained from analytical considerations. Three main types of antennas are investigated in this thesis, including **travelling-wave antennas (TWAs), low-profile monopolar antennas and reconfigurable antennas**.

The overall contributions of this thesis can be listed concisely as

1. Various novel antenna designs, based on equivalent magnetic current sources, with unique characteristics or significant improvement in performance compared to that available in the literature.

2. The thorough understanding of those antennas based on analytical models using the field equivalence principle as the common underlying technique.

3. Different practical aspects related to those antennas such as design of feeding structures, antenna optimisations towards enhanced specifications or maximisation of the frequency tuning range in reconfigurable antennas.

A detailed list of contributions for each type of antennas will be shown in the next section as an overview of the thesis.

1.3 Thesis Overview

The thesis is divided into 8 chapters, including the Introduction and Conclusion chapters (Fig. 1.5). The main contributions of the thesis are divided into 3 major parts, each with a specific theme. The first part, discussed in Chapter 2 and Chapter 3, will examine variations of travelling-wave half-mode substrate-integrated waveguide (HMSIW) antennas and their optimisations. For these antennas, the field equivalence principle is used to analyse the radiation patterns of the antennas based on other analytical methods required to obtain the field distribution along the antenna aperture. The second part, presented in

Chapter 4, is about low-profile monopolar antennas designed based on an interpretation as magnetic-current loops using the field equivalence principle. The last part, spanning over three chapters, covers a wide range of reconfigurable antennas targeting various applications. The field equivalence principle is used to understand the antenna operational mechanisms. It also is the main inspiration opening concepts of different novel designs. Throughout the thesis, equivalent magnetic dipole and magnetic-current loop are derived from the antenna structures using this main technique. Each major part of the thesis is broadly self-contained.

1.4 Original Contributions

The topic and original contributions in each chapter are as follows.

- Chapter 2 reviews the HMSIW structure and its TWA applications. It is noted that using the field equivalence principle, this antenna can be shown to be equivalent to a magnetic dipole. A variational process to analyse the propagation constant of several HMSIW variations related to this thesis is proposed. The main contribution of this chapter is a semi-analytical model that is general and applicable for any nonuniform continuous-source TWA. This analysis is based on a lossy transmission line model of TWAs which takes reflections along the antenna into account. Different aspects of the antennas, including the near-field distribution and the effect from the feeding structure on the radiation patterns, are explored with the aid of the semi-analytical model. Finally, a transition for the integration of the HMSIW antenna into metallic structures, working in the millimetre-wave regime, is demonstrated.

- Chapter 3 focuses on the antenna optimisations with various performance targets. These include wideband operation and different pattern syntheses for the HMSIW antennas discussed in Chapter 2. The optimisation is based on the semi-analytical model proposed in Chapter 2 with the aid of different global optimisation techniques. Finally, a reliability-aware optimisation method for wideband antenna is demonstrated. For illustration, the wideband HMSIW antenna is chosen as an optimisation example. Nevertheless, the proposed framework is general and applicable

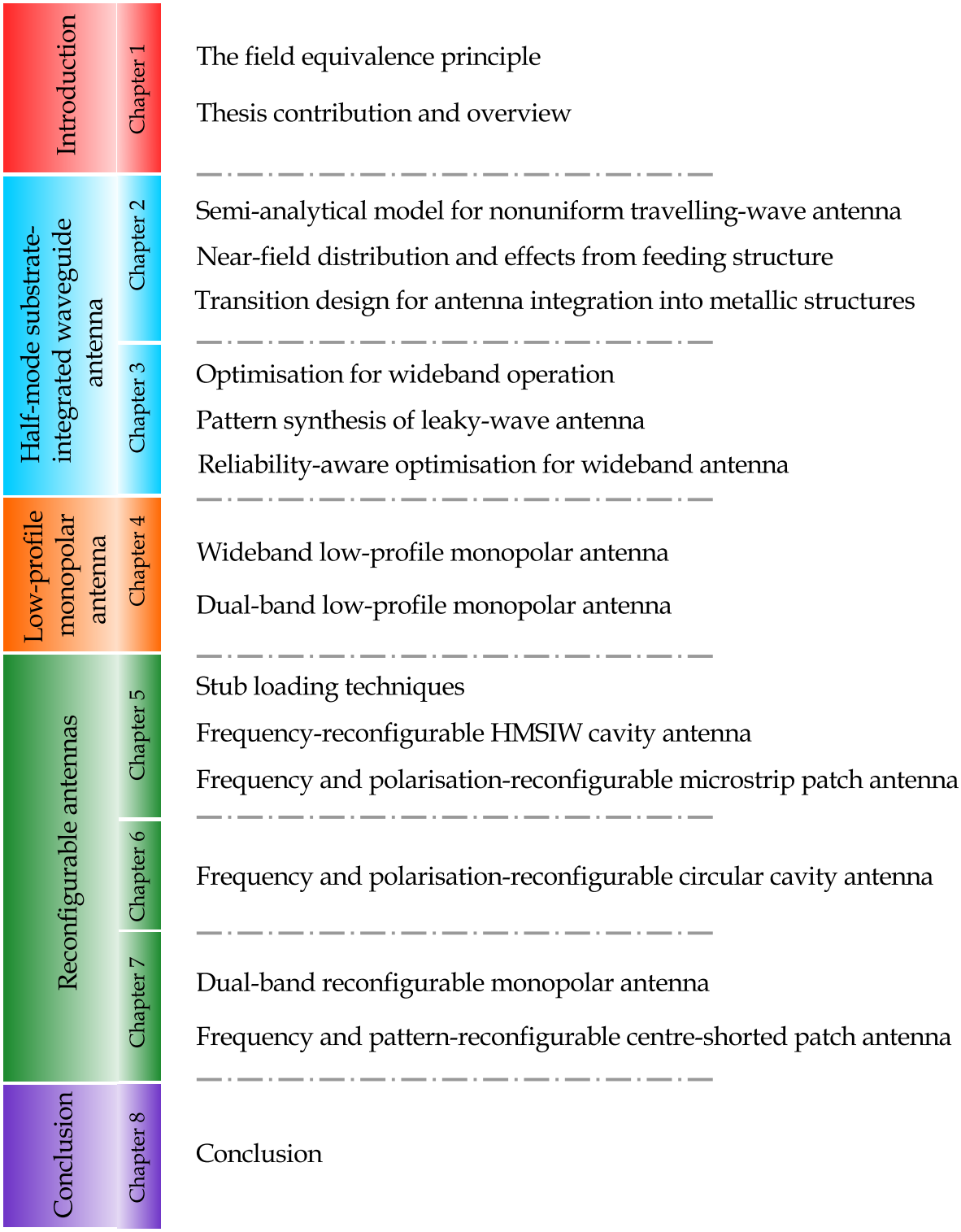

Figure 1.5. Thesis outline and contribution

for any wideband antenna provided that the reflection coefficient can be obtained in a fast manner.

- Chapter 4 is dedicated to low-profile monopolar antennas. Two novel designs are proposed in this chapter, including a wideband and a dual-band antenna. These designs are based on the addition of symmetrical slots on a patch, in designs which are inspired from the field equivalence principle of equivalent magnetic current loops. These antennas are investigated targeting the integration onto vehicle and helmet applications.

- Chapter 5 starts with a frequency-reconfigurable antenna based on an HMSIW cavity, where the tuning mechanism utilises varactors loaded with rectangular stubs. It is noted that the antenna is also equivalent to a magnetic dipole radiating on a ground plane whose effect can be removed with image theory. This reconfiguring method is extended for various different types of substrate-integrated circuits, including a microstrip patch, a quarter-patch and a quarter-mode substrate-integrated waveguide (QMSIW).

- Chapter 6 then proposes a novel frequency- and polarisation-reconfigurable antenna. In this design, the position and length of the equivalent magnetic-current source is reconfigured to change the resonance frequency and polarisation of the antenna.

- Chapter 7 demonstrates different reconfigurable realisations of the low-profile monopolar antennas. The dual-band antenna discussed in Chapter 5 is further developed with an independent reconfigurability in the two operating frequency bands. Finally, the monopolar mode in a microstrip patch antenna is utilised together with the conventional TM^{z}_{100} mode to design a radiator that can change its radiation pattern in a continuous range of frequency.

Chapter 2

Half-Mode Substrate-Integrated Waveguide Antennas

THIS chapter first reviews the concept of half-mode substrate-integrated waveguide (HMSIW) and its applications to design travelling-wave antennas (TWAs). A semi-analytical model based on transmission line matrices for this antenna type is demonstrated. The analysis is general and applicable for any nonuniform continuous-source TWA provided that the propagation constants for different cross-sections are available. The field equivalence principle is used to analyse the antenna's near-field and far-field radiations. Different aspects of the antennas, including the near field distribution, the transitions and its effects on the radiation patterns will also be explored. Based on this study, a feeding technique to integrate the HMSIW antennas into metallic structures in millimetre-wave regime is proposed.

2.1 Introduction

Since its introduction in 2006 [3], the half-mode substrate integrated waveguide (HMSIW) has been intensively investigated for many applications, especially due to its benefits at higher microwave frequencies. Many HMSIW antenna applications have been introduced in literature, including uniform [4–6] and periodic leaky-wave antennas (LWAs) [7–10]. The HMSIW has also been used as the "host" structure to design composite right-left handed (CRLH) LWA [11]. In all cases, as the power radiates from an array of slots or a long aperture, the obtained radiation patterns are highly directive. These radiation patterns are also frequency-dependent with a frequency-scanning main beam as a fundamental characteristic of LWAs [12]. Targeting different applications, a wideband omnidirectional travelling-wave antenna based on a tapered HMSIW has been introduced in [13] fed by a direct perpendicular coaxial-line transition [14]. Another realisation of the wideband tapered HMSIW on a circular ground plane has also been proposed in [15].

This chapter reviews the HMSIW structure and its TWA applications, including the uniform and non-uniform continuous-source structures. *For clarification, this thesis does not consider periodic LWAs as in [7–11].* The original contributions of this chapter include a generalised semi-analytical model which is applicable for any nonuniform continuous-source TWAs (published in [16]). The near-field distribution and the effects of the feed on radiation patterns are studied thoroughly based on this analytical model (published in [17]). A further main contribution is a millimetre-wave antenna designed for flush integration into metallic structures. This includes a dedicated feeding structure to reduce ripple level in the radiation pattern (published in [18]).

This chapter is structured as follows. Section 2.2 explains the HMSIW concept as an introductory background. The propagation constant analysis of the HMSIW and its variations are also shown here as part of the thesis' contributions. Section 2.3 reviews two HMSIW antenna applications that are relevant to this thesis. Section 2.4 presents the full analysis of the antenna, in which the aperture-field distribution is also examined. Finally, based on the proposed analytical model, Section 2.5 studies the effects from the feeding structure on the antenna radiation patterns. Finally, Section 2.6 presents a wideband millimetre-wave antenna targeting metallic structure integration with the minimised radiation ripples in its broad-beam pattern.

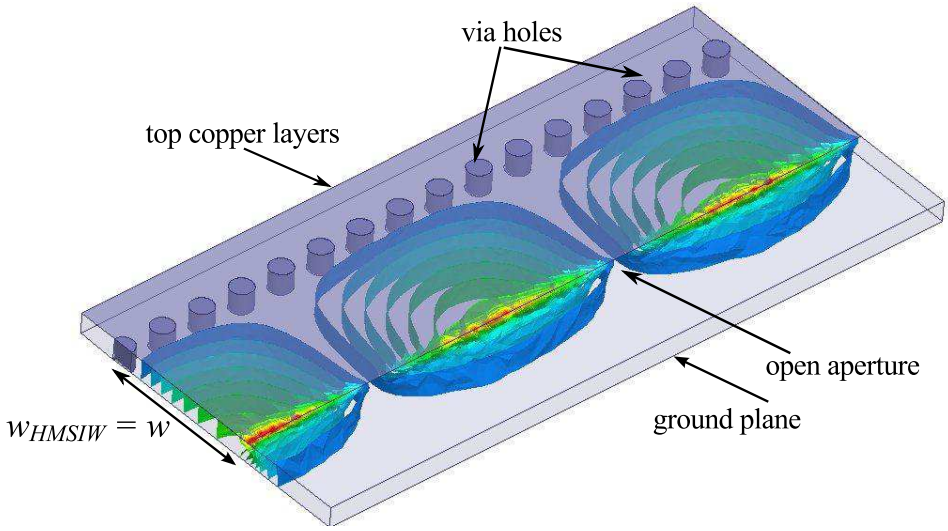

Figure 2.1. Field distribution for the fundamental mode of the HMSIW.

2.2 Half-Mode Substrate-Integrated Waveguide

2.2.1 Structure

The HMSIW is created by cutting an SIW into a half and extending the substrate from the open aperture side (Fig. 2.1). Since the thickness of the substrate is typically small compared to the operating wavelength, the aperture can be approximated as a perfect magnetic conductor (PMC), i.e. with perpendicular magnetic field. Therefore, the field distribution inside of the HMSIW is nearly half of that of an SIW. In the first introduction of this structure [3], the HMSIW was used as a transmission line at higher frequency due to a slightly lower loss compared to the SIW [19] and its advantage of smaller size. Later, it has been used more extensively to design LWA due to high radiation loss when operating close to cutoff [4, 13, 15, 20–22]. The structure is in fact the same as a half-width microstrip line, proposed at almost the same time [5, 23]. In these publications, the authors described the structure as half of a microstrip line working in the first high-order mode [24, 25]. Thus, interestingly, the structure can be interpreted as either half of an SIW or half of a microstrip line in the EH_1 mode. In fact, the half-mode-SIW interpretation has fostered the utilisation of this structure to design various microwave components such as [26–29]. For clarification, the term HMSIW is used throughout this thesis instead of half-width microstrip line.

The HMSIW has several variations. The following discusses those relevant to this thesis. The first one is the truncated HMSIW in which the extended substrate from the aperture side is removed (Fig. 2.2a). This structure has been used to design a wideband omni-directional horizontally-polarised antenna [13] and is reviewed in the next section. The second variation is the truncated HMSIW with additional infinite ground plane at the aperture (Fig. 2.2b). This structure is a substrate-integrated version of the travelling-wave slot antenna proposed in [30]. The millimetre-wave antennas discussed in Section 2.6 utilise this structure. Finally, another variation is the SIW with a longitudinal slot (Fig. 2.2c). This slot forces the field on the longer side to become a half-mode of a rectangular waveguide ($TE_{0.5,0}$ mode), as similarly as in the HMSIW. The field on the other side is typically small. This structure is useful when slot antennas on a large ground plane are desirable. Another advantage of this structure is that it can be fed using an SIW [31]. This structure is chosen to validate the analysis proposed in Section 2.4.

2.2.2 Propagation Constant

As one type of transmission line, the HMSIW can be characterised by its propagation constant. For the conventional HMSIW (Fig. 2.1) which can be treated as a half-width microstrip line, the propagation constant can be calculated analytically using the transverse resonance method (TRM) [32–34]. This method is well-known and is not discussed here for brevity. Instead, this section presents the use of a variational method to analyse the three variations of the HMSIW mentioned above. This technique follows the treatments in [30] with modifications depending on the considered geometry. It is noted that the use of the classical TRM method is not applicable in these considered structures since analytical formulas for the aperture impedance are not available.

Firstly, in all cases, the via holes walls are approximated as solid perfect electric conductor (PEC) walls using the effective width formula for an SIW. The correction term for the SIW width is [35]

$$\Delta = \frac{d^2}{0.95s}\,, \tag{2.1}$$

where d is the via hole diameter and s is the spacing between two adjacent vias. For Variation I and II, $w = w' - \Delta/2$ and for Variation III, $w = w' - \Delta$ and $a = a' - \Delta/2$ (see bottom figures in Fig. 2.2).

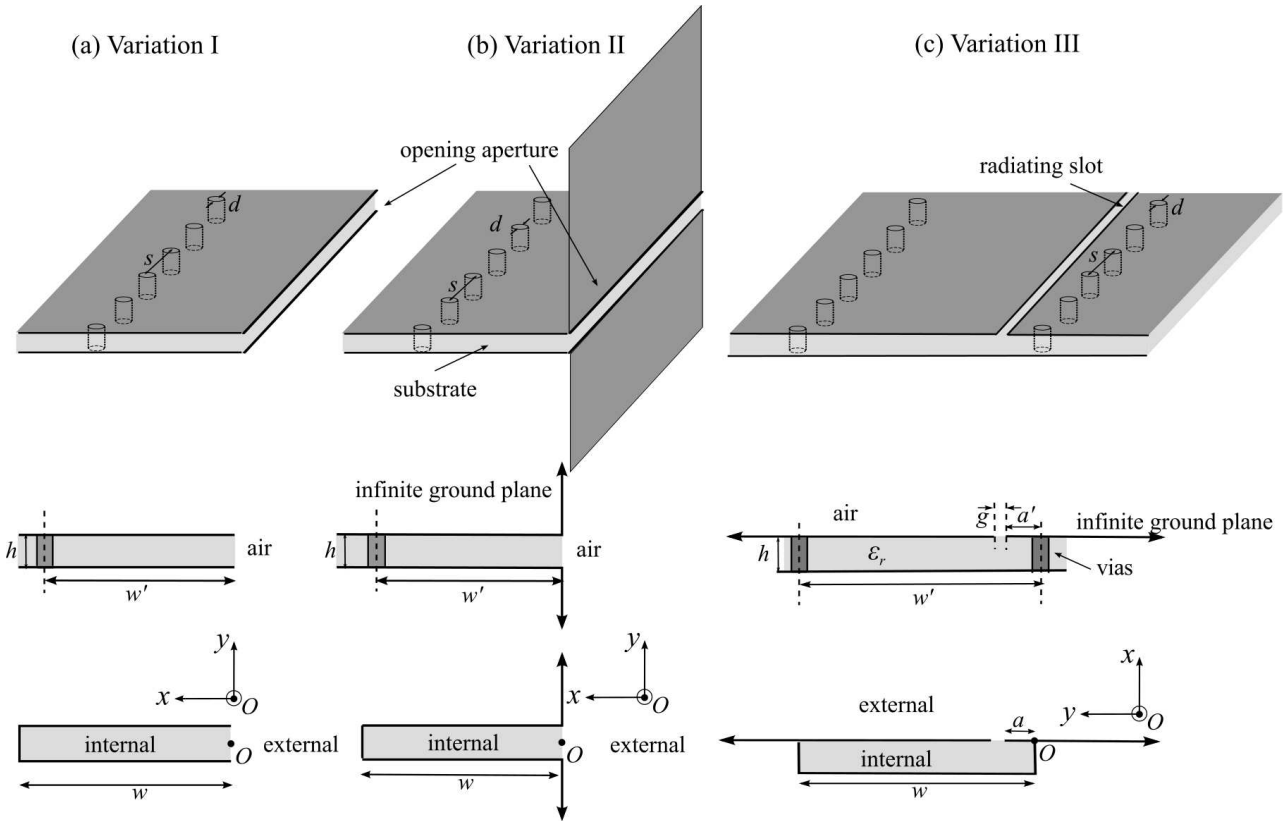

Figure 2.2. Variations of HMSIW. (a) The truncated HMSIW; (b) The truncated HMSIW with infinite ground plane; (c) the SIW with longitudinal slot. From top to bottom are the 3D-view, cross-section and its equivalent waveguide with solid PEC wall.

The space is now divided into internal and external regions with the radiating aperture as the boundary. The method employs a stationary expression for the propagation constant γ

$$\Phi(\gamma) = \int_{\text{slot}} \left[E_y({}^{i}H_z - {}^{e}H_z) + E_z({}^{i}H_y - {}^{e}H_y) \right] dy = 0, \tag{2.2}$$

where ${}^{i}H$ and ${}^{e}H$ are the internal and external magnetic fields corresponding to an assumed tangential electric field E_y and E_z in the slot [30]. It is noted that in Fig. 2.2, the coordinates are chosen such that the radiating apertures are in yz-plane. The assumed electric field distribution in the aperture (or slot) is chosen in accordance with the mode of propagation. The stationary equation (2.2) implies that a first-order change in the assumed

field distribution in the slot results only in a second-order change in the propagation constant. Therefore, by applying a reasonable assumption for the tangential field distribution in the slot, γ can be calculated with a high accuracy.

In the three considered cases, since the aperture size, i.e. radiating slot, is typically relatively narrow, a straightforward assumption on the electric field $(E_y = 1, E_z = 0)$ allows significantly simplifying the analysis while still yielding reasonably accurate results. With this assumption, equation (2.2) becomes

$$\Phi(\gamma) = \int_{\text{slot}} ({}^{i}H_z - {}^{e}H_z)dy = 0. \tag{2.3}$$

To evaluate $\Phi(\gamma)$, the field equivalence principle is first applied to obtain the equivalent magnetic current in the slot (see Chapter 1.1.1). An orthogonal mode expansion inside the waveguide with appropriate boundary conditions is used to obtain ${}^{i}H_z$. For the external field, two cases are considered:

- Without ground plane (Variation I): Since the antenna thickness is relatively small, the approximated equivalent problem is a single magnetic current source $\mathbf{M} = -\hat{\mathbf{n}} \times \mathbf{E}$ radiating into free space.
- With an infinite ground plane (Variations II and III): This case is similar to the aperture antenna with an infinite ground plane discussed in Section 1.1.2. Image theory can be used, which results in doubling the equivalent magnetic current $\mathbf{M} = -2\hat{\mathbf{n}} \times \mathbf{E}$.

The detailed procedure of derivation can be found in the Appendix of [30]. Here only closed-form expressions for the field integrals are shown. For the internal field,

$$\begin{aligned}\int_{\text{slot}} {}^{i}H_z(\gamma)dy &= \frac{j}{\omega\mu}\left[\frac{g^2 l_0}{w}\cot l_0 h\right. \\ &\quad \left. +2\sum_{n=1}^{\infty} X_n \cot l_n h \left(\frac{\ln w}{(n\pi)^2} + \frac{1}{w l_n}\right)\right]\end{aligned} \tag{2.4}$$

with

$$l_n = \sqrt{\epsilon_r k_0^2 + \gamma^2 - \left(\frac{n\pi}{w}\right)^2}. \tag{2.5}$$

where $k_0 = \omega/c$ and ϵ_r is the relative permittivity of the substrate. For Variation I and II, X_n is evaluated as

$$X_n = \left(\sin\frac{n\pi h}{w}\right)^2, \tag{2.6}$$

For Variation III, X_n is evaluated as

$$X_n = \left(\sin\frac{n\pi(g+a)}{w} - \sin\frac{n\pi a}{w}\right)^2, \tag{2.7}$$

For the external field,

$$\begin{aligned}\int_{\text{slot}} {}^{e}H_z dy &= \frac{1}{m\omega\mu}\left[g\kappa_e\left(\int_0^{\kappa_e g} H_0^{(2)}(u)du - H_1^{(2)}(\kappa_e g)\right)\right. \\ &+ \left.\lim_{u\to 0} uH_1^{(2)}(u)\right], \end{aligned}\tag{2.8}$$

with

$$\kappa_e = \sqrt{k_0^2 + \gamma^2} \tag{2.9}$$

and $H_i^{(2)}$ is the i^{th}-order Hankel function of second kind (noting that for Variations I and II $g = h$, i.e. the slot size is the same as the antenna thickness). The factor $m = 1$ if there is an infinite ground plane (Variation II and III) and $m = 2$ if there is no ground plane (Variation I). The stationary equation can be efficiently solved by an iterative Newton's process. The first guessed root of equation (2.3) can be chosen as

$$\gamma_0 = \sqrt{\left(\frac{\pi}{2w}\right)^2 - \epsilon_r k_0^2} \tag{2.10}$$

by approximating the HMSIW as the half-mode waveguide with a PMC wall at the aperture location. It is worth mentioning that the variational method has also been further investigated to successfully analyse different types of folded substrate-integrated waveguide, published in [36]. These results are put in Appendix A as a side result of this thesis.

Figures 2.3 show the results of the propagation constant γ for the cases of truncated HMSIW and slot HMSIW (Variations I and III). The multi-line method [37] is used to obtain γ from Ansys HFSS simulation. Very good agreement between analysis and numerical calculation is obtained, which validates the analytical method. Best results are obtained in

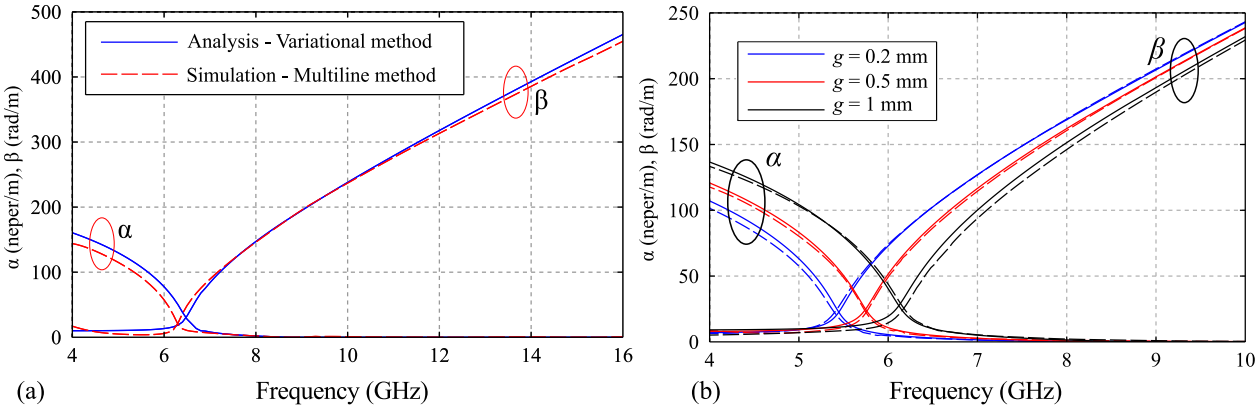

Figure 2.3. Validation of variational method. (a) Results for the truncated HMSIW (Variation I) with $w' = 7$ mm, $h = 1.524$ mm, relative permittivity $\epsilon_r = 2.5$, $d = 1.05$ mm and $s = 1.2$ mm. (b) Results for the SIW with longitudinal slot (Variation III) with $w' = 10$ mm, $a' = 1.5$ mm, $h = 0.787$ mm, $\epsilon_r = 2.2$, $s = 1$ mm, $d = 0.6$ mm.

the case of Variation III, i.e. with infinite ground plane, and small radiating slot size g. This is expected because when g is decreased, the assumed field distribution $(E_y = 1, E_z = 0)$ in the slot becomes more accurate. The next part of this section will describe a process to include dielectric and conductor loss in the calculation with a validating example using Variation II.

Extension to Include the Dielectric and Conductor Loss

The method above can be extended to include the dielectric and conductor loss, which becomes a crucial factor as the frequency increases. As an illustration, the truncated HMSIW with an infinite ground plane (Variation II) is used to validate the technique presented here. Firstly, the dielectric loss is incorporated into the variational analysis above by using the complex relative permittivity $\epsilon_r' = \epsilon_r(1 + j \tan\delta)$ where $\tan\delta$ is the loss tangent of the material. Secondly, the effect of conductor loss can be added by considering that the conductor loss in the HMSIW is close to that of an equivalent rectangular waveguide with the same height and the width of $a = w_{RG} = 2w$. An analytical formula for the conductor loss in a rectangular waveguide can be found in [38] (equation (66) p. 353, applicable for TE_{10} mode). For a well-designed HMSIW, the leakage loss of the spacing of via holes should be negligible compared to the dielectric and conductor losses, especially at high

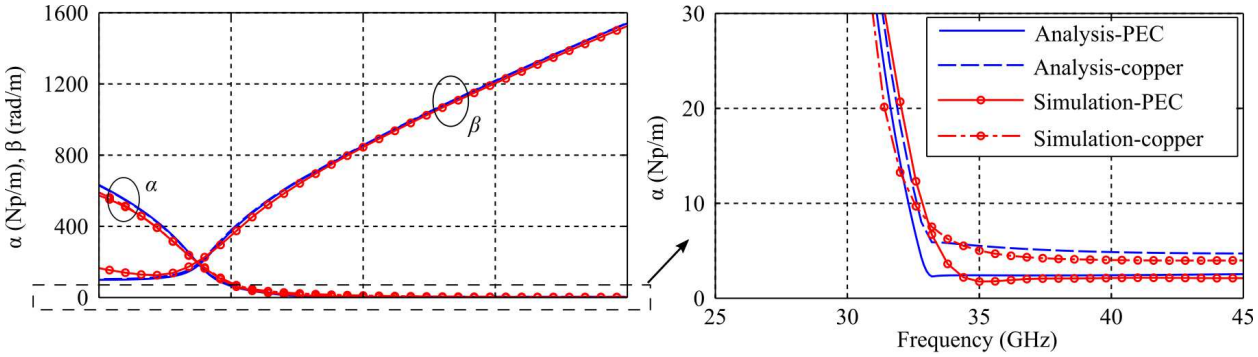

Figure 2.4. Propagation constant of the truncated HMSIW with infinite ground plane. The HMSIW width $w = 1$ mm and the dielectric loss $\tan\delta = 0.0019$ is considered in all cases. The right figure is a zoom-in of the left figure for visualising α. The legends are the same for both figures. The material chosen is Roger Duroid 6006 with thickness $h = 0.254$ mm and relative permittivity $\epsilon_r = 6.15$.

frequencies [39]. Figure 2.4 shows the comparison of the theoretically analysed propagation constant with results from full-wave simulation using the multi-line method [37]. Very good agreement between analysis and simulation is obtained which validates the proposed calculation method. The small discrepancy can be explained by the limitation of the equivalent rectangular waveguide model of the HMSIW when considering the conductor loss.

2.3 HMSIW Antenna Applications

For completeness, this section briefly summarises two types of TWAs based on the HMSIW structure that are relevant to this thesis. These antennas are chosen since radiation occurs along their aperture, for which the field equivalence principle can be applied. The consideration excludes periodic LWAs such as in [7] where the radiations occurs at perturbations such as slots. *For clarification, this section 2.3 is not part of the original contributions of this thesis.*

2.3.1 The Beam-Scanning Leaky-Wave Antenna

Since the HMSIW structure has radiation losses when operating close to cutoff, it can be used to design LWAs. The simplest design is the uniform structure proposed in [4, 5]. As a LWA, the power is progressively radiated along the open aperture. Thus, the antenna has high directivity with a very simple feeding structure, e.g. a tapered microstrip transmission line. The main beam depends on the propagation constant, which in turn is a function of frequency. Thus, as similar as any LWA, this type of antennas also possesses frequency-dependent scanning ability:

$$\theta_m(f) = \cos^{-1}\left[\frac{\beta(f)}{k_0(f)}\right] \tag{2.11}$$

where θ_m is the main beam direction defined with 0° in the guiding-wave direction and 90° at broadside. Furthermore, the antenna profile can be modified to reduce the sidelobe level as demonstrated in [40, 41]. This is further discussed in Chapter 3.

2.3.2 The Wideband Antenna

This antenna has been proposed in [13] targeting wideband operation and omnidirectional radiation pattens. The design was based on the same concept, i.e. high radiation loss of the HMSIW close to cut-off but with a different approach. In this design, the cut-off frequency is forced to increase along the length of the antenna by progressively tapering the HMSIW width as shown in Fig. 2.5a. The wave is guided along the HMSIW structure until it reaches the position where the cut-off frequency is close to the operating frequency, i.e. where the radiation losses from the open side of the guide become significant and the antenna starts to radiate intensively (Fig. 2.5b). Since the structure is planar, it acts as a short magnetic-current source radiating into free-space. As a results, the antenna achieves omnidirectional radiation patterns across a wide range of frequencies. This antenna was fed by a wideband perpendicular transition from a coaxial line that was proposed in [14].

Although this antenna type had been published before my Ph.D. candidature in [13], many aspects of this design are studied with much more insight and depth in this thesis. It is importantly noted that many later sections in Chapter 2 and 3 will refer to this antenna (Fig. 2.5).

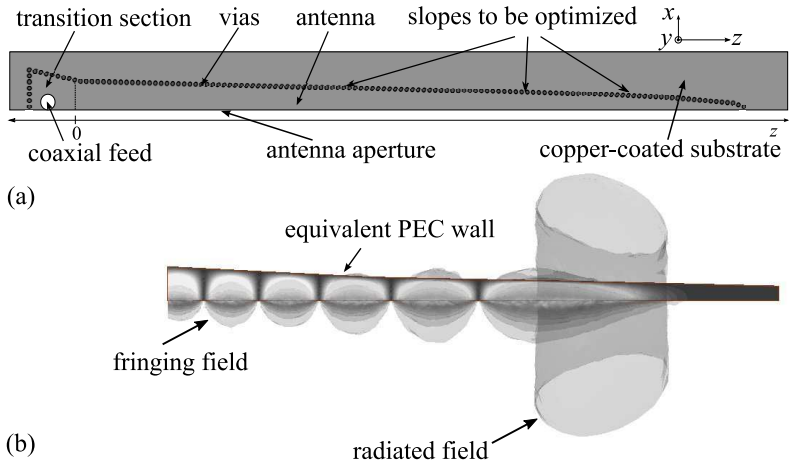

Figure 2.5. Design of a wideband antenna based on HMSIW. (a) Antenna structure [13]; (b) 3D representation of the field distribution.

Due to the difference in the radiation mechanism, in this thesis, the term travelling-wave antenna (TWA) **includes both antenna types** above while the term leaky-wave antenna (LWA) refers **only to the first type** (the highly directive beam-scanning antenna). It should be noted that the term TWA is more general and includes LWA [40].

2.4 Antenna Analysis

This section is the core contribution in this chapter. The nonuniform continuous-source travelling-wave antennas are thoroughly analysed using a lossy transmission line model, which is based on a waveguide circuit theory found in [42]. The conventional HMSIW with the substrate and ground plane extended from the open aperture, and the SIW with longitudinal slot (see Section 2.2) are chosen to validate the proposed analysis. These particular examples are selected here due to their simplicity, ease of fabrication and continuous-source profile. The findings in this section are published in [16]. The results are also compared with the traditional approach for analysing TWA [40] to demonstrate the accuracy improvement achieved with the proposed technique.

This section starts by revising the classical analysis of TWA as a background. Then the proposed model and analysis are presented, followed by a validation on the near-field distribution of the conventional HMSIW. A process to include a transition structure for

accuracy improvement is then illustrated, followed by the calculation of the far-field pattern.

2.4.1 Classical Analysis of TWA

The classical analysis of TWAs can be found comprehensively in [40]. Its main aspects will be briefly revised here to emphasise the critical assumptions employed in this analysis.

A continuous-source TWA is described by the varying propagation constant $\gamma(z) = \alpha(z) + j\beta(z)$ along the guiding direction, i.e. z-direction. Here $\gamma(z)$ can be calculated using various analysis methods such as transverse resonance method (TRM), variational method [40] or modal analysis [43]. Alternatively, it can also be obtained through simulation [7, 19, 37, 44] or experiment [40].

For the analysis of the radiation properties of a LWA, the source distribution function $A(z) = |A(z)|e^{j\psi(z)}$ is required to be computed. Here $A(z)$ is the equivalent current travelling along the antenna with phase $\psi(z)$. The radiation pattern can be readily calculated as a Fourier transform of $A(z)$.

The aim is to determine $A(z)$ from $\gamma(z)$. The traditional approach relates the attenuation constant α with the power along the source

$$2\alpha(z) = -\frac{1}{P(z)}\frac{dP(z)}{dz}. \tag{2.12}$$

For simplicity, assuming the lossless case (only radiation loss is present), $p_R = -dP(z)/dz$ can be interpreted as the power radiated per unit length. Therefore, p_R may be written as

$$p_R = C|A(z)|^2. \tag{2.13}$$

Combining these two equations, one can easily derive

$$|A(z)|^2 = \frac{1}{C}\alpha(z)e^{-2\int_0^z \alpha(\tau)d\tau}. \tag{2.14}$$

The phase $\psi(z)$ is simply

$$\psi(z) = -\int_0^z \beta(\tau)d\tau. \tag{2.15}$$

As Walter pointed out in Chapter 4 of [40], equation (2.13) is only true when considering the infinitesimal element dz radiating in isolation. This means the above analysis neglects

the reflections along a non-uniform structure and is only an approximation for travelling-waves [40]. Furthermore, the constant of proportionality C for an infinitesimal element dz is also assumed to be constant along the antenna, which is apparently not correct if the cross-section varies.

In summary, although the classical analysis is simple and provides a closed-form solution for the source distribution of any TWA, the aforementioned assumptions should always be considered before application. Under these assumptions, the classical analysis does not determine the true field propagating along the TWA. Instead, it links radiated power intensity to the magnitude of source distribution, i.e. equation (2.13). One of the biggest advantages of this analysis is that only the propagation constant $\gamma(z)$ is required to be computed. Modal field analysis is only needed to some extent in order to identify the polarisation of the TWA radiation pattern. It is noted that due to its simplicity, closed-form formulas and accurate prediction on the main beam direction, this type of analysis has still been regularly used in the recent literature [45–47].

2.4.2 Proposed Model and Analysis

The proposed analysis treats any smoothly varying non-uniform TWA as a lossy transmission line (TL) with variable complex impedance and propagation constant along its length. The theoretical framework described in [42] by Marks and Williams, which provides an accurate circuit model for travelling-wave structures is applied. Since a circuit model with voltage and current waves is involved, the analysis assumes a single mode propagating along the wave-guiding structure. This is a reasonable assumption since many TWAs are designed in the single-mode operation region of their host waveguide (so that only one set of propagation constant $\gamma(z)$ is considered). A generic non-uniform continuous-source TWA is illustrated in Fig. 2.6a.

The general idea of the analysis is to discretise the TWA into small sections which can be then approximated as uniform transmission lines (UTL). These small sections (illustrated Fig. 2.6b) can then be cascaded to obtain the network parameters of the whole structure. This would have been straightforward if the characteristic impedances would be real, but this is not the case for TWAs - hence the theory in [42] is utilised. It is emphasised that although the general concept is based on [48], the present analysis shows a much

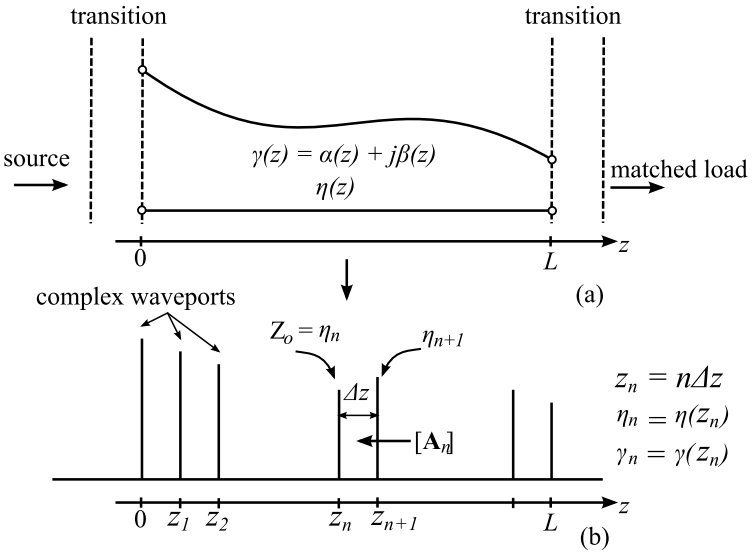

Figure 2.6. Nonuniform travelling-wave antenna. (a) A generic representation of nonuniform TWA: $\gamma(z)$ is the propagation constant along the antenna, η is the wave impedance which can be calculated from γ depending on the propagating mode, L is the antenna length; (b) Discretised model to analyse a non-uniform TWA.

more systematic approach and is general for a travelling-wave in a lossy single-mode transmission line. For completeness, the circuit model for a uniform lossy waveguide is summarised first and its application to calculate the field distribution along a non-uniform TWA is demonstrated.

Circuit model for a uniform section

In contrast to the traditional approach (Section 2.4.1), this model actually examines the physical field of a travelling-wave

$$\mathbf{E}_t = c_+ e^{-\gamma z}\mathbf{e}_t + c_- e^{\gamma z}\mathbf{e}_t \equiv \frac{v(z)}{v_0}\mathbf{e}_t \tag{2.16}$$

$$\mathbf{H}_t = c_+ e^{-\gamma z}\mathbf{h}_t - c_- e^{\gamma z}\mathbf{h}_t \equiv \frac{i(z)}{i_0}\mathbf{h}_t \tag{2.17}$$

where $\mathbf{e}_t$ and $\mathbf{h}_t$ are the normalised transverse modal field distribution, which are independent on z in a uniform section; v_0 and i_0 are normalisation constant of the waveguide voltage $v(z)$ and current $i(z)$. The normalisation constant for power and characteristic impedance are respectively [42]

$$p_0 = \int_S \mathbf{e}_t \times \mathbf{h}_t^* \cdot \hat{\mathbf{z}} dS = v_0 i_0^* \tag{2.18}$$

$$Z_0 = v_0/i_0 = |v_0|^2/p_0^* = p_0/|i_0|^2 = \frac{|v_0|^2}{\int_S |\mathbf{e}_t|^2 dS}\eta. \tag{2.19}$$

where η is the wave impedance, which satisfies $\hat{\mathbf{z}} \times \mathbf{e}_t = \eta \mathbf{h}_t$ and S is the cross-section of the waveguide, which in an assumption is the whole transverse plane for a LWA. When formulating this circuit model for a UTL, v_0 can be chosen arbitrarily and the modal field $\mathbf{e}_t$ can be normalised by any non-zero constant. Thus, only the phase of Z_0 is fixed, which is the same as that of the wave impedance η. The forward and backward travelling wave intensities are then defined respectively as

$$a_0 \equiv \frac{\sqrt{Re(p_0)}}{2v_0}(v + iZ_0);\ b_0 \equiv \frac{\sqrt{Re(p_0)}}{2v_0}(v - iZ_0) \tag{2.20}$$

By this definition, the travelling-wave is continuous and thus, it is possible to cascade series-connected two-port networks.

Field distribution calculation

The TWA is discretised into small sections as illustrated in Fig. 2.6b. Each interface between two adjacent sections is treated as one waveguide port. At each port, v_0 and $\mathbf{e}_t$ can always be selected and normalised such that

$$v_0(z) = 1 \text{ and } \int_S |\mathbf{e}_t(z)|^2 dS = 1. \tag{2.21}$$

This simple choice makes the characteristic impedance identical to the wave impedance $Z_0 = \eta$ (see equation (2.19)). The normalised constant of the travelling-wave intensity in equation (2.20) is then reduced to

$$\frac{\sqrt{Re(p_0(z))}}{2v_0(z)} = \frac{\sqrt{Re(\eta(z))}}{2|\eta(z)|}. \tag{2.22}$$

This is very convenient since $\eta(z)$ can be calculated from $\gamma(z)$ depending on the propagating mode of the travelling-wave.

At this stage, all necessary normalisation parameters are defined, and the analysis can proceed as follows: The ABCD-matrix of each approximately uniform section is calculated as

$$\begin{aligned}[\mathbf{A}_\mathrm{n}] &= \begin{bmatrix} A_n & B_n \\ C_n & D_n \end{bmatrix} \\ &\approx \begin{bmatrix} \cosh(\gamma_n \Delta z) & \eta_n \sinh(\gamma_n \Delta z) \\ \frac{1}{\eta_n}\sinh(\gamma_n \Delta z) & \cosh(\gamma_n \Delta z) \end{bmatrix}.\end{aligned} \tag{2.23}$$

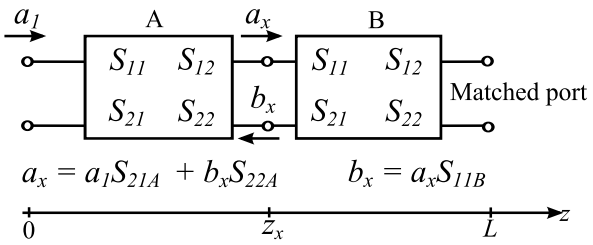

Figure 2.7. Voltage distribution calculation. Two series-connected two port network for the calculation of the voltage at the junction

Fig. 2.6b defines and illustrates how $[\mathbf{A}_n]$ is computed from γ_n and η_n.

The voltage at a particular position z_x along the antenna is calculated from the S-parameters of two series-connected two-port networks as illustrated in Fig. 2.7. These S-parameters are obtained by converting the corresponding cascaded ABCD-matrices with two complex port impedances [42] (see Appendix B). Under the normalisation of (2.21), the two equations in (2.20) can be combined to yield

$$v(z_x) = \frac{|\eta_x|}{\sqrt{Re(\eta_x)}}(a_x + b_x), \tag{2.24}$$

where η_x is the wave impedance at $z = z_x$. By relating a_x with a_1 and b_x using S-parameters of each section A and B, $v(z_x)$ can be obtained from (Fig. 2.7)

$$a_x + b_x = (S_{11B} + 1)\frac{S_{21A}}{1 - S_{22A}S_{11B}}a_1. \tag{2.25}$$

Let $v(0)^+$ and $\eta(0)$ be the forward voltage and the wave impedance at $z = 0$. From (2.24) and (2.25), the voltage at any position along the antenna is

$$v(z_x) = v(0)^+(S_{11B} + 1)\frac{S_{21A}}{1 - S_{22A}S_{11B}}\frac{|\eta_x|}{|\eta(0)|}\sqrt{\frac{Re(\eta(0))}{Re(\eta_x)}}. \tag{2.26}$$

It is noted that the calculation of these S-parameters can be carried out simultaneously when cascading the ABCD-parameters of each section.

From equation (2.16), $\mathbf{E}_t$ can be obtained as

$$\mathbf{E}_t(z) = \frac{v(z)}{v_0}\mathbf{e}_t = v(z)\mathbf{e}_t(z). \tag{2.27}$$

Hence, the electric field $\mathbf{E}_t$ can be calculated if $\mathbf{e}_t$ is known, provided $\int_S |\mathbf{e}_t(z)|^2 dS = 1$. Typically, finding $\mathbf{e}_t$ requires solving a boundary condition problem in 2 dimensions. For

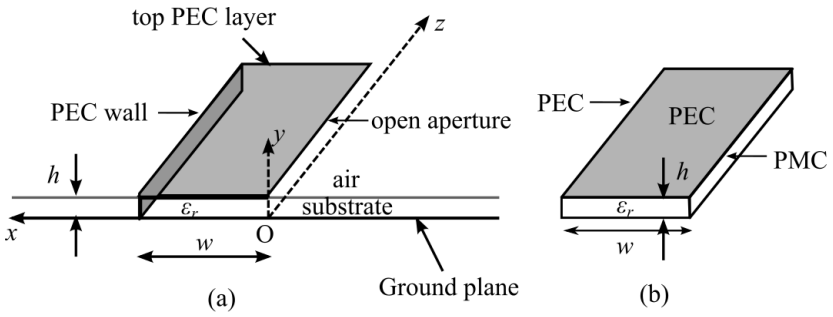

Figure 2.8. HMSIW structure. (a)The conventional HMSIW and (b) its corresponding unperturbed structure. The PEC wall can be realised by via-holes with accurate width conversion formula [49].

typical TWAs, a reasonable approximation can be made considering that the structure is a perturbation from a waveguide for which an exact solution of modal field is available. Thus, a good estimation is $\mathbf{e}_t \approx \mathbf{e}_{0t}$ where $\mathbf{e}_{0t}$ is the unperturbed modal solution. Furthermore, provided that the cross-section does not vary significantly along the TWA, one may just approximate $\mathbf{e}_t$ as constant versus position, in which case the field becomes simply proportional to the voltage $v(z)$.

2.4.3 Aperture-field Validation

As an initial validation, the aperture-field distribution will be calculated using the proposed method in comparison with the traditional approach and simulations using full-wave numerical software Ansys HFSS. The first structure chosen for investigation is the conventional HMSIW. For readers' convenience, the structure is shown again here in Fig. 2.8. The fundamental mode of a HMSIW is the half-mode $TE_{0,0.5}$, thus the wave impedance is calculated as

$$\eta_{TE}(z) = \frac{j}{\omega\gamma(z)}. \tag{2.28}$$

For demonstration of improvement over the classical analysis, a HMSIW with nonuniform profile is considered. The selected material is Rogers Duroid 5880 with relative permittivity $\epsilon_r = 2.2$ and thickness $h = 31$ mil $= 0.787$ mm. The antenna length is chosen as $L = 200$ mm. A simple linear width profile is selected as

$$w(z) = w_{start}(1 - Kz) \tag{2.29}$$

where the tapering constant $K = (w_{start} - w_{end})/L$ and w_{start} and w_{end} are start and end widths of the HMSIW. The voltage $v(z)$ along the waveguide is then obtained following the analysis in Section 2.4.2. To determine the waveguide field distribution, the HMSIW can be considered as a perturbation from an ideal rectangular waveguide with a perfect magnetic conductor at one side as illustrated in Fig. 2.8b. Therefore, the modal electric field $\mathbf{e}_t$ can be written approximately as

$$\mathbf{e}_t(x, y, z) \approx \sqrt{\frac{1}{w(z)h}} \cos\left(\frac{\pi x}{2w(z)}\right) \cdot \hat{\mathbf{y}}, \tag{2.30}$$

in which the normalisation condition in equation (2.21) is also satisfied. Thus, the field distribution at the antenna aperture $(x = 0)$ can be approximated as

$$\mathbf{E}(x = 0) \propto \frac{v(z)}{\sqrt{w(z)}} \hat{\mathbf{y}}. \tag{2.31}$$

Fig. 2.9 shows the analysis and simulation for the aperture field distribution at $f = 8$ GHz for $w_{start} = 9$ mm, $L = 200$ mm and $w_{end} = 5$ mm ($K = 0.02$). Excellent agreement can be observed between the proposed analysis and the corresponding simulation, which validates the accuracy and correctness of the analysis. From these results, three expected physical features can be noticed:

1. The distributed reflections along the waveguide due to the tapering effect result in a standing-wave.

2. The structure radiates extensively when the length reaches a certain value, i.e. $z \geq 160$ mm. This is because α starts increasing sharply as the width is reduced close to the cut-off of the waveguide [19].

3. Before this position of extensive radiation, the field strength increases slightly along z since the width is decreased and the power density should be increased (without much radiation).

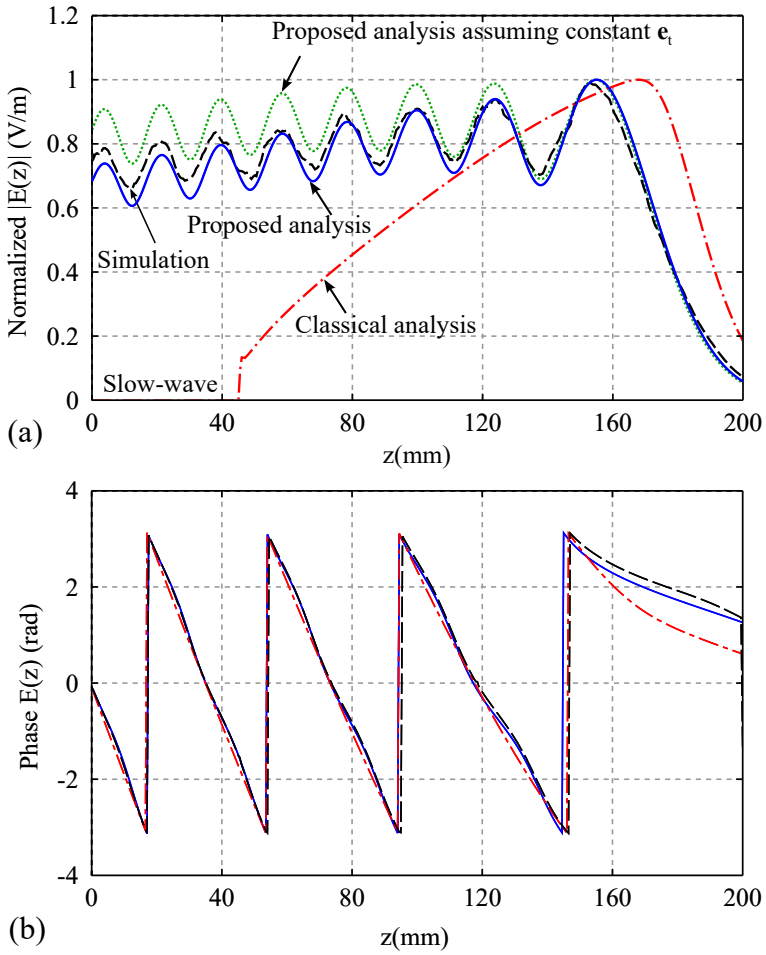

Figure 2.9. Aperture field distribution of the tapered HMSIW. Normalised aperture field ($x = 0$) of the a tapered HMSIW at $f = 8$ GHz for $w_{start} = 9$ mm, $L = 200$ mm and $w_{end} = 5$ mm ($K = 0.02$): (a) Magnitude; (b) Phase. The legend is the same for both figures: solid lines for proposed analysis; dotted lines for proposed analysis assuming constant $\mathbf{e}_t$; dot-dashed line for classical analysis and dashed lines for simulation.

The results for the source of radiations using traditional approach [40] (Section 2.4.1) is also included in Fig. 2.9. It can be observed that the classical analysis result exhibits a large discrepancy compared to simulation. In Fig. 2.9, when $z \in (0, 45)$ mm, the classical analysis yields zero field distribution because $\alpha(z) = 0$ in this region, i.e. the slow-wave region. These considerations take into account the fact that the slow-wave does not radiate and this part can thus be excluded in the calculation of the near-field and far-field. Although this is a reasonable assumption, it is however not rigorously true because the non-radiating property of slow-wave is only exact for infinitely long and continuous

waveguide. As soon as non-uniformity or discontinuities are included, which is the case for any finite-length LWA, radiation (even if weak) will occur. It can be concluded that the classical analysis may give a reasonable prediction on the far-field pattern but fails to yield physically meaningful aperture-field or near-field distributions.

It can be noticed further that if the cross-section along the antenna does not vary significantly, it is possible to simply approximate $\mathbf{E} \propto v(z)\hat{\mathbf{u}}$ where $\hat{\mathbf{u}}$ is the unit vector of electric field polarisation. As demonstrated in Fig. 2.9a (dotted line), this still provides a reasonable approximation on the aperture field distribution of the antenna. The near-field distribution of this type of tapered LWA has been validated through experiment in [50].

Using the field equivalence principle, the source distribution of a LWA, i.e. the equivalent current, can be shown to be proportional to near-field distribution. In summary, based only on the knowledge of the propagation constant $\gamma(z)$ (similar to the classical approach), using the proposed analysis, one can always obtain a much more accurate prediction on the radiation source distribution of a LWA than the traditional approach (using $\mathbf{E} \propto v(z)\hat{\mathbf{u}}$). A very accurate prediction of the field can be obtained if a close approximation of the modal field is available, e.g. as provided in this case through (2.30).

As a validation for the generality of the method, the substrate-integrated waveguide (SIW) with continuous longitudinal slot is also investigated. As proposed in [31], to reduce the cross-polarisation, the slot is kept straight while the shape of the PEC side walls is altered along the waveguide (Fig 2.10). The width of SIW is kept constant as $w_{SIW} = 10$ mm. Other parameters are substrate thickness $h = 0.787$ mm, relative permittivity $\epsilon_r = 2.2$, antenna length $L = 150$ mm and slot width $g = 0.2$ mm. The shape of the SIW is defined using parameter x_0, which is chosen in this investigation case as a cosine function

$$a(z) = k_1 + k_2 \sin(\frac{\pi z}{L}). \tag{2.32}$$

Figure 2.11 shows the analysed and simulated electric field distribution on the slot at $f = 7$ GHz for the case $k_1 = 2.5$ mm and $k_2 = -2$ mm. Similar features as for the previous case can be observed, which further demonstrates the general applicability of the proposed model.

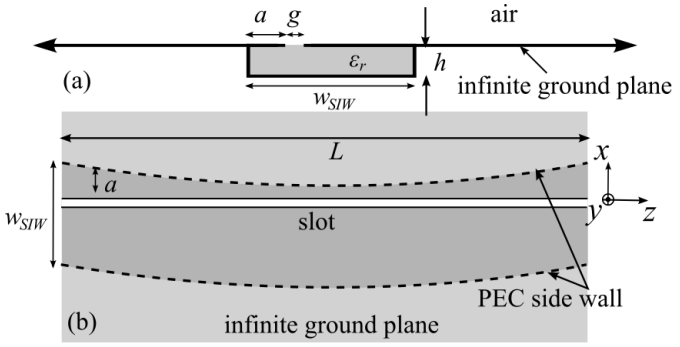

Figure 2.10. A slotted SIW LWA with meadering side walls. (a) Cross-section; (b) Top view.

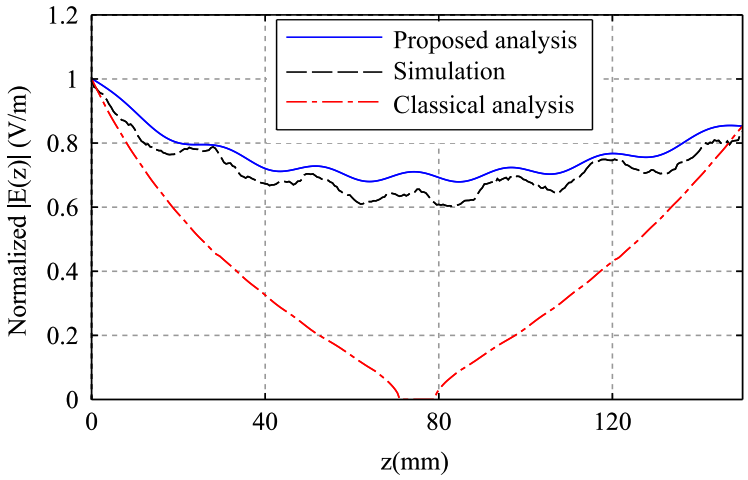

Figure 2.11. Normalised magnitude of aperture electric field of a non-uniform slotted SIW.

2.4.4 Method Limitation for Rapidly Changing Structure

As stated in Section 2.4.2, the assumption for the proposed analysis is that only one mode is propagating along the waveguide. This implies that the results will degrade for increasingly rapid profile variations of the leaky-wave structure, as these can excite higher-order modes. In order to illustrate this feature, a HMSIW with the width profile

$$w(z) = w_0 - w_A \sin(\frac{2\pi z}{L_p}) \tag{2.33}$$

is considered. The highest variation in the width is $w_{\max}/w_{\min} = (w_0 + w_A)/(w_0 - w_A)$ and the maximum slope of the width with respect to the guiding direction is $2\pi w_A/L_p$. Figure 2.12 shows the analysed and simulated near-field distribution at $f = 8$ GHz (wavelength $\lambda = 37.5$ mm) for different values of w_A and L_p while w_0 is fixed at 9 mm for an

antenna length $L = 150$ mm. It can be confirmed from Fig. 2.12 that the accuracy of the analysis decreases with increasing w_A and decreasing L_p. It is noted that rapidly changing TWAs are often used in periodic structures [51, 52], which is not the general type of problem addressed in this thesis. In contrast, for many of applications of continuous-source TWA structures, the method still shows an excellent agreement and high degree of improvement compared to the classical formula as further shown in Chapter 3.

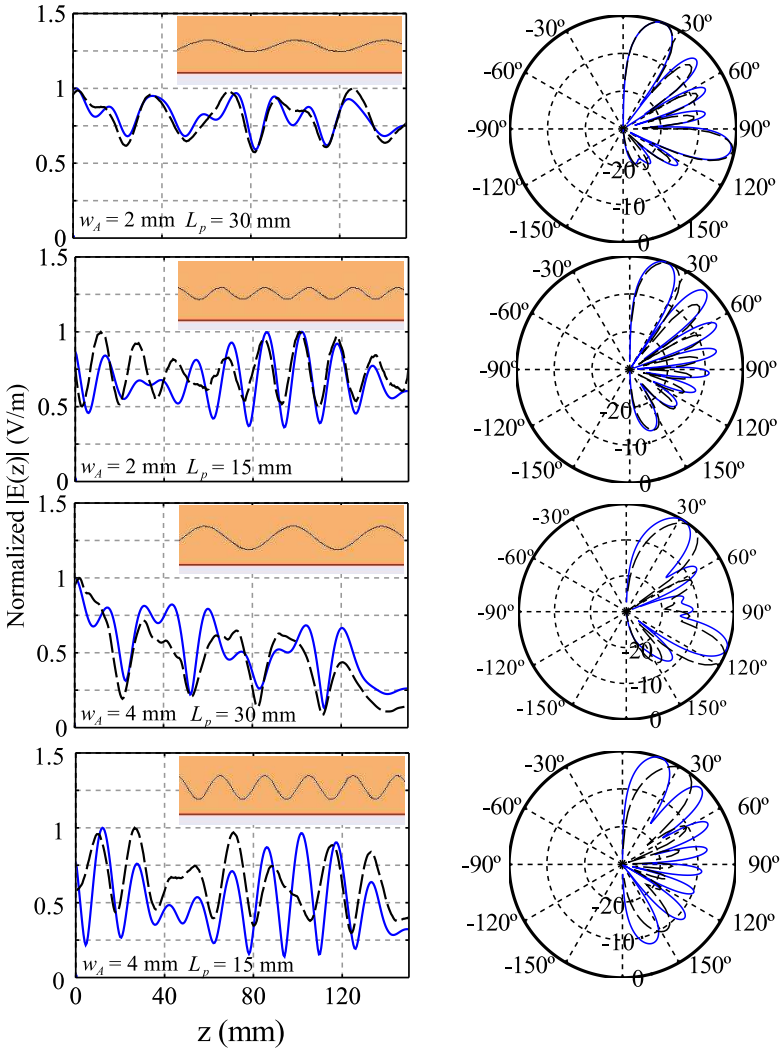

Figure 2.12. Aperture field of more rapidly changing HMSIWs. Normalised magnitude of aperture field of more rapidly changing HMSIWs and the corresponding normalised radiation pattern at $f = 8$ GHz (width profile shown in equation (2.33), $w_0 = 9$ mm, $L = 150$ mm). Blue solid lines: analysis, black dashed lines: simulation. The insets show top views with the same scale of the width and length of the HMSIWs.

2.4.5 Inclusion of Feeding or Load Transition Structure

Typically, the feeding and load transitions can be designed to provide nearly perfect impedance matching for relative narrow band antenna. However, for wideband designs, e.g. devices with about 80% relative bandwidth such as in [13, 15], the effect of the feeding/load transitions should be included for more accurate prediction on S-parameters. This section will demonstrate how this can be carried out with the aid of a numerical simulation tool.

The general concept is simply to obtain the ABCD-matrix of the feeding structure from simulation and then cascade it with the ABCD-matrix of the LWA (Fig. 2.6)

$$[\mathbf{A}_{\text{structure}}] = [\mathbf{A}_{\text{transition1}}] \cdot [\mathbf{A}_{\text{antenna}}] \cdot [\mathbf{A}_{\text{transition2}}]. \tag{2.34}$$

However, extreme care needs to be taken when simulating the feed to obtain $[\mathbf{A}_{\text{transition}}]$. This is because by definition, ABCD-matrix relates the voltage and current at two ports, which in turn depend on the simulated port impedance. Furthermore, the port impedance Z_0 depends on the definition used in the simulator.

In [42], Marks and Williams showed that the scattering parameter of a travelling-wave is constant with the normalisation factor of v_0. Therefore, to obtain the correct ABCD-matrix to be used in equation (2.34), one should simulate the transition structure using a matched port, e.g. without normalisation on impedance when using ANSYS HFSS. This will yield the true S-parameter of the travelling-wave. Then these obtained S-parameters can be converted into ABCD-matrix as shown in the Appendix B [42]. When performing this conversion, the port impedances at the interfaces between the antenna and the transitions (Fig. 2.6a) are the characteristic impedances that are chosen for the LWA, i.e. $\eta(0)$ and $\eta(L)$ (Fig. 2.6b).

The effect of including the feeding structure will be demonstrated in Chapter 3, Section 3.3 where fully optimised antennas are designed together with their transitions. It is worth emphasising that the transition can be typically designed and simulated separately from the antenna. The ABCD-matrix can be extracted once only to be placed in the pattern synthesis or any optimisation process. Therefore, the above procedure can improve the accuracy for the prediction of the S-parameters of the whole structure without noticeably increasing the design time.

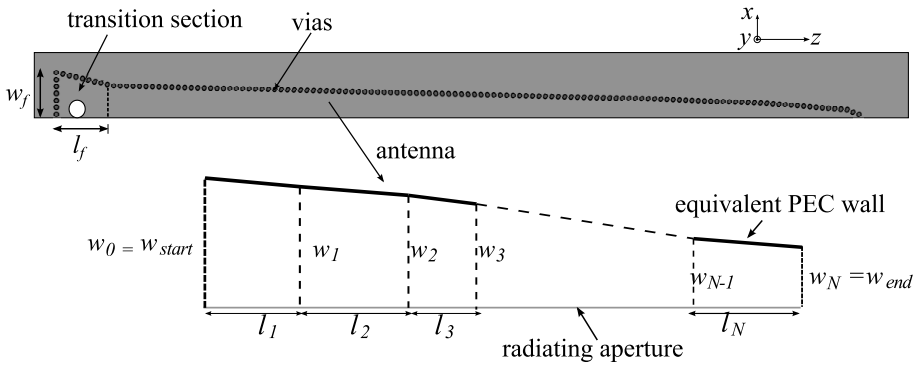

Figure 2.13. Geometry of a wideband tapered HMSIW antenna. This antenna was presented in [48].

Table 2.1. Dimensions of the wideband tapered HMSIW optimised for bandwidth 6.7 GHz to 17 GHz.

widths	w_0	w_1	w_2	w_3	w_4	w_5	w_6	w_7	w_8	w_9
values (mm)	7.0	6.5	6.0	5.5	5.0	4.5	4.0	3.5	3.0	2.5
lengths		l_1	l_2	l_3	l_4	l_5	l_6	l_7	l_8	l_9
values (mm)		34.55	23.91	20.38	16.46	15.52	13.31	10.79	9.88	15.77

2.4.6 Antenna Radiation Patterns

Once the field distribution can be calculated along the radiating aperture of the antennas, the field equivalence principle can be used to obtain the radiating source. Basically, the radiating source is proportional to the aperture-field distribution $A(z)$. The far-field pattern $E(\theta)$ is then calculated using the well known formula [40]

$$E(\theta) = G(\theta) \int_0^L |A(z')| e^{j[\psi(z') + k_0 z' \cos\theta]} dz'. \tag{2.35}$$

where $G(\theta)$ is the element pattern.

For illustration, a wideband tapered HMSIW antenna (Fig. 2.13 - see more in Section 2.3.2) optimised for the bandwidth from 6.7 GHz to 17 GHz is considered. This antenna was presented in [48]. The width profile of this antenna is shown in Table 2.1. The transition parameters are $l_f = 14$ mm and $w_f = 10$ mm. The substrate is chosen as Roger Ultralam 2000 with relative permittiviy $\epsilon_r = 2.2$ and thickness $h = 1.524$ mm. To obtain an accurate prediction on the far-field pattern, the field distribution in the feeding section should be

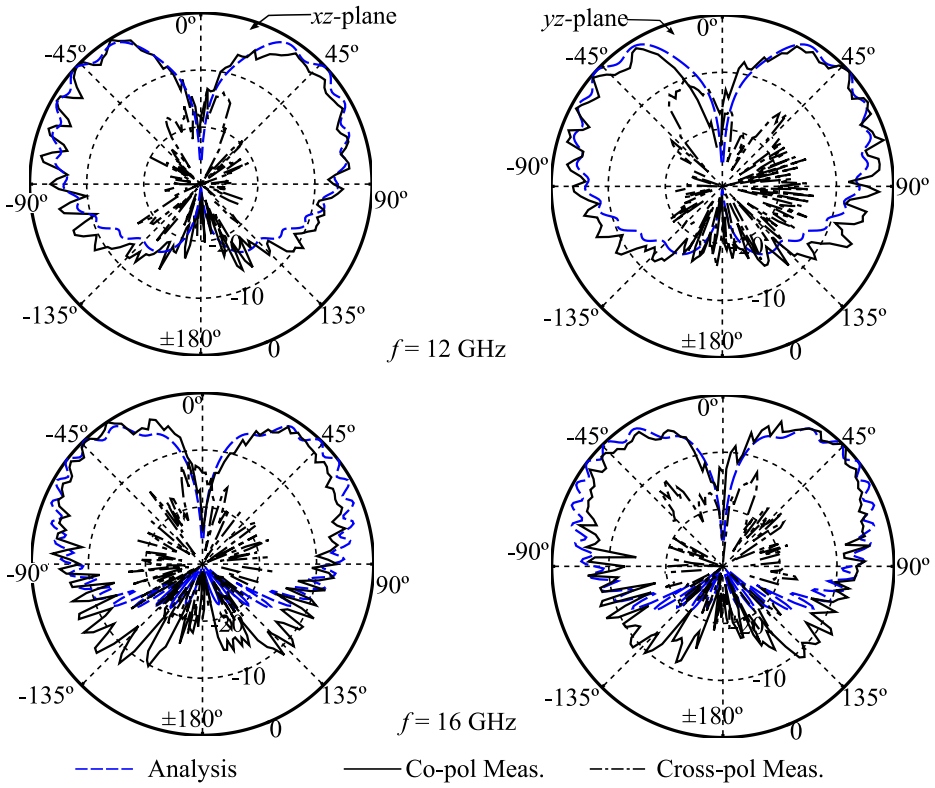

Figure 2.14. Far-field radiation patterns of the wideband tapered HMSIW antenna. The antenna shown in Fig. 2.13 with geometry defined in Table 2.1 is used for illustration.

taken into account. This is carried out using the Green's functions for a rectangular waveguide terminated by a short circuit at it ends [53]. The treatment can be found in [48] and is not shown here as it is not part of the thesis contribution.

The analysis presented in the previous section is used to calculate the aperture field distribution $A(z)$ from which the equation 2.35 is used to calculate the far-field pattern. The results are plotted in Fig. 2.14 for two frequencies in the operating band. As expected from the radiation mechanism explained in Section 2.3.2, gain patterns with two symmetrical broad beams in the xz- and yz-planes are obtained. Analysis and measurement show good agreement, which further validates the proposed analysis. It is noted that both results show certain levels of ripples in the patterns. The origin of these ripples are investigated in the next section. Extensive numerical and measurement validations on various far-field patterns will be shown later in Chapter 3 together with different antenna optimisations.

2.5 Effect of Feeding Structure on Radiation Patterns

The parasitic effects from the feed and termination on the far-field pattern of the HMSIW antenna with highly tapered width-profile mentioned in Section 2.3.2, are thoroughly investigated in this section. The motivation is to study the ripples in the radiation pattern as shown in Fig. 2.14. The original contribution of this section has been published in [17].

This section first shows the analytical computation of the electric field in the near-region of the antenna based on the analytical model proposed in the previous section and the field equivalence principle. From this result, the effects of the feed and termination on the pattern are determined.

2.5.1 Near-field Calculation

In order to physically explain these ripples, the electric field in the vicinity of the antenna is calculated and compared with simulation. For this investigation, the antenna shown in Fig. 2.13 with geometry defined in Table 2.1 is used. The aperture field distribution is computed using the lossy transmission line model in Section 2.4. The coordinates used for the near-field calculation is defined in Fig. 2.15. The x-axis separates the transition and antenna sections. By using the field equivalence principle, the antenna is approximated as a magnetic dipole radiating into free space with magnetic current $\mathbf{M}$ whose magnitude is proportional the aperture field distribution.

For demonstration, the field in half xz-plane ($y = 0, x < 0$) will be calculated and shown in this section. Similar field distributions are observed in other planes containing the z-axis since the radiation pattern is almost omnidirectional in the xy-plane. The field at position $P(x, 0, z)(x < 0)$ is given as [2]

$$E_y = -E_\phi = -\int_{-l_f}^{L} \frac{jkhM_z(z')\sin\theta}{4\pi r}\left[1 + \frac{1}{jkr}\right] e^{-jkr} dz'. \tag{2.36}$$

where

$$r = \sqrt{(x^2 + (z - z')^2}, \tag{2.37}$$

$$\theta = \tan^{-1}\left(\frac{-x}{z - z'}\right)(0 \leq \theta \leq \pi), \tag{2.38}$$

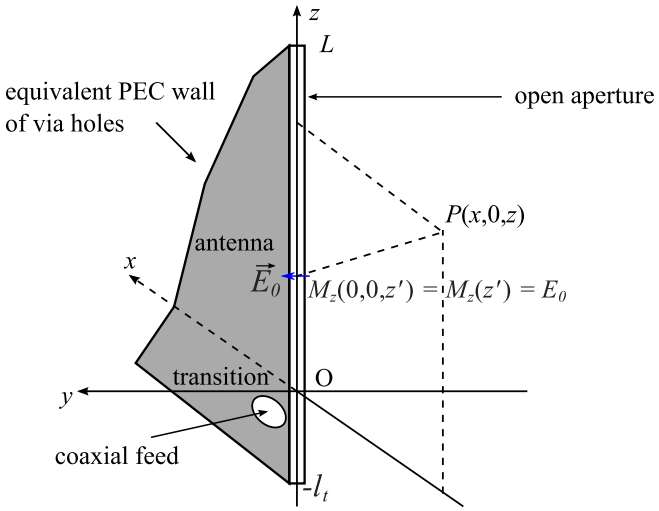

Figure 2.15. Near-field calculation set up. Coordinate system used for calculation of the near-field distribution of the antenna shown in Fig. 2.13.

h is the thickness of the substrate, l_f is the length of the transition section, L is the length of the antenna and $k = \frac{\omega}{c}$ is the free-space wavenumber.

Equation (2.36) can be computed easily by a discretisation of the antenna aperture along the z-axis. The semi-analytically calculated electric field in the vicinity of the antenna is shown in Fig. 2.16. The corresponding simulated magnitude of electric field strength is shown Fig. 2.17. It is noted that the field strengths are normalised not to the maximum value in the half xz-plane but are capped to a chosen value for a better visualisation of the field far away from the antenna. Very good agreement between analysis and simulation verifies the computation approach. It can be observed from Fig. 2.16 and 2.17 that the antenna mostly radiates around the cut-off position. The wavefronts are almost circular around a centre located approximately at the cutoff position. This is reasonable as the antenna was optimised to achieve a low directivity pattern. It is worth noting that if the rate of tapering is not fast enough, the antenna radiation mechanism will evolve towards that of a uniform LWA.

Examining the near-field radiations from Figs. 2.16 and 2.17, one can observe a weaker secondary source of power radiation located at the transition, i.e., close to the feeding point. This is reasonable because a slow-wave radiates at field discontinuities [40], pp.14-15. This secondary radiation interferes with the main radiation and causes the ripples in

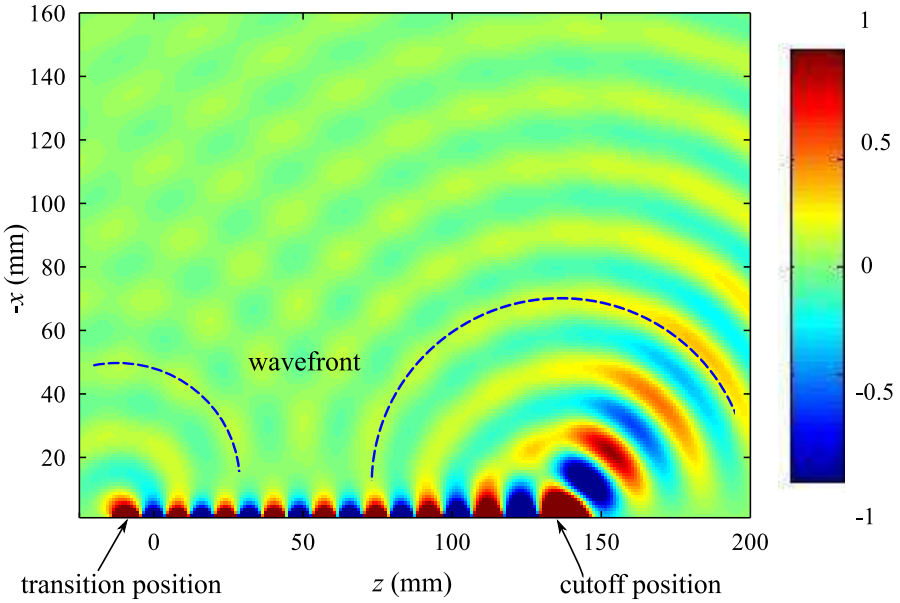

Figure 2.16. Calculated electric field $E_\phi = -E_y$ in xz-plane at $f = 14$ GHz.

the far-field pattern. For a given antenna geometry, the level and the number of the ripples depend on the operating frequency. When the frequency is higher, the wavelength is shorter and the distance between the main radiation at cutoff and the transition is longer, which causes more ripples in the pattern. Another observation is the decrease in the ripple level with increasing frequency, which can be explained by the fact that more energy concentrates inside the substrate at the transition position at higher frequency.

2.5.2 Simulation Results with No Discontinuity at the Transition

It has been shown that the ripples in the radiation pattern come from parasitic radiation at the transition position. In order to verify that this is the only source of the ripples, an identical antenna with a very large feeding waveport is simulated using a commercial electromagnetic simulation tool (HFSS) as shown in the Fig. 2.18. Although there is still some diffraction at the edge, the waveport is large enough to avoid any significant radiation or diffraction at the transition of the antenna.

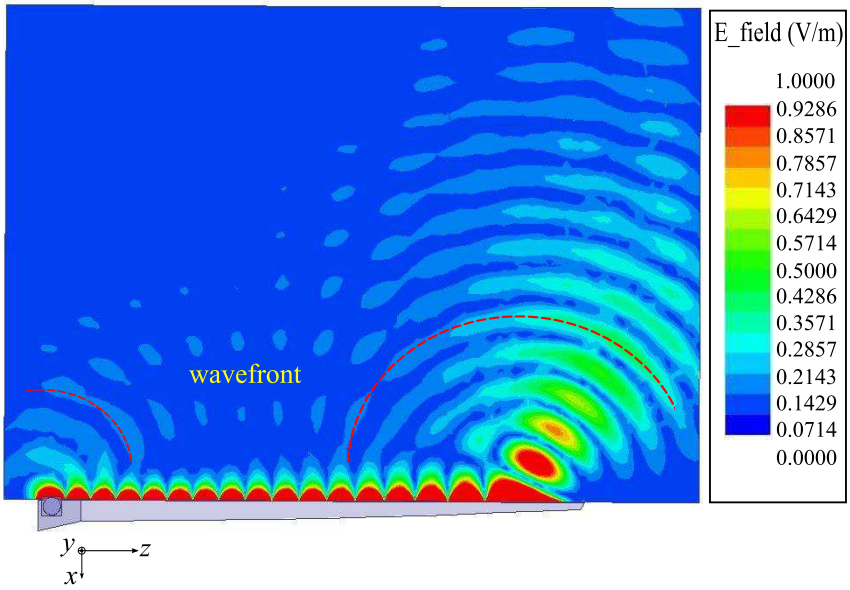

Figure 2.17. Simulated electric field magnitude $|E_\phi| = |E_y|$ in xz-plane at $f = 14$ GHz.

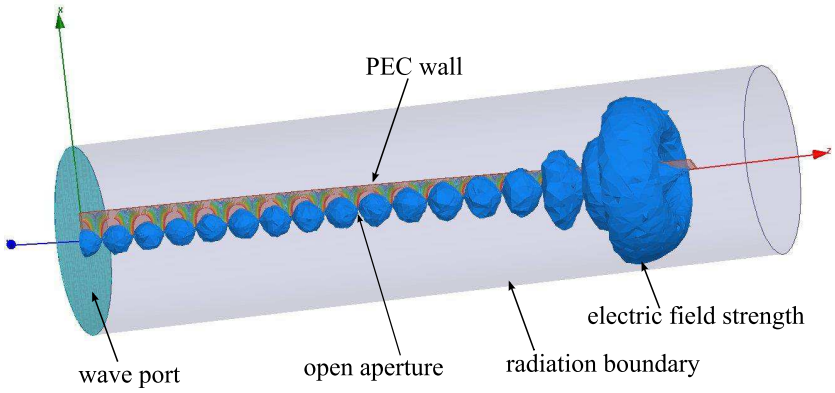

Figure 2.18. HFSS simulation setup to remove the discontinuity at the transition. Field strength is shown for $f = 14$ GHz.

The radiation pattern of such a conceptual antenna is shown in Fig. 2.19 with dash-dot curve. This radiation pattern exhibits a very broad beam with almost no ripple compared to the analytically computed and numerically simulated radiation patterns of the practical antenna with transition section, also depicted in Fig. 2.19. This confirms that the observable ripples do not come from either reflected waves inside the tapered HMSIW or multiple radiations at different angles along the antenna (noting that the phase constant β varies along the antenna length), which initially seems to be a reasonable explanation.

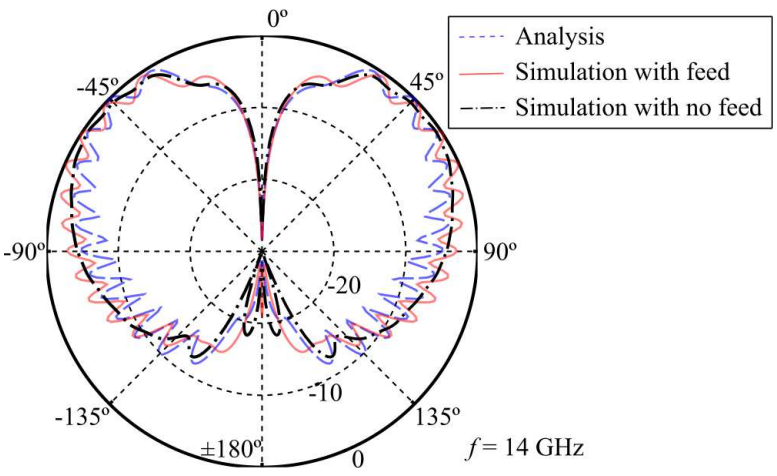

Figure 2.19. Analytical and simulated radiation patterns. The dot-dash curve is the simulated radiation pattern of the conceptual antenna with nearly perfect feed shown in Fig. 2.18. The dash and solid curves show the calculation and simulation, respectively, of the radiation pattern of the antenna with transition. All patterns are plotted at $f = 14$ GHz.

2.5.3 Recommendation for Reduction of Parasitic Ripples

In case of a uniform LWA, reduction in the pattern ripples are typically achieved by varying the attenuation constant α or making the antenna longer [54]. For the highly tapered HMSIW antenna (Fig. 2.5), reducing level of ripples does require different techniques since the problem lies at the transition section rather than at the load as in case of a uniform LWA.

The analysis shown above suggests that in order to reduce the level of ripples for the tapered HMSIW antenna, one should reduce the radiation at the transition. This can be partly achieved by increasing the relative permittivity and decreasing the thickness of the substrate so that most of energy close to the transition remains well confined within the waveguide. Ultimately, a transition that can minimise the discontinuity in the field is the most desirable. Such a transition is shown in the next section in a design of millimetre-wave antennas integrated into metallic structures.

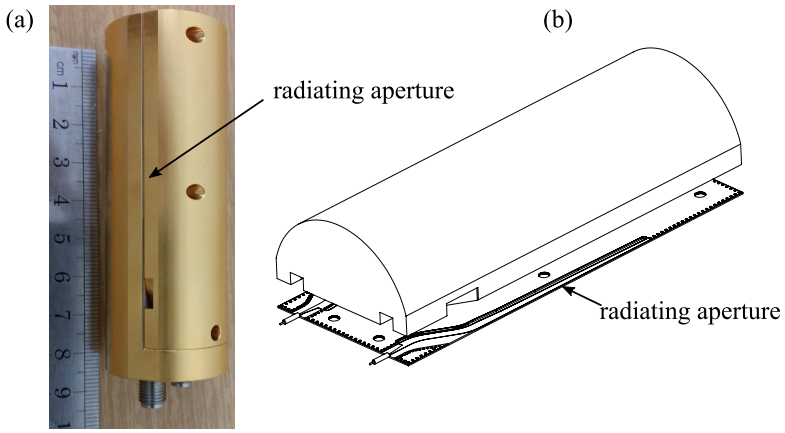

Figure 2.20. HMSIW antenna integrated into cylindrical pole. (a) Photograph of the fabricated device with two antennas integrated in a metallic pole. (b) Antenna assembly diagram (bottom half is half of the conducting pole and is not shown)

2.6 Transitions for Minimising Radiation Ripples

In this section, the transitions for the wideband HMSIW antenna (Fig. 2.5 and 2.13) adapted for the metallic structure integration in millimetre-wave regime with minimised radiation ripples are proposed.

The first design objective is to integrate the antenna into a cylindrical pole with the coaxial connector at the base as shown in Fig. 2.20. In this configuration, the antenna operates as a magnetic dipole radiating on a ground plane (Variation II - see Section 2.2). As demonstrated above, the antenna may exhibit clearly defined ripples in the broad beam elevation radiation patterns (H-plane). In order to reduce the level of these ripples, the unwanted parasitic radiations at the feed-side transition need to be reduced by providing a continuous wideband transition. This is realised starting from a coaxial connector to a shielded microstrip line then to a curved feeding HMSIW line connected to the antenna as shown in Fig. 2.21a. For clarification, selected cross-sections along the transition are shown in Fig. 2.21b.

Figure 2.21 suggests that the transition angle ψ should be small enough to minimise the field discontinuity from the half-shielded feeding HMSIW to the antenna, which radiates to half free-space. However, a smaller value of ψ will result in a longer transition (for a fixed distance l_c from the coaxial connector to the antenna edge). This consequently increases the total losses in the structure. A compromise value for this angle is chosen as 30°.

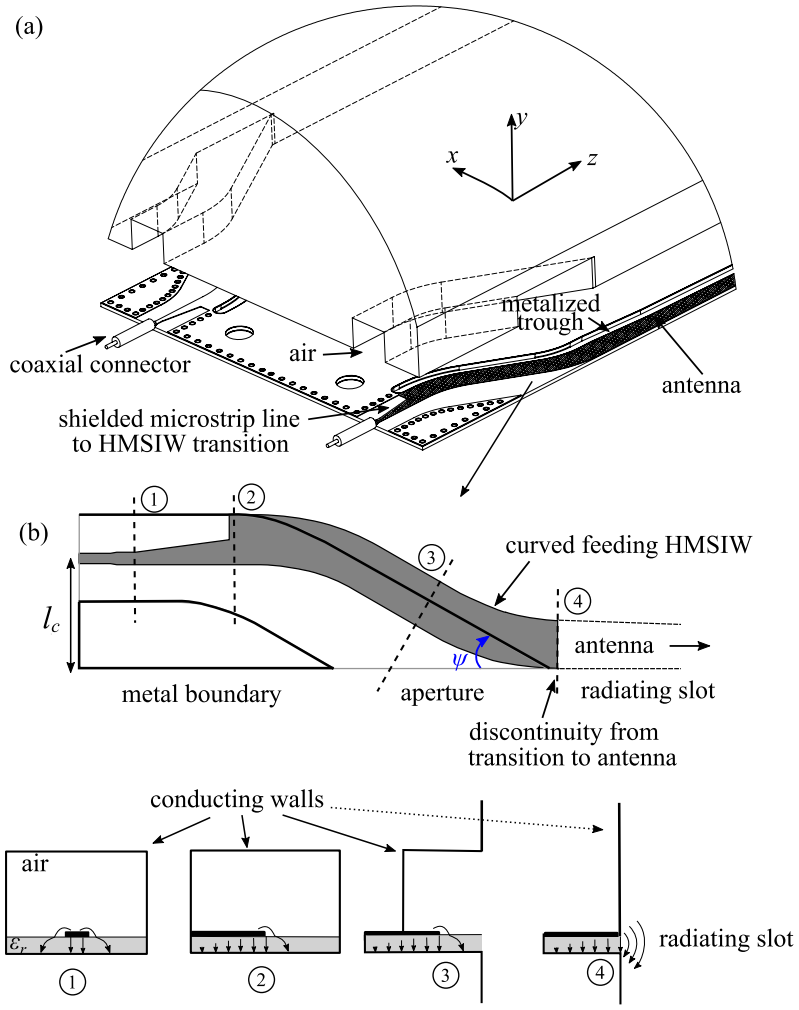

Figure 2.21. The transition for the HMSIW antenna integrated into cylindrical pole. (a) Details of the transition design, (b) Cross-sections along the transitions.

Additionally, the two curves of the feeding HMSIW (Fig. 2.21b) should be carefully optimised to minimise the transition length while keeping the return loss within a satisfactory level, i.e. 20 dB. Figure 2.22 shows the S-parameters for the transition with a matched port at the antenna side.

With the presence of the pole, which forms an electrically large curved ground plane, the antenna aperture radiation becomes directive into half free-space. Thus, the pole can integrate two identical antennas to cover the whole free-space. Finally, for illustration, the radiation patterns of the antenna at a particular frequency using this proposed transition and a conventional tapered microstrip transition are shown in Fig. 2.23. It is clear that a

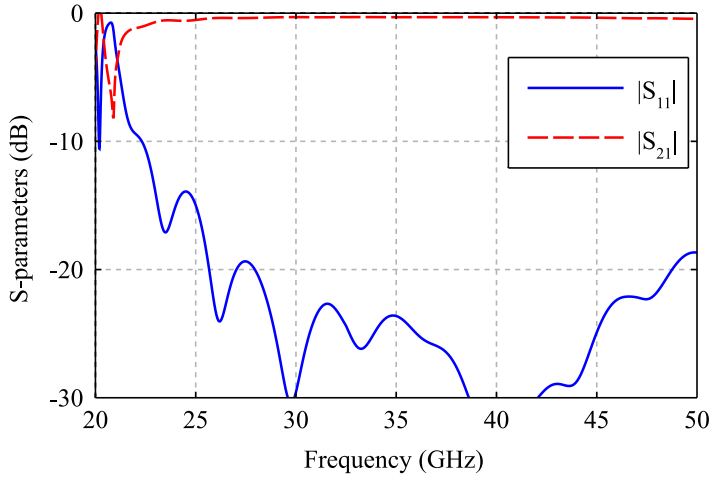

Figure 2.22. Simulated reflection and transmission coefficients of the designed transition.

careful design of the transition is required to reduce the ripples in the pattern. The above design can be adapted for integration into a flat metal plate. The design details of this antenna are shown in Fig. 2.24. In this design, the coaxial connector is fed perpendicularly from behind a flat metal plate. The connector inner pin is connected to a microstrip line which transitions to a 90-degree bent HMSIW line and then to the antenna. It is noted that the transition angle ψ is kept as 30°. This requires a 60° bend in the initial part of the HMSIW (see Fig. 2.24a).

Further results on the radiation patterns, gain and efficiency of these antennas will be shown in the next Chapter, which dedicates to the antenna optimisations.

2.7 Conclusion

This chapter has reviewed the concept of half-mode substrate-integrated waveguide (HMSIW) and its applications for travelling-wave antennas (TWAs). The variational method has been presented as a powerful technique to accurately calculate the propagation constant of different HMSIW variations. A semi-analytical model based on transmission line matrices for this antenna type has been proposed. The analysis is general and applicable for any nonuniform continuous-source TWA provided the propagation constants for different cross-sections are available. The field equivalence principle has been used to analyse the antenna's near-field and far-field radiations. Different aspects of the antennas,

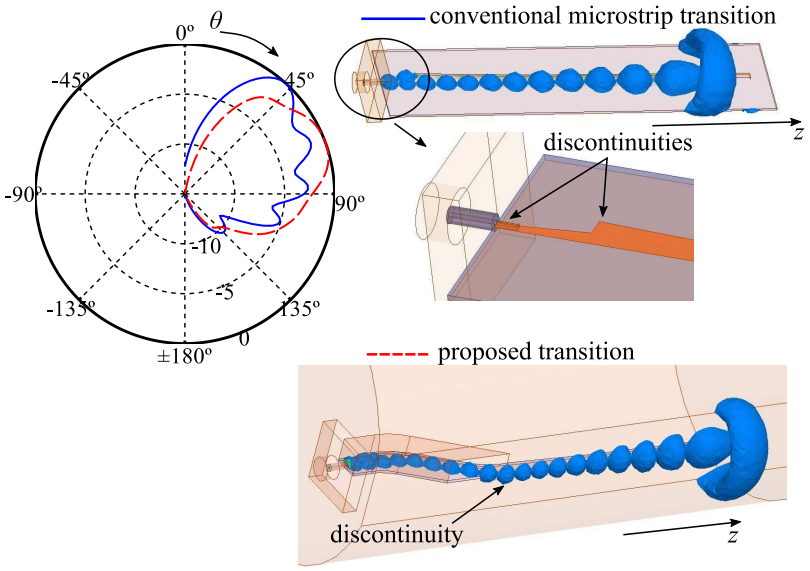

Figure 2.23. Simulated radiation pattern and field distribution with different transitions. Detailed design of the proposed transition can be found in Fig. 2.21.

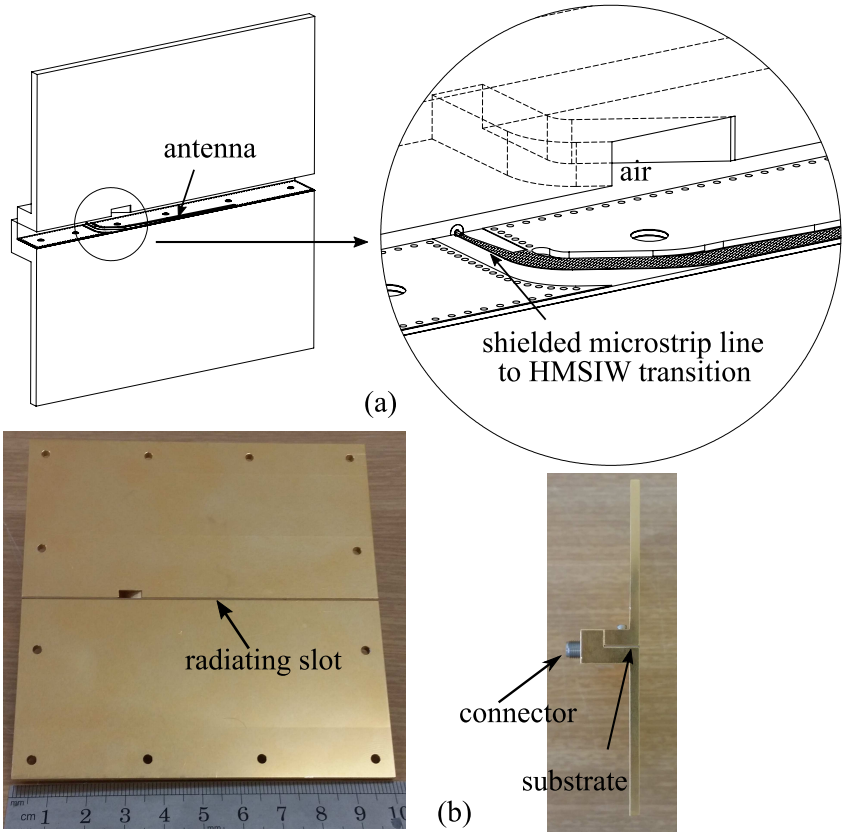

Figure 2.24. Adaptation of the HMSIW antenna integrated into flat metal plate. (a) Antenna assemble; (b) Fabricated antenna photograph.

including the aperture-field distribution, the transitions and their effects on the radiation pattern have been investigated. Based on these results, transition designs that minimise radiation pattern ripples for the application of metallic structure integration have been presented. It should be noted that further analysis, simulations and measurement results will be demonstrated in the next chapter, where the antennas discussed here are optimised and validated towards various performance targets.

Chapter 3

Optimisation of Nonuniform Travelling-Wave Antennas

MULTIPLE optimisations of the antennas discussed in the previous chapter are presented. The optimisations are shown for various performance targets, including for wideband operation or specific radiation patterns. Finally, an optimisation that includes the parameter uncertainties and the fabrication tolerances is proposed, towards reliable performance despite manufacture variations.

3.1 Introduction

The two types of antennas considered in the first major part of this thesis are the leaky-wave antennas (LWAs) with directive patterns and the travelling-wave wideband antennas with very broad beam patterns. This chapter is dedicated to a general framework of optimisations applicable to both antenna types. The first section presents the optimisation of the wideband HMSIW antenna. Although a preliminary version of the technique had been presented in [48], *i.e. before this PhD candidature*, the optimisation is adapted and refined here for the wideband millimetre antenna integrated into metallic structure, whose transitions was discussed in Section 2.6. The second section proposes a general method to perform pattern synthesis with LWAs utilising the semi-analytical model proposed in Section 2.4.2 and global optimisations. It is noted that all these optimisations utilise the lossy transmission line model proposed in the previous chapter to efficiently solve the antenna. Typical time to obtain an optimised set of antenna parameters is in range of 5 to 15 minutes (considering around 0.1s per parameter set) while it would take tens of weeks if using numerical simulation tools (where each simulation is between 15 to 30 minutes). The last section demonstrates a reliability-aware optimisation for wideband antenna that takes into account the uncertainties in material parameters and fabrication process. This proposed procedure is applicable to any wideband antenna in which a fast solution is available. The method can also be further extended into different cases such as optimising the sidelobe level in the LWA radiation patterns.

It is also noted that, in this chapter, the final results of the optimised antennas are also successfully demonstrated with prototypes, as an ultimate validation of the analysis and design concept proposed in the previous chapter and the optimisation techniques presented in this chapter. The original contributions in this chapter have been published in [16, 18, 55, 56].

3.2 Optimisation of Wideband Antennas

In this section, the optimisation of the wideband tapered HMSIW antennas in [48] is adapted for the millimetre-wave antenna integrated into metallic structure proposed

in Section 2.6. Then the final results are shown as a validation of the design and optimisation process.

3.2.1 Antenna Optimisation

In general, the optimisation of the antenna can be carried out using any global optimisation method. In this investigation, two of the most popular techniques, i.e. particle swarm optimisation (PSO) [57] and genetic algorithm (GA) [58] have been tried. It has been found that for the tapered wideband HMSIW antenna, PSO tends to arrive to the optimal solution faster than GA due to smaller number of optimised variables. Thus, the PSO is used for the antenna in this section. For a target bandwidth from 30 GHz to 40 GHz, the antenna is divided into 4 sections where all the widths w_i and lengths l_i are parameters in the optimisation (Fig. 3.1). In this investigated case, we target for maximum gain at broadside. The cost function is chosen as

$$C = \begin{cases} 1/G_{\min} + c_2 L_{ant} \text{ if } |S_{11}|_{\max} < |S_{11}|_{tg} \\ 1/G_{\min} + c_1(|S_{11}|_{\max} - |S_{11}|_{tg}) + c_2 L_{ant} \text{ otherwise} \end{cases} \tag{3.1}$$

where $G_{\min}$ is the minimum linear gain at broadside across the bandwidth; $|S_{11}|_{\max}$ is the maximum reflection coefficient (in dB) across the bandwidth; $|S_{11}|_{tg}$ is the threshold for the reflection coefficient (in dB); $L_{ant} = \sum l_i$ is the antenna length (in mm) and c_1 and c_2 (mm^{-1}) are weighting coefficient.

The optimisation has been carried out for various discrete values of relative permittivity ϵ_r and thickness h. It is found that the cost function is reduced with increasing ϵ_r and decreasing h. This is expected from the investigation shown in Section 2.5: by increasing ϵ_r and reducing h, the fringing field at the transition is decreased and more power is confined within the substrate. This effectively reduces the radiation at the transition and thus the ripples in the radiation patterns. Since G_{min} is defined as minimum linear gain at broadside across the whole bandwidth and since the location of the ripples dips is moving with frequency, reducing the ripples' amplitude helps increasing G_{min}, consequently reducing the cost function C. However, if the substrate is too thin or if the permittivity is too high,

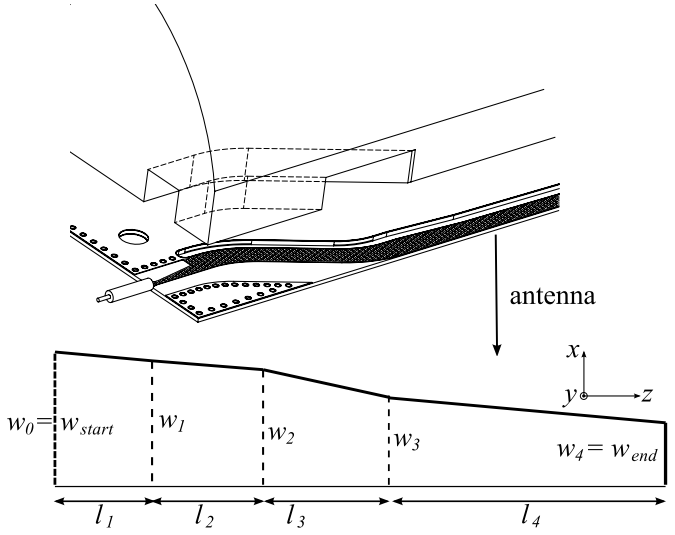

Figure 3.1. The tapered HMSIW to be optimised on 4 linear segments. The top figure shows the integration of the antenna into a metallic structure.

the antenna will need to be very long to satisfy the return loss specification. A good compromise found from optimisation among commercially available substrates is the Rogers Duroid 6006 with thickness $h = 0.254$ mm, $\epsilon_r = 6.15$, and loss tangent $\tan\delta = 0.0019$.

Another critical parameter in the optimisation is $|S_{11}|_{tg}$, i.e. the targeted maximum reflection coefficient across the bandwidth. If the tapering is faster, the effective radiating aperture will decrease; as a result, the antenna radiates closer to broadside at the cost of higher reflections. In the present design case, we set $|S_{11}|_{tg} = -10$ dB as a required specification. Alternatively, if there is no requirement for $|S_{11}|_{\max}$, the optimisation can be carried out for maximum realised gain at broadside, potentially resulting in a $|S_{11}|_{\max}$ larger than -10 dB. Finally, it is noted that a tradeoff between reflections and broadside gain is implicitly made here in the millimetre-wave regime since the loss, which is unavoidable, is higher than the case in [48] and this loss slightly reduces $|S_{11}|$.

The dimensions of the optimised antenna are shown in Table 3.1, as obtained for cost weighting coefficients $c_1 = 0.5$ and $c_2 = 1/60$ (mm^{-1}). The semi-analytically calculated and simulated reflection coefficients of the optimised antenna including the transition are shown in Fig. 3.2. The analysis follows what was presented in Section 2.4. A very good agreement between simulation and analysis is obtained. The result also demonstrates the significance of considering losses in the mm-wave range, following the analysis of the

Table 3.1. Optimised dimensions for the antenna

widths	w_0	w_1	w_2	w_3	w_4
values (mm)	1.500	1.034	0.901	0.835	0.642
lengths		z_1	z_2	z_3	z_4
values (mm)		8.945	6.945	3.142	7.965

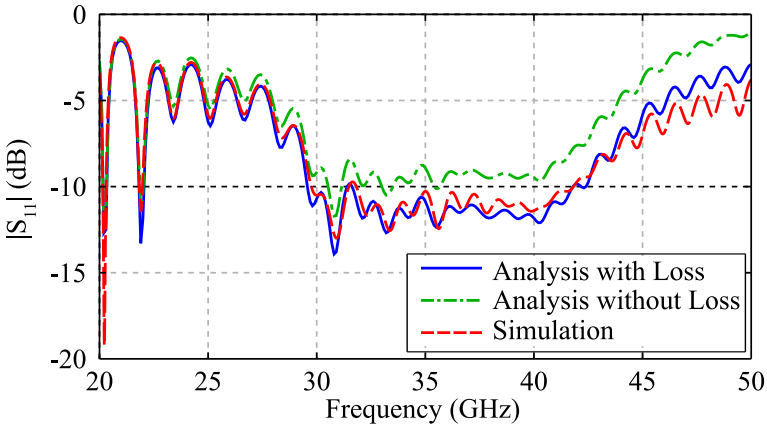

Figure 3.2. Analysed and simulated reflection coefficient of the optimised antenna integrated into cylindrical pole.

propagation constant including conductor and dielectric losses as shown in Section 2.2.2).

3.2.2 Measurement Results - Antennas Integrated into Cylindrical Pole

It is noted that two identical antennas optimised using the above procedure are integrated into a cylindircal pole to provide full space coverage.

Reflection Coefficient

The analysed and measured reflection coefficients for two antennas (left and right) integrated into a cylindrical pole with diameter of 30 mm (as shown in Fig. 2.20) are shown in Fig. 3.3. Due to the limit of the instrumentation, results for frequencies only up to 40 GHz are shown, which nevertheless covers the targeted bandwidth, i.e. 30 GHz to 40 GHz. Good agreement between analysis and measurement is generally obtained. The

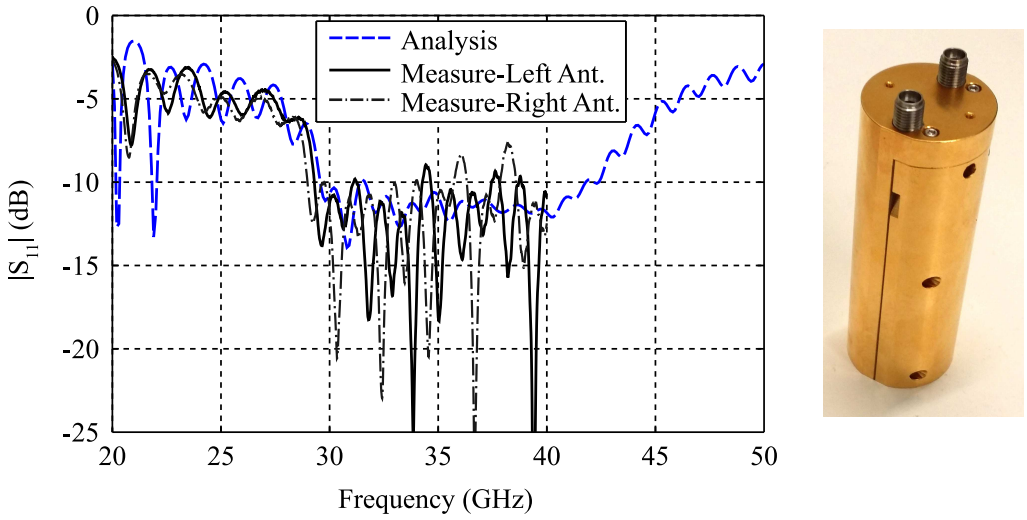

Figure 3.3. Measured reflection coefficient of the antennas integrated into pole.

local breaches of return loss specification come from the fabrication and material tolerances which are expected in the mm-wave regime. Since the pole is electrically large at this frequency range, the coupling between the two antennas is very small, i.e. less than -40 dB. Finally, it is noted that although the antennas were designed targeting a bandwidth from 30 GHz to 40 GHz corresponding to 28% fractional bandwidth, the bandwidth can be in principle extended up to 80% [15,48] by increasing the antenna at the expense of decreasing efficiency at higher frequency.

Radiation Pattern

The realised gain pattern (in dBi) at different frequencies across the bandwidth are shown in Figs. 3.4 and 3.5. The results for the two antennas (left and right) are almost identical to each other so results for only one antenna are shown in these figures. A very good agreement between analysis, simulation and measurement is obtained, which further validates the design procedure. It can be observed that patterns with a very broad beam are obtained across the whole frequency range. This characteristic is unique among LWA where frequency-scanning directive patterns are common. Near-broadside broad-beam patterns with horizontal polarisation and negligible ripples are obtained across the whole bandwidth. The results validate the transition design proposed in Section 2.6 to reduce the ripples in the radiation patterns. Figure 3.5 also shows that two antennas (left and right) can provide a full azimuthal coverage with realised gain better than -2 dBi.

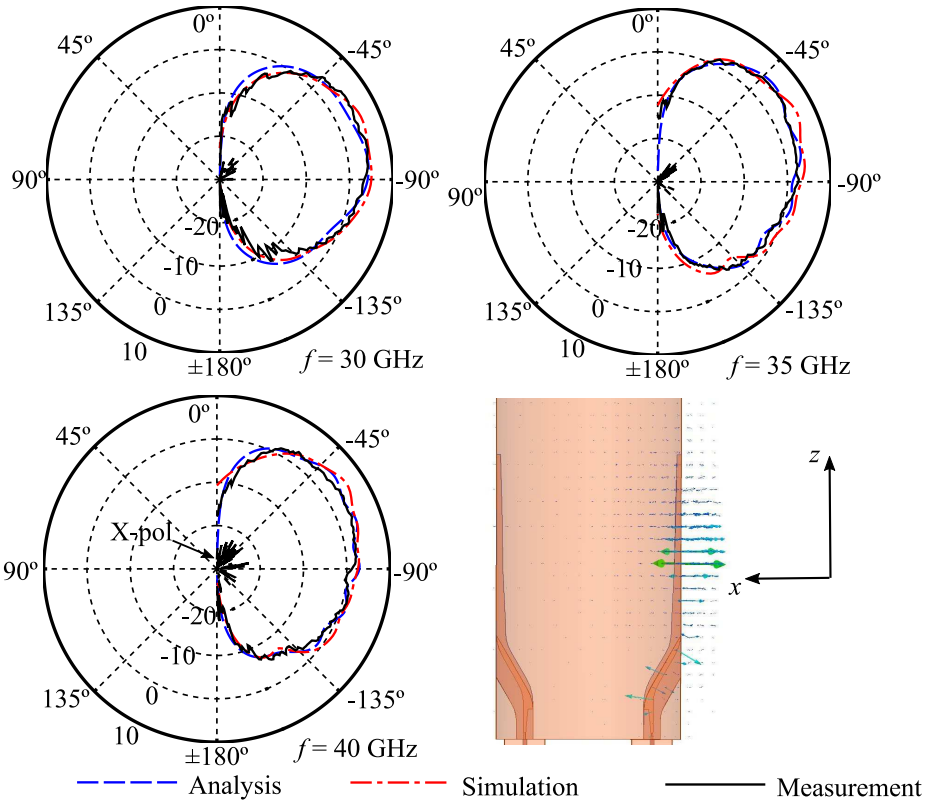

Figure 3.4. Realised gain pattern (dBi) in elevation plane (H-plane) of the antenna integrated into a metallic pole. The antenna is horizontally polarised.

Gain and efficiency

The antenna peak realised gain and broadside gain are shown in Fig. 3.6. Reasonable agreement is obtained between simulation and measurement. The simulated and measured gain at broadside is greater than 2.5 dB and 0.7 dB across the whole frequency range. The simulated efficiency decreases from about 76% to 68% when the frequency is increased from 30 GHz to 40 GHz. At higher frequency, the efficiency is lower because the wave has to travel for a longer distance in the waveguide before reaching the radiation region, where the waveguide width corresponds to cutoff. The measured efficiency is better than 40% and up to 70% in the considered bandwidth, which is expected for a millimetre-wave travelling-wave antenna (TWA) employing metal in the radiating structure. This is inevitable as the aim is to integrate the antenna into metallic structures. The lower measured gain and efficiency is attributed to higher material losses in practice and measurement uncertainties.

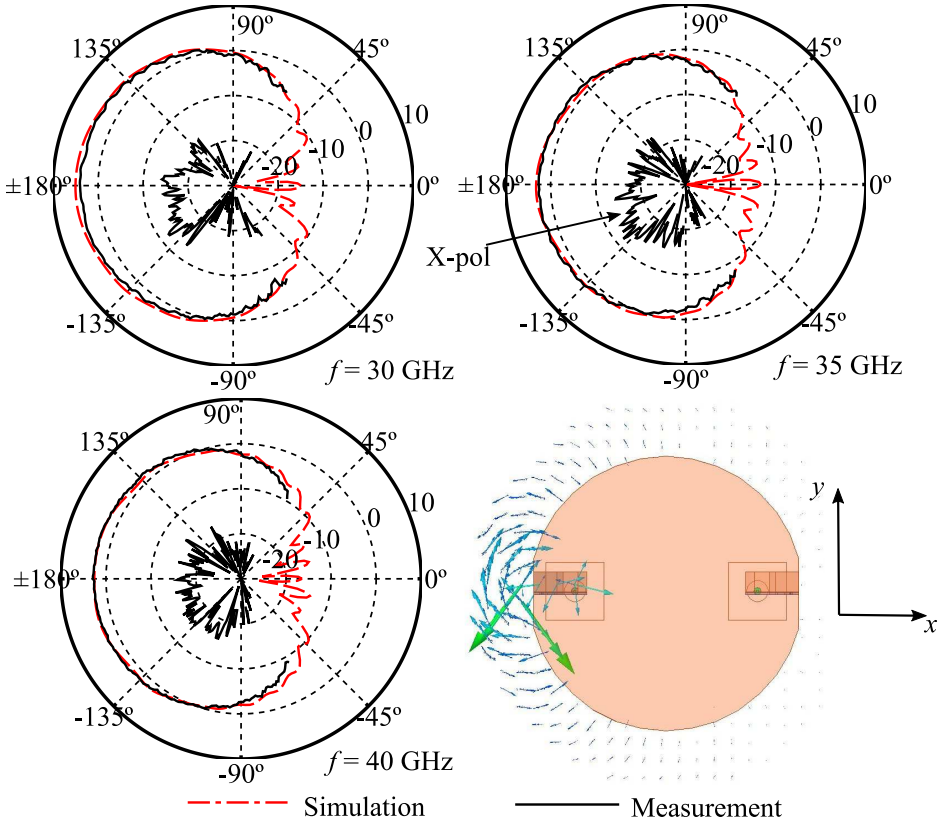

Figure 3.5. Realised gain pattern (dBi) in azimuth plane (E-plane) of the antenna integrated into a metallic pole.

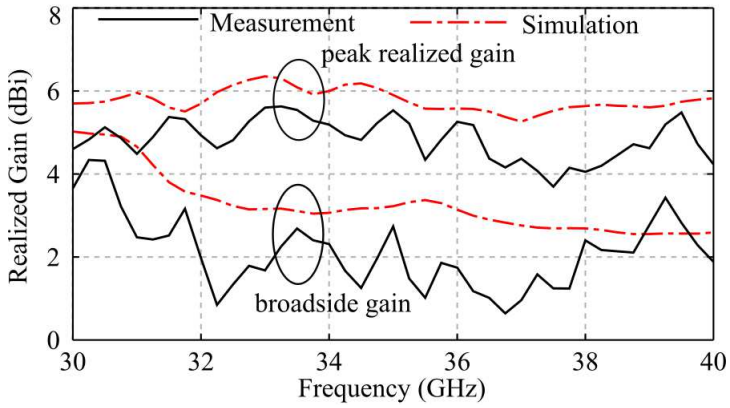

Figure 3.6. Peak realised gain and broadside gain of the (left) antenna integrated into pole.

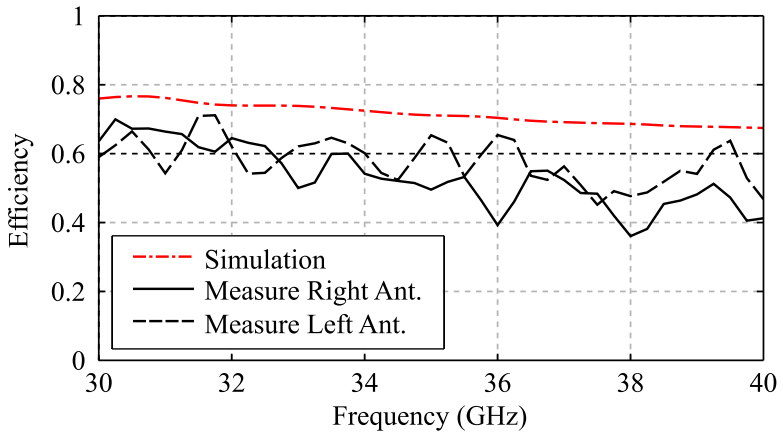

Figure 3.7. Efficiency of the antenna integrated into pole.

3.2.3 Measurement Results - Antenna Integrated into Metal Plate

Finally, for demonstration and completeness, the results for the reflection coefficient and radiation pattern at $f = 35$ GHz of the antenna integrated into flat metal plate (Fig. 2.24) are shown in Figs. 3.8 and 3.9. Again, good agreement between analysis, simulation and measurement is obtained, which further validates the antenna design principle.

The ripples in the azimuth plane (xy-plane) come from the finite ground plane and their amplitude would decrease if the antenna is integrated into a larger metallic platform. Comparing this pattern with the results in Fig. 3.5, it can be concluded that the curved surface of the pole can mimic an infinite ground plane and reduce the ripples in the azimuth plane. Finally, because both antennas operate as magnetic dipoles on a ground plane, the finite ground plane does not have a significant impact on radiation patterns in the elevation plane (H-plane).

3.2.4 Summary of Wideband Antenna Optimisation

In this section, the optimisation for wideband operation of the millimetre antennas integrated into metallic structures has been presented. This optimisation is enabled by the fast semi-analytical model proposed in the previous chapter. It is noted that feeding transitions minimise the ripples in the radiation patterns in elevation plane and allow flush integration as thin radiating aperture into metallic surface. The antenna exhibits nearly omnidirectional horizontally polarised patterns in half free-space across a wide

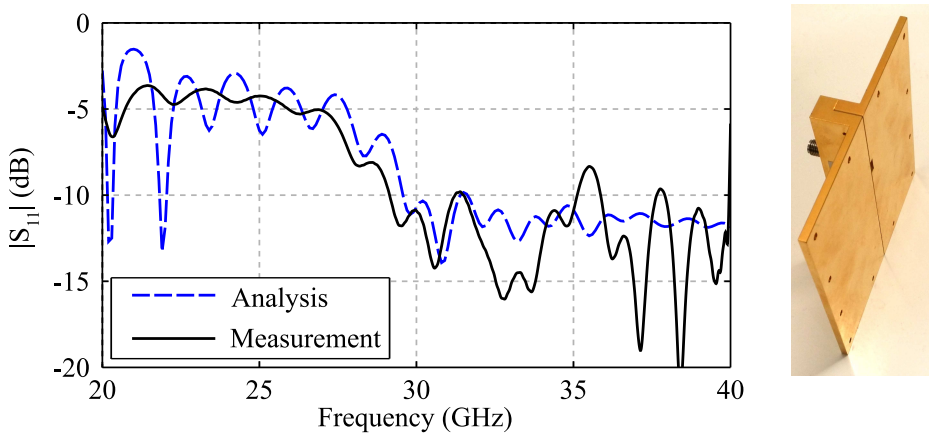

Figure 3.8. Reflection coefficients of the antenna integrated into metal plate.

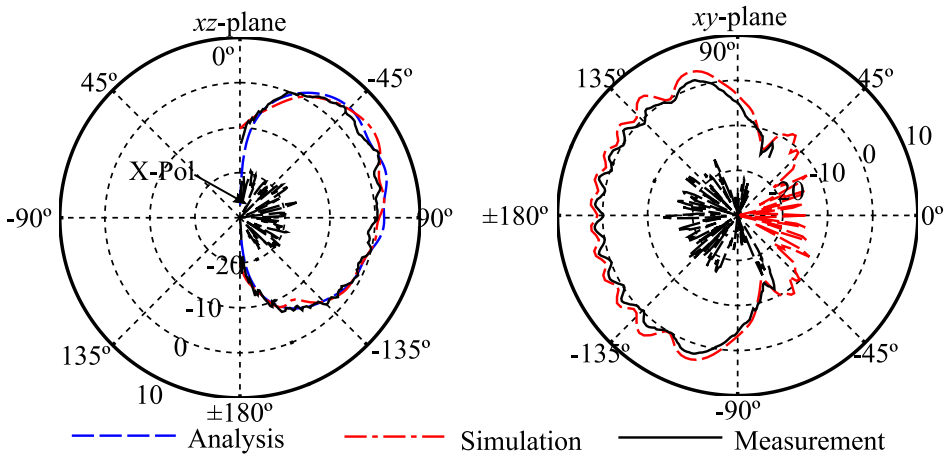

Figure 3.9. Realised gain patterns of the antenna integrated into metal plate. Patterns are shown as dBi at $f = 35$ GHz.

bandwidth from 30 GHz to 40 GHz, which in principle can be extended by increasing the tapered antenna length. The unique characteristics make the proposed antennas excellent candidates for future wireless communication in millimetre-wave regime, such as for indoor broadcasting.

3.3 Optimisation of Leaky-Wave Antenna Patterns

Based on the general transmission line model of TWAs, which include LWAs, proposed in Section 2.4, a method for far-field pattern synthesis utilising global optimisation is demonstrated here. The method shows higher flexibility in the design process compared to the classical LWA analysis approach [12,40,59]. Utilising this method, a pattern synthesis can be carried out without the necessity of independent control on attenuation constant $\alpha(z)$ and phase constant $\beta(z)$ along the antenna length, such as in [47,60].

This section first introduces the method and compares it with the classical approach. Then two specific designs are shown with measurement validation. It is noted that the effect of the inclusion of transition in the analysis is also presented as a validation for the analysis presented in Section 2.4.5.

3.3.1 Method

A LWA can be considered as an array of discrete sources with infinitesimal separations [40,61]. The far-field pattern $E(\theta)$ is calculated from the complex source distribution $A(z)$ as

$$E(\theta) = G(\theta) \int_0^L |A(z')| e^{j[\psi(z') + k_0 z' \cos\theta]} dz'. \tag{3.2}$$

where $G(\theta)$ is the element pattern.

The traditional pattern synthesis is based on the fact that the far-field pattern is a Fourier transform of a near-field or source complex distribution $A(z)$ [40]. The general approach is illustrated in Fig. 3.10 (dotted line). However, as demonstrated in Section 2.4.3, for nonuniform LWA, the classical analysis only yields a rough approximation of the source distribution. Furthermore, assuming that a far-field pattern $E(\theta)$ is specified, this method should also involve an iterative process since the inverse Fourier transform of $E(\theta)$ yields a field distribution $A(z)$ which is generally non-zero everywhere while the LWA always has a finite length. Finally, although closed-forms for $\alpha(z)$ and $\beta(z)$ are provided from $A(z)$ in classical analysis, for many LWAs, $\alpha(z)$ and $\beta(z)$ are inter-dependent. Thus, one may not be able to choose a structure that yields the desired $A(z)$ distribution. Because of this, LWA designers often requires leaky-wave structures with independent control of both $\alpha(z)$ and $\beta(z)$ [12,40,47,60].

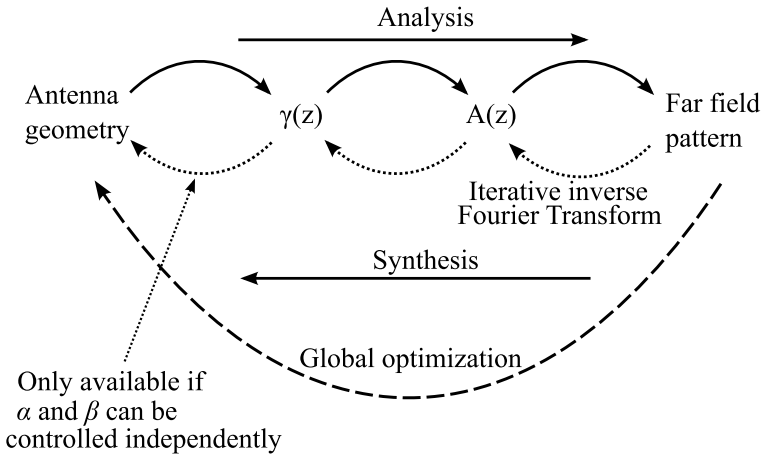

Figure 3.10. Far-field pattern synthesis diagram of a leaky-wave antenna.

In order to circumvent the above issues, a strategy based on a global optimisation method, e.g. Genetic Algorithm (GA), can be used (Fig. 3.10, dashed line). To implement this strategy, the LWA is divided into a number of sections whose geometry can be set to vary linearly. The parameters for each section will be the optimisation variables. The global optimisation will utilise the proposed analysis for an accurate prediction of the near-field source distribution to compute the far-field pattern. With an appropriate cost function, the optimisation will yield a close-to-best result that is available within the structure constraint. In fact, this method of using global optimisation for LWAs was used by Siragusa *et al.* in [62]. However, the process was based on full-wave numerical simulation of the LWA, which was very time-consuming, i.e. 2 weeks. Using the analysis proposed in Chapter 2, a pattern synthesis problem may be carried out in less than 5 minutes on a typical desktop computer (provided the propagation constant γ is available for different structure cross-sections, as analytically, numerically or experimentally determined). It is emphasised that the final optimised result should be validated using full-wave simulation, in which one single simulation is typically sufficient.

It is noted that for most applications, we are not interested in the exact distribution of $E(\theta)$ for all angles but rather some characteristics of $E(\theta)$ need to be satisfied, such as low sidelobe level or maximum gain in a given direction. Thus, a cost function in the global optimisation appears to be a very convenient tool to characterise performance.

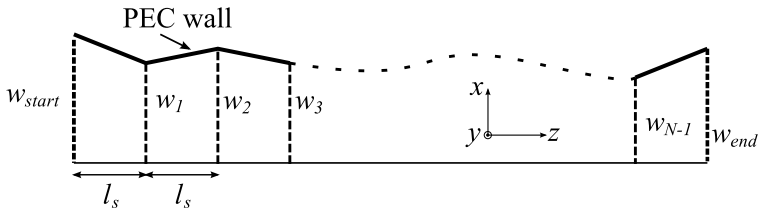

Figure 3.11. The tapered HMSIW to be used for far-field pattern optimisation.

The next section will demonstrate the results for two typical pattern synthesis requirements, namely targeting a low sidelobe level or a wide angular null in the far-field pattern. The structure under investigation will be, without restriction to the generality of the method, the conventional HMSIW LWA (see Section 2.2). It is noted that, for a HMSIW with varying width, the attenuation constant α and phase constant β are inter-dependent and thus, the classical analysis can not be applied in these study cases.

3.3.2 Application: Specific Designs

In this section, the HMSIW is used as basis structure for designing LWAs targeting different far-field specifications. Only the width of the HMSIW is varied along the LWA $w = w(z)$. Other structures can be analysed similarly with the prerequisites that the propagation constant $\gamma(z)$ can be found for a varying cross-section of the waveguide. A preliminary determination of γ can be carried out only once by analysis or simulation and stored in a library to be used in pattern synthesis process. As the conventional HMSIW is used, the analytical solution for γ can be found using the transverse resonance method [32–34], as mentioned in Section 2.2.2. The substrate chosen is the same as that in Section 2.4.3, i.e. Rogers Duroid 5880 with relative permittivity $\epsilon_r = 2.2$ and thickness $h = 31$ mil $= 0.787$ mm. Two antennas have been designed and validated through experiment. Both antennas are terminated by a matched load. Design process and results are shown as follows.

Low Sidelobe Level

The HMSIW is divided into N sections in which the width of HMSIW is set to vary linearly as shown in Fig. 3.11. Each section has the same length of $l_s = L/N$. The desired far-field pattern has a maximum gain at angle θ_{tg} and lowest possible sidelobe level at the

operating frequency f_0. Thus, the cost function can be chosen as

$$C_{LSL} = -c_1 G(f_0, \theta_{tg}) + c_2 SLL(f_0) + c_3[G(f_0, \theta_{tg}) < G^*]. \tag{3.3}$$

The aim of the optimisation is to reduce the cost function; hence, the weighting coefficients c_1, c_2, c_3 are positive to obtain a higher gain and lower sidelobe level (first and second terms in (3.3)). $G(f_0, \theta_{tg})$ is the realised gain at frequency f_0 and angle θ_{tg}, $SLL(f_0)$ is the sidelobe level at frequency f_0 considering the whole angular range. All terms are expressed in dB. The last term is equal to zero when $G(f_0, \theta_{tg}) \geq G^*$ and c_3 otherwise. This term is necessary to ensure that the optimisation does not converge to a broadside LWA with extremly low sidelobe level but small gain at θ_{tg}. A value of 5 dB for G^* is sufficient to avoid the occurrence of this case.

An optimisation result is selected to demonstrate the method. The target frequency is $f_0 = 8$ GHz, the antenna length is $L = 8\lambda_0$ where λ_0 is the free-space wavelength at f_0, and the target direction of maximum radiation is $\theta_{tg} = 30°$. The number of section used in the optimisation is $N = 50$ resulting in 50 variables in the GA. The number of approximately UTL in the analysis of each non-uniform HMSIW is 600 ($\Delta z = 0.5$ mm $= \lambda_0/75$). In this example, it is found that a value of $\Delta z \leq \lambda_0/20$, i.e. the discretisation resolution in the semi-analytical model, gives accurate enough results. Weighting coefficients in equation (3.3) are chosen such that c_1 and c_2 are in the same order, i.e. $c_1 = c_2 = 1$, while c_3 must be much larger than c_1 and c_2 to enforce the gain threshold, i.e. here $c_3 = 50$. A GA MATLAB code based on [58] has been implemented using one-point crossover method with a rate of 50% and uniform mutation with a rate of 2%. The population size is 80 genes and 8 bits are used to represent one variable, which results in 400 bits per gene. The typical number of generations required for convergence is about 50. It is noted that due to the efficient computation using the proposed method, a large population size can be used and a large number of generations can be computed, e.g. compared to [62]. Multiple optimisation runs can be performed to validate and refine the optimised results.

The optimised antenna profile is shown in Fig. 3.12, which demonstrates a similar shape as to the antenna designed in [41] targeting similar optimisation objective, i.e. low sidelobe level. In [41], a cosine field distribution is chosen primarily before calculating the width $w(z)$ while the method in the present method demonstrates higher flexibility and accuracy in the pattern synthesis. A photograph of the fabricated antenna is displayed in Fig. 3.13

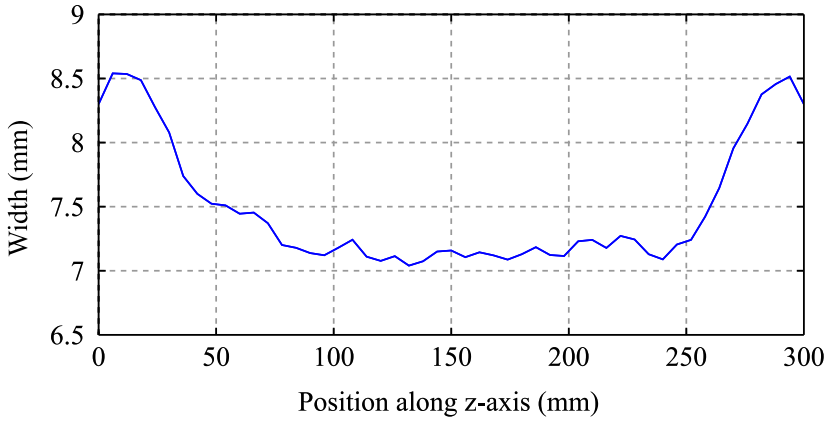

Figure 3.12. Non-uniform HMSIW LWA shape optimised for low sidelobe level.

Figure 3.13. Photograph of the fabricated antennas. Photographs are shown for the antennas optimised for low sidelobe level (top) and wide null (bottom).

(top). It is noted that the PEC walls of the HMSIWs are realised by via holes through an accurate width-correction formula provided in [49].

It is noted that the analysis assumes that conductor and dielectric losses are negligible, which is reasonable in the considered frequency range. Nevertheless, these losses can be taken into account in the model by including them into the overall α as demonstrated in Section 2.2. The simulation results below are shown for the practical case with dielectric substrate loss tangent $\tan\delta = 0.0011$ and copper conductivity $\sigma = 5.8 \times 10^6 S/m$.

The aperture field distribution is shown in Fig. 3.14. Excellent agreement between analysis and full-wave simulation is observed which further validates the proposed method demonstrated in Section 2.4.2. Since the width $w(z)$ does not vary significantly in this case, constant $\mathbf{e}_t$ [equation (2.16)] can be assumed without losing much accuracy (green

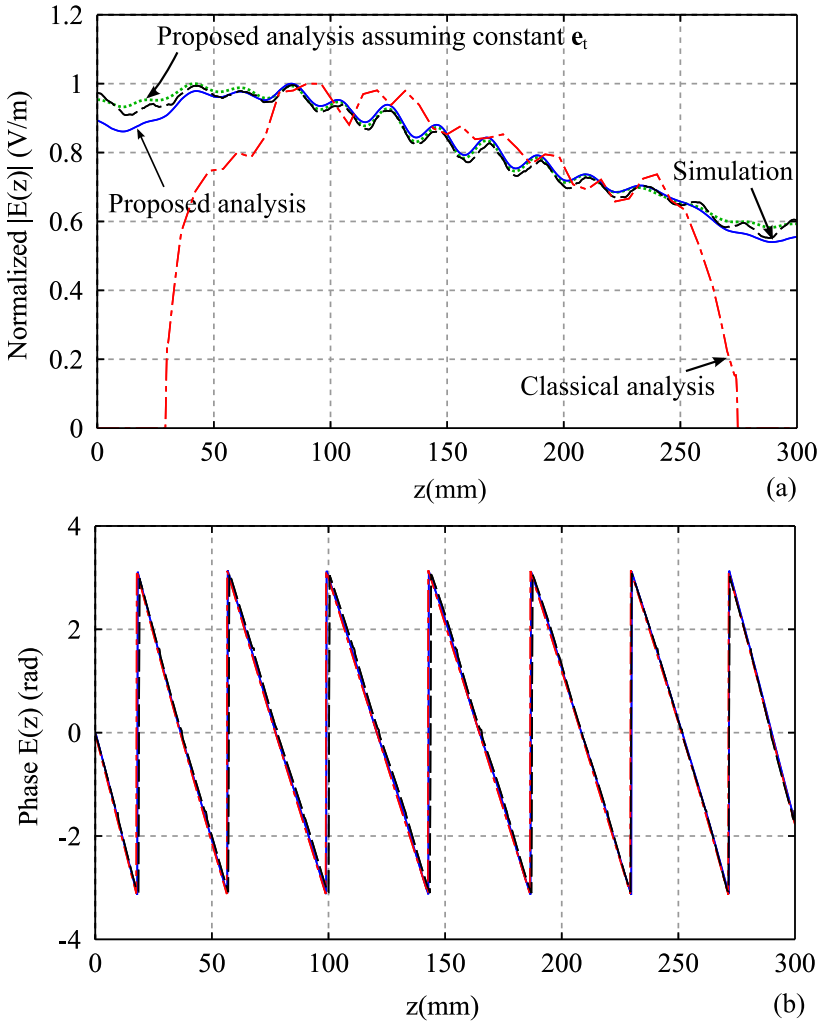

Figure 3.14. Aperture field of the a non-uniform HMSIW optimised for low sidelobe level. (a) Magnitude; (b) Phase. The legends are the same for both figures and consistent with Fig. 2.9.

dotted curve in Fig. 3.14). This is an important point because in many cases, one can obtain a very good prediction of the near-field distribution without spectral modal analysis. In other words, only $\gamma(z)$ is required just as in the classical method.

The analytical and simulated results indicate small distributed reflections along the antenna, which is expected for any non-uniform transmission line. The results using classical analysis (see Section 2.4.1) is also included. As already discussed in Section 2.4.3, the classical analysis result shows large discrepancies, mostly at the transitions between

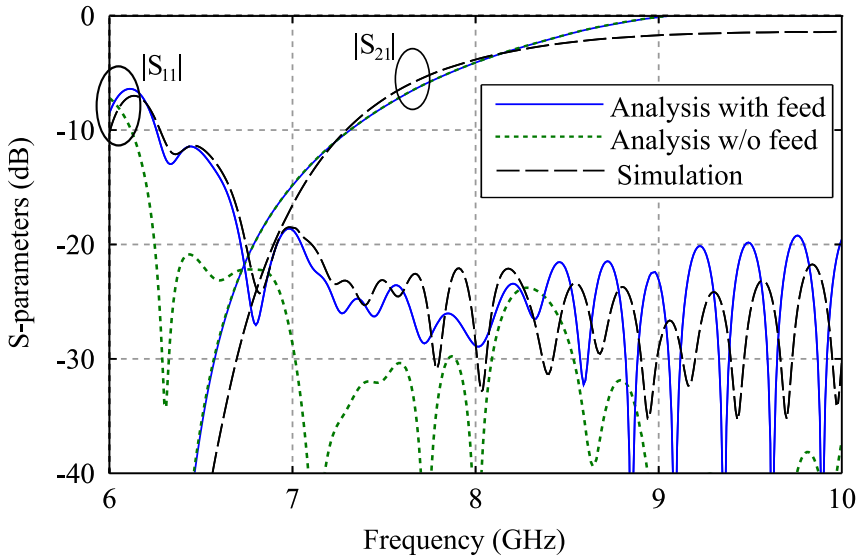

Figure 3.15. Analysed and simulated S-parameters for the HMSIW LWA optimised for low sidelobe level.

slow-wave regions and fast-wave regions. It is also noted that the fluctuation in field distribution in the classical analysis does not arise from reflections since these are not taken into account. Rather, they arise from the fact that $\alpha(z)$ is varying along the antenna.

The analysed and simulated S-parameters are shown in Fig. 3.15 with excellent agreement. For frequency $f \in (7, 10)$ GHz, since the transition provides a very good impedance matching to the antenna, the inclusion of the feed in the analysis is not necessary for this range. However for $f \in (6, 7)$ GHz, the inclusion of the transition in analysis (Section 2.4.5) provides a much better prediction on the S-parameters of the whole structure. This might be crucial for wideband LWA design [48]. The measured S-parameters are shown in Fig. 3.16. Good agreement is also observed. The discrepancy in $|S_{21}|$ comes from the conductor and dielectric losses along the antenna, and also small radiation losses at the connectors, which are not taken into account in the analysis. However, this should not significantly affect the gain as validated by measurement (shown below).

The normalised far-field patterns at $f_0 = 8$ GHz are shown in Fig. 3.17. It can be observed that the classical approach provides correct calculation of the main beam. However, with the assumption that neglects the impact from slow-wave region, the classical calculation fails to obtain the number and level of sidelobes as well as null positions in the pattern.

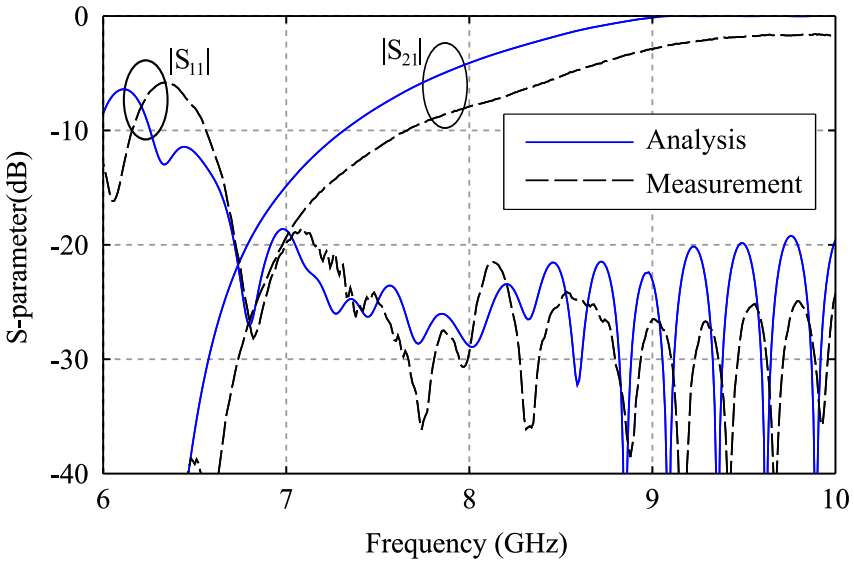

Figure 3.16. Analysed and measured S-parameters for the HMSIW LWA optimised for low sidelobe level.

Furthermore, since the classical analysis neglects the reflection along the antenna, the predicted far-field distribution for back-ward wave, i.e. $\theta > 90^\circ$ is always smaller than the true level.

Using the proposed transmission line model, very good agreement is obtained both with simulations (Fig. 3.17) and measurements (Fig. 3.18). The method predicts very well the relative sidelobe levels and null positions. The discrepancies towards $\theta = 0^\circ$ and 180° are due to finite ground plane realisation. The maximum sidelobe level is -21.5 dB in analysis and -23.8 dB in measurement. The calculated gain is 15.3 dB while the measured gain is 15.6 dB, which also shows a reasonable agreement. The measured cross-polarisation level is less than -15 dB at the main beam.

Wide Null

In this section, a non-uniform HMSIW LWA with same material and thickness as previous section is optimised targeting a wide angular null around the broadside direction. The target of this illustrative optimisation is to achieve an antenna with as high as possible gain at $\theta_{tg} = 50^\circ$, and as small as possible gain in the angular range $\theta_N \in (80^\circ, 100^\circ)$ given the structure material and thickness. The target frequency is $f_0 = 8$ GHz and the antenna length is chosen as $L = 10\lambda_0$, which is comparable with another design targeting

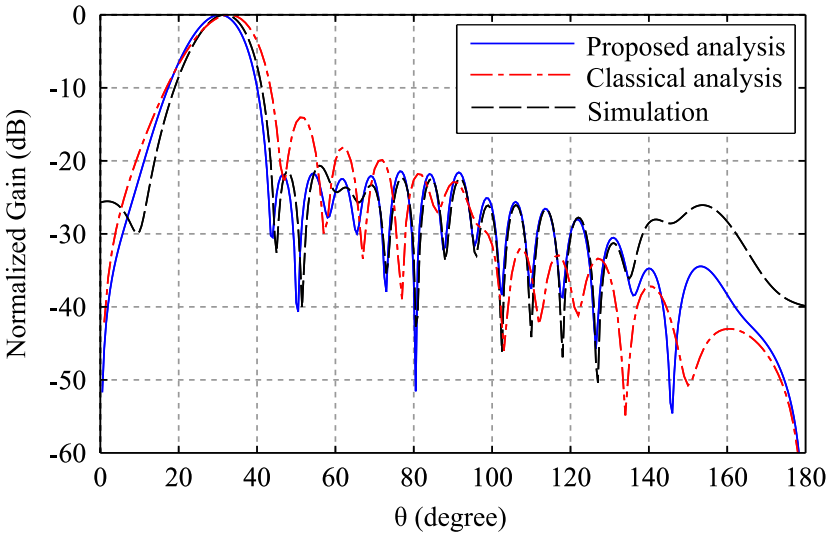

Figure 3.17. Analysed and simulated normalised radiation pattern for the HMSIW LWA optimised for low sidelobe level. Patterns are shown for $f = 8$ GHz.

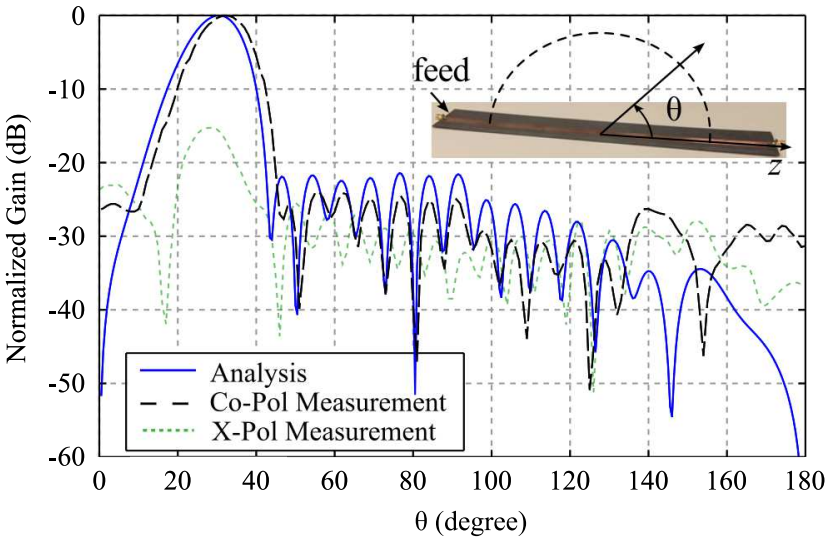

Figure 3.18. Analysed and measured normalised radiation pattern for the HMSIW LWA optimised for low sidelobe level. Patterns are shown for $f = 8$ GHz. The angle θ is defined as in the inset: $\theta = 90^\circ$ corresponds to broadside direction.

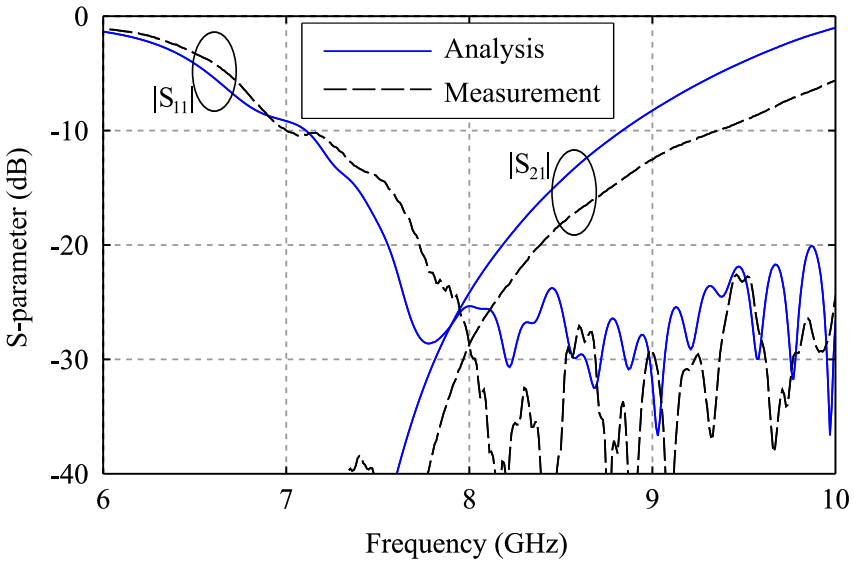

Figure 3.19. S-parameters of the HMSIW LWA optimised for wide null.

similar specification [60]. The cost function can be modified from (3.3) as

$$C_{WN} = -c_1 G(f_0, \theta_{tg}) + c_2 Null(f_0, \theta_N) + c_3[G(f_0, \theta_{tg}) < G^*] \tag{3.4}$$

where $Null(f_0, \theta_N)$ is the maximum gain in the range $\theta_N \in (80^\circ, 100^\circ)$ at the operating frequency f_0. For this optimisation, the antenna is divided into $N = 30$ sections and the length of each approximately UTL is kept as $\Delta z = \lambda_0/75$. The same GA setup as for the previous case is utilised. The photograph of the fabricated optimised antenna is shown Fig. 3.13 (bottom).

Good agreement between the analysed and simulated results for S-parameters can be observed in Fig. 3.19. It is noted that the feeding and termination transitions are included in the analysis. Similar features with the previous case are obtained if performing analysis without transition.

The analysed and measured normalised radiation pattern are shown in Fig. 3.20. The measurement result demonstrates a LWA with a wide null at a level of -36 dB for $\theta \in (80^\circ, 98^\circ)$ and -32 dB for $\theta \in (80^\circ, 100^\circ)$. Again, very good agreement between analysis and measurement validates the accuracy of the proposed model as a significant improvement from the classical approach.

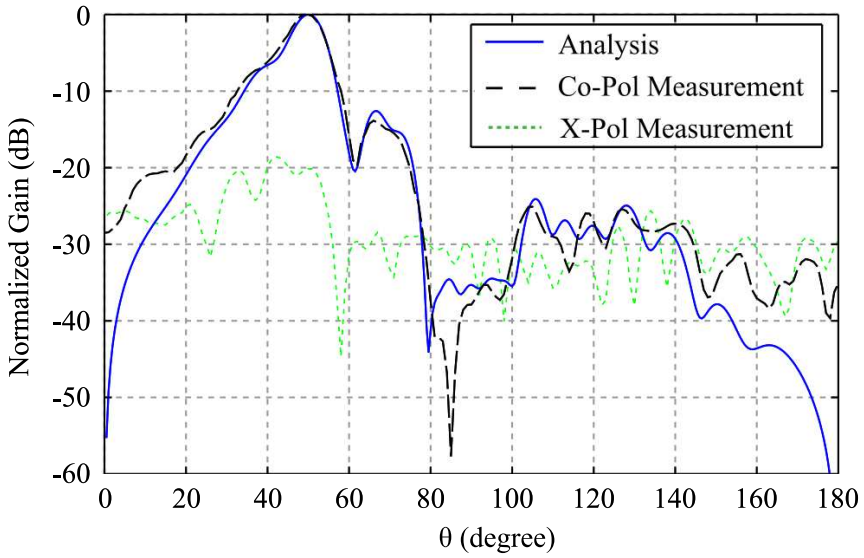

Figure 3.20. Normalised radiation pattern for the HMSIW LWA optimised for wide null. Operting frequency $f = 8$ GHz, the targeting null range is $\theta_N \in (80°, 100°)$.

3.3.3 Summary of Pattern Synthesis

A technique for accurate synthesis of non-uniform continuous-source LWA has been introduced in this section. The method is based on the lossy transmission line model for LWA proposed in the previous chapter. Two LWAs based on HMSIWs have been optimised and demonstrated excellent measurement performances, which ultimately validate the proposed method. It is emphasised here that, under the assumption of single-mode propagation, this method is generally applicable for continuous-source LWAs with a reasonably smoothly varying structure. It may also be applied for periodic LWA with relatively small periodicity. In this type of structures, the radiating elements are very close to each other, and thus can be approximated as a continuous-source structure. This could be an interesting subject for future investigations. Finally, it is also worth mentioning that the method can be used for synthesis of an arbitrary pattern mask. The results can be found in [63].

3.4 Reliability-Aware Optimisation for Wideband Antennas

With the development of increasingly complex systems, the problem of quantifying uncertainty effects in the components and devices' behaviors has gained growing attention in

both the research community and manufacturing industry [64, 65]. If this problem can be addressed during the design process, a significant improvement can be achieved from the viewpoint of efficient manufacture and commercialisation of the final products. In particular for the research development of antennas and microwave devices, statistical reliability analysis has been investigated for example in conjunction with resonance frequency variations for textile antennas [66, 67] or physically transient antennas [68]. A method to integrate EM full-wave analysis with sensitivity analysis for microwave and millimetre-wave structures has been proposed in [69]. In the context of circuits and systems, such analysis has a long history. For instance, the work of Abdel-Malek and Bandler [70], [71], or that of Wojciechowski and Vlach [72], dealt with statistical yield analysis.

In this section, statistical analysis is investigated for optimised wideband antennas, for which slight variations due to fabrication and material tolerances might cause localised breach of specifications within the operation band. For clarification, the considered bandwidth is the impedance bandwidth with criteria $|S_{11}| < -10$ dB. The reliability analysis, conducted in this work, is based on a reliability method which has been proven for its high accuracy and its efficiency in many domains, e.g. structural mechanics [73] and electromagnetic compatibility [74]. This method is a variant of the well-known Monte Carlo method, named as *subset simulation* [73]. It is emphasised that the proposed method is a general framework and can be applied to any wideband antenna as long as a solution can be obtained in a reasonably fast manner, by either analysis, semi-analytical computation or simulation.

The wideband antenna chosen for the analysis is based on a tapered half-mode substrate-integrated waveguide (HMSIW) mentioned in the last chapter (see Section 2.3). This type of antenna is selected for study due to the availability of the semi-analytical model, presented in Section 2.4), that allows computing the antenna characteristics in a very fast manner and with high accuracy

This section starts by demonstrating the reliability analysis theory for a general wideband antenna. Then the application of the reliability analysis to the wideband HMSIW antenna is demonstrated, followed by a sensitivity analysis quantifying the influence of the different design parameters and their role in breaches of specification. Subsequently, the next subsection introduces an algorithm for reliability-aware optimisation for the wideband antenna. Finally, an illustrative measurement result as a final demonstration is shown.

For clarification, the contributions in this section are shared equally between A. Kouassi and myself as the project is a collaboration between the University of Adelaide and the Institut Pascal, France. This has been stated clearly in the publication [55].

3.4.1 Reliability Analysis Theory

Problem Statement

The wideband antenna under investigation can be represented by a deterministic mapping $y = \mathcal{M}(\mathbf{x})$. The vector $\mathbf{x} = (x_1, \ldots, x_n) \in \mathbb{R}^n$, $n \geq 1$ describes the input variables, and y is the quantity of interest provided by the model, for example the reflection coefficient $|S_{11}|$. Generally, the mapping $\mathcal{M}$ can be defined by an analytical expression or a numerical model. Assuming that the element x_i, $1 \leq i \leq n$, are uncertain and modeled as n mutually independent continuous random variables denoted by X_i, $1 \leq i \leq n$, the quantity of interest y becomes a random variable denoted by Y and given by:

$$Y = \mathcal{M}(\mathbf{X}) \,, \tag{3.5}$$

where $\mathbf{X} = (X_1, \ldots, X_n)$. The input vector $\mathbf{x}$ is now viewed as a given realisation of $\mathbf{X}$. It is assumed that the probability density functions (PDF) p_{X_i} of X_i, $1 \leq i \leq n$, are known and therefore due to the mutual independence of the X_i, the joint PDF $p_{\mathbf{X}}$ of $\mathbf{X}$ is also known.

Let $\bar{y}$ be a threshold value for the quantity of interest. A *failure event* is then characterised as

$$E_\mathrm{f} = \{\bar{y} - Y \leq 0\} = \{g(\mathbf{X}) \leq 0\} \,, \tag{3.6}$$

where $g : \mathbf{x} \to g(\mathbf{x}) = \bar{y} - \mathcal{M}(\mathbf{x})$ is the so-called *limit state function*. For an antenna, a failure can occur for example when $|S_{11}| > -10$ dB within the specified operation band, and in this case the failure event E_f would be defined by:

$$E_\mathrm{f} = \{-10 \text{ dB} - |S_{11}| < 0\} \,. \tag{3.7}$$

The occurrence of E_f is quantified by the *failure probability* $P_\mathrm{f} = \mathbb{P}(E_\mathrm{f})$ given by the integral

$$P_\mathrm{f} = \int_{\mathbb{R}^n} \mathbb{I}_{D_\mathrm{fx}}(\mathbf{x})\, p_{\mathbf{X}}(\mathbf{x})\, \mathrm{d}\mathbf{x} \,, \tag{3.8}$$

where $\mathbb{I}_{D_{\mathbf{fx}}}$ is the indicator function of $D_{\mathbf{fx}}$, referred to as the *failure domain* of the wideband antenna, given by

$$D_{\mathbf{fx}} = \{\mathbf{x} \in \mathbb{R}^n : g(\mathbf{x}) \leq 0\} \, . \tag{3.9}$$

In the reliability context, it is usual to analyse the reliability of a system through the failure probability P_{f}. That is why the present objective is to calculate this probability for the problem at hand. A natural strategy for estimating the integral (3.8) is to resort to a crude Monte Carlo procedure [75–77]. However, this approach is not efficient for small failure probabilities [76] since in this case a very large number of simulations is required to get satisfactory results. Many alternatives have been proposed in the literature to increase the efficiency of the Monte Carlo method for the computation of small probabilities [73,75–77]. The study presented in this section used one of them, which is known as *subset simulation* (SS) [73] based on a specific multilevel splitting procedure.

Standard Formulation of the Problem

In accordance with the classical reliability strategy [75], a necessary first step is to rewrite the probabilistic problem (3.8) in a standard Gaussian space (or unit Gaussian space) in which all the random variables become standard Gaussian (with zero-mean and unit standard deviation), mutually independent and uncorrelated. This allows to take advantage of the standard Gaussian space's properties, and the estimation of P_{f} in this new probabilistic space become more convenient. The principle of this transformation is given below.

Let consider a n-dimensional standard Gaussian random vector $\mathbf{U} = (U_1, \ldots, U_n)$, and a given realisation of $\mathbf{U}$ denoted by $\mathbf{u} = (u_1, \ldots, u_n)$. It can be shown that there exists a transformation [75, 78, 79] $T : \mathbf{u} \to T(\mathbf{u}) = \mathbf{x}$, such that the following equalities (in distribution) hold:

$$\mathbf{X} = T(\mathbf{U}) \Leftrightarrow \mathbf{U} = T^{-1}(\mathbf{X}) \, . \tag{3.10}$$

Therefore, in the standard Gaussian space, the limit state function is defined by the mapping $G : \mathbf{u} \to G(\mathbf{u}) = (g \circ T)(\mathbf{u})$. Using this mapping, the failure event takes the form: $E_{\mathrm{f}} = \{G(\mathbf{U}) \leq 0\}$, and the failure domain is rewritten as

$$D_{\mathbf{fu}} = \{\mathbf{u} \in \mathbb{R}^n : G(\mathbf{u}) \leq 0\}. \tag{3.11}$$

As a consequence, the failure probability is given by:

$$P_{\mathrm{f}} = \int_{\mathbb{R}^n} \mathbb{I}_{D_{\mathrm{fu}}}(\mathbf{u})\, \varphi_n(\mathbf{u})\, \mathrm{d}\mathbf{u}\,, \tag{3.12}$$

where $\varphi_n : \mathbf{u} \to \varphi_n(\mathbf{u})$ is the n-dimensional standard Gaussian PDF, such that for all $\mathbf{u} \in \mathbb{R}^n$:

$$\varphi_n(\mathbf{u}) = \frac{1}{(2\pi)^{n/2}} \exp\left(-\frac{\|\mathbf{u}\|^2}{2}\right)\,. \tag{3.13}$$

Equation (3.12) represents the standard formulation of the reliability analysis problem. In reliability context, the methods for estimating P_{f} are implemented from this formulation.

Subset Simulation (SS)

The SS method conceived by Au and Beck [73] is a Monte Carlo procedure known to be particularly efficient for estimating small probabilities, i.e. the probabilities of rare events, with a high accuracy. Indeed, using the same number of simulations, it is proved in [73] that the accuracy of the failure probabilities estimates using SS is considerably higher than those using crude Monte Carlo from the estimates in the order of 10^{-3}. The accuracy of the method does not depend on the dimension n of the integral (3.12), and it has no probability limit in theory. However, in practice in the case of very small failure probabilities (e.g. 10^{-20}) the required computational time can become very high depending on the single simulation's time for used model. It is therefore well suited to our purpose, where a large number of computations will concern failure probabilities under 1%. Its principle is summarised in the following.

Let $\{E_1, \ldots, E_m\}$ $(m \geq 2)$, be a set of events such that $E_m = E_{\mathrm{f}}$, and $E_m \subset E_{m-1} \subset \cdots \subset E_2 \subset E_1$ (where for instance, $E_m \subset E_{m-1}$ means that E_m is a subset of E_{m-1}). Given this successive inclusion rule one can easily find that E_{f} is the intersection of all the events $E_1, \ldots, E_m$ $(m \geq 2)$. Thus, by successive conditioning, P_{f} can be rewritten as a product of m probabilities necessarily larger than P_{f} and therefore easier to estimate. This product is given by:

$$P_{\mathrm{f}} = \mathbb{P}(E_{\mathrm{f}}) = \mathbb{P}(E_1) \prod_{k=1}^{m-1} \mathbb{P}(E_{k+1}|E_k)\,, \tag{3.14}$$

where, for all $k \in \{1, \ldots, m-1\}$, $\mathbb{P}(E_{k+1}|E_k)$ denotes the conditional probability of E_{k+1} given E_k.

To choose the events E_k, $1 \leq k \leq m$, in accordance with the previously introduced inclusion rule, a strategy has been proposed in [73]. On this basis the estimation of P_f requires the computation of the probability $\mathbb{P}(E_1)$ and the conditional probabilities $\mathbb{P}(E_{k+1}|E_k)$, $1 \leq k \leq m-1$. The value of $\mathbb{P}(E_1)$ is estimated using a crude Monte Carlo method, whereas the estimation of the conditional probabilities requires the simulation, for all $k \in \{1, \ldots, m-1\}$, of a random variable distributed according to the conditional distribution of $\mathbf{U}$ given E_k. This simulation is performed in SS, via a Markov Chain Monte Carlo (MCMC) method [76], [77]. The MCMC algorithm used in this work is the Metropolis-Hastings Algorithm, modified by Au and Beck [73].

3.4.2 Reliability Analysis and Sensitivity Analysis of the Wideband HMSIW Antenna

Reliability Analysis

In this section, the reliability analysis presented in section 3.4.1 will be applied for the chosen wideband tapered HMSIW antenna. This antenna type has been discussed in 2.3.2 and investigated thoroughly in the last chapter (noting also that the first part of this chapter has shown the optimisation of this antenna adaptated for metallic structure integration). For readers' convenience and completeness of this section, its geometry is shown again in Fig. 3.21 (similar diagram is shown in Fig. 2.13). The antenna is fabricated using a Rogers Ultralam 2000 substrate with relative permittivity $\epsilon_r = 2.5$ and thickness $h = 60$ mil $= 1.524$ mm. Similarly to the previous sections, the via hole wall of the HMSIW is approximated as a PEC wall [49] and the shape of the antenna can be defined using vectors for the width $\mathbf{w} = [w_0, w_1, ...w_N]$ and length $\mathbf{l} = [l_1, l_2, ...l_N]$, where N is the number of tapered sections. In each section, the antenna tapering is treated as linear (Fig. 3.21b). The antenna length $L_{ant} = \sum l_i$. This antenna can be optimised for a given bandwidth, i.e. for a target reflection coefficient $|S_{11}|_{tg}$ (dB) within the frequency range $[f_{min}, f_{max}]$ [48], using Particle swarm optimisation (PSO) with the cost function of

$$C = \begin{cases} c_2 L_{ant} \text{ if } \max(|S_{11}|) < |S_{11}|_{tg} \\ c_1(\max(|S_{11}|) - |S_{11}|_{tg}) + c_2 L_{ant} \text{ otherwise.} \end{cases} \tag{3.15}$$

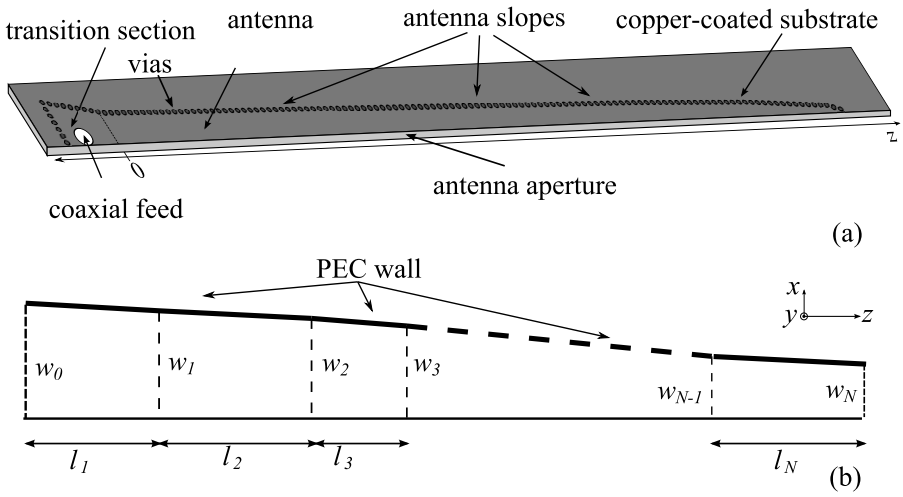

Figure 3.21. The design and model of a wideband antenna based on a tapered HMSIW.

Table 3.2. Means and tolerance values of the antenna design parameters

Random variable	Mean	Absolute tolerance
ϵ_r	2.5	0.14
h (mm)	1.524	1.524×0.05
$\mathbf{w}$ (mm)	variable	0.05
$\mathbf{l}$ (mm)	variable	0.05

It is now assumed that the antenna's parameters ϵ_r, h, $\mathbf{w}$ and $\mathbf{l}$ are affected by uncertainties and modeled as mutually independent random variables. As introduced in Section 3.4.1, the random vector becomes $\mathbf{X} = (\epsilon_r, h, \mathbf{w}, \mathbf{l})$.

In the design problem at hand, means of ϵ_r and h are constant, whereas the means of $\mathbf{w}$ and $\mathbf{l}$ are found in each case as a result of a deterministic optimisation results performed using PSO (similar to what presented in Section 3.2 and [48]). The tolerance for the substrate permittivity and thickness can be found from the datasheet [80] whereas the tolerance for $\mathbf{w}$ and $\mathbf{l}$ is estimated from the available printed circuit milling machine and manufacturing process. The means and absolute tolerances of the considered random variables can be found in Table 3.2. Since the type of these tolerances are not known or specified in the datasheet for both substrate and milling machine, a uniform distribution

Table 3.3. Chosen specifications for the two wideband antennas under investigation

	BW Spec.	BW target	$\|S_{11}\|$ Spec.	$\|S_{11}\|_{tg}$
Ant. I	8–12 GHz	8–12 GHz	-10 dB	-12 dB
Ant. II	7–14 GHz	6.86–14.28 GHz	-10 dB	-10.5 dB

will be assumed for all considered random variables, which is in agreement with the principle of maximum entropy introduced by E. T. Jaynes in [81]. The support of each random variable is given by an interval of $\pm\, t$ around its mean, where t represents the absolute tolerance. Obviously, in practice, some parameters can be correlated, e.g. a slight shift of the substrate may result in all width values being shifted in a same manner. However, without any prior information about the specific nature and amplitude of an eventual correlation, an equiprobability, modeled by mutual independence, has been assumed between all the random parameters. It is noted the analysis can still be utilised if correlations between the variables are known, e.g. using Nataf transformation [75]. It has been empirically found from a few selected cases that a possible correlation between all the widths w_i may result in a slight increase of failure probability, but should not invalidate the conclusions presented for the case without correlation.

The failure probabilities calculations were all performed using the open source code FERUM [82]. As SS is based on simulations of random variables, the failure probabilities estimates will be always given with their coefficients of variation (COV) [73], quantifying the level of accuracy of the estimates. It is noted that small numbers indicate trustworthy results, and COV values below a threshold of 20% are empirically considered acceptable in the reliability research community.

For investigation, two sets of specifications, referred to as "Antenna I" and "Antenna II", are selected as shown in Table 3.3. The optimisation is performed with a target reflection coefficient $|S_{11}|_{tg}$ **below specification and/or wider target bandwidth**. This is considered as a first empirical step to account for uncertainties. The failure is simply defined as

$$\max(|S_{11}|_{[f_{min},f_{max}]}) > -10 \text{ dB} \,. \tag{3.16}$$

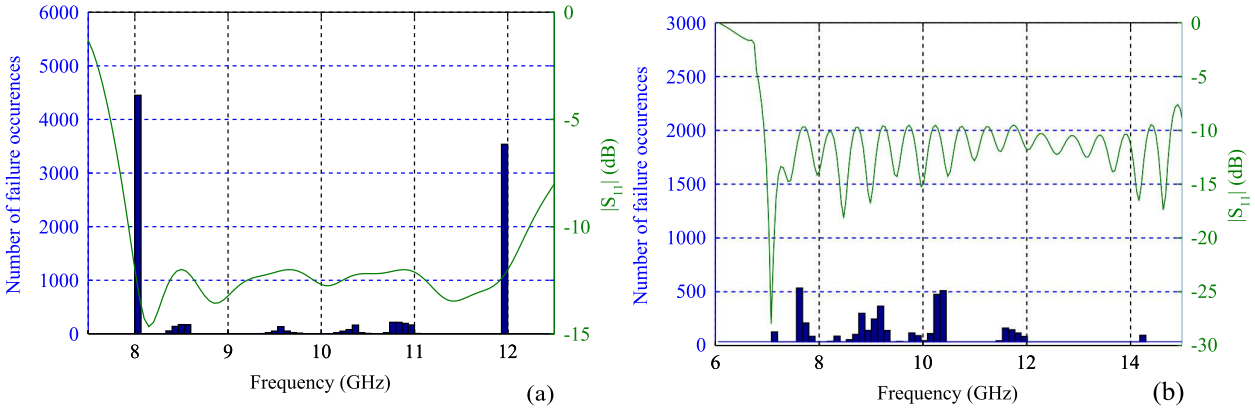

Figure 3.22. Calculated reflection coefficient and histogram of the frequencies at which the failure is observed. The histograms are based on a crude Monte Carlo sampling with 10000 and 5000 random simulations of $\mathbf{X}$ for Antenna I and Antenna II respectively, given in Table 3.3: (a) Antenna I; (b) Antenna II.

The first investigations have been conducted looking for a high accuracy of the failure probability estimates. The goal was to compute these estimates with a COV lower than 1%, representing a very good level of accuracy. The failure probability estimates of the two PSO-optimised antennas, in agreement with this accuracy's criterion, have been reached using 10000 random simulations for Antenna I and 5000 random simulations for Antenna II.

The reliability analysis results shows that the failure probability for the Antenna I is 56% (COV = 0.9%), while the failure probability for the Antenna II is 70% (COV = 0.9%). This indicates that, for both cases, using the target S-parameter values given in Table 3.3 yields a very high probability of specification failure within the bandwidth. This can be expected since the variation in antenna design parameters will almost certainly change the reflection coefficient response. Fig. 3.22 shows the calculated S-parameters for the two antennas, together with the histogram of the frequencies at which the failure is observed. It can be noticed that a majority of the failure events happens at the upper and lower limits of the bandwidth for Antenna I. Since the target bandwidth (BW) for this antenna is exactly the same as the specification, most failures are predominantly attributed to a frequency shift arising from the variations of the substrate relative permittivity ϵ_r. In contrast, for Antenna II, a frequency tolerance is already built in the optimisation by widening the bandwidth target. In this case, most failures occur within the frequency band and can be

attributed to variations on the shape of the antenna ($\mathbf{w}, \mathbf{l}$). These two cases illustrate the importance of choosing appropriate margins to obtain optimised designs.

Global Sensitivity Analysis

In addition to the above reliability analysis of Antenna I and Antenna II, a global sensitivity analysis has been also conducted on the reflection coefficient $|S_{11}|$ of the two sample antennas. The method to obtain the relative importance of each design parameter is explained first, followed by a physical interpretation based on the obtained results.

Method

The global sensitivity analysis is based on the computation of normalised variances of conditional expectations, representing the relative weight of one parameter on the variability of $|S_{11}|$, or the combined weight of the interaction of several parameters. The indices quantifying the weight of one parameter are named first-order sensitivity indices, and those quantifying the weight of the interaction between two (resp. three) parameters, are named second-order (resp. third-order) sensitivity indices. On this basis, the definition of sensitivity indices of higher order is intuitive. These indices are referred to as the Sobol sensitivity indices [83]. When the number of parameters is large, the number of these indices increases very quickly and their interpretation becomes very difficult. For this reason, Saltelli et al. defined in [84] the total sensitivity indices which quantify the importance of one parameter and its interactions with all other parameters, on the variability of a random quantity of interest. These indices allow a more convenient physical interpretation. Here we present the total sensitivy indices derived from the analysis conducted on the $|S_{11}|$ of Antenna I and Antenna II. The study has been performed via a crude Monte Carlo method [76], using the open source code FERUM [82]. The obtained results for the two sample antennas are shown in Fig. 3.23.

Physical Interpretation

The results for Antenna I will be interpreted first. It can be observed that the relative permittivity of the substrate ϵ_r plays the most important role on the variations of $|S_{11}|$. This is as expected because variation in ϵ_r leads to a frequency shift in the bandwidth, thus causes failure at the limits of the frequency range (Fig. 3.22a). For the width w_i of each linearly tapered section, parameters with high importance are at the start and the

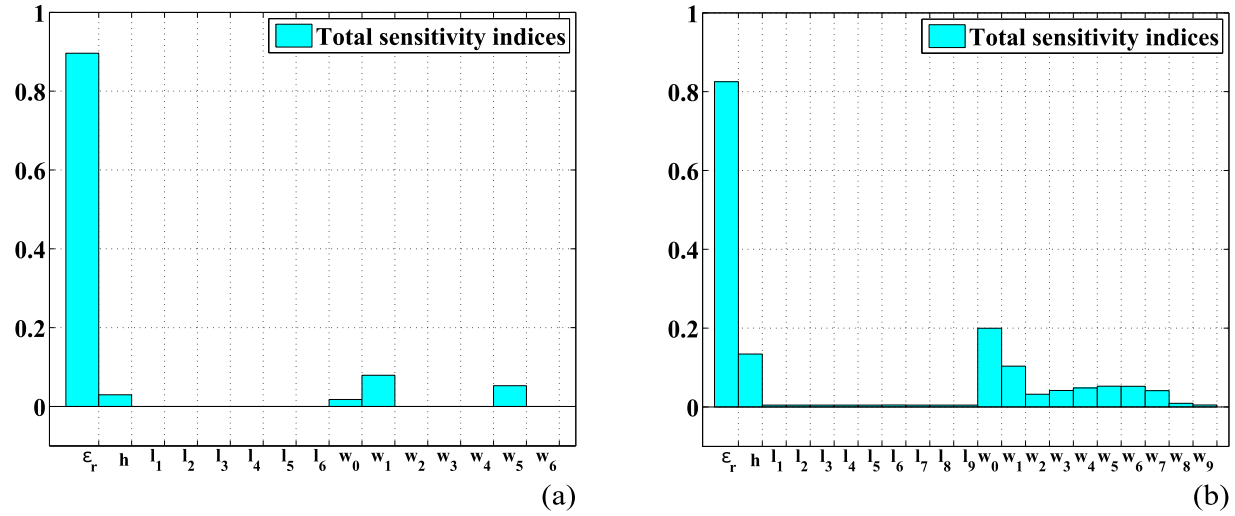

Figure 3.23. Global sensitivity analysis results. Results are conducted on the $|S_{11}|$ of the two sample antennas: (a) Total sensitivity indices for Antenna I, obtained from a crude Monte Carlo method using 170,000 random simulations; (b) Total sensitivity indices for Antenna II, obtained from a crude Monte Carlo method using 230,000 random simulations.

end of the antenna. This is because these widths determine the cutoff frequency at the upper and lower limit frequency.

For Antenna II, it is interesting to observe that ϵ_r still plays a major role on failure events. Since $|S_{11}|_{tg}$ for this antenna is very close to specification, a variation in ϵ_r would change the height of the peaks in $|S_{11}|$ response and might cause failures. As expected, the widths w_i play a more important roles in this antenna as their variations can cause the failures in the mid-range frequencies (Fig. 3.22b).

Finally, for both Antennas, changes on the length of each section yield negligible contribution on the variation of $|S_{11}|$. This can also be predicted since the absolute tolerance of the length (50 μm, Table 3.2) is very small compared to its mean, which is in range of mm for the current investigated antennas.

3.4.3 Reliability-Aware Optimisation

At this current state of the investigation, a straightforward solution to achieve an antenna strictly within specifications is to lower the target reflection coefficient $|S_{11}|_{tg}$ and provide enough safe margin for the bandwidth by extending the frequency range of optimisation

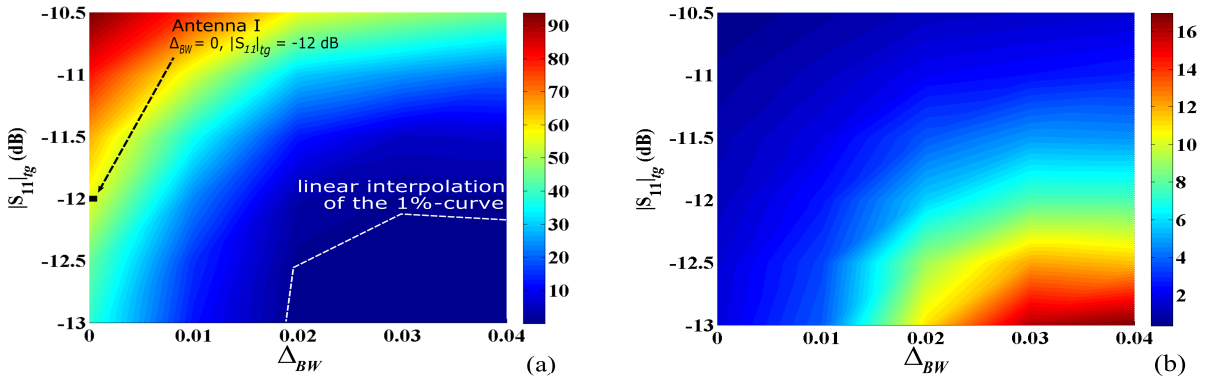

Figure 3.24. Reliability analysis results of Antenna I optimised for 8-12 GHz. Results are plotted with different values of Δ_{BW} and $|S_{11}|_{tg}$: (a) Failure probabilities (in percentage) obtained from SS using 5000 random simulations for assessing the first and conditional probabilities; (b) Associated COVs (in percentage). The specific case presented in Fig. 3.22a is highlighted in Fig. 3.24a.

below f_{min} and above f_{max}. However, by doing this empirically, the length of the antenna will increase and the design will not be optimal any more. Thus, an optimisation process is required. The first part of this section will demonstrate the trend of failure probability when varying the margin for target reflection coefficient and bandwidth. The proposed optimisation algorithm and results will be presented afterwards.

3.4.4 Probability Map

To obtain an initial idea about how the failure probability is improved by lowering the target reflection coefficient and increasing the safe margin for the bandwidth, Antenna I and Antenna II (Table 3.3) are optimised for different $|S_{11}|_{tg}$ and bandwidth margins and then are statistically analysed with the method proposed in Section 3.4.1. The safe margin for the bandwidth is denoted as Δ_{BW} and specifies a new optimisation bandwidth as $[f_{\min}(1-\Delta_{BW}), f_{\max}(1+\Delta_{BW})]$. The results of this reliability analysis as a function of $|S_{11}|_{tg}$ and Δ_{BW} are shown in Figs. 3.24 and 3.25. In order to generate this graph, 30 antennas have been optimised and their reliabilities have been analysed for $|S_{11}|_{tg} \in \{-10.5, -11, ..., -13\}$ dB and $\Delta_{BW} \in \{0, 0.01, ..., 0.04\}$. The 2D-color plot for the whole plane was then obtained using linear interpolation. In both case, the COVs shown

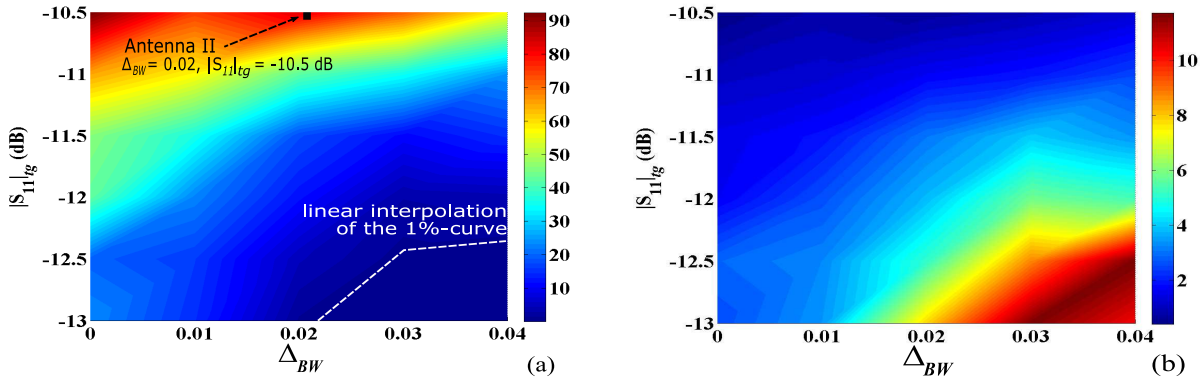

Figure 3.25. Reliability analysis results of Antenna II optimised for 7-14 GHz. Results are plotted with different values of Δ_{BW} and $|S_{11}|_{tg}$: (a) Failure probabilities (in percentage) obtained from SS using 5000 random simulations for assessing the first and conditional probabilities; (b) Associated COVs (in percentage). The specific case presented in Fig. 3.22b is highlighted in Fig. 3.25a.

in Figs. 3.24b and 3.25b are below the mentioned threshold of 20%, indicating the statistical validity of the results, even for regions of smaller failure probabilities (bottom right corner of the graphs).

As can be intuitively expected, it is observed that there is a very high probability of failure when $|S_{11}|_{tg}$ is close to -10 dB and for smaller Δ_{BW}. More importantly, for each given failure probability value P_{f0}, a curve $(|S_{11}|_{tg}, \Delta_{BW})$ can be found so that if the antenna is designed with values $|S_{11}|_{tg}, \Delta_{BW}$ on this curve, it would achieve a failure probability of P_{f0}. One of these P_{f0}-curves for a value of 1% is shown in approximate dashed line the Figs. 3.24 and 3.25. If this curve can be found accurately for a desired failure probability, the best antenna along that curve should be selected, keeping in mind that all designs on that curves have been optimised using the cost function (3.15). Thus, in the case of the considered tapered HMSIW LWA, the objective is to reduce the length of the antenna and the best optimised antenna is simply determined from the shortest L_{ant} found along the P_{f0} curve.

Unfortunately, computing the maps shown in Figs. 3.24 and 3.25 with sufficient resolution can become prohibitively expensive computationally, since the statistical analysis requires large number of cases to be computed. Therefore, the next subsection will present an algorithm aiming at determining P_{f0}-curves with reduced computational effort.

3.4.5 Optimisation Algorithm and Results

On the basis of the finding discussed in the previous section, the P_{f0}-curve for a given value of P_{f0} is approximated using a contour-search algorithm within the 2D map. The first step is to identify appropriate intervals $[|S_{11}|_{tg\,start}\,,\ |S_{11}|_{tg\,end}]$ and $[\Delta_{BW\,start}\,,\ \Delta_{BW\,end}]$ to delimit the search domain for $|S_{11}|_{tg}$ and Δ_{BW}. These intervals can be extended during the search algorithm execution if required. The determination of the P_{f0}-curve requires to find a set values of $|S_{11}|_{tg}$ and Δ_{BW} for which the failure probability of the associated PSO-optimised antenna is lower than but as close as possible to P_{f0}. Thus the proposed algorithm, step by step, makes a choice of $(|S_{11}|_{tg},\ \Delta_{BW})$ and optimises the antenna with these values using PSO, then calculates the failure probability of this antenna using SS. The shift to the next iteration step is made by increasing or decreasing the current value of $|S_{11}|_{tg}$ or Δ_{BW}, by $|S_{11}|_{tg\,step}$ or $\Delta_{BW\,step}$ respectively. In general, this can be considered as a stair-case search algorithm. The choice of the next $|S_{11}|_{tg}$ and Δ_{BW} values at each iteration step is very crucial to get the P_{f0}-curve in a reasonable time. Consequently, at each iteration of the algorithm, the next values of $|S_{11}|_{tg}$ and Δ_{BW} are chosen by taking into account the current values of $|S_{11}|_{tg}$ and Δ_{BW}, and the two last obtained failure probability results. A pseudo-description of the proposed algorithm and further explanations can be found in the Appendix C. Once the P_{f0}-curve is obtained, the optimised antenna is chosen as the one having the minimum length along the P_{f0}-curve (i.e. with a failure probability lower than P_{f0}).

The algorithm has been applied to optimise the tapered HMSIW antennas mentioned before. It is worth mentioning that the necessary condition for such statistical analysis is that a solution for a single case must be fast enough to allow thousands of set of parameters to be evaluated in a reasonable period of time. This is currently not possible using full-wave electromagnetic simulations for a LWA whose structure is long and complex. In contrast, the reliability analysis is feasible for the considered geometry with the semi-analytical approach proposed in Section 2.4 since this model can predict very accurately the reflection coefficient of the antenna over a wide range of frequency. A small issue is a frequency shift between analysis and simulation in the frequency range of $[6, 18]$ GHz, which is due to the error in the calculation of propagation constant (see Fig. 2.3 for HMSIW Variation I). This frequency shift was consistently observed in all antennas examined in [48]. Thus, it

Table 3.4. Algorithm's results

	Antenna I	Antenna II
failure probability (%)	0.83	0.36
coefficient of variation (%)	9.05	13.60
$\|S_{11}\|_{tg}$ (dB)	-12.20	-12.20
Δ_{BW}	0.022	0.027
antenna length (mm)	97.93	160.69
computation time (h)	70	73

can be treated as a systematic error and straightforwardly compensated with a down-shift of computed results.

The algorithm was applied to both Antenna I and Antenna II (for which the specifications were shown in Table 3.3) with the target maximum failure probability of 1%, i.e. $P_{\mathrm{f}0} = 0.01$. At each iteration of the algorithm, the failure probability of the PSO-optimised antenna is performed using 5000 random simulations for Antenna I and 2500 random simulations for Antenna II, for assessing the first and conditional probabilities. These numbers ensure, in the two cases, that a COV lower than 20% is achieved.

The obtained final results are given in Table 3.4. Figures 3.26a and 3.27a show the approximated 1%-curve for the two antennas obtained from the statistical analysis using the proposed algorithm. The figures show two sets of points obtained from the stair-case search algorithm: the red dots indicate cases with failure probability just above 1%, while the blue squares show cases with failure probability just below 1%. The shape of the curve agrees qualitatively with the approximation from linear interpolation shown in Fig. 3.25, however the accuracy of reliability computation is considerably superior to the simple linear interpolation. The length of the antennas L_{ant} along the blue square curves are plotted in Figs. 3.26b and 3.27b, and this data is used to obtain the optimised result with shortest length. It is noted that all antennas on those curves keep the failure probability less than the target of 1%. Some outlier points can be observed, which is not unexpected since the statistical analysis is inherently an approximation process. Nevertheless, the trend of the

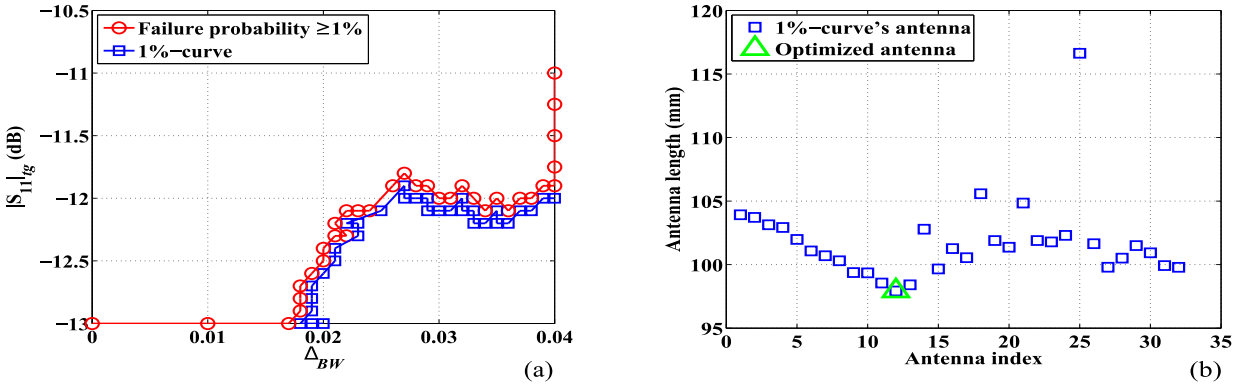

Figure 3.26. Optimisation algorithm results for Antenna I. (a) Approximation of the 1%-curve; (b) Determination of the optimised antenna.

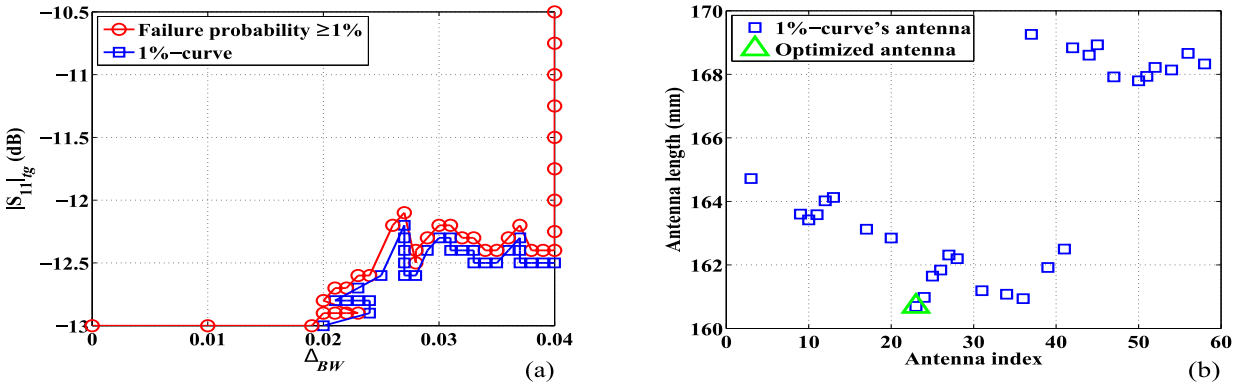

Figure 3.27. Optimisation algorithm results for Antenna II. (a) Approximation of the 1%-curve; (b) Determination of the optimised antenna.

curve can be still clearly recognised and optimised results, i.e. the green triangular points in Figs. 3.26b and 3.27b, are obtained.

It is worth emphasising that the outcome of this process is the determination of optimised margins for reflection coefficient and bandwidth. As discussed before, simply relaxing the specifications does not provide an optimal solution and may even result in a longer antenna with no control on the failure probability.

3.4.6 Measurement Results

Statistical validation of the findings presented in the previous sections is not possible within our laboratory since an ultimate verification of a statistical analysis would involve

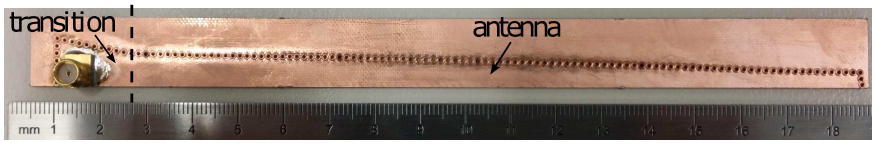

Figure 3.28. Photograph of a fabricated prototype of Antenna II.

a mass manufacture. Nevertheless, comments on a fabricated prototype (Antenna II) will be provided as supporting evidence. These measurements only serve as an example demonstration for the final product of the reliability-aware optimisation.

A prototype with Antenna II specifications (optimised for $7-14$ GHz) with calculated failure probability under 1% has been fabricated (Fig. 3.28). The reflection coefficient over the target frequency range has been measured and it can be observed from Fig. 3.29 that the final antenna is a success. It is noted that the systematic error of 2.8%-frequency shift is taken into account in the analysis curve (Fig. 3.29), which shows an excellent agreement between analysis and simulation. The achieved bandwidth is from 6.78 to 14.57 GHz with maximum reflection coefficient of -10.9 dB. The variations especially noticeable at the peaks of the reflection response are attributed to variations in the parameters of the antenna. These results exemplify the safety of the reliability-aware optimisation, but also suggests that the antenna will become more likely to fail if designed at higher $|S_{11}|_{tg}$.

3.4.7 Summary of the Reliability-Aware Optimisation

In this section, a reliability analysis and a reliability-aware optimisation of the wideband HMSIW antenna has been investigated. The statistical analysis is valuable on different levels. Firstly, it has helped identifying the important parameters responsible for the antenna failure probability. Moreover, it has given a deep insight into the antenna design sensitivity, and even allowed quantifying the effects of uncertainties for the considered type of antenna. Based on the proposed analysis framework, a wideband antenna with bandwidth from 7 GHz to 14 GHz has been optimised for a failure probability of less than 1%, and a prototype has been successfully tested for illustration.

Furthermore, the analysis presented in this section is emphatically not limited to the tapered HMSIW antenna but can be generalised to other antennas optimised for impedance bandwidth, where one of the main specifications is that the reflection coefficient $|S_{11}|$ over

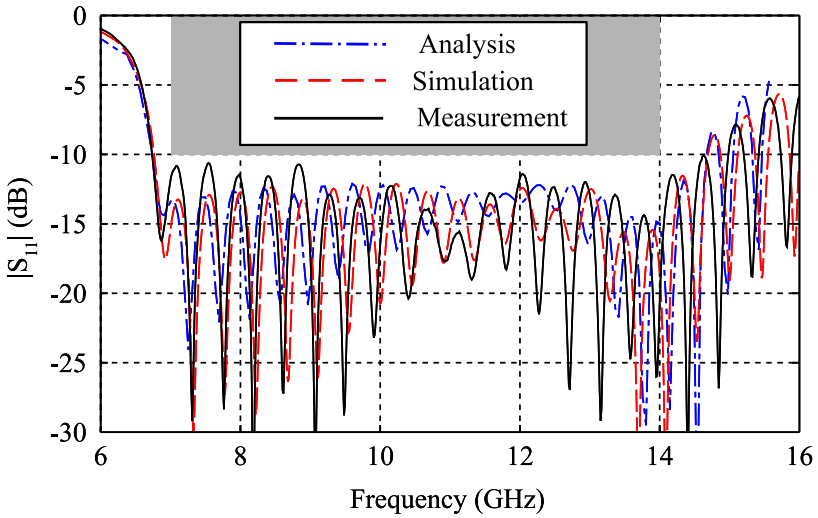

Figure 3.29. Reflection coefficient results of the reliability-aware-optimised wideband antenna. analysed, simulated and measured reflection coefficient of a wideband tapered HMSIW design for a bandwidth from 7 GHz to 14 GHz. The analysis result includes correction of the systematic error with 2.8% frequency shift.

frequency range (f_1, f_2) must be less than a specified level. This does not exclude narrow band antennas. Moreover, the proposed method can also be tailored to target any other specifications, for example in terms of radiation patterns, gain or beamwidth. One further investigation on the optimisation of sidelobe level of leaky-wave antenna has been published in [56]. The current limitation is that this antenna must be solvable in a very fast manner for an extensive and accurate statistical calculation. It is expected that this limitation will improve with a fast-paced development and improvement of the numerical simulation tools and computing hardware. Finally, the proposed framework can be extended to tolerance and reliability analysis for antennas for which an analytical approximation or a surrogate model are available to efficiently describe design parameter dependency. In this general case, the accuracy of the considerations is limited by the accuracy of the model.

3.5 Conclusion

This chapter has proposed three optimisation methods for LWAs with illustrations of their applications to HMSIW antennas. The optimisations have been shown for various targets,

including for wideband operation, different radiation patterns and a reliability-aware optimisation procedure that includes the uncertainty in the fabrication process. Measurement results of all antennas have been presented, which not only validate the optimisation techniques, but also the transmission line model for travelling-wave antennas (TWAs) proposed in the last chapter.

Chapter 4

Low-Profile Monopolar Antennas

THIS chapter presents the original contributions of the thesis dedicated to low-profile monopolar antennas based on edge-shorted centre-fed patches. Using the field equivalence principle, these antennas can be shown to radiate as equivalent magnetic-current loops. This concept is extended in this chapter with the addition of symmetrical slots on the patch to further minimise the antenna size for wideband operation. Furthermore, the same principle can be applied to further lower the profile of a dual-band radiator without affecting its omnidirectional patterns and vertical polarisation. For wideband operation, two practical applications of the antennas, including the integration onto vehicles and onto helmets are examined.

4.1 Introduction

The first realisation of a low-profile monopolar antenna is dated back to the 1950s with some early work done by Seeley [85]. In the 1990s, Delaveaud *et al.* independently designed and patented a similar antenna with two shorting wires [86,87]. More recently, Lau and Luk proposed a wideband monopole antenna based on a circular patch and four symmetrical wires [88]. Since then, this antenna concept has drawn increasing attention from both the research community and industry due to its capability to produce vertically polarised omnidirectional radiation patterns across an ultra-wide range of frequencies with low-profile configuration [89–96]. The antenna's operational principle can be explained using the field equivalence principle and image theory as described in Chapter 1. The radiation problem is then approximately equivalent to a magnetic-current loop radiating into free space [97,98]. Because of this, the antenna exhibits monopolar radiation pattern with vertical polarisation. In order to achieve a wide operational bandwidth for this type of antennas, the space between the shorted patch and the ground plane needs to be judiciously chosen. Thus, research efforts have been concentrating on miniaturising these antenna types, focusing on optimisation of the height of the structure, while retaining a wide bandwidth and high radiation efficiency.

Table 4.1 shows a comparison of some recent and notable designs of this type of antenna, where H, L, W are the height, length and width of the antenna, respectively, and λ_{min} is the free-space wavelength at the minimum operating frequency. In this table, BW denotes the fractional bandwidth and VSWR is specified for the reported bandwidth. Other comparisons can be found in [94,96].

In general, there is a trade-off between antenna dimensions: height, width and length, and bandwidth. The designs in [92,96] from Behdad's research group show the smallest height for the antenna is achieved at the expense of increasing VSWR to 3:1 and 2.7:1, respectively, which may limit the antennas' suitability for transmission applications. The design in [91] has a relatively small antenna height yet the lateral size is quite large, i.e. $0.360\lambda_{min}$. Similar tendencies can also be observed in [90,93]. As can be seen from [94, 95] in Table 4.1, the reduction of the lateral size from $0.204\lambda_{min}$ to $0.189\lambda_{min}$ increases the VSWR. Furthermore, the antennas in [94] and [96] require feeding networks, which increases the complexity of the design.

Table 4.1. Performance comparison amongst state-in-the-art low-profile monopolar antennas.

Work (year)	H/λ_{min}	L/λ_{min}	W/λ_{min}	BW	VSWR
[90], 2008	0.071	0.287	0.287	6.54:1	1.93:1
[91], 2011	0.053	0.360	0.360	4:1	2:1
[92], 2013	0.033	0.240	0.240	4:1	3:1
[93], 2013	0.069	0.365	0.344	2.73:1	1.93:1
[94], 2014	0.085	0.189	0.189	5.5:1	2.2:1
[95], 2014	0.087	0.204	0.204	3.92:1	1.93:1
[96], 2015	0.046	0.260	0.260	8.5:1	2.7:1
This work (car)	0.068	0.208	0.208	2.91:1	1.93:1
This work (hel.)	0.061	0.213	0.213	3.06:1	1.93:1

While some antenna applications might require a bandwidth of multiple octaves, the others might be satisfied with a narrower frequency range or a multi-band design. The original contributions of this chapter are two novel antenna designs, including:

1. A wideband design with reduced antenna height while retaining the planar size and balancing it with the operating bandwidth,

2. A dual-band design with significantly reduced antenna height.

For both antennas, the antenna structure remains simple with stable omnidirectional radiation patterns and vertical polarisation at all operating frequencies. The VSWR is to be kept as 1.93:1 which corresponds to $|S_{11}| < -10$ dB.

For the antennas in this chapter, the field equivalence principle plays a major role in understanding the antenna radiation mechanisms as well as adding different functions, or improving the antenna radiation characteristics. The central technique used for both antennas is the addition of symmetrical slots on the top of the shorted patch. This technique is inspired from the field equivalence principle as these slots create another magnetic-current loop. The addition of these slots do not increase fabrication complexity, yet they can contribute to the antenna miniaturisation as well as provide a better VSWR response across a wide frequency range of about 3:1, as later demonstrated for the wideband antenna. For the dual-band application, this additional magnetic-current loop opens another

resonance band, which can be easily controlled and optimised by varying the position and length of each slot.

This chapter consists of two main parts. The wideband design and its applications for the integration onto vehicles and helmets are demonstrated first. The symmetrical slots are introduced in this part. The findings in this part have been published in [99]. Afterwards, the dual-band design is presented, where the slot geometry is tailored for obtaining and optimising the upper band operation.

4.2 Wideband Design

In this section, the antenna structure is proposed first, followed by a study of key features and parameters. As a special application case, the adaptation of this antenna design onto a curved ground plane, leading to possible integration onto a helmet is then investigated (some helmet antennas can be found in [100, 101]). Finally, measurements for both antennas, i.e. integrated onto vehicles and onto helmets, are presented. The beneficial effects of the helmet shape on radiation patterns and antenna height reduction are also discussed.

4.2.1 Antenna Structure

The detailed antenna design is illustrated in Fig. 4.1. The antenna consists of a square single-sided copper-clad substrate forming a patch, which is placed at a distance h above a ground plane. At the edge of the substrate, four shorting copper rods are placed centrally to force the patch into its magnetic current loop radiation mode. These shorting rods also structurally support the substrate. The selected patch substrate material is Rogers Duroid 5880, with relative permittivity $\epsilon_r = 2.2$ and thickness $h_s = 1.575$ mm.

The antenna is fed perpendicularly at the centre of the patch using a coaxial connector. To provide good impedance matching, the coaxial connector inner pin is attached to a conductive cone [95]. The antenna thickness can be further reduced by using a ring gap [90] instead of an air gap between the top patch and the cone as in [95]. On the top of the patch, four symmetrical tapered slots are introduced to achieve antenna miniaturisation and a lower reflection coefficient while not degrading the antenna pattern omnidirectionality. As mentioned, this can be explained using the field equivalence principle, with the

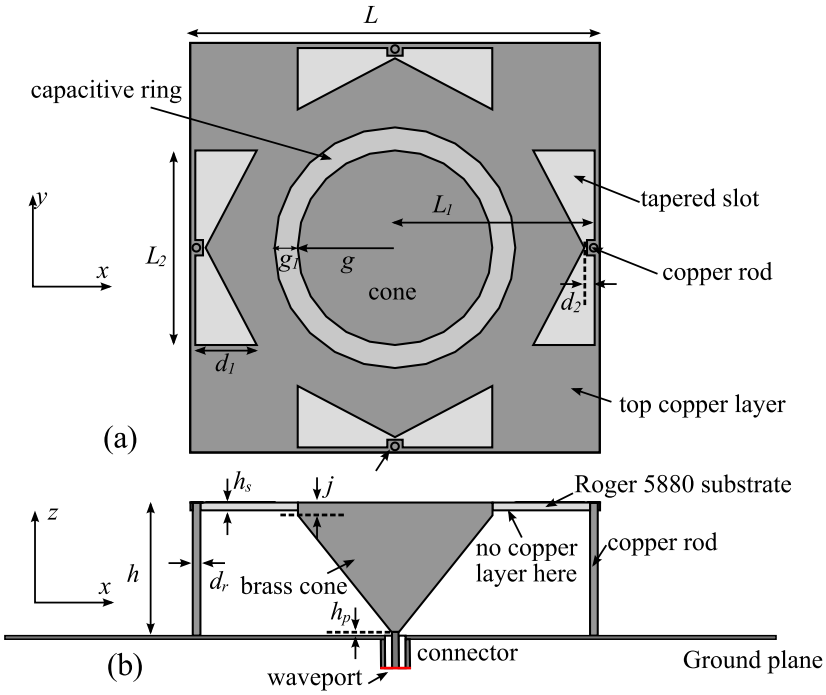

Figure 4.1. The design of a wideband low-profile monopolar antenna employing symmetrical slots above a large flat ground plane. (a) top view, (b) side view. Darker shaded areas represent the conductor whilst lighter shaded areas denote the substrate.

fields in these slots being equivalent to a magnetic current loop. Thus, the arrangement of the four slots also radiates omnidirectionally with vertical polarisation.

The antenna design has been optimised to target relatively low frequencies, i.e. from about 800 MHz to 2300 MHz with optimised dimensions (Fig. 4.1) summarised in Table. 4.2.

4.2.2 Key-Feature and Parameter Study

The effects of adding symmetrical slots are first demonstrated, followed by key-parameter study. For illustration, selected antenna design parameters are varied individually while keeping other parameters constant as shown in Table 4.2.

Effects of Introducing Slots

The effect of the symmetrical tapered slots is demonstrated in Fig. 4.2. The −10 dB-bandwidth of the antenna without slots extends from about 1 GHz to 1.2 GHz, and is

Table 4.2. Parameters of the optimised antenna for integration onto vehicles.

Par.	Value (mm)	Par.	Value (mm)	Par.	Value (mm)
d_1	12	g_1	4.5	h_s	1.575
d_2	2	j	2.5	L	80
d_r	1.5	h	26	L_1	39
g	19	h_p	0.75	L_2	38

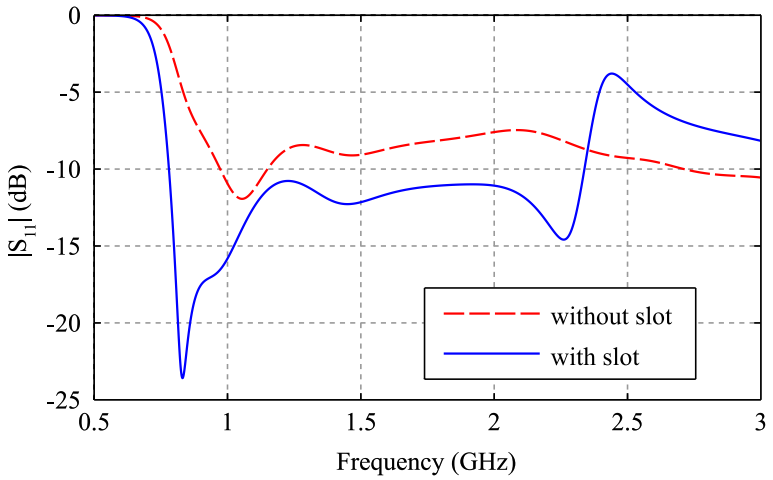

Figure 4.2. Reflection coefficient of the proposed antenna with and without tapered slots.

followed at frequencies above 1.2 GHz by a region of higher reflection coefficient, i.e. -7 dB to -8 dB. Although Fig. 4.2 shows the result for only one configuration, it has been found that this type of response is consistently observed for various parameter sets. Essentially, by adding the slots, the resonance frequency of the patch decreases by about 17% allowing further antenna miniaturisation. To verify this feature, the electric field distributions at lower and higher frequencies in the operating band are shown in Fig. 4.3 using the same scale. It can be qualitatively observed that at lower frequencies the radiation is emitted from both slots and edges of the patch. At higher frequencies, most radiation originates from the slots and hence the response in this frequency range depends dominantly on the slot dimensions.

To further demonstrate the benefits of the slots, we compare our slotted geometry with one of the most recent designs with the same $|S_{11}|$ specification, i.e. in [95] (see Table 4.1). Firstly, Fig. 4.4 shows the reflection coefficient for the antenna in [95] optimised for sizes

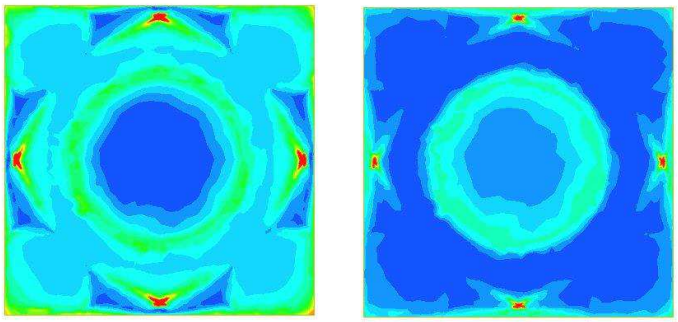

Figure 4.3. Field distribution of the antenna with additional slots. Simulated magnitude of complex electric field at two different frequencies. The field is plotted at the top metal layer of the patch.

of $80 \times 80 \times 26$ mm^3 and $108 \times 108 \times 26$ mm^2, compared to our antenna design. In these antennas, the ground plane size remains at 280×280 mm^2. It can be concluded from Fig. 4.4 that to make the antenna in [95] operate from 800 MHz while keeping its height at 26 mm, the antenna size needs to be increased to about 108 mm, i.e. by 35%, with additional difficulties to lower the reflection coefficient below -10 dB. By adding slots, the structure is miniaturised while keeping the bandwidth within the specification (the blue solid curve in Fig. 4.4). The simulated -10 dB-bandwidth of the final design is 780 MHz to 2350 MHz. Table 4.1 shows that our design reduces the antenna height by 20% while retaining the lateral size at the expense of relative bandwidth.

Ground Plane

The first antenna design is intended for vehicle integration and has been initially designed with an infinite ground plane using a numerical simulation tool (Ansys HFSS). The reflection coefficients for this antenna using different ground plane sizes have been simulated and the results are shown in Fig. 4.5. These results show that to obtain a satisfactory reflection coefficient over the targeted bandwidth, the ground plane should be at least 220×220 mm^2. A higher return loss for the smaller ground plane is due to the thinner effective height of the structure. For experimental measurements, the ground plane size 280×280 mm^2 is selected, which corresponds to $0.737\lambda_{min} \times 0.737\lambda_{min}$ in terms of the

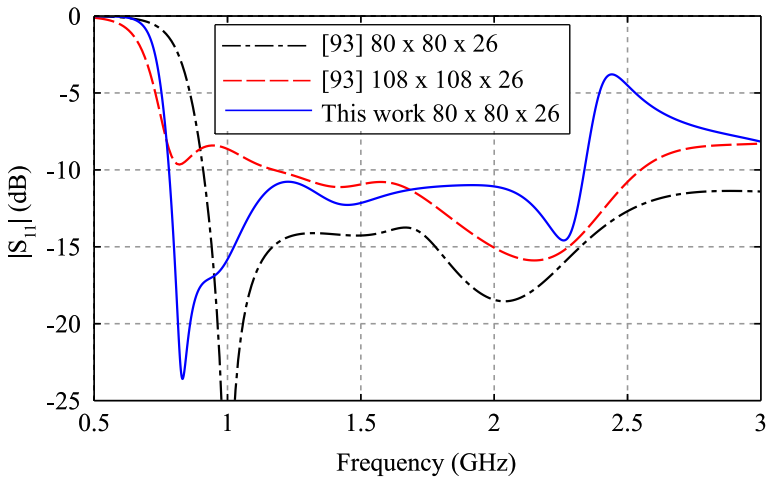

Figure 4.4. Simulated reflection coefficient of the proposed antenna. Comparison is made between the proposed antenna and the antenna optimised using a recently proposed technique in [95] with comparable size and frequency specification. The units are in mm.

wavelength at the minimum frequency of operation. This ground plane size is comparable with the design in [95] ($0.653\lambda_{min} \times 0.653\lambda_{min}$), and is much smaller than what is presented in [91] ($1.37\lambda_{min} \times 1.37\lambda_{min}$).

Antenna Height

Figure 4.6 shows the effect of the antenna height on the reflection coefficient while keeping other parameters constant. As expected a smaller h results in a degraded response at lower frequencies. For the case of $h = 30$ mm, although $\max(|S_{11}|) > -10$ dB, the antenna could in principle be re-optimised (with other parameters) to obtain a response within specification. On the other hand, for the case of $h = 22$ mm, achieving the specification $|S_{11}| < -10$ dB is not practically possible; thus, an optimised $h = 26$ mm is chosen. In addition, for an antenna with smaller h, the patch size needs to be significantly increased to keep the lower limit of the bandwidth at about 780 MHz (as suggested by the results in Fig. 4.4).

Slot Dimensions

Figure 4.7 shows the simulated reflection coefficients for various slot dimensions d_1 and L_2. It should be noted that the largest dimension of each slot increases with increasing

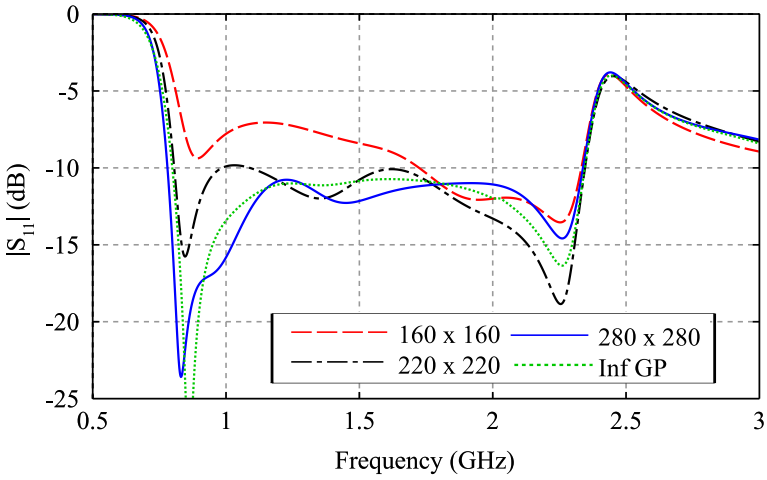

Figure 4.5. Reflection coefficient for different ground plane sizes. The units are in mm.

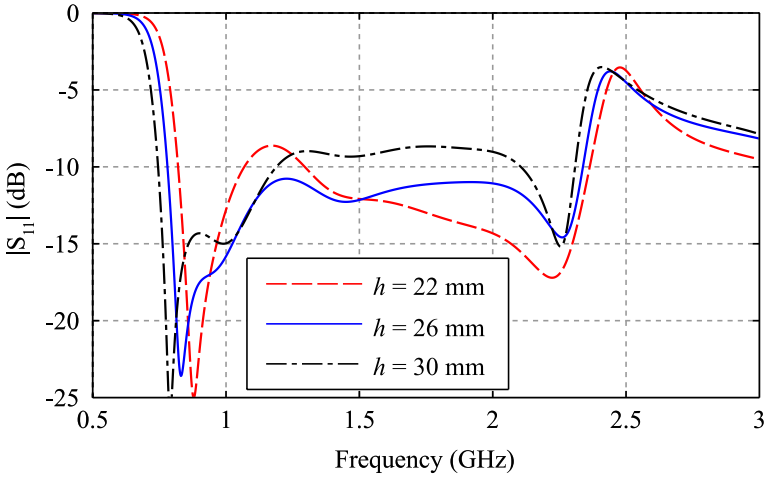

Figure 4.6. Reflection coefficient for different antenna heights.

either d_1 or L_2. It can be observed that smaller slots increase the resonance frequency at the upper end of the bandwidth. This effect verifies that the resonance at the higher frequency mostly depends on the slot dimensions. Furthermore, larger slots (the two curves with $L_2 = 54$ mm in Fig. 4.7) slightly decrease the minimum operation frequency in the bandwidth, i.e. from 780 MHz to 750 MHz. This effect is as expected since the slot geometry contributes to overall miniaturisation (see Section 4.2.2 and Fig. 4.3). In summary, the bandwidth can be extended by reducing the slot size at the expense of an increase of $|S_{11}|$ at the middle-ranged frequencies and a slight increase of the minimum operating frequency. Large slots are recommended when miniaturisation has higher priority

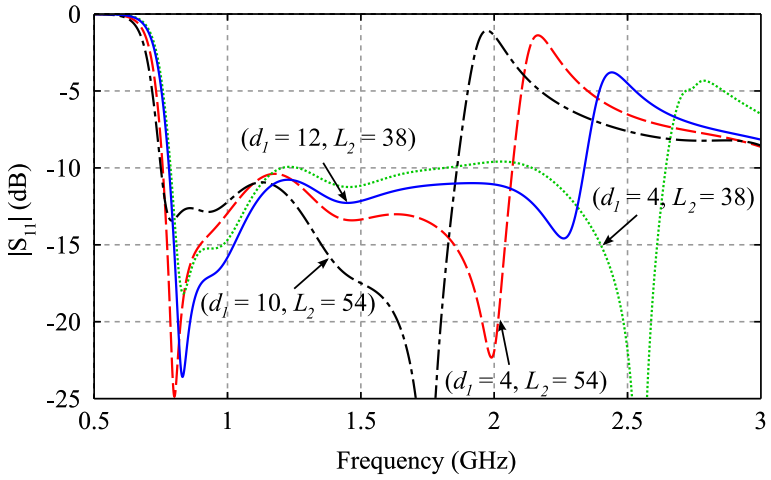

Figure 4.7. Reflection coefficient for different slot sizes. The units for d_1 and L_2 are mm.

than bandwidth. In this design, as a compromise, a medium slot size has been chosen to achieve an impedance bandwidth of about 3:1 (blue solid curve in Fig. 4.7).

The above parameter study can be used as a guideline to optimise the antenna. First, the base antenna without slot should be simulated. The antenna thickness h can be set to be around $0.07\lambda_{\text{min}}$ initially while the patch size L can be chosen initially around quarter-wavelength at the minimum operating frequency. Then the tapered symmetrical slots are added on the top of the patch. Two parameters d_1 and L_2 are optimised with a trade-off among the reflection coefficient and the minimum operation frequency.

4.2.3 Adaptation for Integration onto Helmet

The previous antenna design is adapted for integration onto a curved ground plane, e.g. a helmet, as illustrated in Fig. 4.8. This helmet is made of multiple layers of aramid and phenolic resin with a measured relative permittivity of about 3.7 and a loss tangent of 0.04. Typical helmet dimensions are about $160 \times 240 \times 260\,\text{mm}^3$. In this design, the ground plane made of copper tape is placed inside the helmet (at the bottom layer) and the helmet material is utilised as a dielectric to further reduce the antenna height. To provide additional separation of the ground plane from the head, another layer may be placed below the ground plane that may also be used as a platform for additional electronics [101].

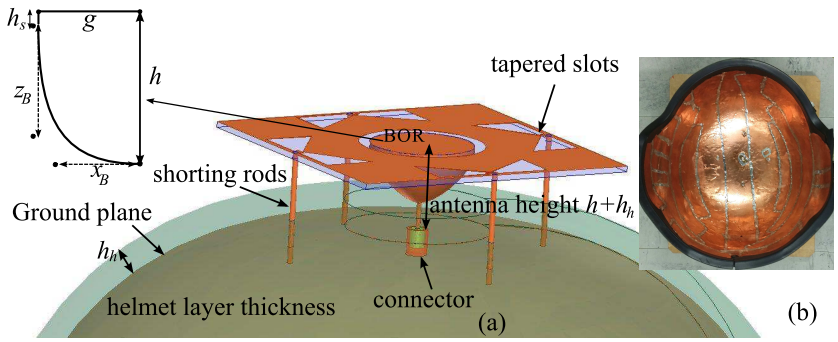

Figure 4.8. Adaptation of the design for integration onto a helmet. (a) The BOR is created from a third-order Bézier curve. (b) The ground plane is made of copper tape covering the entire bottom layer of the helmet.

Table 4.3. Parameters of the optimised antenna for integration onto helmet.

Par.	Value (mm)	Par.	Value (mm)	Par.	Value (mm)
d_1	14	g_1	3	h_s	1.575
d_2	2	h_h	7	L	80
d_r	1.5	h	16	L_1	38.5
g	14	x_B	4	L_2	33
		z_B	6		

The antenna has been optimised for a total antenna height of $H = h + h_h = 23$ mm including helmet thickness of $h_h = 7$ mm (Table 4.1). This means that the antenna thickness seen from the top of the helmet is only $h = 16$ mm. For this design, it is found that replacing the conductive cone by a body of revolution (BOR) [90] to increase the capacitance between the cone and the ground plane yields a better impedance matching. The BOR is created by rotating a third-order Bézier curve specified by two parameters x_B and z_B as demonstrated in Fig. 4.8a. Due to the tapering effect of the curved ground plane, the antenna can be optimised to achieve a smaller height than the planar configuration without significantly increasing the antenna size.

The optimised parameters for the helmet antenna are shown in Table 4.3. Simulation and measurement results for this antenna will be shown in the next section.

4.2.4 Measurement Results

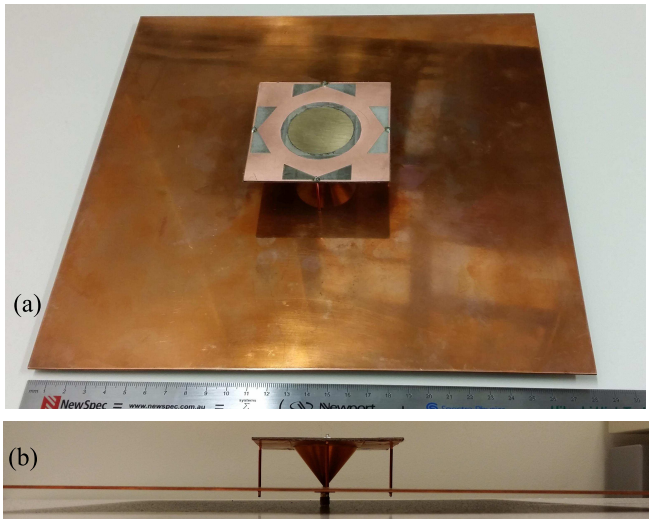

Figure 4.9. Photograph of the antenna on a flat ground plane for a vehicle application. (a) top view, (b) side view.

Vehicle Antenna

A photograph of the fabricated vehicle antenna is shown in Fig. 4.9. The simulated and measured reflection coefficient results are shown in Fig. 4.10. These results show an excellent agreement, which validates the design and optimisation process. The antenna exhibits a specified $\max(|S_{11}|) \leq -10$ dB within the bandwidth 780 MHz to 2310 MHz.

The simulated and measured antenna gain patterns (in dBi) at two different frequencies are shown in Fig. 4.11. The antenna radiates omnidirectionally across the operating band. In the elevation plane, the antenna exhibits monopole-like radiation patterns: these patterns are conical to the upper plane due to the presence of a finite ground plane. Because of this, the maximum realised gains in the two fundamental planes are different. Similar patterns can be found in other low-profile monopolar antennas with finite ground planes [90–96].

The simulated antenna efficiency is almost 100% across the operating frequency range. The simulated and measured maximum gain of the antenna are shown in Fig. 4.12. Reasonable agreement between simulation and measurement is obtained, which indicates high antenna efficiency. A higher fluctuation on the gain measurement across the bandwidth can be attributed to measurement errors, e.g. the multi-path loss in a non-ideal

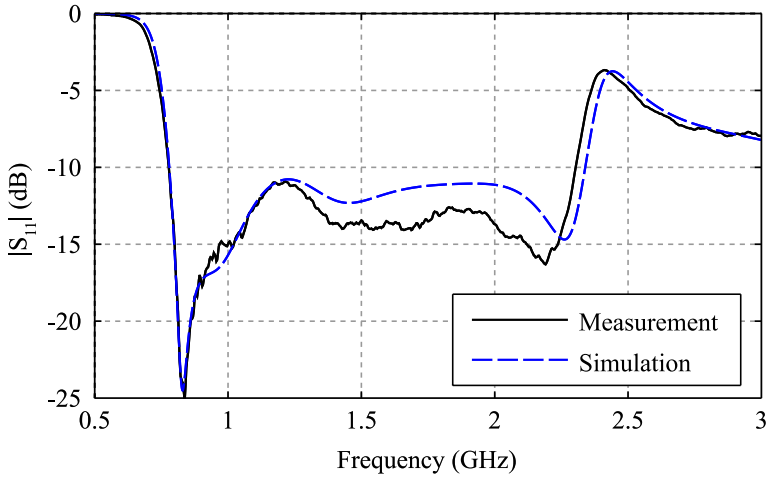

Figure 4.10. Simulated and measured reflection coefficient of the vehicle antenna.

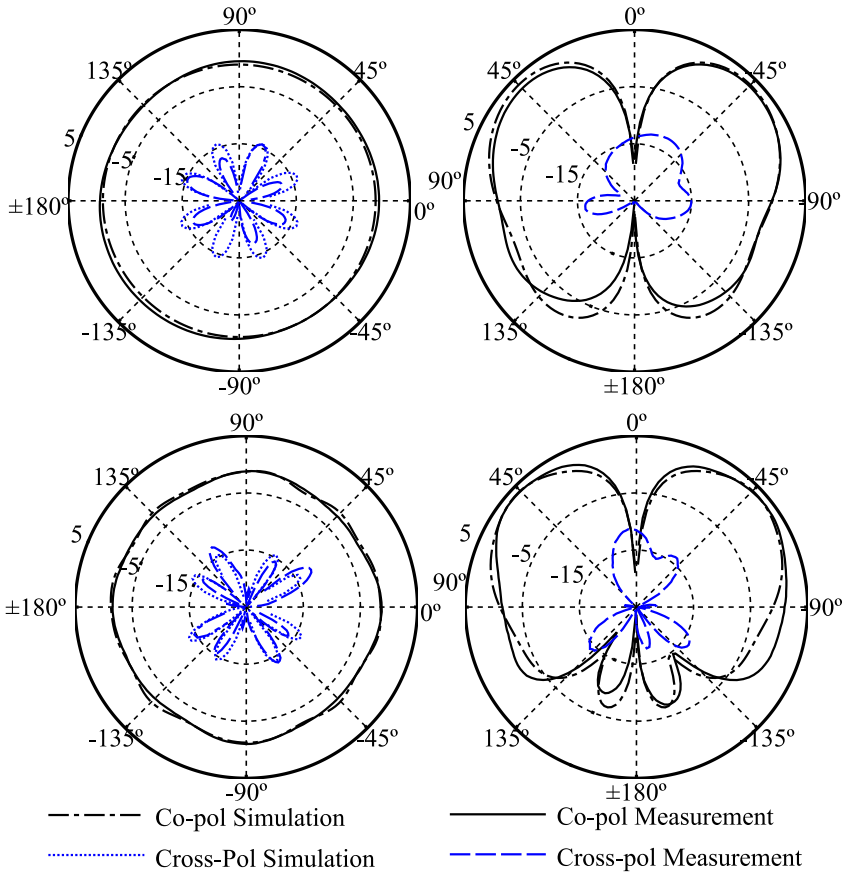

Figure 4.11. Gain patterns (dBi) of the vehicle antenna. Patterns are plotted for azimuth (left) and elevation (right) plane at $f = 0.9$ GHz (top) and 1.8 GHz (bottom).

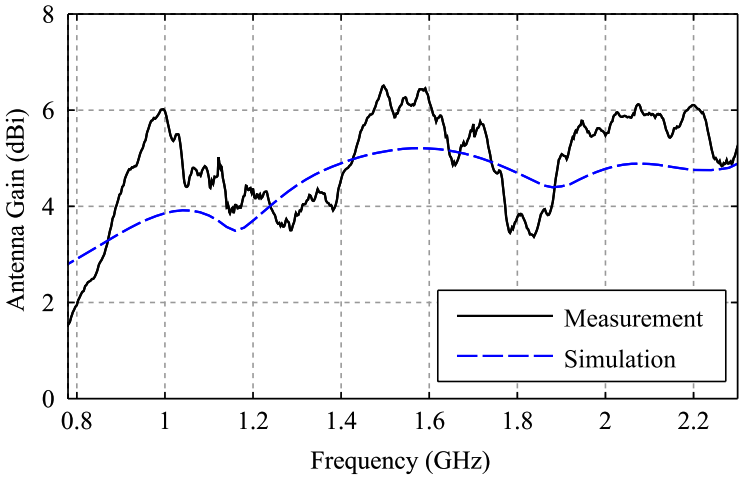

Figure 4.12. Simulated and measured gain of the vehicle antenna.

anechoic chamber, which is known to occur for low frequency measurement in our university facilities.

Helmet Antenna

The results for the reflection coefficient of the helmet are shown in Fig. 4.13. Reasonable agreement between simulation and measurement is obtained. The maximum measured reflection coefficient is about -9 dB. This minor increase of the reflection coefficient may be the result of fabrication imperfection and variation on helmet geometries, e.g. the curvature is not constant in all directions. These results also show that placing the helmet on a phantom has a very small impact on $|S_{11}|$.

The helmet antenna gain patterns (in dBi) and maximum gain are shown in Figs. 4.14 and 4.15, respectively. Due to the effect of the curved ground plane, the antenna achieves maximum radiation closer to broadside direction, especially at higher frequencies, compared to the large planar ground plane implementation. Since the antenna patterns are not conical to the upper plane, the maximum gain is slightly lower than for the vehicle antenna. However, gain in the broadside direction is slightly higher. Although the helmet material is quite lossy (loss tangent of 0.04), the simulated radiation efficiency is still more than 97% across the operating bandwidth since the radiation process mostly originates from the air region above the helmet. The reasonable agreement between simulated

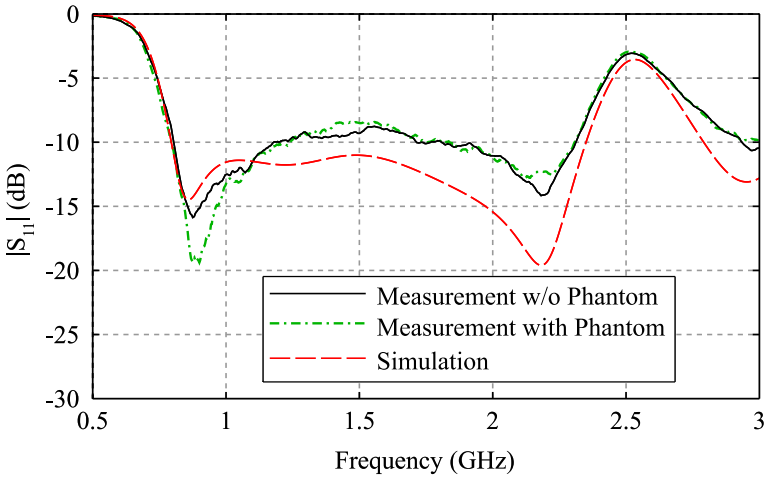

Figure 4.13. Simulated and measured reflection coefficient of the helmet antenna with and without phantom.

and measured gain (shown in Fig. 4.15) also indicates high antenna efficiency. Some discrepancies between the simulated and measured gain are due to the imperfection of the anechoic chamber at low frequency band and the difficulty in simulating exactly the shape and electromagnetic properties of the helmet material.

As the pattern exhibits radiation nulls at $\theta = 0^\circ$ and 180° and with the presence of a ground plane at the bottom layer of the helmet, the antenna radiation should not significantly be affected by the body [101]. To verify this, measurements of the antenna radiation patterns in the xy-plane, i.e. broadside direction ($\theta = 90^\circ$), have been carried out with the helmet placed in free-space and on a phantom (Figs. 4.16 and 4.17). These results show that the presence of the phantom has a minimal effect on the radiation pattern and antenna gain. In summary, the helmet antenna is a good candidate for transmission applications requiring an omnidirectional radiation pattern and vertical polarisation.

4.3 Dual-band Design

In this section, the antenna design for dual-band application is showed first, followed by a key-parameter study. Based on this study, an antenna design procedure is proposed. Finally, measurement results are presented as a validation of the proposed concept.

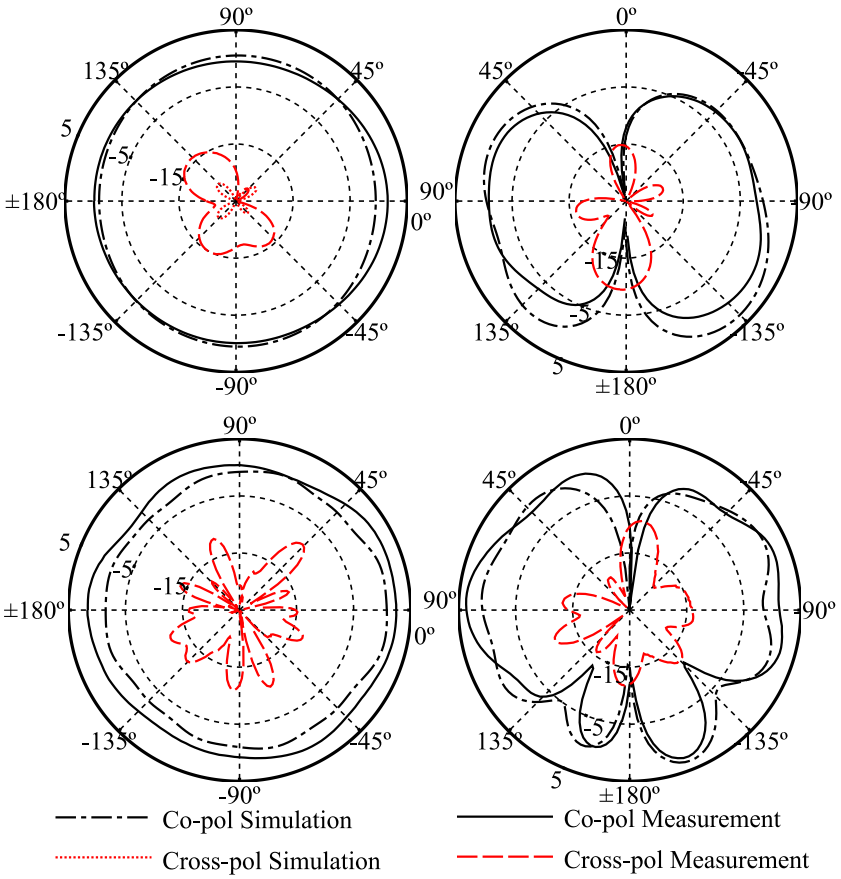

Figure 4.14. Gain patterns (dBi) of the helmet antenna. Patterns are plotted for azimuth (left) and elevation (right) plane at $f = 0.9$ GHz (top) and 1.8 GHz (bottom).

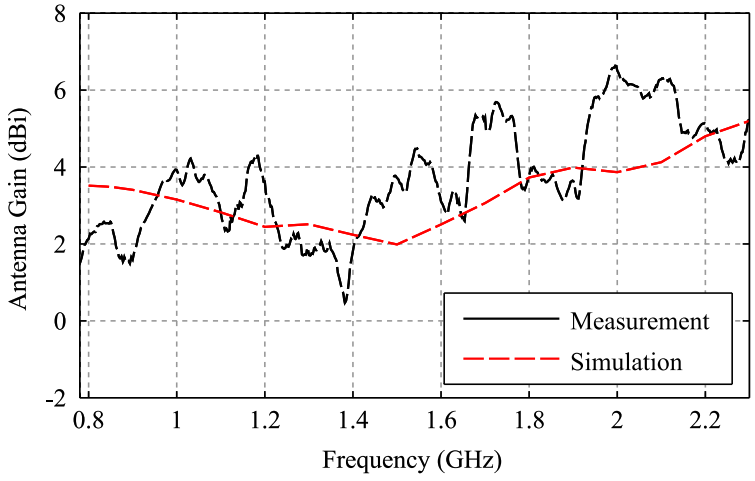

Figure 4.15. Simulated and measured gain of the helmet antenna.

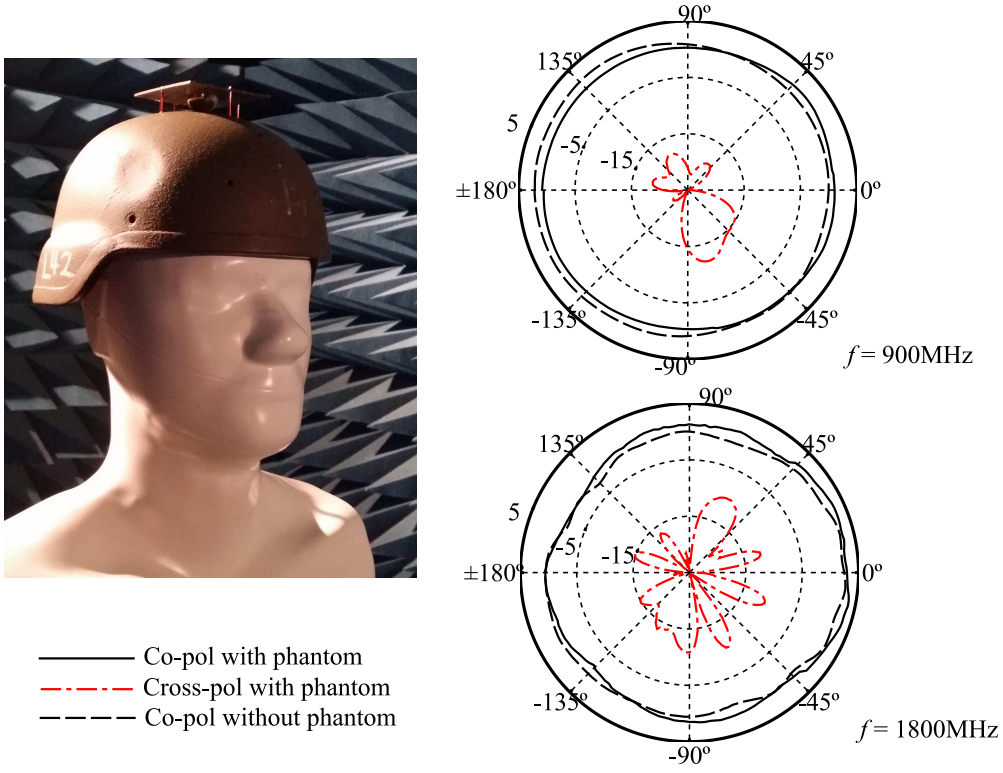

Figure 4.16. Measurement results with phantom. The antenna placed on a phantom for measurement (left) and the measured gain patterns (dBi) with/without the phantom in the xy-plane (right).

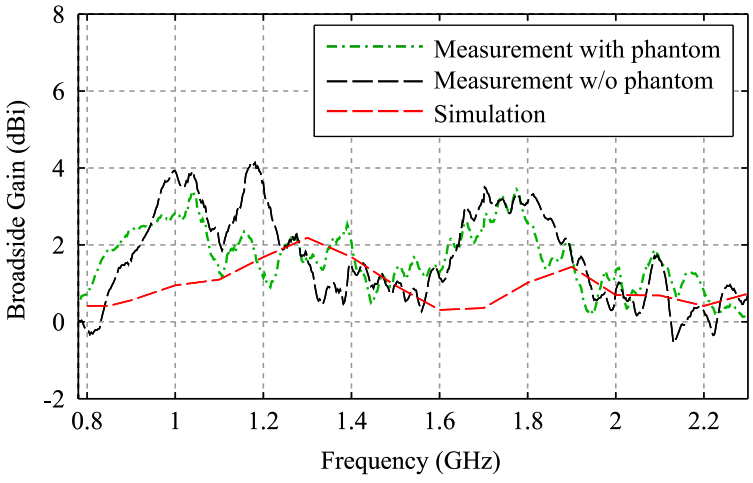

Figure 4.17. Broadside gain of the helmet antenna. Simulated and measured broadside gain ($\theta = 90°$) of the helmet antenna with and without the phantom.

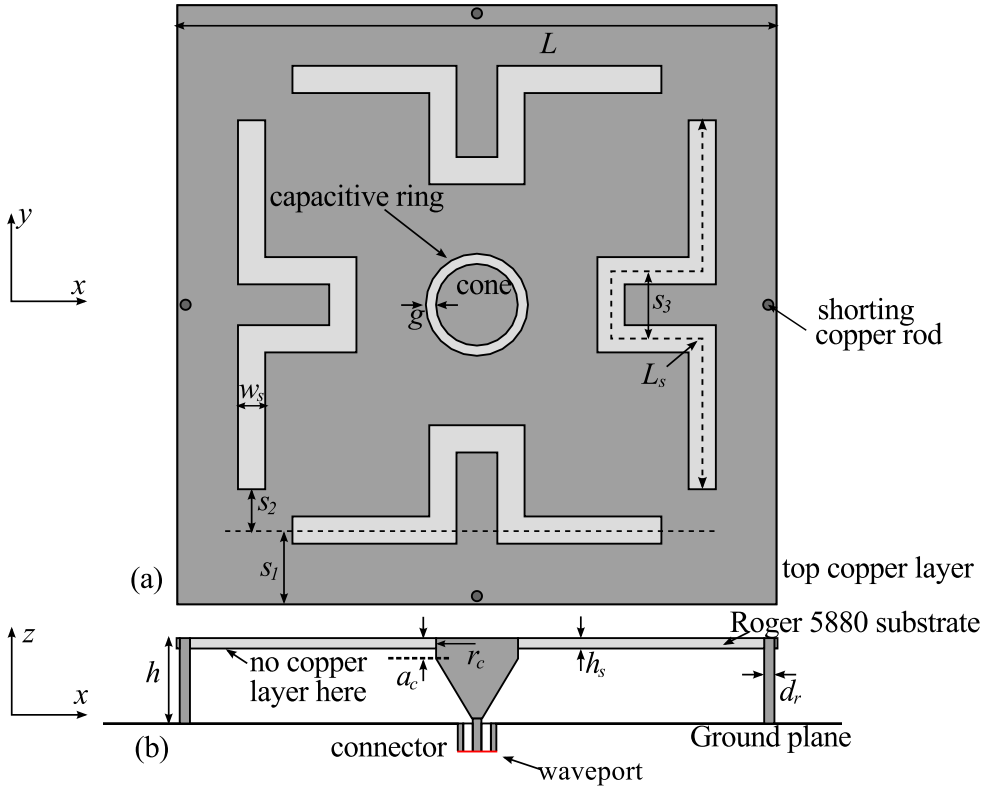

Figure 4.18. Design of a low-profile dual-band monopole antenna. (a) top view; (b) side view. Darker shaded areas represent the conductor while lighter shaded areas denote the substrate. L_s is the total slot length measured along the centre of each slot.

4.3.1 Antenna Structure

The design of the antenna is illustrated in Fig. 4.18. The antenna structure is based on the previous wideband design, i.e. consisting of a patch with four shorting copper rods forcing the patch to radiate in a magnetic current loop mode. The feeding technique is also similarly adapted: the connector inner pin is attached to a conductive cone [95], which is separated from the patch by a ring gap.

The main difference from the previous design is on the other hand, that the antenna height is much further reduced (wideband operation is no longer achievable with this height) and the geometry of four symmetrical slots is tailored to obtain another resonance band. As shown in Fig. 4.18, the shape of these slots is meandered to gain more flexibility in choosing the resonance frequency, e.g. the slot length L_s can be made longer for a lower

Table 4.4. Parameters of the optimised and fabricated dual-band antenna.

Par.	Value (mm)	Par.	Value (mm)	Par.	Value (mm)
L	88	h	12.5	h_s	1.524
r_c	6	a_c	3	g	1.5
w_s	4	s_1	10.9	s_2	6
s_3	10	L_s	85	d_r	1.5

resonance frequency. Additionally, this approach offers degrees of freedom in optimising the impedance matching, for which the distances s_1 and s_2 play a significant role.

To gain further understanding of the radiation mechanism, the same antenna without the slots has been simulated and compared with the proposed design. The simulation of $|S_{11}|$ for the case without slots shows one narrow resonance followed by high reflection at higher frequency. This result is expected for this type of antenna when the antenna height is further reduced as demonstrated in the previous section. The introduction of four symmetrical slots creates another frequency bands as observed in Fig. 4.19. Furthermore, as a beneficial side effect of the slots, the resonance frequency at the lower band also decreases. The lowering of the first resonance frequency is the result of increasing the effective length of the magnetic current loop. Thus the proposed slots also contribute to an antenna miniaturisation of about 10%.

The field distributions at the two resonance frequencies of the optimised antenna are shown as an inset in Fig. 4.19. Similarly to the previous design, it can be qualitatively observed that at the upper band, radiation mostly originates from the slots on the patch while at the lower band, radiation primarily comes from the antenna apertures under the edges of the grounded patch.

4.3.2 Parameter Study and Design Procedure

In this section, the most relevant parameters that control the two resonances are studied. These parameters include s_1, s_2 which define the location of the slots, as well as L and L_s which are the lengths of the patch and slots respectively. The effect of ring gap g is also examined, since it determines the capacitance between the cone and the patch and is important for impedance matching. The antenna height h is chosen depending on the

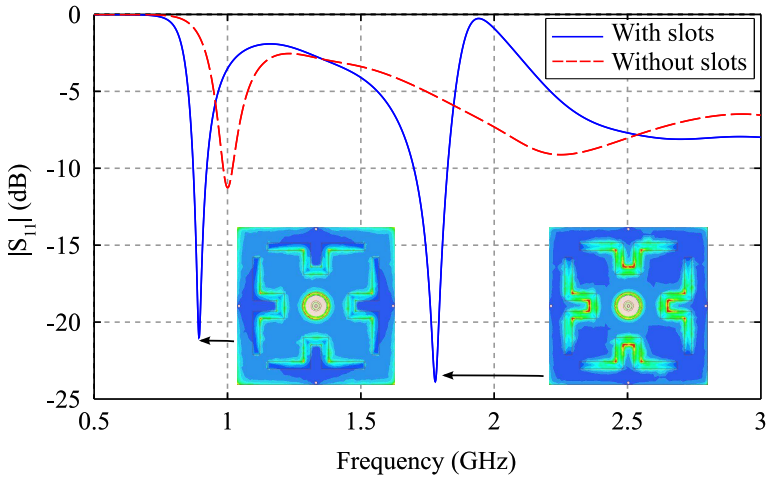

Figure 4.19. Simulated reflection coefficient of the optimised antenna and the antenna without slots.

targeted antenna bandwidth, which can be done simply by plotting an approximate h-bandwidth curve obtained using parametric simulation sets. Since the height-bandwidth trade-off is well known, this aspect is not elaborated here. Similarly, analysis of other parameters, i.e. a_c, r_c, d_r, w_s, s_3 is not presented in detail as they can be chosen in a wide range of values and do not significantly affect the results.

The ground plane size was chosen as $280\times$ 280 mm^2, i.e. $0.82\lambda_{\text{min}} \times 0.82\lambda_{\text{min}}$ where λ_{min} is the free-space wavelength at the minimum operating frequency. It should be noted that an increase of the ground plane dimensions corresponds to an increase of the effective antenna thickness, which results in an increase of the antenna bandwidth. Depending on the application, the antenna can be optimised with an infinite ground plane to mimic integration onto a large metallic object, e.g. vehicle.

The simulation results of the reflection coefficient with varying g while keeping other parameters constant are demonstrated in Fig. 4.20. These results support the dominant effect of g on the impedance matching at both frequency bands, leading to a choice of $g = 1.5$ mm.

The effects of varying s_1, s_2, L and L_s are illustrated in Fig. 4.21. In these plots, only the parameter being considered is varied while the others are fixed at the optimised values listed in Table 4.4. Denoting f_1 and f_2 as the resonance frequencies of the lower and upper band, respectively, it can be observed that when varying s_1 or s_2, both f_1 and f_2 change with a

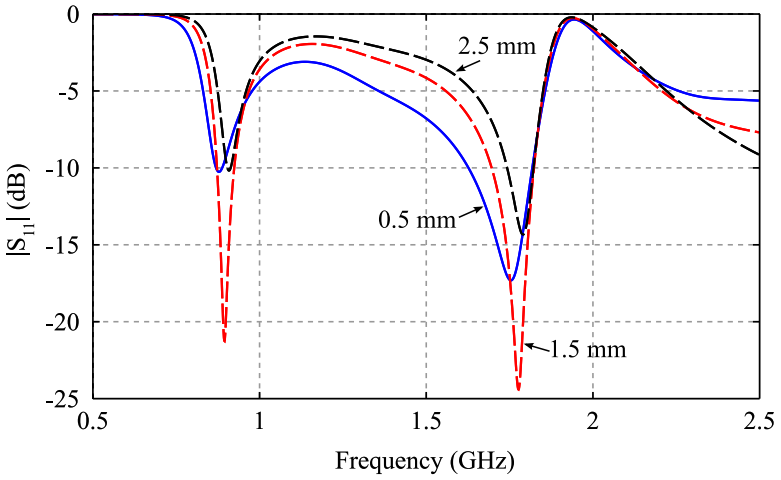

Figure 4.20. Simulated reflection coefficient when varying capacitive gap g.

trade-off in the reflection coefficient between two bands. On the other hand, when s_1 and s_2 are fixed, i.e. the slots position relative to the edge of the patch remains unchanged, the resonance frequency of each band can be controlled almost independently by varying the patch size L and slot length L_s. This is an important feature which will be utilised to design a reconfigurable antenna with independent control of two frequency bands in Chapter 7. Although f_2 can be controlled independently by L_s (Fig. 4.21c), increasing L_s beyond 90 mm (to reduce f_2) may degrade the impedance matching. In this case, s_1 may be decreased to obtain a better matching at f_2 (Fig. 4.21a). A similar approach can be used to increase f_2 or varying f_1. In summary, these four sub-figures can be used as a guideline to optimise both reflection coefficient and resonance frequencies of this dual-band antenna.

Based on the above results, the following design procedure for the antenna with two resonance frequencies f_1, f_2 is suggested.

1. Start from the design without slots. Based on the targeted bandwidth, choose the antenna height h. Choose L and optimise r_c, g to obtain a resonance frequency about 10% greater than the desired f_1 (this will later allow to account for the effect of slots on the lower band). The parameters a_c is not critical and can be chosen as slightly larger than h_s. Very good matching is not required for this step.

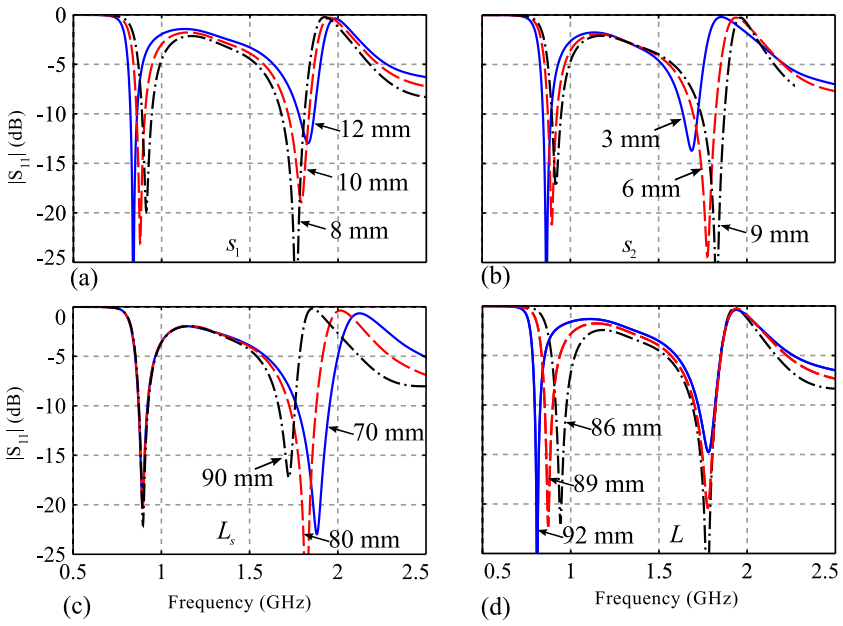

Figure 4.21. Parameter study of the dual-band monopolar antenna. Simulated reflection coefficient when varying: (a) s_1, (b) s_2, (c) L, (d) L_s (from left to right, top to bottom).

2. Add the slots. Choose $L_s \approx \lambda_2/2$ where $\lambda_2 = c_0/f_2$ as an initial value. Optimise w_s, s_1, s_2 to obtain satisfactory matching at both frequency bands. The parameters r_c and g, which control the ring gap, may be adjusted for better matching if necessary. Parameter s_3 is not critical and can be chosen as $s_3 \approx 2r_c$.

3. Tune the two resonance frequencies by separately varying either L (for f_1) or L_s (for f_2).

4. Fine-tune the parameters, especially r_c, g to achieve the specified matching criterion, h for bandwidth and L, L_s for resonance frequencies.

4.3.3 Measurement Results

The targeted bandwidths for this dual-band design is 880 MHz to 915 MHz and 1710 MHz to 1785 MHz (GSM bands). Due to the possible variation of material properties and tolerances in the fabrication process, the antenna has been optimised in simulation to achieve a slightly wider bandwidth, namely 873 MHz to 922 MHz (5.46%) and 1699 MHz to 1825 MHz (7.15%). To achieve this, the height of the antenna is chosen as $h = 12.5$ mm,

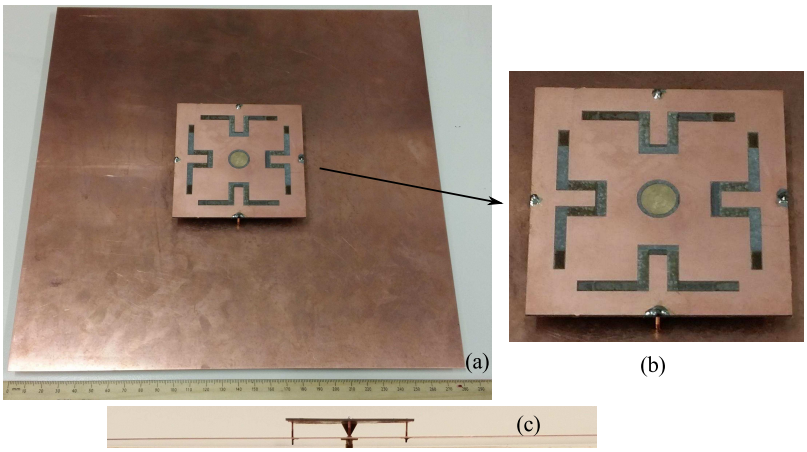

Figure 4.22. Photograph of the fabricated low-profile dual-band monopole antenna. (a) top view; (b) zoom of the antenna; (c) side view.

which corresponds to 0.0367λ at the lowest frequency of operation. A photograph of the fabricated antenna is shown in Fig. 4.22. Experimental validation is described as follows.

Reflection Coefficient

The results for reflection coefficient are shown in Fig. 4.23. Excellent agreement was obtained between simulation and measurement. The measured $|S_{11}| \leq -10$ dB bandwidths are from 876 MHz to 918 MHz and 1702 GHz to 1825 GHz, which cover the targeted bandwidths. The matching at the resonance frequencies is better than -18 dB.

Radiation Patterns

The normalised radiation patterns at the centre frequency of each band are shown in Fig. 4.24. These measurements are in very good agreement with the simulation results for all patterns. The antenna radiates omnidirectionally at both frequency bands with the measured variations in azimuth-plane of less than 0.87 dB for $f = 0.9$ GHz and less than 1.43 dB for $f = 1.75$ GHz. In the elevation plane, the antenna exhibits monopole-like patterns. These patterns are conical to the upper plane due to the presence of a finite ground plane, as discussed in the previous section.

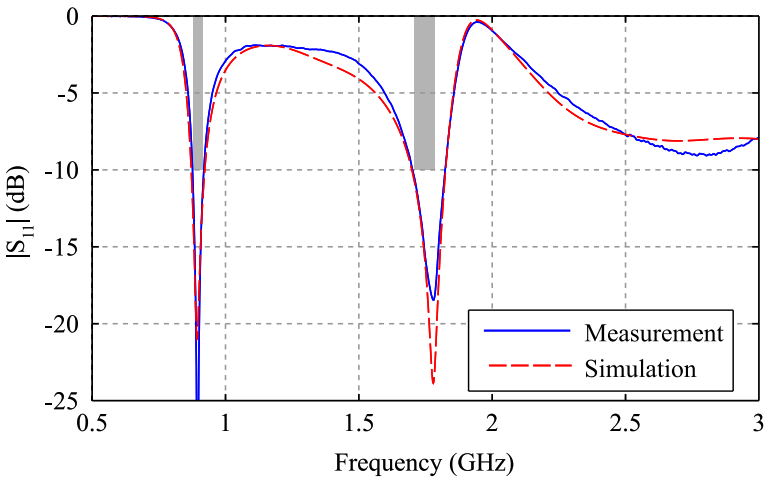

Figure 4.23. Measured and simulated reflection coefficient of the fabricated antenna. Shaded areas indicate the target frequency bands.

Antenna Gain and Efficiency

The measured and simulated realised gain of the antenna are shown in Fig. 4.25. The simulated antenna efficiency is nearly 100% at both frequency bands. The good agreement between simulation and measurement for the gain indicates high antenna efficiencies. The antenna gain at lower band is 3 dBi and for upper band, it reaches approximately 6 dBi. This difference in gains is expected as the radiation patterns become more conical towards the upper plane ($\theta < 90°$) at higher frequencies due to effect of the electrically larger ground plane.

4.4 Conclusion

Two designs of low-profile monopolar antennas utilising symmetrical radiating slots on an edge-shorted patch have been proposed in this chapter. These slots are equivalent to an additional magnetic-current loop, thus they can either contribute to antenna miniaturisation (for wideband design) or create another resonance band (for dual-band design). For wideband operation, two realisations for integration onto vehicles and helmets have been presented. The results for the helmet integration demonstrate a better radiation performance at broadside as well as a further height reduction compared to a flat ground plane.

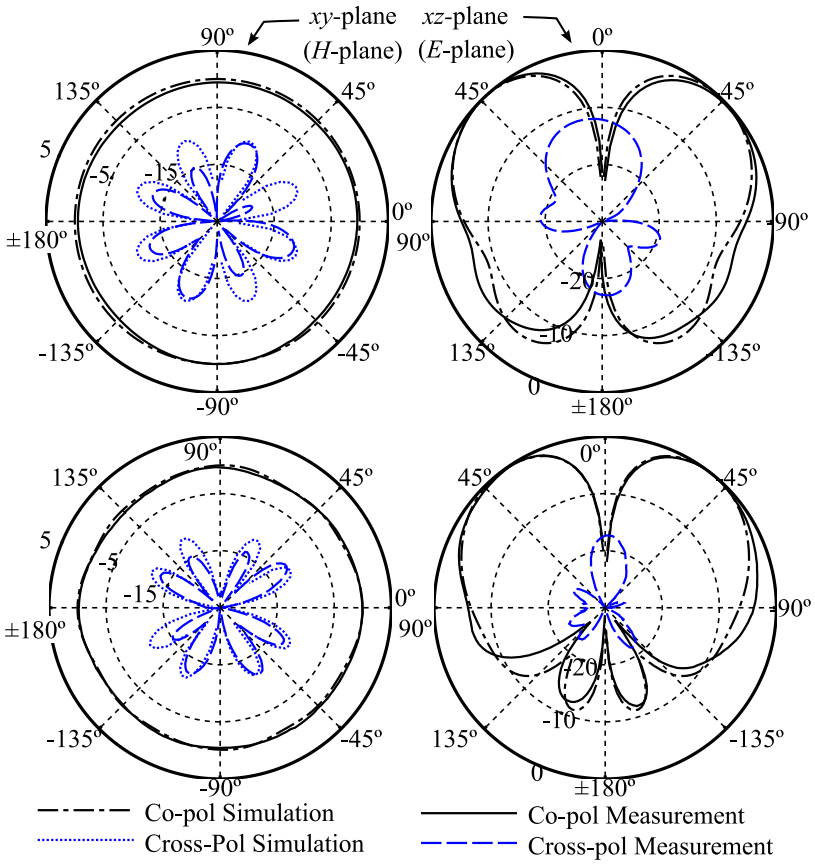

Figure 4.24. Normalised radiation patterns of the dual-band antenna. (a) H-plane, 0.9 GHz; (b) E-plane, 0.9 GHz; (c) H-plane, 1.75 GHz; (d) E-plane, 1.75 GHz. The simulated cross-polarisation in E-plane is smaller than -30 dB hence is not visible in the presented patterns.

For the dual-band design, based on a study of slot parameters, a step-by-step design procedure for the antenna has been proposed, which allows for a straightforward adaptation for operation at other frequencies.

All presented antennas exhibit stable omnidirectional radiation patterns with vertical polarisation at all operating frequencies. Measurement results are in good agreement with simulations, indicating high radiation efficiency and satisfactory omnidirectionality of the antenna pattern. The proposed dual-band antenna designs can be useful when the design requirements target very low antenna height and operation in specific frequency bands. The high efficiency and low reflection coefficient at resonances also make the antenna suitable for transmitter application.

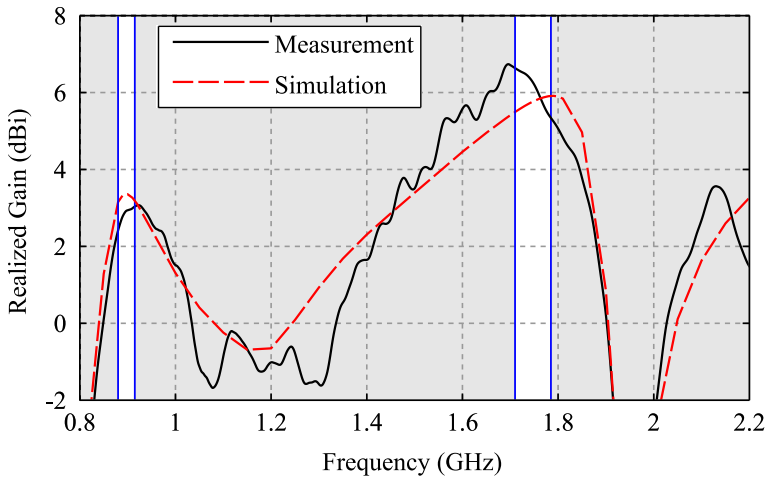

Figure 4.25. Measured and simulated realised gain of the fabricated dual-band antenna. Light areas are the target bandwidths.

Chapter 5

Stub-Loaded Reconfigurable Antennas

THIS chapter introduces a family of reconfigurable antennas based on stub-loaded substrate-integrated circuits. In the first section, a frequency-reconfigurable antenna based on a stub-loaded half-mode substrate-integrated cavity is studied thoroughly. The operational principle and analysis presented here provide a foundation for the second section, which discusses a fully functional frequency- and polarisation- reconfigurable antenna based on a stub-loaded microstrip patch. Finally, using the proposed technique, other reconfigurable antennas, including structures based on a quarter-wave patch and a quarter-mode substrate-integrated waveguide, are discussed.

5.1 Introduction

In the emergence of modern smart systems, an antenna with frequency, polarisation and pattern agility becomes more and more desirable. As a consequence, increasing attention and efforts have been recently placed on designing reconfigurable antennas, especially in substrate-integrated circuit technology [102–104]. This chapter is dedicated to a family of reconfigurable antennas based on stub-loaded substrate-integrated circuits. The original contributions have been published in a series of reconfigurable antennas papers in [105–111].

This chapter is structured into three sections. In the first section, the analysis and design of a frequency-reconfigurable antenna based on a stub-loaded half-mode substrate-integrated cavity are presented. It is noted that the half-mode substrate-integrated cavity (for convenience, we shall call it HMSIW cavity) can be interpreted as a magnetic-dipole using the field equivalence principle. The design is then extended to a microstrip patch antenna with its reconfigurabilities in both operating frequencies and polarisation, namely including 3 linear polarisation (LP) and 2 circular polarisation (CP) states. Finally, a family of these stub-loaded reconfigurable antennas, including additionally a quarter-mode substrate-integrated cavity and a quarter-wave patch, is introduced to demonstrate the versatility of the tuning mechanism.

In this chapter, the field equivalence principle is used to interpret the antenna radiations as magnetic dipoles radiating on a ground plane. Thus broadside radiation patterns can be predicted. The field equivalence principle is also used to explain the relative level of cross-polarization for different types of antennas based on substrate-integrated waveguide (SIW) technology and microstrip patch.

5.2 Half-Mode Substrate-Integrated Cavity Antenna

As shown in Chapter 2, the radiation from the open aperture of a half-mode substrate-integrate waveguide (HMSIW) close to cutoff can be utilised to design travelling-wave antennas (TWAs). Another method to design a radiator based on this structure is to create a resonant cavity by placing two shorting walls along the guiding direction of the HMSIW.

This technique has been exploited to design cavity resonator antennas in [112, 113]. Similarly, a quarter-mode substrate-integrated waveguide (QMSIW) cavity [114] has been proposed and utilised for a wearable antenna application [115]. Using the field equivalence principle and image theory, the radiation problem can be approximated as a magnetic-current source with the open-aperture length radiating into free-space. It is noted that this antenna is the substrate-integrated version of the third example in Section 1.1.2 (Fig. 1.3a).

For reconfigurable applications, a compact antenna based on HMSIW cavity has been proposed in [116]. This antenna radiates at the resonance frequency of an inter-digital capacitor slot. Therefore, the structure is miniaturised but exhibits large cross-polarisation and modest gain (measured minimum and maximum gain reported at -4 dB and 1.8 dB respectively [116]). A similar tuning principle has been applied to design a dual band reconfigurable eighth-mode substrate-integrated waveguide (EMSIW) antenna [117]. As an alternative design targeting higher efficiency and linearly polarised radiator, this section studies the use of varators and loading stubs, proposed in [118] for guided-wave applications, to design a reconfigurable antenna based on the HMSIW cavity. This antenna works as a cavity resonator which is in principle different from [116], where the resonance is determined by the capacitive slot. Thus the antenna demonstrates a high performance in terms of antenna gain, reflection coefficient and tuning range at the cost of slightly increased size. A comprehensive theoretical analysis of the structure is also presented, which not only allows an efficient design and optimisation process but also gives more critical insight into the antenna operational principle.

This section starts by highlighting the design and operational principle of the proposed antenna, followed by a detailed theoretical analysis of its tuning resonance frequency. The optimisation to achieve a desired tuning range for a chosen (or given) capacitance range is then thoroughly described. Finally, measurements on an antenna realisation will be shown to validate the proposed method, followed by a short summary.

5.2.1 Antenna Design and Operational Principle

The design of the antenna is illustrated in Fig. 5.1. The antenna consists of an HMSIW cavity loaded with straight stubs arranged periodically in longitudinal direction along the aperture (z-axis). The antenna is equivalent to a magnetic-current source $\mathbf{M}$ radiating

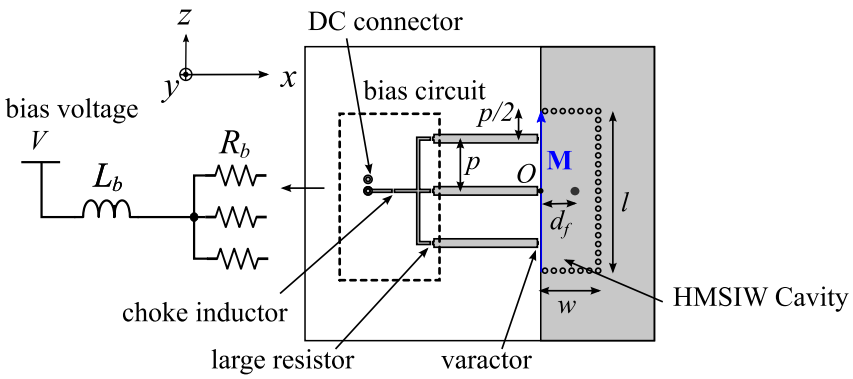

Figure 5.1. A reconfigurable antenna based on a periodically loaded HMSIW cavity. Using the field equivalence principle and image theory, the antenna can be shown to be equivalent to the magnetic current **M** radiating into free space.

on a ground plane, whose effect can be removed by image theory (Fig. 5.1). The stubs act as high-impedance transmission lines and do not significantly contribute to radiation. The presented realisation considers 3 stubs, and the choice of this number will be discussed in Section 5.2.2, as a trade-off between tunability range and antenna complexity. The varactors are placed at the edge of the open aperture joining the top layer of the HMSIW with the stubs. At the other end of the stubs lies the bias circuit for the varactors which consists of resistors followed by a choke inductor. The resistance values are chosen large enough to prevent RF current from flowing into the bias circuit but small enough to avoid power loss in the resistors. The varactor model used in the present design is of type MA46H120 from MACOM Technical Solutions with maximum reverse leakage current in the tuning voltage range of $I_{R(max)} = 100$ nA [119]. Based on this and numerical verification using ANSYS HFSS, the chosen values for the bias circuit in this design are $R_b = 1\,\mathrm{M}\Omega$ and $L_b = 100$ nH (Fig. 5.1). With this choice of R_b, the DC power consumption of the structure is less than $P = I^2_{R(max)} R_b = 10$ nW per resistor.

It is well-known that the resonance frequency of a rectangular cavity depends on the wavenumbers in the three Cartesian coordinate axes x, y, z. By terminating the HMSIW with short-circuit walls in longitudinal direction (the short circuit walls are placed at half-period spacing from the first and last stub, see Fig. 5.1), the wavenumber in z-axis is kept constant. Therefore, changing the wavenumber in transverse direction, i.e. x-axis, will change the resonance frequency of the cavity. This can be achieved by using variable

reactive loads as suggested in [120, 121] and utilised in [118, 122]. To increase the tuning range and provide additional capability for impedance manipulation, the varactor is loaded with a stub of certain length protruding from the aperture (Fig. 5.1). Using transmission line theory, the impedance loaded at the edge of the waveguide can be easily changed by adjusting the stub size. A similar approach has been proposed in [123] to design a reconfigurable circular monopolar patch antenna where stubs were realised as sector-shaped patches. The utilisation of stub impedance transformation has also been proposed in a different context [124] to design a corrugated substrate-integrated waveguide without via-holes. The stubs' width and length will be optimised to achieve the desired tuning range (shown in Section 5.2.3).

The antenna is fed perpendicularly from a coaxial line placed at the centre ($z = 0$) of the cavity (Fig. 5.1). The centre pin goes through the substrate and contacts the top layer of the HMSIW. The transverse position $x = d_f$ of the coaxial pin is optimised using a numerical simulation tool to achieve good impedance matching in the entire tuning range. This is carried out after the optimisation process necessary to obtain the dimensions of the HMSIW and the loading stub. The effect on the matching of varying the feed position has been studied in [125] and will be discussed in Section 5.2.3.

5.2.2 Theoretical Analysis

In this section, the theoretical calculation of the resonance frequency will be presented first. The proposed analysis requires calculating the impedance periodically loaded at the open aperture of the HMSIW and this will be shown in next part of this section. Finally, the last part of the section compares the analytical solution with various numerical results to provide a first validation of the proposed method.

Resonance Frequency

The resonance frequency of a metallic rectangular cavity can be calculated as

$$f_r = \frac{c_0}{2\pi\sqrt{\epsilon_r}}\sqrt{k_x^2 + k_y^2 + k_z^2} \tag{5.1}$$

where ϵ_r is the relative permittivity of the inner medium (assuming relativity permeability $\mu_r = 1$) and k_x, k_y, k_z are the wavenumbers in x, y and z-directions, respectively. For a

substrate-integrated cavity, the thickness h of the substrate is very small compared to the size of the waveguide. Therefore, it can be assumed that $k_y = 0$. Additionally, for the cavity considered here, due to the short-circuits at the start and end of the waveguide, the wavenumber in longitudinal direction is fixed at

$$k_z = \frac{\pi}{l} \tag{5.2}$$

to force zero electric field at the two ends of the cavity for the fundamental mode. Thus, in order to find the resonance frequency, the wavenumber in x-direction is required. This can be obtained by following the analysis described in [118], which yields an approximation of the wavenumber for a periodically loaded HMSIW. Although this approximation succeeded in describing the modal behavior of the waveguide, it is not sufficiently accurate to obtain the propagation constant and hence to calculate the resonance frequency in the proposed structure. In order to improve the accuracy of the analysis, it is modified as follows: the width of HMSIW is adjusted using the effective width formula provided in [19]

$$w_e = w' + \Delta w \tag{5.3}$$

where w' is the effective width that takes the effect of via size and spacing into account [126] and Δw is the correction for the fringing field of the HMSIW [19] (Fig. 5.2). The HMSIW is equivalent to an ideal half-rectangular waveguide with a PMC wall at one side and a width of w_e whereas the reactive load is still placed at $x = w'$ (Fig. 5.2). In order to simplify the analysis, the loaded impedance jB is assumed to remain unchanged with the introduction of the PMC wall, which was also assumed in [118]. The analysis then follows what is described in [118] with two changes: equation (9) in [118] is modified as

$$H_{x3} - H_{x2} = \delta(x - w') \cdot jBhE_{y3} \tag{5.4}$$

and matrix $\mathbf{A}_2$ is thus changed to

$$(\mathbf{A}_2)_{mn} = \frac{\sin(k_{cn}w')\sin(k_{cm}w')}{k_{cn}}, \tag{5.5}$$

where B is the susceptance loaded at the open aperture of the HMSIW. This is a crucial modification to obtain an accurate propagation constant in the waveguide, especially when the correction term Δw is significant. This case occurs when using a thick and/or

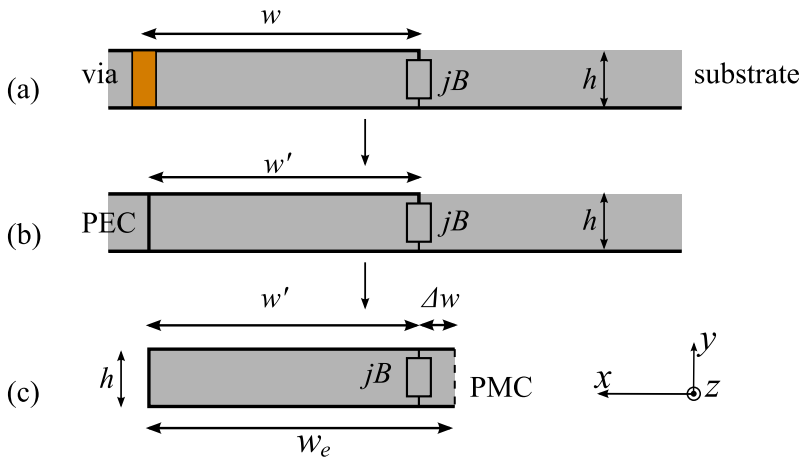

Figure 5.2. Equivalent model for a reactively loaded HMSIW. (a) original periodically loaded HMSIW, (b) equivalent HMSIW with PEC wall, (c) equivalent half-rectangular waveguide.

low permittivity substrate, which increases the fringing field at the open aperture of the HMSIW. Once the propagation constant γ of the Floquet mode propagating in the periodically loaded HMSIW is calculated, the wavenumber in x-direction is calculated as

$$k_x = \sqrt{k_0^2 \epsilon_r + \gamma^2}. \tag{5.6}$$

Substituting the results of (5.2) and (5.6) into (5.1), the resonance frequency f_r can be finally obtained.

Impedance Loaded at the Aperture

This section demonstrates the analysis of the impedance loaded at the aperture of the HMSIW (Fig. 5.3(a)). First, the fringing field at the end of the open-circuit stub is compensated by an equivalent additional length Δl, for which a closed-form formula is given in [127] (Fig. 5.3b). Second, using transmission line theory, the impedance at the other end (i.e. at varactor position) is calculated as

$$Z = -jZ_{m0} \cot\left[\beta_m (l_{stub} + \Delta l)\right] \tag{5.7}$$

where l_{stub} is the length of the stub; Z_{m0} and β_m are the characteristic impedance and phase constant of the stub modeled as a microstrip tranmission line [128]. The gap l_v between the stubs and HMSIW aperture can be taken into account using the equivalent circuit model proposed in [129] with three capacitors C_s, C_{P1} and C_{P2} (Fig. 5.3b). Although

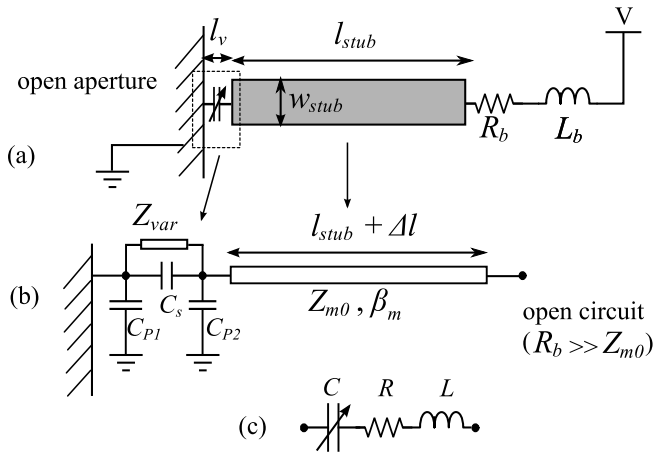

Figure 5.3. Analysis of the impedance loaded at the aperture. (a) Design of the loading stub; (b) equivalent circuit and transmission line model for the stub; (c) equivalent circuit for the impedance Z_{var} of the varactor.

the empirical expressions for these capacitances in [129] are valid for the case where the ratio between the two microstrip line widths are less than or equal to 3, it will be shown that they still provide a good enough approximation for the gap capacitance.

The only unknown parameter at this stage is the impedance Z_{var} of the varactor which can be obtained as a first approximation from datasheet provided by the manufacturer [119]. However, since the datasheet does not provide the capacitance in a full range of reverse bias voltages, independent measurements on the impedance of the varactor have been carried out. This measurement is necessary to improve the accuracy for predicting the resonance frequency based on the analytical model. Fig. 5.3c shows the equivalent circuit of the varactor where the capacitance is calculated as [130]

$$C(V) = \frac{C_{JO}}{(1 + V/V_J)^M} + C_{par} \tag{5.8}$$

with C_{par} being the parasitic capacitance of the varactor. Based on this model, the measurement results are then processed utilising a curve fitting tool to obtain all parameters of the varactor. The measured values of the varactor parameters can be found in Table 5.1. The varactor capacitance C varies from 1.304 pF to 0.149 pF when changing the reverse bias voltage from 0 V to 18 V. Finally, the impedance or susceptance loaded at the aperture of the HMSIW can be simply calculated using circuit theory.

Table 5.1. Varactor parameter values

R	L	C_{J0}	V_J	M	C_{par}
2 Ω	0.05 nH	1.2 pF	4.155 V	1.97	0.1044 pF

Numerical Validation

In this section, analytical and numerical results for the resonance frequency at different capacitance values for different structure dimensions will be compared to validate the analytical model. The selected substrate material is Rogers Duroid 5880 with relative permittivity $\epsilon_r = 2.2$ and thickness $h = 1.524$ mm. Via hole spacing and diameter are chosen as $s = 1.85$ mm and $d = 1.05$ mm. The gap between the stubs and HMSIW aperture is $l_v = 0.66$ mm, which corresponds to the length of the varactor. The HMSIW size is chosen as $l = 37$ mm and $w = 13.875$ mm, noting that this is selected for illustration in this section only, while optimised value will be presented in Section 5.2.3. Three varactors ($n = 3$) are used in the design and thus the period $p = l/3$. Fig. 5.4 shows the resonance frequency at different capacitance values for the cases of $l_{stub} = 0, 10$ and 20 mm while the stub width w_{stub} is fixed at 2 mm. It can be observed that when $C \to 0$, the three curves converge to the same value which is the resonance frequency of the HMSIW without any loading stub. When $C \to \infty$, the three curve converge to different values corresponding to the resonance frequency of the stub-loaded HMSIW with the varactors acting as short-circuits between the open aperture and the stubs. When there is no stub ($l_{stub} = 0$), the resonance frequency remains almost unchanged with varying capacitance values. This is as expected since in the absence of stubs, the aperture remains an open-circuit no matter what value of varactor capacitance is chosen. This is very different from the circumstances in [118] and [121] where the capacitors or varactors are terminated by a short-circuit, which results in a more complicated bias circuit. Figure 5.4 shows that longer stub results in a wider tuning range. It is noted however that the stub length should not be chosen to be more than about half guided wavelength at the highest frequency to avoid a bandgap in the tuning range. This bandgap phenomenon was also observed in [118].

Fig. 5.4 suggests that for the range of capacitance offered by an actual varactor (illustrated by the shaded capacitance range in Fig. 5.4), the stub length l_{stub} needs to be optimised together with the HMSIW dimensions l and w to achieve a target tuning range, e.g. S-band. Such an optimisation and its results will be shown in the next section. Fig. 5.4 also

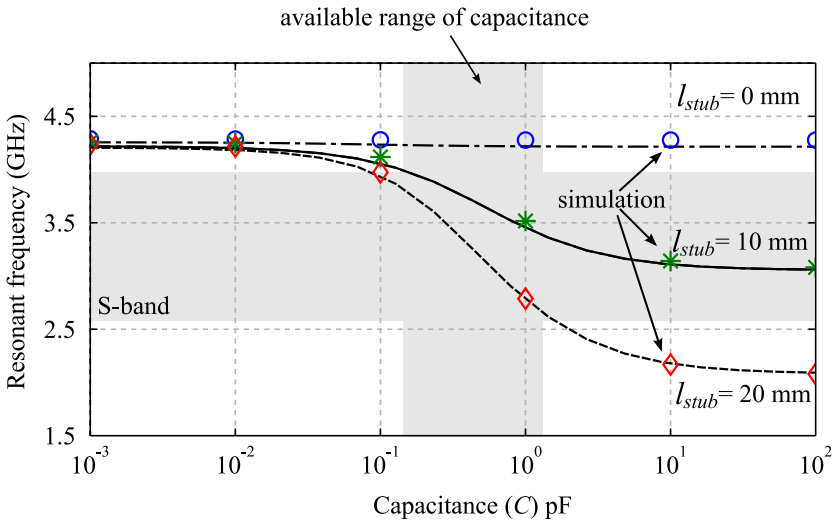

Figure 5.4. Resonance frequency at different capacitance values. Continuous curves are analytical results while discrete points are simulation results. Chosen structure dimensions are $w = 13.875$ mm, $l = 37$ mm, $w_{stub} = 2$ mm, $l_v = 0.66$ mm, $h = 1.524$ mm, $s = 1.85$ mm, $d = 1.05$ mm and $n = 3$.

demonstrates that larger tuning range can be obtained with wider range of capacitance value C.

The next investigation considers the appropriate number of varactors to be used. Fig. 5.5 shows the variation in resonance frequency for different number of varactors while keeping all other dimensions constant. It is noted that varying the number of varactors only changes the period p as $p = l/n$. It can be observed especially from simulation that using more varactors can slightly improve the relative tunability range and miniaturise the antenna. However, more varactors increase the antenna's complexity and cost. Depending on the application, one may choose a priori a suitable number of varactors or may include this number as a parameter into the optimisation. A compromise value for the number of varactors is $n = 3$ and it will be used for the optimisation in the next section.

In general, a good agreement is observed between analysis and simulation across a very wide range of parameters with a relative error below 2% for most of the cases. A discrepancy at low value of C when $n = 5$ is conjectured to be due to the error in the equivalent circuit model of the gap between the stub and the waveguide aperture (C_s, C_{P1} and C_{P2} [129]). Nevertheless, Fig. 5.4 and 5.5 still demonstrate the validity of the proposed analysis. Moreover, the theoretical calculation time for a set of parameters is around

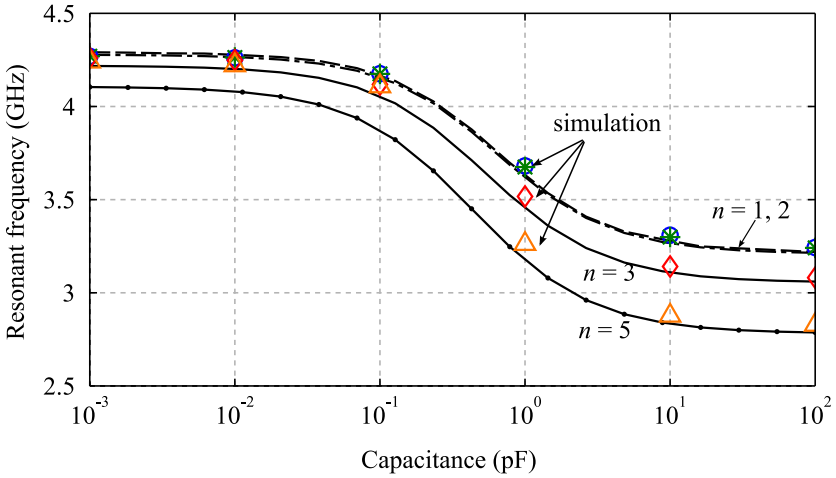

Figure 5.5. Resonance frequency at different capacitance values with different number of varactors (n). Continuous curves are analytical results while discrete points are simulation results. Chosen structure dimensions are $w = 13.875$ mm, $l = 37$ mm, $l_{stub} = 10$ mm, $w_{stub} = 2$ mm, $l_v = 0.66$ mm, $h = 1.524$ mm, $s = 1.85$ mm and $d = 1.05$ mm.

50 ms, which is much faster than a full-wave numerical simulation, and allows an efficient optimisation on the antenna tunability. Further comparison between measurement and analysis results can be found in Section 5.2.4.

5.2.3 Optimisation and Parameter Study

In this section, a detailed investigation on the antenna optimisation will be presented. The target frequency range is from 2.60 GHz to 3.95 GHz (waveguide S-band). The substrate material, substrate thickness and via dimensions are chosen as in previous section. The parameters to be optimised are w_{stub}, l_{stub}, w and l, i.e. the stub and HMSIW size. The goal of the optimisation is to obtain the largest tuning range centred at $f_{cS} = (2.60 + 3.95)/2 = 3.275$ GHz. The first part of this section shows the optimised results for different "host" HMSIW sizes and discusses their impact on the antenna performance. The second part considers the choice of antenna dimensions from the viewpoint of impedance matching. Finally, the last part shows a specific design and discusses the impact of the stub size on the tuning range.

Optimisation

The HMSIW dimensions l and w are chosen first before optimizing the stub size. This means that for a given "host" HMSIW cavity, the parameters l_{stub} and w_{stub} are optimised to achieve the largest tuning range centred at $f_{cS} = 3.275$ GHz. Let $f_{r,\max}$ and $f_{r,\min}$ be the maximum and minimum resonance frequency corresponding to the minimum and maximum values of varactor capacitance respectively. The relative tuning range is defined as

$$TR = 2\min(f_{r,\max} - f_{cS}, f_{cS} - f_{r,\min})/f_{cS} \tag{5.9}$$

(which is possibly negative if $f_{r,\max} < f_{cS}$ or $f_{cS} < f_{r,\min}$). This definition of TR is simple and forces the optimised tuning range to extend from the centre towards both upper and lower limits of the S-band. With just 2 variables (l_{stub}, w_{stub}) the optimisation can be carried out efficiently using a Newton's process. The maximum tuning range TR obtained for different HMSIW sizes is shown in Fig. 5.6. It can be observed that in general when either HMSIW cavity width or length becomes smaller, a larger tuning range can be obtained. However, when the HMSIW dimensions are reduced further than a particular value, shown as the white dashed curve shown in Fig. 5.6, the optimised tuning range does not improve significantly. Moreover, reducing the size of the HMSIW results in larger values of the optimised stub size, which reduces radiation efficiency and increases cross-polarisation.

Impedance Matching

A further condition is that the value of (w, l) must allow an optimised feed position $x = d_f$ for which a given impedance matching specification is satisfied over the whole tuning range. This optimisation can be carried out for the single parameter d_f using a numerical simulation tool. Figure 5.7 shows typical results of the minimum of $|S_{11}|$ for different normalised feed positions d_f/w at the upper and lower limit of the tuning range. Three different values of l/w are selected for illustration, noting that the tuning range remains the same in all three cases, i.e about 2.6 GHz to 3.95 GHz. It can be observed from Fig. 5.7 that when l/w decreases towards 1, it becomes more difficult to find a trade-off feed position such that $\min(|S_{11}|) < -10$ dB across the tuning range. As an empirical rule of thumb, for impedance matching, it is recommended that (w, l) should be chosen with a

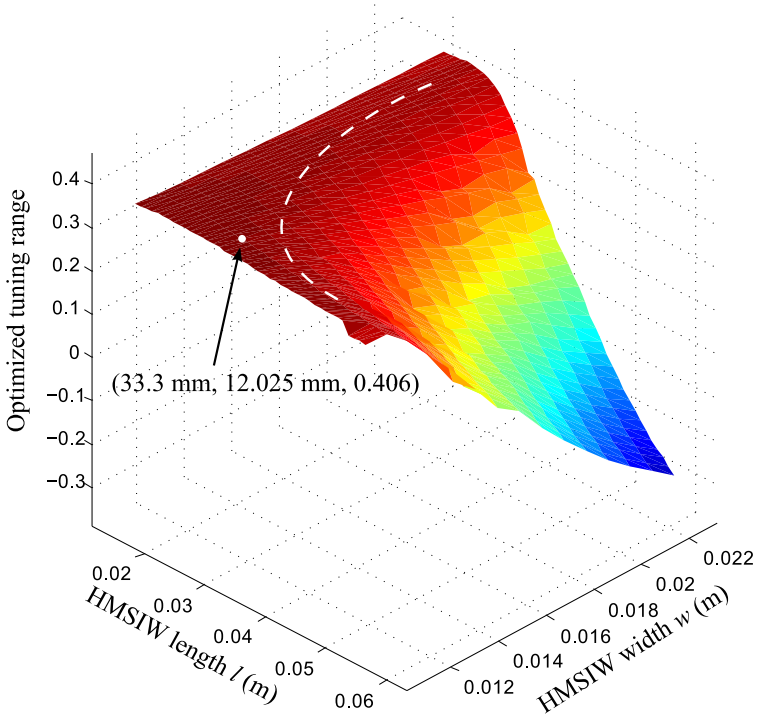

Figure 5.6. Optimised tuning range (TR) for different HMSIW size.

ratio l/w of at least 1.3. It is also noted that higher ratios of l/w (as a rule of thumb beyond 3.5) will excite a higher-order mode with resonance frequency close to the fundamental mode.

Specific S-band design

For the study case presented in this chapter, the aim is to cover the whole S-band with low cross-polarisation (less than -20 dB in both E and H-planes, see Section 5.2.4) and high efficiency (requiring larger open aperture). Therefore, the HMSIW dimensions are chosen as $w = 12.025$ mm and $l = 33.3$ mm (the white dot in Fig. 5.6), which also allows an optimised feed position for impedance matching as discussed in previous section and shown in the final result. The optimised value for the stub dimensions are then $l_{stub} = 21.58$ mm and $w_{stub} = 1.77$ mm. This length of stub corresponds to $0.31\lambda_g$ where λ_g is the guided wavelength at the centre frequency for the quasi-TEM wave travelling along the stub. The calculated range of resonance frequency for this HMSIW size is from 2.61 GHz to 3.94 GHz, which corresponds to 40.6% relative tunability range. This should still cover the

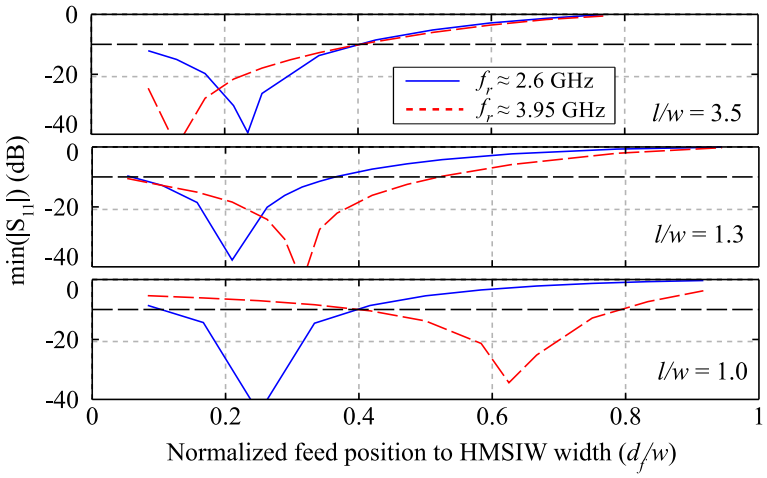

Figure 5.7. Impedance matching study. Minimum of $|S_{11}|$ at the upper and lower limit of the tuning range for different normalised feeding positions. Legends are the same for all three subfigures.

whole S-band when considering the 10-dB bandwidth, since numerical simulation shows a minimum bandwidth of 1.3% for a specific capacitance value (results will be shown in Section 5.2.4).

Figure 5.8 shows the calculated tuning range TR for different lengths and widths of the loading stubs when the HMSIW size is fixed at its selected value $w = 12.025$ mm and $l = 33.3$ mm. The stub length l_{stub} varies from 5 mm to 30 mm, which corresponds to about $0.07\lambda_g$ to $0.44\lambda_g$. It can be observed that the length of the stub is the most important parameter to obtain the desired tuning range. When the stub length l_{stub} is about 22 mm, changing w_{stub} does not significantly change TR. However, if $l_{stub} < 20$ mm, increasing w_{stub} can slightly increase the tuning range. This is because increasing width can make the electrical length of a microstrip line become slightly longer and thus effectively increase l_{stub} towards its optimal value (i.e. 21.578 mm as shown previously). These results demonstrate the significance of an optimisation process to achieve the widest target tuning range starting from given varactor capacitance range values.

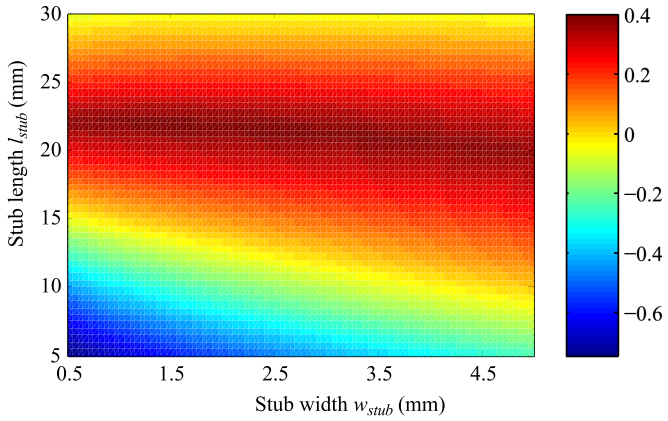

Figure 5.8. Tuning range of the reconfigurable HMSIW cavity antenna. Tuning range (TR) for different stub size ($w = 12.025$ mm and $l = 33.3$ mm).

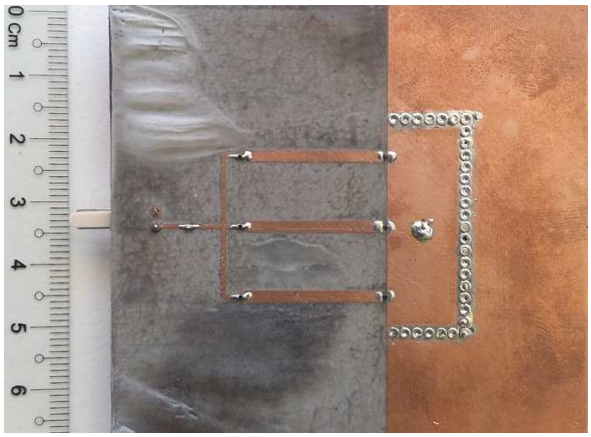

Figure 5.9. Photograph of a reconfigurable HMSIW cavity resonator antenna.

5.2.4 Measurement Results

This section demonstrates and compares the analysis, simulation and measurements results of the antenna tuning range and radiation characteristics. A picture of the manufactured antenna can be found in Fig. 5.9.

Reflection Coefficient and Tuning Range

The simulated and measured reflection coefficients at different values of reverse bias voltage are shown in Fig. 5.10. In general, there is a very good agreement between the simulation and measurement. At higher voltage (corresponding to lower capacitance and higher resonance frequency) the measured depth of $|S_{11}|$ is higher than its simulated value. This

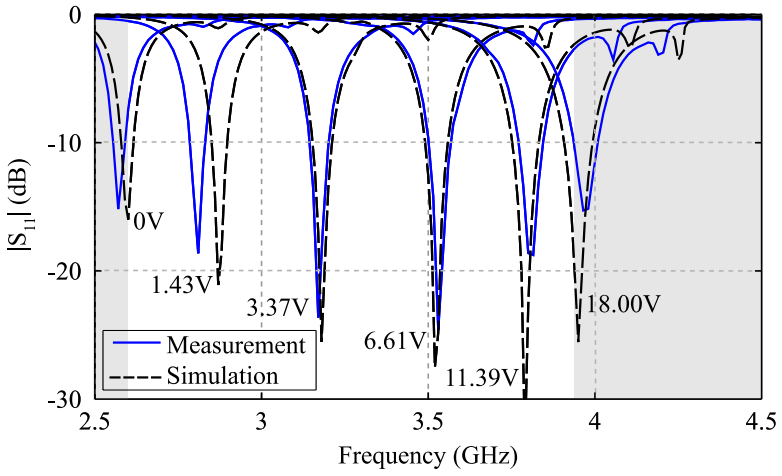

Figure 5.10. Reflection coefficient at different reverse bias voltages. White area is S-band.

is because the internal resistance R of the varactor also increases when voltage increases (which is not accounted for in simulations). Nevertheless, the measured return loss at the resonance frequency across the whole tuning range is greater than 15 dB. The measured resonance frequency range extends from 2.57 GHz to 3.97 GHz while the actual tuning range with the common criteria $|S_{11}| < -10$ dB is from 2.56 GHz to 4.01 GHz which corresponds to a relative tuning band of 44.1%. The measured and simulated relative bandwidth remains stable at about 1.5% when voltage V increases from 0 V to 18 V (minimum of 1.3% at $V = 0$). This instantaneous bandwidth of the antenna at a specific reverse bias voltage can be increased by increasing the thickness and/or decreasing the permittivity of the substrate, similarly as for a microstrip antenna.

Fig. 5.11 shows the analytical, simulated and measured resonant frequencies for different reverse bias voltages. Slightly larger discrepancies between analysis and measurements are observed at lower frequencies, where the slope of the curve is steeper, and thus fabrication tolerances have a larger effect. Nevertheless, generally very good agreement can be observed which further validates the proposed analysis method.

Radiation Pattern, Gain and Radiation Efficiency

The normalised radiation patterns in xy- and yz-plane for different resonance frequencies at different reverse bias voltages are shown in Fig. 5.12. Good agreement between simulation and measurement can be observed in all patterns. The antenna has radiation

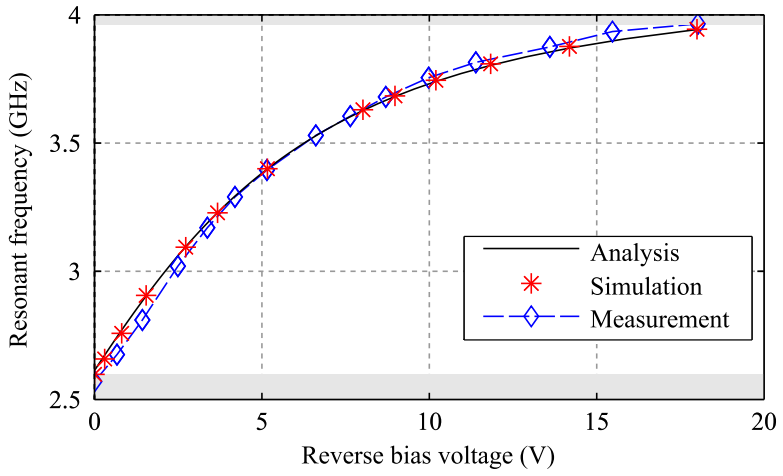

Figure 5.11. Analysis and measurement of resonance frequency across different reverse bias voltages. White area is S-band.

patterns of a magnetic dipole on a finite ground plane with maximum gain in broadside, i.e. y-direction ($\theta = 90, \phi = 90°$), which is similar to the HMSIW cavity antenna proposed in [112]. The chosen ground plane size is 72 mm $\times$ 74 mm which corresponds to $0.78\lambda_0 \times 0.81\lambda_0$ (λ_0 is the free-space wavelength of the centre frequency of the tuning range). Normalised cross-polarisation is approximately below -20 dB in both E- and H-planes. This shows that the designed loading stubs have a small impact on the radiation pattern of the antenna. Figure 5.12 also indicates that the patterns remain stable across the whole tuning range from 2.57 GHz to 3.97 GHz. This confirms the reliability of the antenna performance in the operational tuning band.

The simulated and measured antenna gain are shown in Fig. 5.13. The measured gain rises from 2.1 dB to 6.1 dB as the resonance frequency increases from 2.57 GHz to 3.97 GHz, which is in an acceptable agreement with the simulated gain. About 1 dB (0.93 dB on average) additional loss in measurements may come from antenna fabrication imperfections and experimental error. Numerical simulation shows the antenna efficiency increases from 37% to 91% within the tuning range, while the measured efficiency is estimated to increase from 31% to 71%. The lower efficiency at lower frequency is due to the power loss on the internal resistance of the varactor and smaller effective aperture length. This phenomenon of reducing efficiency at low frequencies has been also observed and explained in other work such as [123, 131].

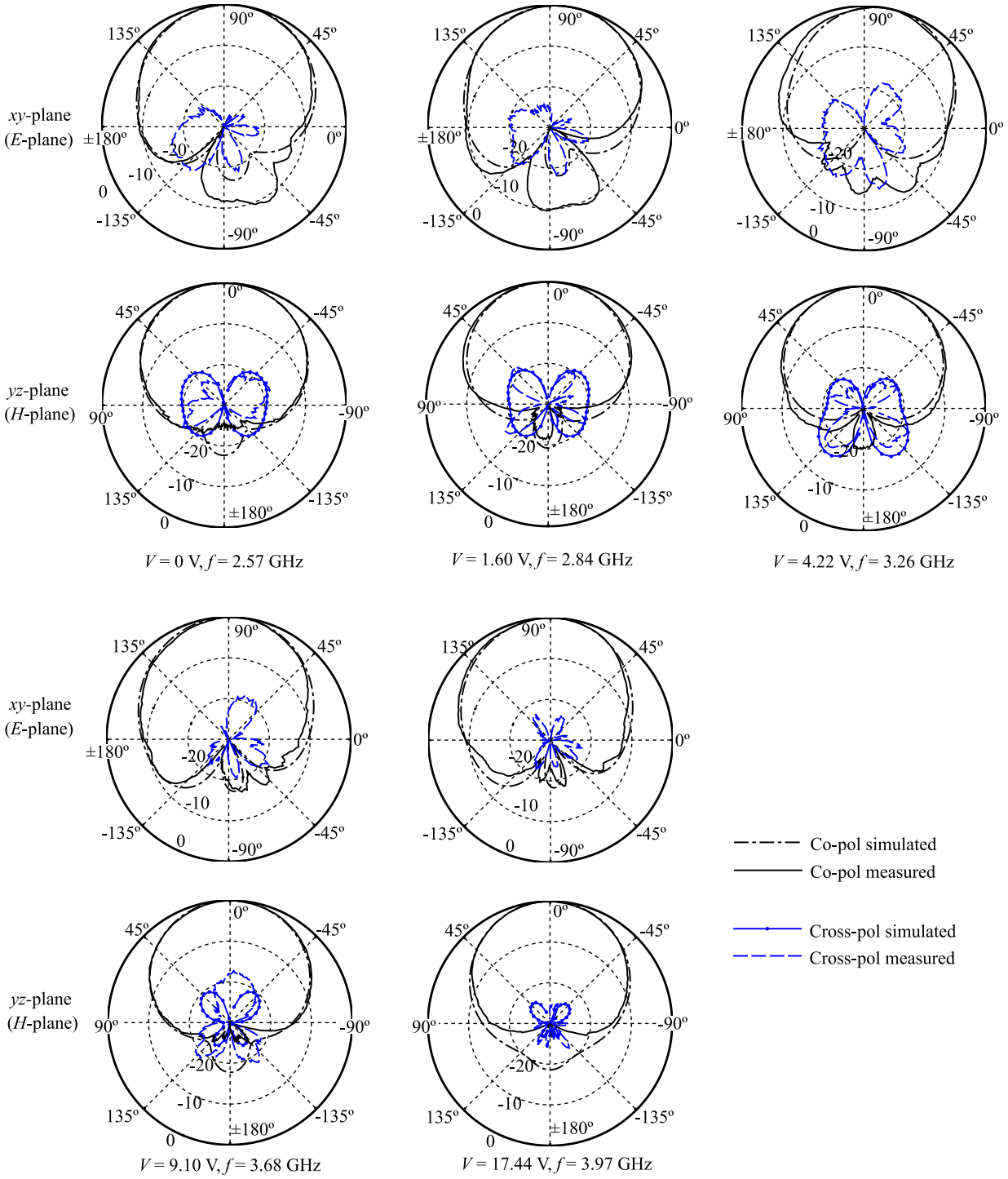

Figure 5.12. Radiation patterns of the reconfigurable HMSIW cavity antenna. Patterns are plotted at $f = 2.57, 2.84, 3.26, 3.68, 3.97$ GHz from left to right, top to bottom.

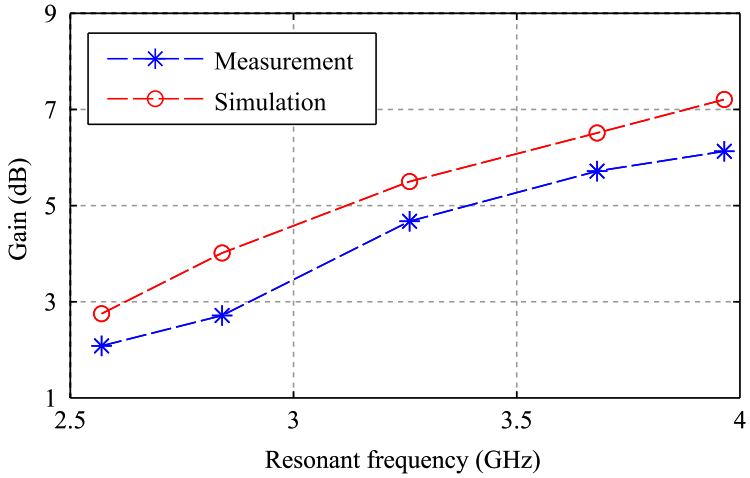

Figure 5.13. Simulated and measured gain of the reconfigurable HMSIW cavity antenna.

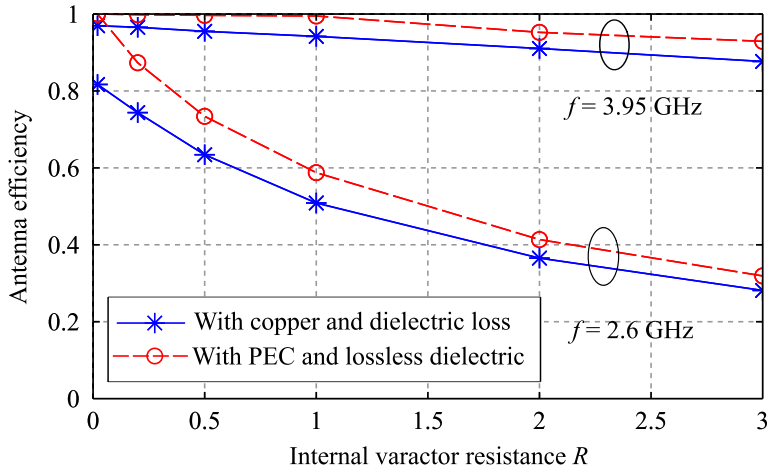

Figure 5.14. Simulated radiation efficiency for different values of internal resistance R of the varactor.

To investigate further on the source of the losses of the structure, the antenna efficiency is simulated with different value of internal resistance R of the varactor for two cases: firstly with perfect materials and secondly including copper and dielectric loss. The results are shown in Fig. 5.14. It can be observed that the efficiency reduction mostly come from the loss in the varactor at lower frequency. When $R = 0$, the antenna efficiency only decreases from 97% to 82% within the tuning range. This demonstrates that the antenna performance can be significantly improved with high-quality varactors.

Table 5.2. Performance comparison. Performance comparison between the proposed antenna and the antennas in [116] and [123]

	This work	[116]	[123]
No. of Var.	3	1	8
ϵ_r	2.2	2.2	2.33
Size	$0.36\lambda_0 \times 0.37\lambda_0$	$0.26\lambda_0 \times 0.11\lambda_0$	$0.95\lambda_0 \times 0.95\lambda_0$
Tunability	44.1%	18.2%	25.5%
$S_{11,\text{max}}$	-15 dB	-8 dB	-11 dB
Gain_{max}	6.1 dB	1.8 dB	5.9 dB
Gain_{min}	2.1 dB	-4 dB	1.8 dB
Radiation pattern	broadside	broadside	omnidirectional

Comparison with Published Results

Table 5.2 shows a comparison on the performance of the antenna with the other recently proposed reconfigurable antennas in [116] and [123], where λ_0 is the free-space wavelength of the centre frequency of the tuning range corresponding to each antenna. These two antennas are chosen due to their similarity in structure (in [116]), and principle (in [123]). The antenna in [116] is an HMSIW cavity radiating at an inter-digital slot while in [123], the antenna has similar design principle of varying the loaded impedance at the aperture but operates as an omnidirectional antenna.

Compared to [116], the antenna demonstrates significant improvements in the radiation characteristics at the cost of increased antenna size and number of varactors. It is noted that the proposed antenna achieves a large tuning range as a result of an optimisation with an accurate analytical solution. Comparison among other reconfigurable antennas at similar frequency range in literature can be found in [116].

5.2.5 Summary of Reconfigurable HMSIW Cavity Antenna

A reconfigurable antenna based on a periodically loaded HMSIW cavity has been proposed. The measured tuning range of the antenna covers the whole S-band with more

than 44% relative tunability range. A detailed theoretical analysis of the resonance frequency has been provided which allows an efficient and optimised design of the antenna. With a fast optimisation process, the proposed antenna shows a significant improvement in the radiation performance and reflection coefficient compared to other published reconfigurable antennas using similar structure or principle. The antenna also exhibits good stability of its radiation pattern across the whole tuning range which makes it a reliable candidate for future communication systems. The principle and analytical model presented in this section provide a foundation for other reconfigurable antennas based on varactors and loading stubs shown in the next sections.

5.3 Microstrip Patch Antenna

Frequency-reconfigurable linearly polarised microstrip antennas have been proposed in the literature with various techniques such as utilising: switches loaded with folded dipoles [132], varactors loaded with shorting posts [133, 134], varactors with a near-field resonant parasitic monopole [135] and tuning devices with a slotted patch [136, 137] or a low-profile monopolar patch [123, 138]. Compact reconfigurable antennas have also been proposed in [116, 139, 140]. However, as discussed in [141], fewer attempts have been placed on frequency-reconfigurable circularly polarised radiating device. Most of the available antennas can only be switched between LP and CP and/or between right hand circular polarisation (RHCP) and left hand circular polarisation (LHCP) in a specific frequency band [142–147]. Recently [141] and [148] proposed frequency-reconfigurable circularly polarised antennas with continuous tuning range of about 25% utilising varactors controlled with a single tuning bias voltage. However, the operation frequency of these antennas can only be tuned for either RHCP or LHCP. It is noted that a versatile microstrip antenna that can be fully reconfigured in both frequency and polarisation (LP, RHCP and LHCP) in a wide continuous frequency range is very challenging to obtain.

Table 5.3 summarises some recent notable reconfigurable microstrip antennas that can be tuned in polarisation and/or frequency. The tunability is defined as percentage frequency tuning range. Although the antenna in [133] provided a wide tuning range with LP at $0°, 45°$ and $90°$ and very good isolation among these states, CP has not been reported or considered. Beside, the authors in [147] demonstrated an antenna which is capable of all

Table 5.3. Performance of selected recently published reconfigurable microstrip patch antennas.

		[133]	[147]	[141]	This work
LP	Tunability	50%	not tunable	N/A	40%
	$\|S_{11}\|_{max}$	-10 dB	-17 dB	N/A	-9.8 dB
	$Gain_{min}$	-2.6 dB	Not shown	N/A	2.6 dB
	$Gain_{max}$	6.4 dB	Not shown	N/A	7.3 dB
CP	Tunability	N/A	not tunable	25%	40%
	$\|S_{11}\|_{max}$	N/A	-18 dB	-12 dB	-12 dB
	$Gain_{min}$	N/A	Not shown	2.5 dB	2.0 dB
	$Gain_{max}$	N/A	Not shown	5.8 dB	$>$ 8.1 dB
	Both RHCP & LHCP	N/A	Yes	No	Yes

types of polarisation, but the reconfigurability aimed at switching between different polarisations in a single frequency band. As discussed, the antenna in [141] is only capable of one sense of CP and the tunability is limited as only one bias voltage is used. The authors in [149] proposed an antenna with both polarisation and frequency tunability; however, very limited results for CP were discussed or presented. Furthermore, a systematic approach to design a reconfigurable antenna for a given frequency range and varactor tuning values is still lacking in these papers.

Based on the analytical model and technique learned in Section 5.2, this section proposes an antenna design with both frequency and polarisation agility in a wide tuning range using a fast optimisation process. The proposed approach significantly reduces the design and optimisation time while delivering a reasonable accuracy on the estimated tuning range.

This section starts by describing the antenna design and operation principle. Then the optimisation for the antenna tuning range based on an analytical model demonstrated in Section 5.3.2. Finally, the simulation performed with Ansys HFSS and measurement results of the fabricated antenna at various frequencies and different polarisation configurations are presented in Section 5.3.3.

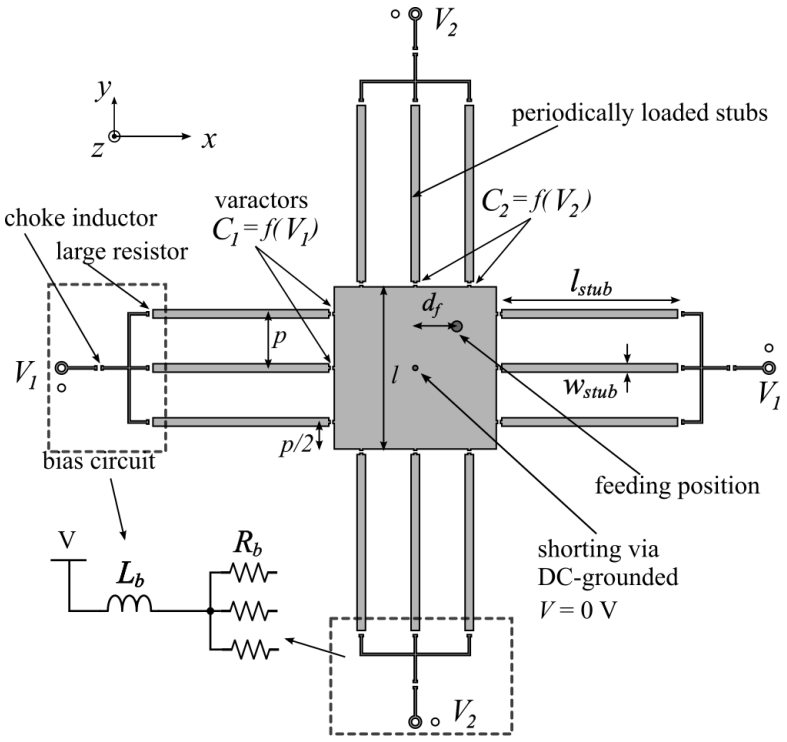

Figure 5.15. Design of a reconfigurable stub-loaded microstrip patch antenna.

5.3.1 Antenna Design and Operation Principle

The antenna consists of a square microstrip patch and twelve identical stubs distributed evenly at the four edges of the patch (Fig. 5.15). The spacing between the stubs is $p = l/3$ where l is the patch size. The varactors (MACOM MA46H120) bridge the stubs with the patch edges, i.e. the patch "radiating slots". At the other end of the stub lies the bias circuit for the varactor which consists of a resistor followed by a choke inductor. The chosen values for the bias circuit are $R_b = 1$ MΩ and $L_b = 100$ nH, similar to the HMSIW cavity design in the previous section.

The varactors and stubs are divided in two groups: x- and y-direction (Fig. 5.15). Each group is connected to an independent DC bias voltage (V_1, V_2). In this configuration, the patch needs to be DC-grounded, which is achieved by placing a shorting via at the patch centre. This shorting via does not change the radiation modes of the microstrip patch since electric field at the centre is zero for both x- and y-oriented mode. The stubs do not only provide another degree of freedom for impedance manipulation (as shown in the previous section) but also allow different voltages to be tuned independently.

The antenna feeding position lies in the diagonal line of the square patch (Fig. 5.15) to excite both TM_{10} and TM_{01} modes. The variable capacitance of the varactor can be calculated using (5.8) with measured parameters found in Table 5.1. The varactor internal resistance R averaged over the frequency range is estimated to be $R \approx 2\ \Omega$. When a group of varactors is tuned, the wavenumber in the corresponding direction changes as demonstrated and analysed in Section 5.2. Therefore, by varying (V_1, V_2) independently, the resonance frequency of the x- and y-oriented modes can be controlled. When $V_1 = V_2$, the two orthogonal modes are excited with the same phase and magnitude, thus the antenna radiates with 45° LP. When V_1 and V_2 are different by a correct amount, CP radiation can be realised [150]. The rotating sense can be switched by simply swapping the two voltage values. When the bias voltages V_1 and V_2 are sufficiently different from each other, two modes are excited at different frequencies and the antenna operates as a dual-band antenna with 0° and 90° LP in the respective bands.

5.3.2 Analysis and Optimisation

Analysis

The analysis is based on the transmission line model of the loading stubs and the cavity model proposed in Section 5.2. It is performed with the following steps. Firstly, a periodically loaded quarter-wave patch antenna is considered (Antenna I, Fig. 5.16a). This antenna is similar to the antenna proposed in Section 5.2 except that the short circuit walls of the HMSIW are replaced by open circuits. The field equivalence principle can be still used, yielding two additional magnetic-current sources on the two new open sides of the antenna. These two magnetic-current sources ($\mathbf{M}_1, \mathbf{M}_2$ in Fig. 5.16a) are 180° out of phase and cancel each other at broadside, i.e. z-direction. Therefore, they can be neglected as similarly as in the analysis of a conventional patch antenna. Similarly as for a quarter-wave patch, the resonance frequency of this antenna at the fundamental mode is calculated as

$$f_r = \frac{c_0}{2\pi\sqrt{\epsilon_r}} k_x \tag{5.10}$$

where k_x is the wavenumber in x-direction of a periodically loaded HMSIW [118] and ϵ_r is the relative permittivity of the substrate. The details on the calculation of k_x can be found in Section 5.2.2.

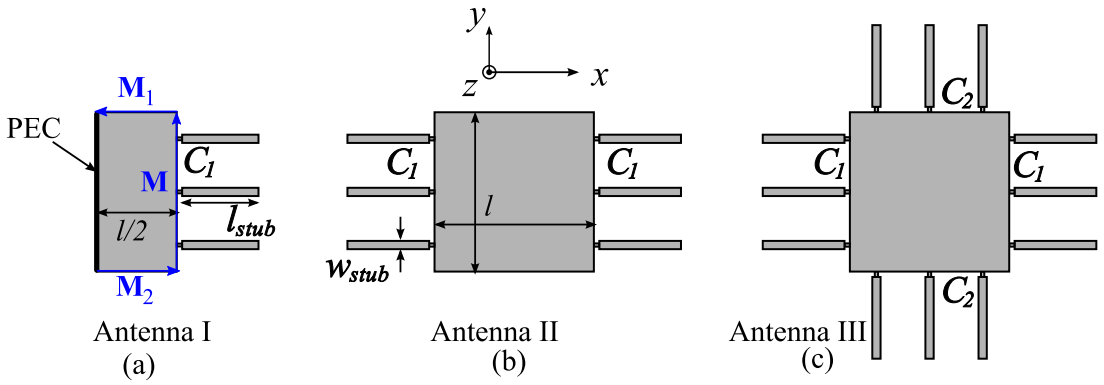

Figure 5.16. Steps to analyse the proposed reconfigurable microstrip patch antenna. (a) Periodically loaded quarter-wave patch antenna; (b) Microstrip patch antenna with reconfigurability in one direction; (c) Fully functional antenna.

Secondly, since the mode in a quarter-wave patch antenna is just a half-mode of the full patch antenna, the resonance frequency of Antenna II (Fig. 5.16b) is the same as that of Antenna I. At this stage, by varying the capacitance value of the varactor, the resonance frequency of Antenna II can be varied and predicted with high accuracy using this analytical model.

Finally, a second set of stubs is added in the other dimension of the square patch to allow reconfiguration of the orthogonal mode, leading to Antenna III (Fig. 5.16c). Unfortunately, the resonance frequency of the TM_{10} or TM_{01} mode of the fully functional antenna, i.e. Antenna III, depends on both V_1 and V_2. This can be explained as follows. If the capacitance of the varactors $C_2 = 0$, Antenna III becomes identical to Antenna II with open circuits in y-direction. However, when V_2 varies, C_2 also varies and takes a non-zero value. This increases the effective width of the antenna in y-direction and thus slightly affects the wavenumber in x-direction (results will be shown in Section 5.3.3). Being aware of this effect, the optimisation is performed for **the simpler case of Antenna II** to obtain the desired frequency tuning range with a given range of capacitance value. The tuning range is then compared between Antenna II and Antenna III (with the same antenna dimensions) to observe and if necessary correct any discrepancy.

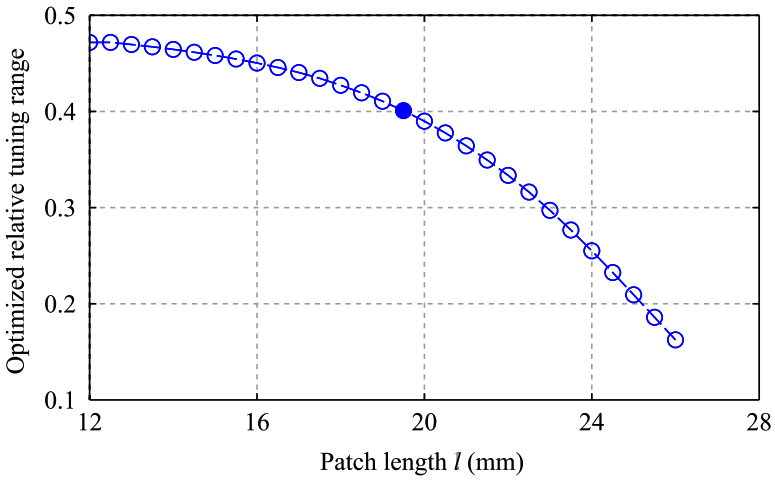

Figure 5.17. Optimised relative tuning range for different patch sizes (Antenna II).

Optimisation

The optimisation is carried out efficienctly using the process described in Section 5.2.3 targeting for $TR = 40\%$ centred at $f_c = 3$ GHz, i.e. $[2.4, 3.6]$ GHz. (TR is defined in equation (5.9)). The optimised parameters are the stub dimensions (l_{stub}, w_{stub}) and the antenna size l. The selected material is Roger Duroid 5880 with $\epsilon_r = 2.2$ and thickness $h = 1.524$ mm. The same varactor type is used as before, i.e. with measured tuning of $[1.304, 0.149]$ pF, corresponding to a reverse bias voltage from 0 V to 18 V.

Figure 5.17 shows the optimised tuning range TR for different values of l. It can be observed that when l decreases, the optimised TR increases. When l becomes smaller than 17 mm, the TR improves only marginally further. However, the patch becomes smaller which results in a decreased antenna efficiency. Thus, there is a trade-off between antenna size, tuning range and efficiency. The loading-stub technique proposed in this chapter provides the flexibility in choosing the desired trade-off during the antenna design process. For the purpose of conceptual demonstration, this section aims to design an antenna with 40% tuning range, therefore $l = 19.5$ mm is chosen (full dot, Fig. 5.17). In this case, the optimised stub dimensions are $l_{stub} = 21.16$ mm and $w_{stub} = 1.01$ mm.

The analysed and simulated resonance frequencies as a function of the varactors' capacitance C_1 for the optimised Antenna II are shown in Fig. 5.18. The result for the Antenna III which has the same dimensions as the optimised Antenna II is also plotted for the special case $C_1 = C_2$. For Antenna II, very good agreement between analysis and simulation is

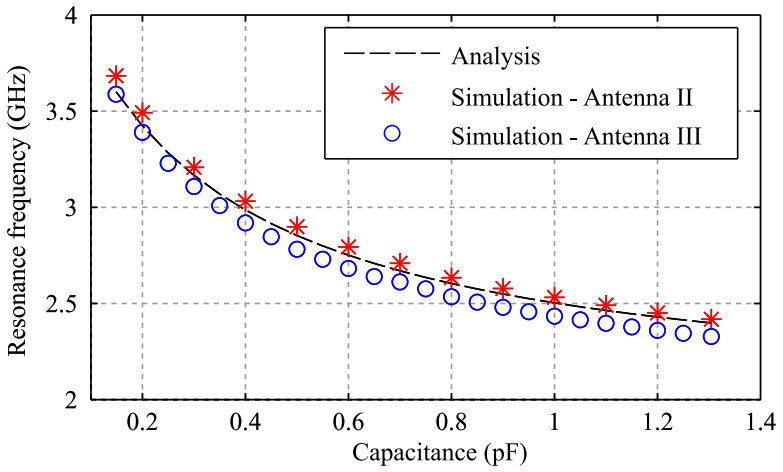

Figure 5.18. Analysed and simulated resonance frequency of Antenna II. The simulated result for Antenna III is plotted for the case of $C_1 = C_2$, i.e. 45° LP, which corresponds the maximum tuning range of Antenna III.

observed across the whole tuning range, which validates the optimisation process and the analytical model proposed in Section 5.2. For the fully functional Antenna III, the absolute frequency range is shifted down by about 2% to 3%. This is as expected since adding C_2 increases the effective width of the patch, and thus decreases the resonance frequency.

Although the analysis can only give the resonance frequency for the Antenna II, it still provides a quick and reasonably accurate estimation on the antenna tuning range. A 2-3% shift to lower frequency in the tuning range can be corrected through straightforward scaling in an iterative design procedure. In this section, for illustration, the dimensions of the fully functional antenna are kept the same as the optimised Antenna II. It is noted that the tuning range for CP operation is by nature slightly narrower than the optimised tuning range for LP because CP is based on two slightly shifted orthogonal LP resonances.

The feeding position $(x, y) = (d_f, d_f)$ is then optimised using HFSS to obtain a satisfactory reflection coefficient across the tuning range. The simulation shows a trade-off for the reflection coefficient between the case for 45° LP ($C_1 = C_2$) and other polarisation states. Since 0° and 90° LP are also available, we opted to slightly lower the requirement for 45° LP for the presented design, to obtain better $|S_{11}|$ for all other polarisations. The chosen feeding position is $d_f = 5$ mm. Using this value, numerical simulations predict that $|S_{11}|$ throughout the tuning frequency range is better than -9.5 dB for 45° LP and better than -10 dB for all other polarisation configurations. The measurement result shown in the

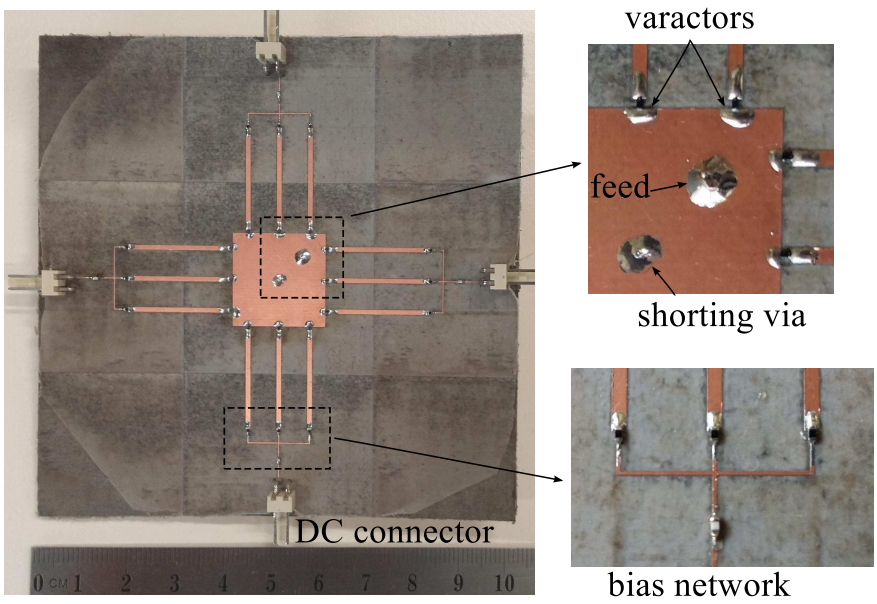

Figure 5.19. Photograph of the fabricated reconfigurable patch antenna with DC bias network.

next section will confirm a $|S_{11}|$ better than -9.8 dB in all polarisation states across the whole tuning range.

5.3.3 Simulation and Measurement Results

This section starts by discussing the tuning process to obtain CP radiation with the proposed concept. Then the $|S_{11}|$ parameter and axial ratio (AR) for the designed structure will be presented followed by the antenna radiation patterns (in all polarisation configurations) and antenna gain. A photograph of the fabricated antenna can be found in Fig. 5.19

Tuning Bias Voltage for CP

For a rectangular microstrip patch antenna, CP radiation is achieved with a single feed when the two orthogonal fundamental modes are excited with 90° phase difference [150]. This is achieved for example by independently adjusting the length and width of the patch. The required resonance frequency f_{r1} and f_{r2} of two modes TM_{10} and TM_{01} can be adjusted by changing V_1 and V_2, and hence C_1 and C_2. Since these resonance frequencies f_{r1} and f_{r2} depend on both C_1 and C_2, the antenna is tuned using numerical simulations to

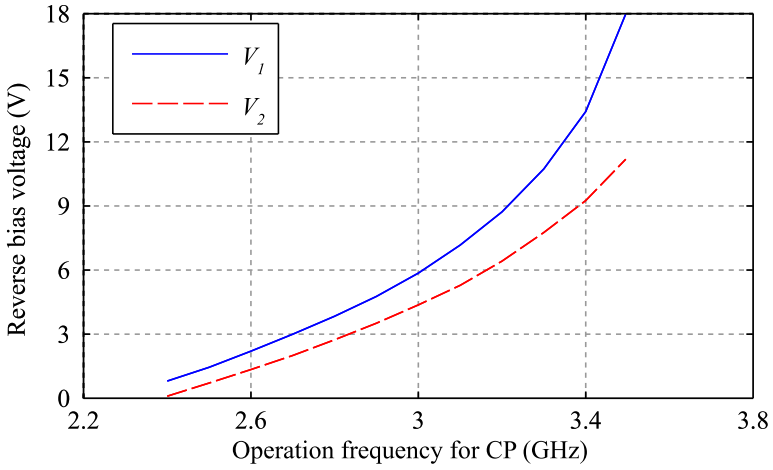

Figure 5.20. Tuning bias voltages. Simulated tuning bias voltages for RHCP radiation as a function of operation frequency. LHCP is obtained by swapping the values of V_1 and V_2.

obtain the smallest axial ratio (AR) at different frequencies and maximum corresponding 3 dB AR-bandwidth. When performing this, starting values for V_1 and V_2 can be estimated from the blue-circle curve in Fig. 5.18 and the varactor model $C = C(V)$ given in equation (5.8). The simulated reverse bias voltages necessary to obtain CP at different frequencies are shown in Fig. 5.20. By swapping the values of V_1 and V_2, the sense of CP is reversed.

Reflection Coefficient and Axial Ratio

The simulated and measured reflection coefficient for 45° LP at different combination of reverse bias voltages (V_1, V_2) are shown in Fig. 5.21a. Good agreement between simulation and measurement can be observed. The antenna can be tuned to work with 45° LP from 2.31 GHz to 3.70 GHz. For 0° and 90° LP (results shown in Fig. 5.21b), the tuning range is slightly smaller since V_1 and V_2 must be separated enough for satisfactory isolation between two resonance modes. The estimated tuning range in this case is from 2.40 GHz to 3.45 GHz with maximum cross-polarisation of -10 dB (patterns will be shown later). Measured results show $|S_{11}|$ smaller than -9.8 dB at resonance frequencies for all LP states.

Considering now operation in CP, the reflection coefficient and axial ratio (AR) at different voltage combinations (V_1, V_2) are shown in Fig. 5.22. Good agreement between simulation and measurement can be observed. The antenna can be tuned for CP with AR and

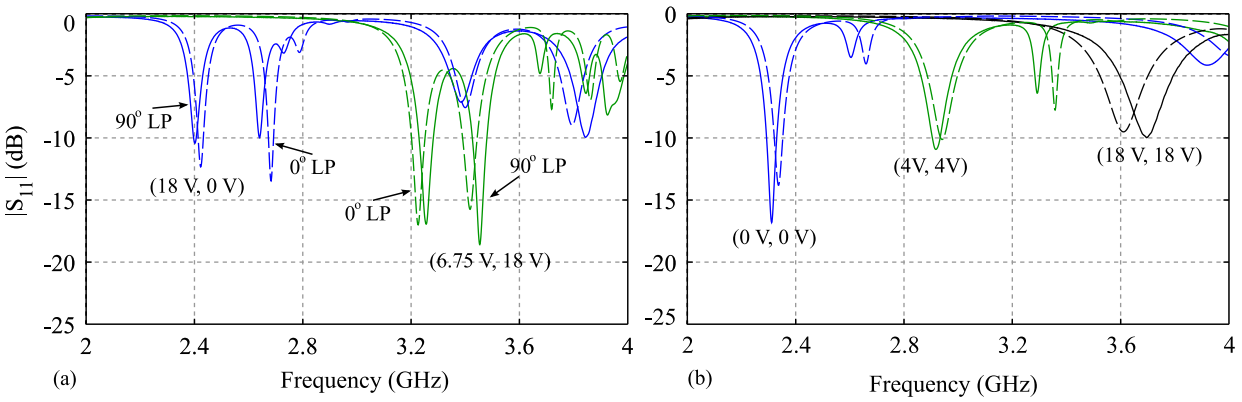

Figure 5.21. Reflection cofficient results for LP operation. Results are shown for two combinations of (V_1, V_2): (a) 45° LP; (b) 0° and 90° LP. Solid lines are measured results and dashed lines are simulated results. It is noted that the results for the case $(V_1, V_2) = (0, 18)$ V are the same as for $(18, 0)$ V except that the resonance frequencies for 0° and 90° LP are interchanged.

$|S_{11}|$ less than 1.6 dB and -12 dB, respectively from 2.36 GHz to 3.54 GHz. The 3-dB AR instantaneous bandwidth increases from 0.72% to 0.96% in the tuning range. These values are typical for a single feed circularly polarised microstrip patch antenna [151].

Three-dimensions (3D) plots for the reflection coefficient as a function of varactor capacitance value and frequency are presented in Fig. 5.23. The results are shown for 3 cases of constant C_1, i.e. 0.2 pF, 0.45 pF and 1.1 pF while C_2 is varied in the whole range of varactor capacitance value, i.e. 0.149 pF to 1.304 pF. Very good agreement between simulation and measurement can be observed which ultimately validates the antenna functions. The parasitic resonances originate from higher-order modes of the antenna, e.g. TM_{11} and the monopolar mode discussed in Chapter 4 and 7. Furthermore, it can be observed that the resonance frequencies vary in a smaller range when C_1 is fixed at a larger value. This is because larger C_1 increases the effective size of the patch and thus reduces the tuning range (Fig. 5.17).

Finally, it is known that the use of varactors limits the power handling capability [152], which might restrict application especially in transmission mode. All presented measurements have been performed with an injected level power of -5 dBm, but it has been verified that the antenna performance does not change at least until an input power of $+5$ dBm (a corresponding value of -5 dBm is reported in [152]). This suggests that the

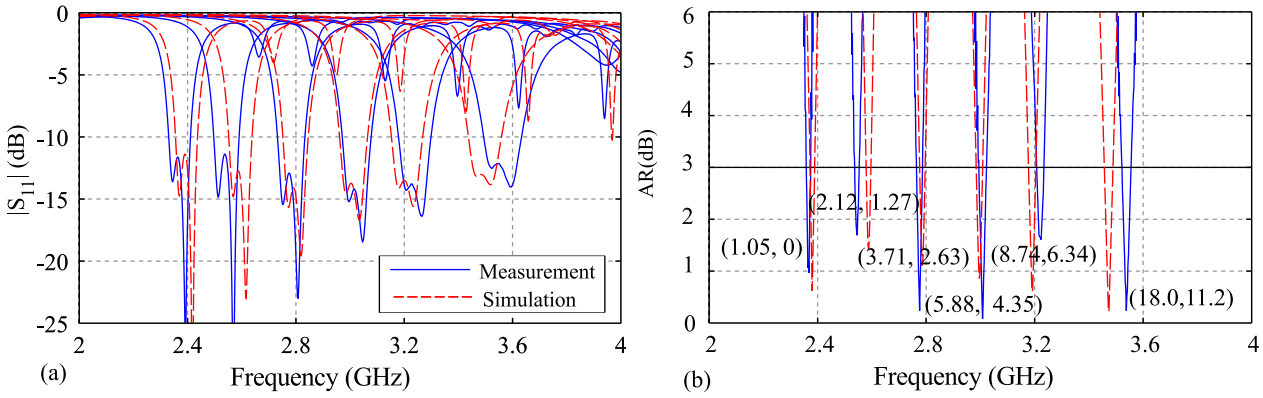

Figure 5.22. Reflection coefficient and axial ratio for RHCP operation. (a) Reflection coefficient; (b) Axial ratio. Different combinations of bias voltages are chosen. The number in bracket shows the values of (V_1, V_2) in volts (obtained from Fig. 5.20).

parallel arrangement of several varactors extends the power handling capability, which can be a key advantage compared to tuning with a single varactor.

Radiation Pattern and Gain

The normalised radiation patterns for selected frequencies in 3 cases of LP operation are shown in Fig. 5.24. The simulated cross-polarisation level remains below -15 dB. Measured results show a higher cross-polarisation which could be due to the experimental error, e.g. to the limited dynamic range of our anechoic chamber. Nevertheless, the measured cross-polarisation is still less than -10 dB across the tuning range.

The radiation patterns for CP with two senses of rotation at $f = 3.01$ GHz are shown in Fig. 5.25. The result confirms that the antenna can be simply switched between RHCP and LHCP by swapping the bias voltages. A cross-polar level of lower than -15 dB can also be observed in both pattern sets. For further validation and illustration, the results for RHCP at two other frequencies, at the lower and upper upper limits of the operating frequency range, are shown in Fig. 5.26. Reasonable agreement between simulation and measurement can be observed in all patterns in Fig. 5.24-5.26, which validates the proposed antenna functions. Furthermore, the radiation patterns are stable in all polarisation configurations across the whole frequency tuning range.

The results for antenna gain when operating with CP are shown in Fig. 5.27. Good agreement between simulation and measurement is observed especially when $f \geq 2.75$ GHz.

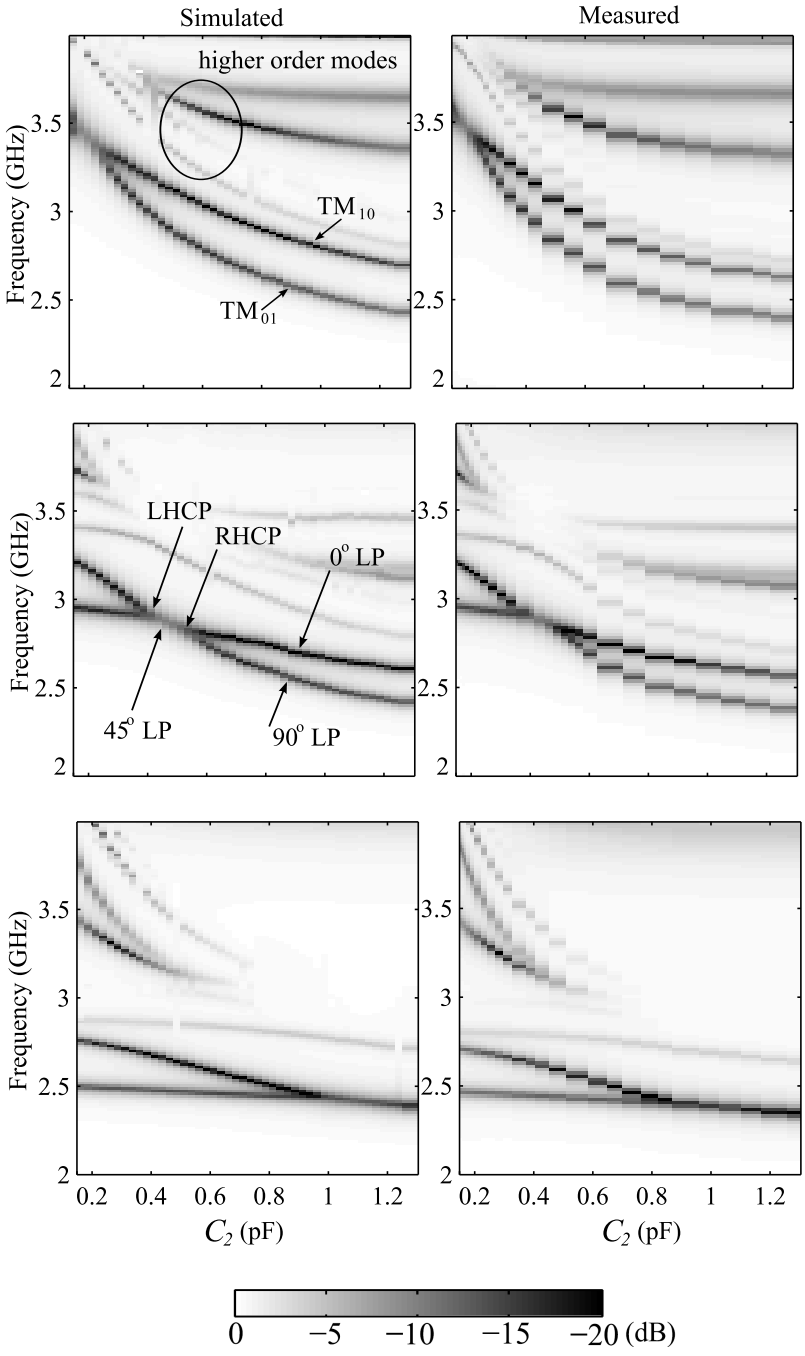

Figure 5.23. 3D plot of reflection coefficients. 3D plot of the simulated and measured reflection coefficient when varying C_2 and fixing C_1 at $0.2, 0.45$ and 1.1 pF, respectively from top to bottom.

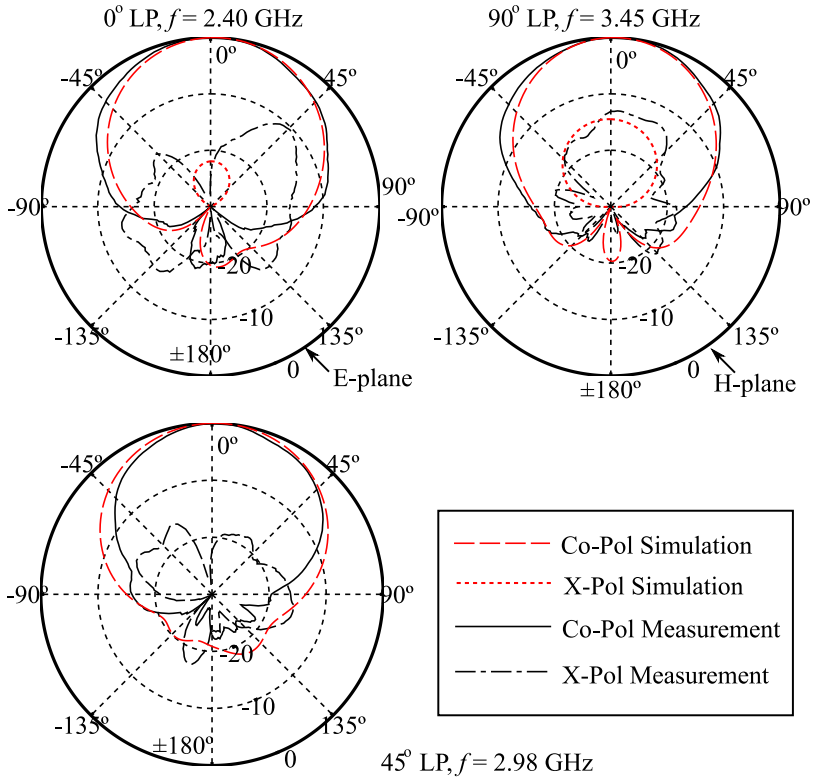

Figure 5.24. Radiation pattern results for LP operation. The patterns are plotted for 0°, 90°, 45° LP at selected frequencies in xz-plane ($\phi = 0°$).

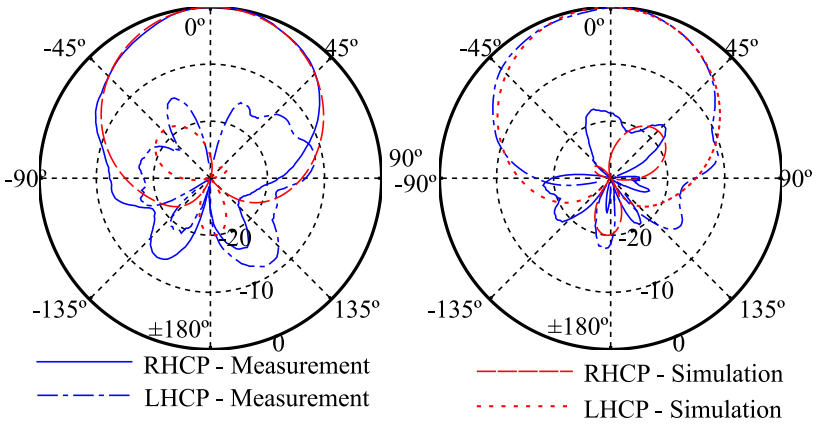

Figure 5.25. Normalised radiation patterns (xz-plane) for CP operating at 3.01 GHz. The bias voltages are chosen as $(V_1, V_2) = (5.88\ \text{V}, 4.35\ \text{V})$ for RHCP (left); and $(V_1, V_2) = (4.35\ \text{V}, 5.88\ \text{V})$ for LHCP (right).

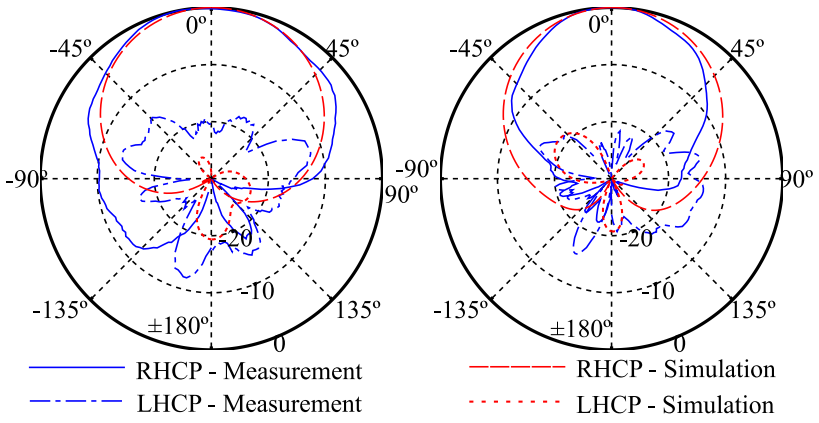

Figure 5.26. Normalised radiation patterns (xz-plane) for RHCP operating at 2.36 GHz and 3.54 GHz. The bias voltages are chosen as $(V_1, V_2) = (1.05\text{ V}, 0\text{ V})$ and $(18.0\text{ V}, 11.2\text{ V})$ respectively. Discrepancy in the case $(18.0\text{ V}, 11.2\text{ V})$, i.e. the pattern in the right, is due to the up-shift in resonance frequency at the limit of the tuning range on measurement (see Fig. 5.22), and possibly the imperfection in fabrication as well as measurement setup.

The simulated radiation efficiency increases from 40% to 88%, when increasing the frequency through the operation range. Based on this and the gain values in Fig. 5.27, the measured efficiency is estimated to increases from 25% to about 90% when the operating frequency increases from 2.36 GHz to 3.54 GHz. The simulated and measured gains of some recently published reconfigurable patch antennas are shown in Table 5.3 for reference, noting that the various materials and frequencies render a direct comparison difficult. A similar reduction on antenna efficiency at lower frequency is observed in other varactor-tuned reconfigurable antennas in the literature [123, 133, 141]. This has also been discussed in Section 5.2 for the case of stub-loaded HMSIW cavity antenna: the antenna efficiency mostly depends on the quality factor of the varactor, especially at lower frequency (lower reverse bias voltage). Also as expected, the measured gain of the antenna when operating with LP follows the same trend as in CP, with an increase from about 2.6 dB to 7.3 dB when the resonance frequency increases from 2.40 GHz to 3.45 GHz.

5.3.4 Summary of Reconfigurable Microstrip Patch Antenna

A reconfigurable antenna design offering both frequency and polarisation agility has been presented. The microstrip antenna employs periodically loading stubs with varactors to

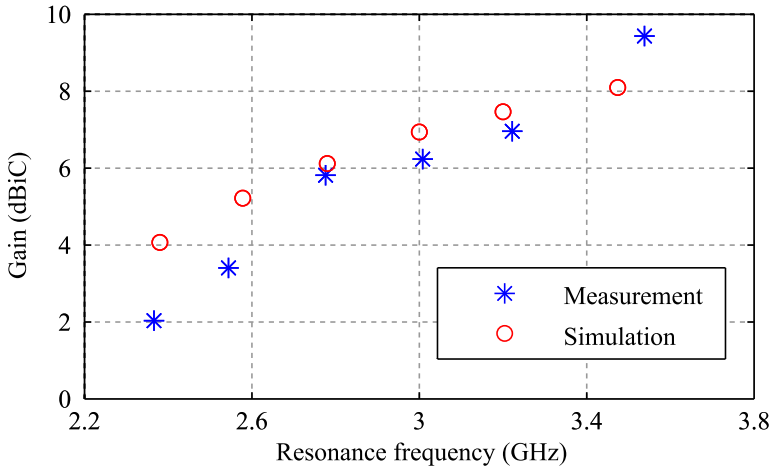

Figure 5.27. Simulated and measured gain of the reconfigurable patch antenna operating with circular polarisation.

manipulate the antenna aperture impedance and hence, the resonance frequency. A simple DC bias network is required, with two independently adjustable voltages. Good agreement between simulated and measured results in all polarisation configurations across a wide tuning range of frequency (around 40% centred at 3 GHz) has been demonstrated. The antenna is suitable for integration into smart communication systems where polarisation diversity, frequency tunability and pattern stability are required.

5.4 Family of Stub-Loaded Reconfigurable Antennas

From the results presented in Sections 5.2 and 5.3, a family of stub-loaded reconfigurable antennas based on substrate-integrated circuits is further developed and summarised for a systematic view demonstrating the versatility of the tuning concept. These include the HMSIW cavity, the quarter-wave patch, the quarter-mode substrate-integrated waveguide (QMSIW) cavity and the microstrip patch reconfigurable antennas. The evolution of these structures are shown in Fig. 5.28.

Starting from the HMSIW cavity (Fig. 5.28a), one can cut it into a half to form a QWSIW [114], and then place a varactor loaded with a rectangular stub to obtain the frequency-reconfigurability (Fig. 5.28b). Alternatively, the two shorting side walls can be removed and the structure becomes a quarter-wave patch (Fig. 5.28c) with radiation mechanism explained in the previous section. This antenna has been extended into the stub-loaded

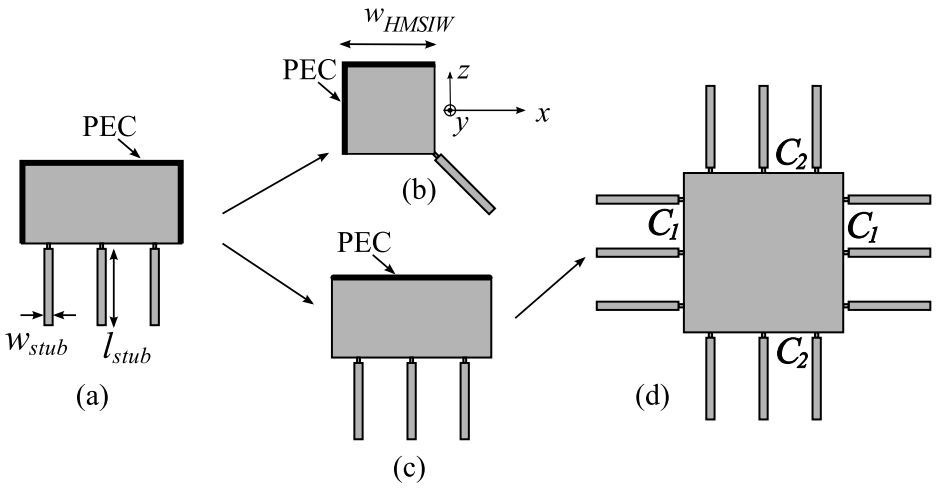

Figure 5.28. A family of stub-loaded reconfigurable antennas. The structures are based on: (a) HMSIW; (b) QMSIW; (c) Quarter-wave patch; (d) Microstrip patch. Bold lines represent PEC-walls.

microstrip patch with additional polarisation reconfigurability (Section 5.3). Since the stub-loaded HMSIW cavity and microstrip patch antenna have been investigated previously, in this section, the results for the QMSIW cavity and quarter-wave patch are presented. It is noted that only selected simulation results are shown here as a further illustration of the techniques proposed in this chapter.

5.4.1 QMSIW Reconfigurable Antenna

Figure 5.28b shows a possible design of a stub-loaded QMSIW with a single varator. The antenna operates with 45° linear polarisation (LP). Utilising the cavity model of QMSIW and the analysis in Section 5.2.2, the resonance frequency of this structure can also be predicted to high accuracy. In this investigated case, the wavenumbers in x- and z-direction k_x and k_z are the same and can be found from the analysis with the periodicity $p = 2w_{QMSIW}$ and loaded reactance B depending on the stub dimensions and bias voltage (Fig. 5.28b).

For demonstration, a QMSIW reconfigurable antenna is optimised for a frequency tuning range of 30% centred at $f_{ct} = 2$ GHz, i.e. $[1.7, 2.3]$ GHz, using the same varactor as in previous section. The chosen substrate material is Rogers Duroid 5880 with relative permittivity of $\epsilon_r = 2.2$ and thickness $h = 3.175$ mm. The optimised antenna parameters are $w_{QMSIW} = 27.8$ mm, $w_{stub} = 1$ mm, $l_{stub} = 32.8$ mm. The simulated and analysed

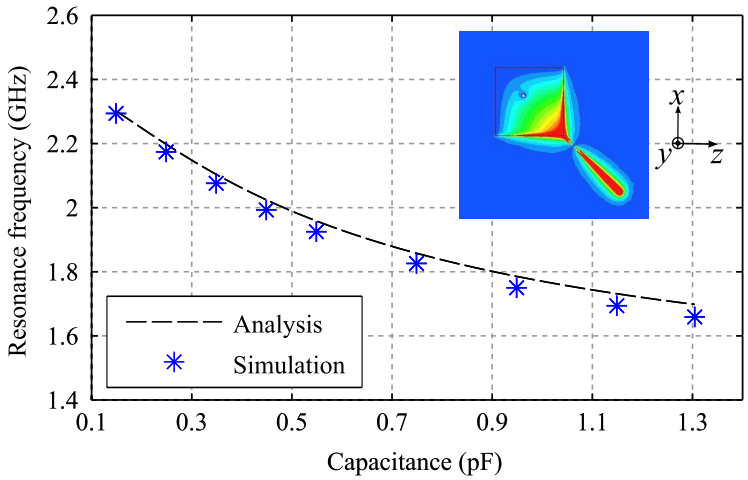

Figure 5.29. Analysed and simulated resonance frequency of a reconfigurable antenna based on a QMSIW cavity. Inset: field distribution at a resonance frequency ($f_r = 2$ GHz, obtained when $C = 0.45$ pF).

resonance frequencies are shown in Fig. 5.29 with an inset showing field distribution at a resonance frequency. Very good agreement is observed which validates the analytical model and optimisation process.

The simulated reflection coefficients for different capacitance values C of the varactors are shown in Fig. 5.30. The antenna achieves a simulated -10 dB-tuning range of $[1.65, 2.31]$ GHz with $\min(|S_{11}|) < -14$ dB across the tuning range.

It is noted that, a similar reconfigurable antenna based on QMSIW was proposed in [153]. In this design however, instead of using a loading stub, the varactor was short-circuited at one end. Furthermore, the antenna in [153] was designed based on full-wave simulation. In contrast, the design method presented in this chapter demonstrates a higher flexibility in the design and is amenable to automated optimisation because it is based on fast semi-analytical calculations (Section 5.2.2).

5.4.2 Quarter-Wave Patch Reconfigurable Antenna

The quarter-wave patch loaded with stubs has been briefly mentioned when analysing the reconfigurable microstrip patch antenna in Section 5.3. Here, the design is further developed with the stub-folded configuration for antenna miniaturisation (Fig. 5.31a)

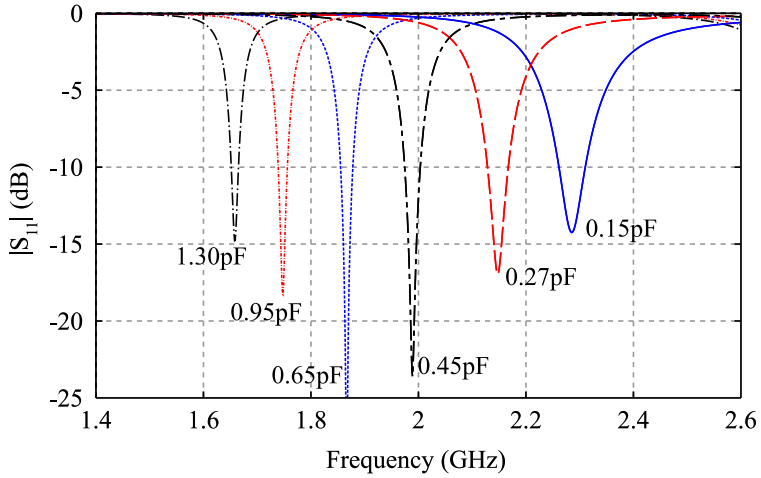

Figure 5.30. Simulated reflection coefficients of the optimised QMSIW reconfigurable antenna.

In this design, the quarter-wave patch is placed on the top substrate, while the middle metal layer is used as ground plane. One varactor is placed at the centre of the radiating aperture; it is then connected to a via that goes through the two substrates to the other side of the structure. On the bottom layer, i.e. below the ground plane, this connecting via is attached to an open-circuited microstrip stub with an effective length of l_{stub} (Fig. 5.31b). The designer is free to orientate the stub to suit any purpose. Here a folded configuration that fits entirely within the area below the quarter-wave patch on the top layer is chosen. The stub can be modeled as a bent microstrip transmission line to calculate the reactance loaded at the radiating aperture of the antenna. By electronically tuning the varactor, the reactance loaded at the open aperture is varied and the resonance frequency of the structure can be controlled. The bias circuit for the varactor follows the previous design: a large resistor is placed at the end of the stub, followed by a choke inductor and then the DC voltage connector.

The antenna is fed perpendicularly through a feeding via at position $(x, y) = (d_f, 0)$, the origin O being at the centre of the radiating aperture. In this design, a microstrip line on the bottom layer is used to feed the antenna.

The simulated reflection coefficient of an antenna optimised for operation in a band centred at around 3 GHz is shown in Fig. 5.32 for different varactor capacitances C. The chosen substrate is Rogers Duroid 5880 with relative permittivity $\epsilon_r = 2.2$ and thickness $h_s = 1.575$ mm. The antenna dimensions are $l = 18$ mm and $w = 13$ mm. The total

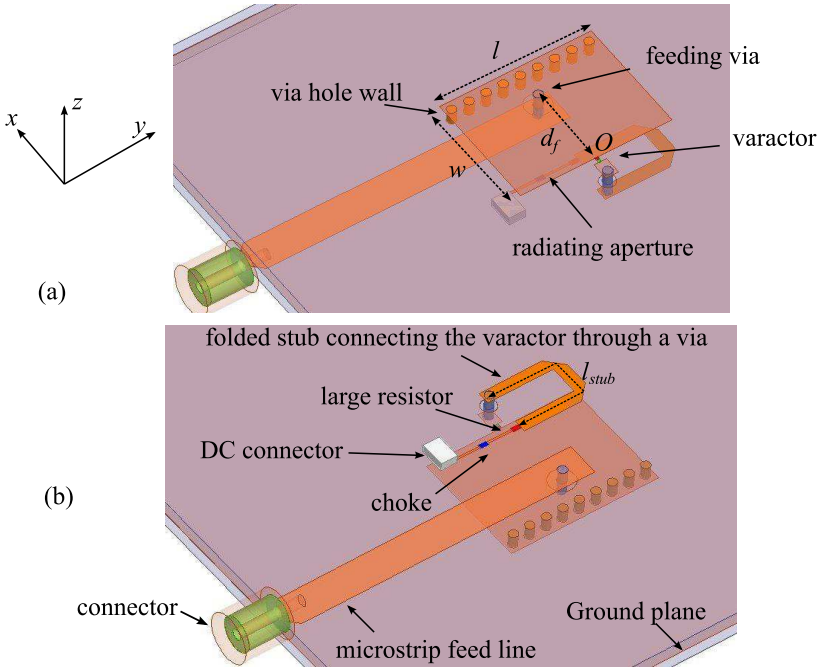

Figure 5.31. Design of a frequency-reconfigurable quarter-wave patch antenna employing folded loading stub. (a) Top view, (b) bottom view.

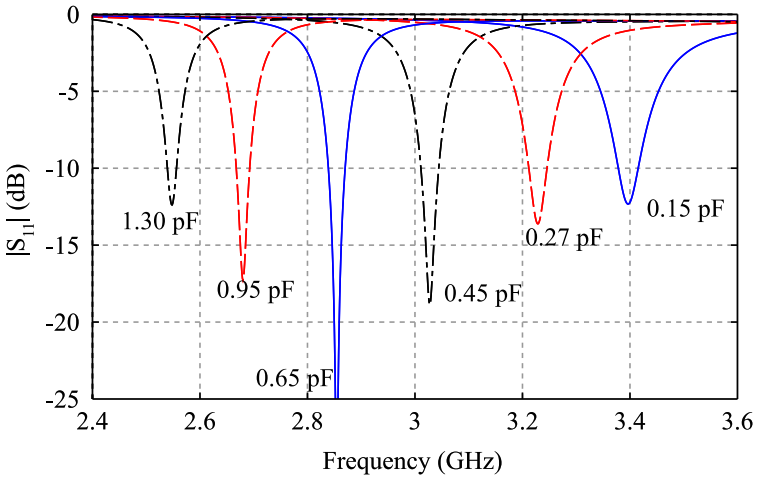

Figure 5.32. Simulated reflection coefficient of the reconfigurable quarter-wave patch antenna.

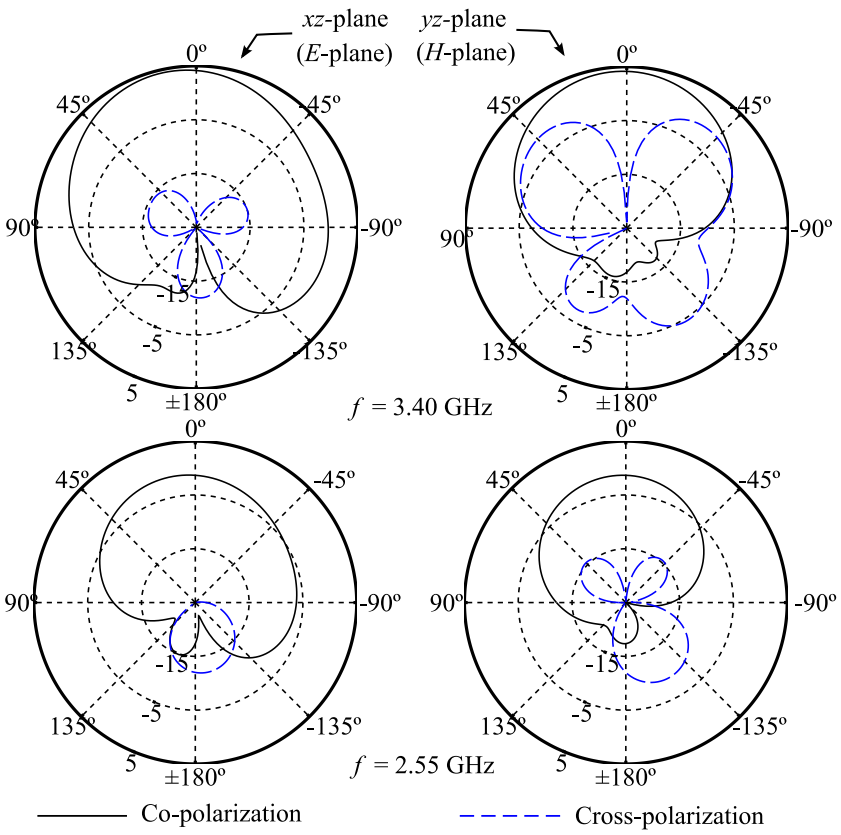

Figure 5.33. Simulated realised gain patterns of the reconfigurable quarter-wave patch antenna. Results are shown at the upper and lower frequency limit of the tuning range $f = 3.40$ GHz (top) and $f = 2.55$ GHz (bottom).

length of the stub is chosen as $l_{stub} = 21$ mm. The return loss at the resonance frequencies has been optimised to be higher than 12.3 dB across the tuning range from 2.55 GHz to 3.40 GHz, i.e. corresponding about 28% fractional tunability.

The simulated realised gain patterns of the antenna at the lower and upper limit frequency of the tuning range are shown in Fig. 5.33. The realised gain of the antenna is -1.2 dB at $f = 2.55$ GHz and increases to 4.4 dB at $f = 3.40$ GHz. The planar size of the antenna is only $0.13\lambda_0 \times 0.15\lambda_0$ where λ_0 is the free-space wavelength at the lower frequency limit of the tuning range, i.e. $f = 2.55$ GHz. It is noted that the compact antenna proposed in [116] has the size of $0.11\lambda_0 \times 0.25\lambda_0$ with the tuning range of 20% and a simulated gain of -1.8 dB at the lower frequency limit. This proposed antenna also demonstrates a very compact design with linear polarisation, whereas [116] was designed for polarisation diversity environment. The simulated antenna efficiency increases from 23% to 90% when

the resonance frequency increases from 2.55 GHz to 3.40 GHz. It is noted that for the HMSIW cavity antenna in Section 5.2, the lowest simulated efficiency was about 37%. In the presented case, since the antenna is even more compact, the lower efficiency also comes from higher conductor loss. Furthermore, since all the feeding and bias circuit structure are located on the bottom layer, it is possible to shield those components and avoid parasitic radiation from them.

Figure 5.33 shows a larger cross-polarisation level compared to the results for the HMSIW cavity antenna (Fig. 5.12). The cross-polarisation comes from two extra magnetic-current source on the two opening side walls of the quarter-wave patch (Fig. 5.16). The results in this section again demonstrates the trade-off among size, polarisation purity, and efficiency in this family of reconfigurable antennas.

5.5 Conclusion

The original contributions of this chapter is a family of reconfigurable antennas based stub-loaded substrate-integrated circuits with thorough analysis and optimisation processes. Two novel designs, including a HMSIW cavity and a microstrip patch antenna loaded with varactors and rectangular stubs have been investigated and validated with measurement results. Two other designs based on QMSIW and quarter-wave patch with folded stub for antenna miniaturisation have also been discussed as a further illustration of this versatile technique. The proposed antennas demonstrate significant improvements compared with the existing literature.

Chapter 6

Polarisation- and Frequency-Reconfigurable Cavity Antennas

THIS chapter presents a polarisation- and frequency-reconfigurable antenna inspired by the concept of equivalent magnetic-current source. The key principle is to employ an array of PIN diodes to reconfigure the length and position of an equivalent magnetic-current source formed at the circumference of a circular cavity. By doing this, the resonance frequency and field polarisation can be tuned systematically. An antenna using 24 PIN diodes clustered in groups of four has been designed together with a dedicated switching voltage network arrangement. This particular realisation of the antenna can change the linear polarisation in six different angles and at five discrete frequencies as validated through measurements of a fabricated prototype. Based on the proposed principle, quasi-continuous frequency- and polarisation-reconfiguration is feasible using individual control of a large number of switching devices.

6.1 Introduction

Compared to the varactor used in the previous chapter, RF switches such as PIN diodes and MicroElectroMechanical System (MEMS) switches have a major advantage of being controlled by fixed supply voltages. In principle, an RF switch connects or disconnects two conducting parts of an antenna structure and thus their application is opening many possible ways to design reconfigurable antennas. In [154–156], RF switches were used to connect different parts of a patch to realise polarisation- and frequency-reconfigurable antennas. The references [142, 143, 157, 158] proposed antennas that can be switched between either two linear polarisation (LP) states or two circular polarisation (CP) senses. Both LP and CP-reconfigurability were combined and demonstrated in [145–147, 159]. RF switches have also been used to design beam-steerable antennas [22, 160, 161], wideband polarisation-reconfigurable antennas [162–165], and an UWB antenna with a reconfigurable notch [166].

A common feature of all above mentioned switched antennas is that their operation is fundamentally limited to a number of discrete polarisation states and frequency bands. Although [154–156] showed designs capable of obtaining various pattern, polarisation, and frequency configurations, their adaptation generally requires long lasting optimisation using numerical simulation since there is no systematic method available to predict the antenna behaviour at each state. These difficulties in design can limit the suitability of these antennas in real-time applications.

In this chapter, the field equivalence principle is used as a main tool to derive an antenna structure that can reconfigure the operating frequency and linear polarisation angle in a quasi-continuous manner. The proposed antenna utilises the symmetry of a centre-fed circular patch with switchable shorting vias densely distributed along the edge of the patch. These shorting vias can be turned ON and OFF using PIN diodes to create a shallow cavity with an open section on its sidewall, forming a radiating aperture. The field equivalence principle is used to interpret the antenna as a variable magnetic-current source. Different antenna resonance frequencies and polarisations are obtained by changing its size and position. In this design, polarisation angle and resonance frequency resolution depend on the number of switchable vias being used on the circumference of the circular patch and this number can be chosen at design time to suit the application. For demonstration, a

simple realisation of this type of antenna will be shown here, for which the operation can be switched between six different polarisation states at five discrete frequencies (although one of the frequency states is restricted by antenna efficiency – as shown in Section 6.4.3). The findings in this chapter have been published in [167]

The chapter is structured as follows. The antenna's operational principle is described in Section 6.2, followed by a quick estimation of the resonance frequency of the structure. Section 6.3 elaborates on practical aspects of the antenna design, including biasing, matching and dimensioning. Finally, Section 6.4 shows the simulated and measured results for the frequency and polarisation reconfigurability of a fabricated prototype, and is followed by conclusions.

6.2 Antenna Principle and Resonance Frequency Estimation

6.2.1 Operational Principle

The antenna concept is illustrated in Fig. 6.1. The antenna consists of a centre-fed circular patch of radius R on a substrate with a ground plane at the bottom. A shorting wall, which is modeled as a perfect electric conductor (PEC) closes a section of the patch edge to form a cavity, while a section of the patch periphery is left open with an opening angle α. Using the field equivalence principle, it can be shown that the antenna operates as a magnetic current $\mathbf{M}$ radiating on a ground plane (Fig. 6.1a), with broadside being the maximum radiation direction. The resonance frequency of this structure depends on the size of the patch, i.e. radius R, and the size of the open aperture determined by the angle α. Furthermore, in the case depicted in Fig. 6.1a, the centre of the equivalent magnetic current $\mathbf{M}$ is at $\phi = 0°$, i.e. on the x-axis and defines the polarisation of the electric field in the far-field. Thus, it is clear that this antenna can also change its polarisation by changing the position of the open aperture.

The PEC walls can be realised by an array of shorting vias with small enough spacing (Fig. 6.1b), similarly to a substrate-integrated waveguide (SIW) [126]. The position and size of the open aperture can be varied by connecting and disconnecting these shorting

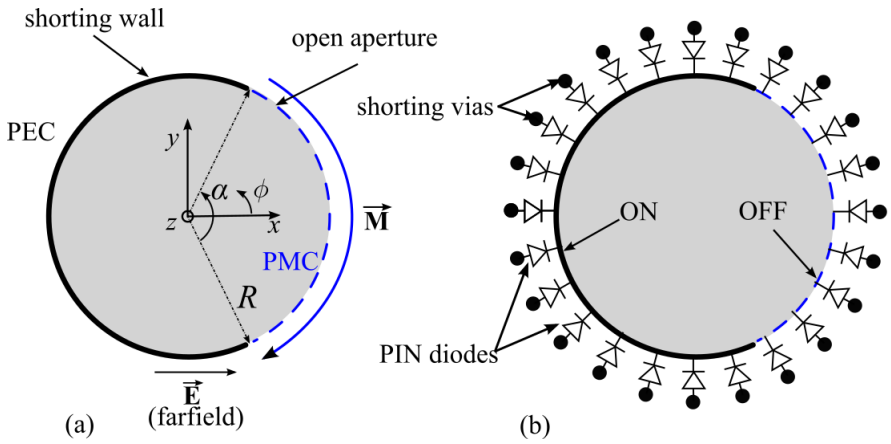

Figure 6.1. The concept of a polarisation- and frequency-reconfigurable antenna. (a) Top view of a circular cavity with shorting wall and an open side, and (b) its reconfigurable version using PIN diodes.

vias with the patch. These connections can be implemented using PIN diodes between the patch and the vias that are controlled by DC bias voltages. To realise this type of antennas, MEMS switches may also be used in the same configuration although they are not considered here in fabrication.

6.2.2 Estimation of the Cavity Resonance Frequency

When the substrate thickness is relatively small compared to the operational wavelength, the thin open aperture can be modeled approximately as a perfect magnetic conductor (PMC). Deriving the resonance frequency for this cavity involves solving Helmholtz's equation in a circular cross-section with mixed boundary conditions. This is usually not tractable analytically and requires approximations or the use of numerical techniques. Since the antenna resonance frequency will be influenced by the specific configuration and the imperfection of the tuning devices, a simple crude estimation of the resonance frequency that can be used to obtain initial design parameters in a fast manner is sought.

The consideration is based on the limiting cases. Firstly, when the opening angle α tends to zero, the structure resonates in the TM^z_{010} mode of a closed cylindrical cavity. This mode has an exact resonance frequency of

$$f_U = \lim_{\alpha \to 0} f_r(\alpha) = \frac{2.405 c_0}{2\pi R \sqrt{\epsilon_r}}, \tag{6.1}$$

where c_0 is the free-space speed of light, ϵ_r is the relative permittivity of the substrate and $f_r(\alpha)$ is the resonance frequency as a function of α. This equation yields the upper limit of the operating frequency. Secondly, the lower limit of resonance frequency is obtained when α tends to 2π, with a single shorting point on one side. At this limit, the antenna operates as a planar-inverted F-antenna (PIFA) with a quarter-wave length corresponding approximately to half of the antenna circumference plus its height [168] (an alternative empirical formula can also be found in [169]). This resonance frequency can be estimated with a reasonably good accuracy as

$$f_{\mathrm{L}} = \lim_{\alpha \to 2\pi} f_r(\alpha) = \frac{c_0}{4(\pi R + h))\sqrt{\epsilon_r}}, \tag{6.2}$$

where h is the thickness of the substrate. This formula yields the lower limit of the tuning range. For an arbitrary value of $\alpha \in (0, 2\pi)$, the resonance frequency is found empirically to be roughly decreasing exponentially from f_{U} to f_{L} when α increases linear from 0 to 2π:

$$f_r(\alpha) = f_{\mathrm{U}} e^{-k\alpha} \text{ where } k = \frac{1}{2\pi} \ln\left(\frac{f_{\mathrm{U}}}{f_{\mathrm{L}}}\right). \tag{6.3}$$

Figure 6.2 shows the simulated and estimated resonance frequencies of the structure depicted in Fig. 6.1a. The result shows that equations (6.1) and (6.2) yield accurate predictions of the limits of the tuning range whereas equation (6.3) for $f_r(\alpha)$ generally underestimates the resonance frequency in the range $\alpha \in (0, 2\pi)$.

6.3 Practical Design

As discussed in the previous section, the shorting wall on a section of the patch edge can be configured using PIN diodes and shorting vias. In order to maintain the reconfiguration symmetry of the antenna, it is fed perpendicularly from a coaxial probe at the centre of the patch. Furthermore, various aspects have to be considered at the design stage: the number of PIN diodes to be used, the bias network configuration to control these PIN diodes and the impedance matching across the tuning range. In this section, these aspects will be successively discussed followed by the presentation of a practical design of the antenna.

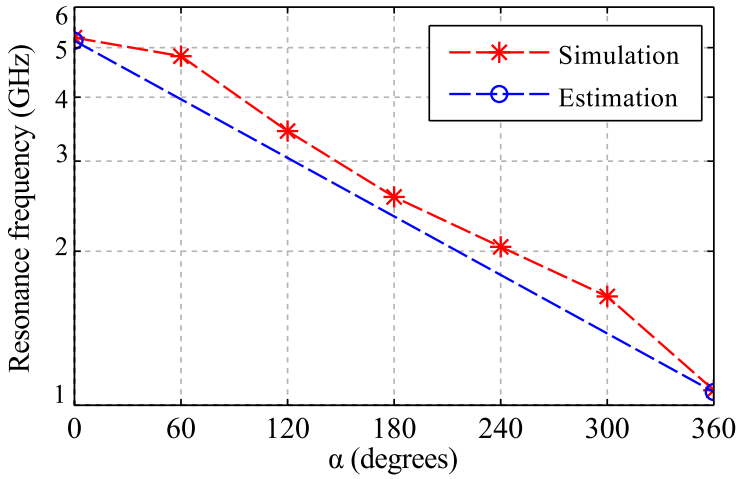

Figure 6.2. Resonance frequency of the circular cavity in Fig. 6.1a. The calculation is performed with $R = 15$ mm and $\epsilon_r = 2.2$.

6.3.1 Number of PIN Diodes

The number of PIN diodes needs to be determined based on the desired resolution of the discrete reconfigurable states and the density of vias required to form cavity walls.

Denoting N as the number of PIN diodes used in Fig. 6.1b and assuming independent control, the open angle α can take any discrete value in the form of $2\pi m/N$ where m is the number of PIN diodes that are switched OFF. This yields $N-1$ possible operating frequencies for the antenna (noting $m \neq 0$ and $m \neq N$). A continuous antenna tuning range may be achieved in principle if the -10 dB-bandwidth at different stages overlaps to cover the whole tuning range (f_L, f_U). Furthermore, the antenna can also operate with N different polarisation states $\phi = 2\pi m/N$, where $m = 0, ..., N-1$.

It is then noted that the number of PIN diodes should be large enough to effectively create an equivalent solid PEC wall along the antenna edge. This requirement may result in the number of necessary PIN diodes and shorting vias being more than required to achieve the desired resolution of reconfiguration states. Therefore, in practice, these PIN diodes may also be grouped in clusters and controlled simultaneously using modular switches. In this case, the above analysis for the state resolution still applies with N being the number of diode clusters.

To validate the concept, later in this chapter an antenna with 24 PIN diodes is demonstrated. These PIN diodes are divided into $N = 6$ clusters, each consisting of 4 adjacent

diodes, which are connected to a DC-bus strip and controlled by a single bias voltage (either 5 V or -5 V). In this configuration, the antenna can be switched between 6 different polarisation states, i.e. corresponding to $\phi = m2\pi/6$. The design is shown in Fig. 6.3.

It should be emphasised that the presented antenna design illustrates and proofs the proposed concept: The clustering of PIN diodes reduces the complexity of the bias circuit for physical implementation of switches and in-house fabrication. In practice, if each PIN diode is controlled individually by a single switch, a more sophisticated control system may be required to control a large number of switches, similarly to [155, 156].

6.3.2 Bias Network

The bias circuit diagram for each PIN diode is shown in Fig. 6.4. In order to separate the DC signal and RF signal, the bias circuit requires:

1. A DC blocking capacitor $C_b = 47$ pF being placed between the diode and shorting via,
2. An RF blocking inductor $L_b = 47$ nH being placed between the diode and DC voltage, and
3. DC grounding of the patch by placing an RF blocking inductor $L_g = 370$ nH at position $(x, y) = (R_p, 0)$ ($\phi = 0$, see Fig. 6.3), followed by a shorting via.

It is noted that L_g should be large enough to effectively realise an RF open circuit at this position of the patch. This L_g choice will maintain antenna symmetry when switching between different polarisation states.

In order to minimise the scattering effects of the bias components on the antenna performance, the bias network including DC supply voltages and switches is realised on a second substrate integrated below the ground plane. To achieve this, thin wires going through the substrate are used to connect each DC-bus strip to the switch and power supply network that is located below the ground plane.

The implementation of the bias circuit is shown in Fig. 6.4. A more flexible control on the polarisation and resonance frequency is in principle possible by controlling each PIN

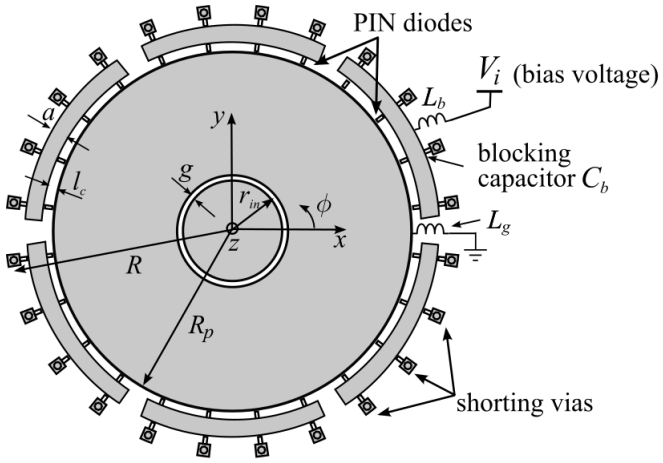

Figure 6.3. A practical design of the proposed antenna. 24 PIN diodes are divided into 6 groups, each of which is controlled by a DC bias voltage (see Section 6.3.1 and 6.3.2).

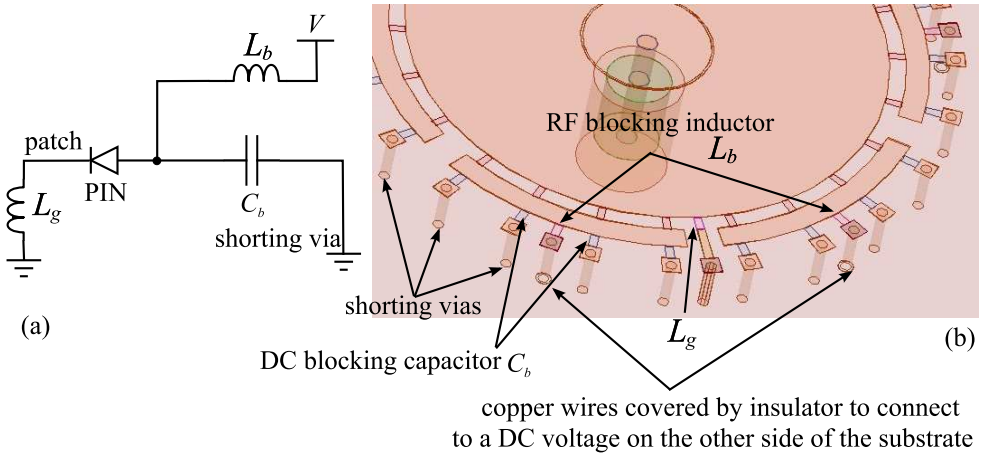

Figure 6.4. Bias circuit implementation. (a) The design of bias circuit of the PIN diodes and (b) its implementation in HFSS simulation.

diode independently. In this case, the bias network will have a similar set up but it will require additional bias components.

6.3.3 Impedance Matching

For impedance matching, a capacitive concentric ring is utilised in the centre of the circular patch (Fig. 6.3). This technique has been used for the monopolar antennas proposed

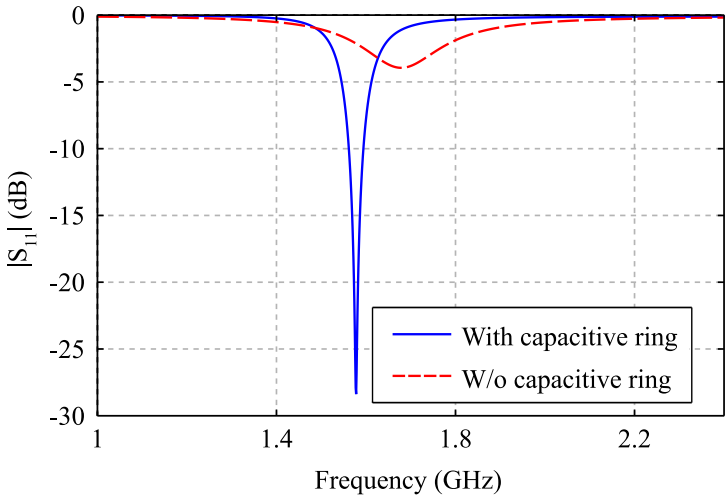

Figure 6.5. Reflection coefficient of the antenna with and without capacitive ring. Results are shown for the case $\alpha = 180°$

in Chapter 4. Two parameters g and r_{in} are carefully optimised using Ansys HFSS to obtain satisfactory matching across the tuning range. It is noted that r_{in} can be chosen in a wide range while g is optimised strictly to provide a correct amount of capacitance to broadly compensate the inductance of the feeding probe in the various states of the cavity. Figure 6.5 shows the simulated reflection coefficient of the antenna with and without the optimised capacitive ring for $\alpha = 180°$.

6.3.4 Antenna Design

Based on the above discussion, an antenna design has been developed and simulated using Ansys HFSS. The PIN diodes used in this design are of type MADP-042305-13060 (MACOM Technical Solutions) with reverse bias capacitance of 0.15 pF and forward bias resistance of 1.3 Ω [170]. The selected substrate is Rogers Duroid 5880 with thickness $h = 3.17$ mm, relative permittivity $\epsilon_r = 2.2$ and loss tangent $\tan\delta = 0.0009$. A single PIN diode is modeled as a lumped capacitor with $C_{PIN} = 0.15$ pF in OFF state, or as a lumped resistor with $R_{PIN} = 1.3\ \Omega$ in ON state. The cavity is chosen without impinging on the generic applicability of this design in such a way that the lowest resonance frequency is 1 GHz. The optimised antenna parameters are $r_{in} = 4$ mm, $g = 0.13$ mm, $R = 19.1$ mm, $a = 1.5$ mm, $R_p = 15$ mm and $l_c = 1$ mm (see Fig. 6.3).

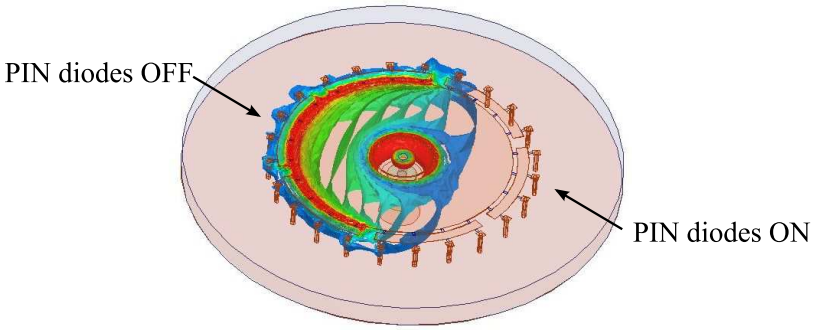

Figure 6.6. Simulated electric field distribution. Results are show for the case $\alpha = 180°$

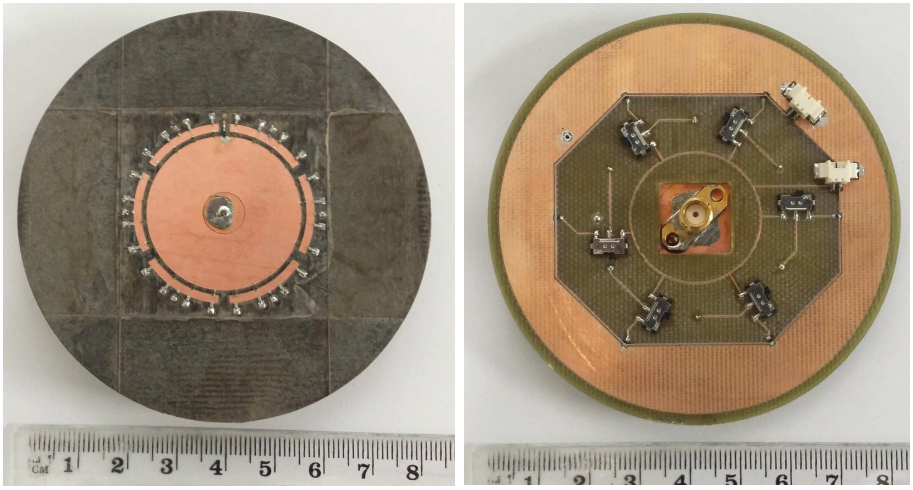

Figure 6.7. Photographs of the top and bottom layers of the antennas. The ground plane is in the middle of the two substrate layers. Rogers Duroid 5880 is used for the antenna while the bias network is implemented in FR4.

Figure 6.6 shows the electric field distribution in a particular state of the antenna. As expected, the electric field is close to zero near the shorting wall, while it reaches its maximum at the open aperture. This electric field distribution is similar to a half-mode substrate-integrated waveguide cavity discussed in Chapter 5. By switching ON and OFF the appropriate PIN diodes, the polarisation and resonance frequency of the antenna can be varied. Figure 6.7 shows photographs of the top and bottom view of the fabricated antenna prototype.

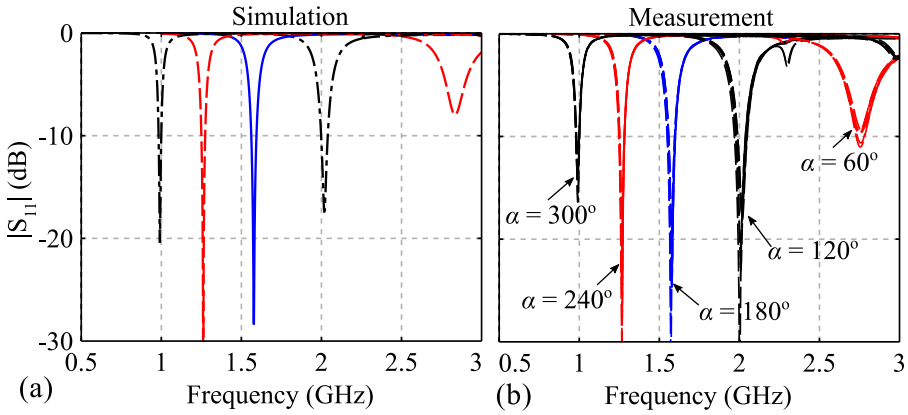

Figure 6.8. Reflection coefficient of the antenna for different value of open angle α. (a) simulation; (b) measurement. The measurement results are shown with 6 different polarisation states simultaneously as overlapped curves.

6.4 Simulation and Measurement Results

6.4.1 Frequency Reconfigurability

Figure 6.8 shows the simulated (left) and measured (right) reflection coefficients of the fabricated antenna at five different resonant states $\alpha = 2\pi m/6$ $(m = 1,..,5)$. Six different polarisation states ($\phi = 2\pi m/6$ where $m = 0,...,5$) are simultaneously plotted in Fig. 6.8b as overlapped curves. We observe firstly that there is a very good correspondence between the simulations and measurements. Secondly, the overlapped curves are nearly indistinguishable, indicating that the resonance frequency does not change when the polarisation states change. These results verify that the RF blocking inductor L_g for grounding the patch (see Fig. 6.3) does not noticeably affect the symmetry of the antenna.

The results show that the antenna can be switched between five different frequencies. However, when $\alpha = 300^\circ$ ($f = 1.00$ GHz), the antenna has very low efficiency that limits the practical use of this state, as will be discussed in the next section. It is emphasised here again that more frequency states can be obtained if each diode is controlled independently, in which case the difference between two adjacent resonance frequencies Δf decreases. A sufficient number of independently controlled PIN diodes may lead to a continuous -10 dB-bandwidth tuning range. Additionally, if required, a wider bandwidth of a single frequency state can be increased by increasing the antenna thickness.

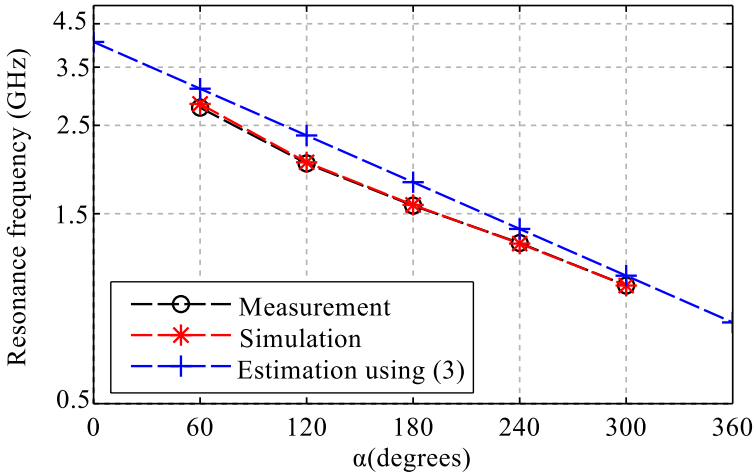

Figure 6.9. Resonance frequency for different open angle α. α is defined in Fig. 6.1a.

Figure 6.9 shows the simulated and measured resonance frequencies in different states together with the corresponding estimated values from equation (6.3). The overestimation of the resonance frequency is attributed firstly to the non-zero spacings between shorting vias which slightly increases the open angle α in the realisation. Secondly, it comes from the imperfection of the PIN diodes when switched OFF, with a capacitance of $C = 0.15$ pF which is close but not equal to an open-circuit at RF. This capacitance increases the effective size of the patch. Overall, the proposed estimation equations can be used to obtain initial design parameters, which can be tuned for a given PIN diode capacitance through full-wave simulations.

The normalised radiation patterns at 4 different resonance frequencies $f = 1.26, 1.57, 2.00$ and 2.76 GHz, corresponding to $\alpha = 240^\circ, 180^\circ, 120^\circ$ and 60°, respectively, are shown in Fig. 6.10. All patterns are plotted at the polarisation state of $\phi = 0^\circ$. Reasonably good agreement is obtained between the simulation and measurement results for all patterns. The higher cross polarisation in the measured E-plane patterns are attributed to scattering effects of the connecting wires at the back of the antenna and the imperfection of our anechoic chamber for these relatively low frequency measurements. These scattering effects also cause a distortion in the co-polarisation at low frequency, i.e. $f = 1.26$ GHz.

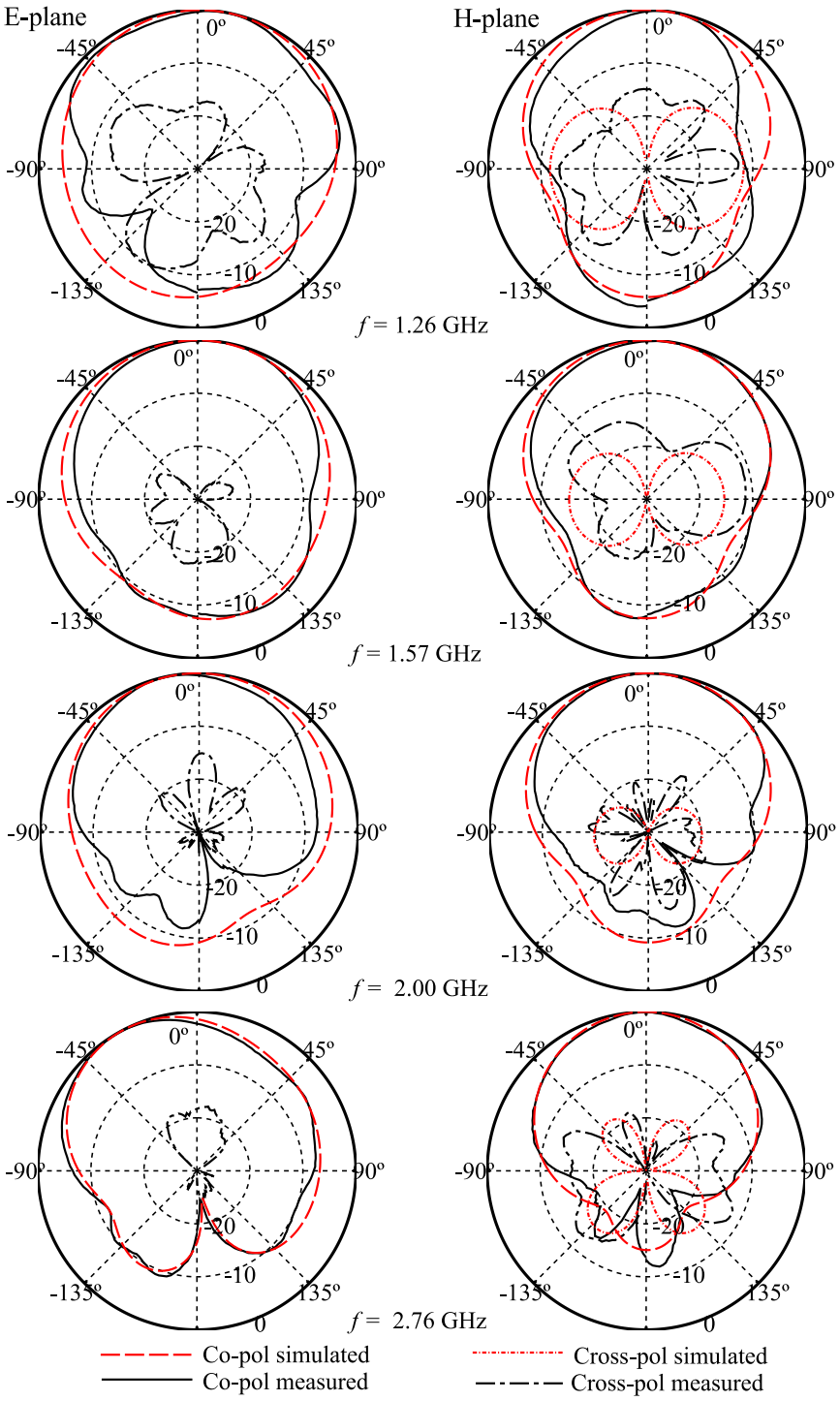

Figure 6.10. Radiation pattern results. Simulated and measured normalised radiation patterns at different resonance frequencies for different open angle $\alpha = 240°, 180°$ and $120°$ (from top to bottom). The simulated cross-polarisations in E-plane is well below -30 dB and are not visualised in the plots.

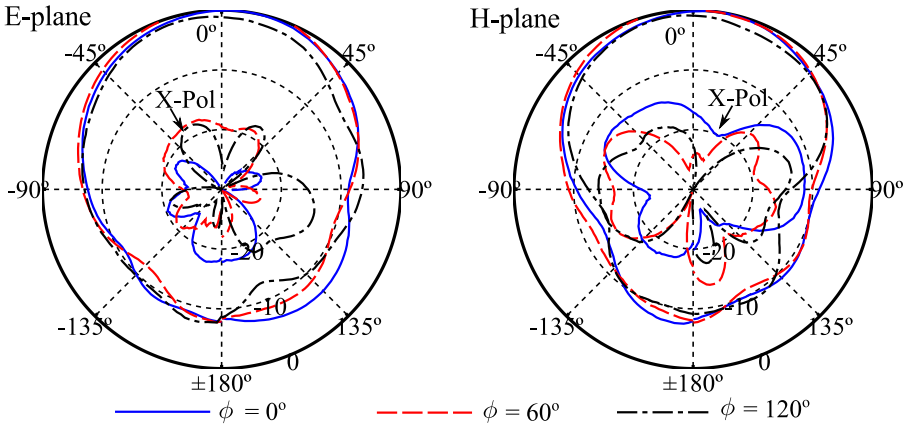

Figure 6.11. Polarisation reconfigurability results. Measured radiation patterns at $f = 1.57$ GHz ($\alpha = 240°$) at different polarisation states $\phi_P = 0°, \phi_P = 60°$ and $\phi_P = 120°$. The patterns are normalised to state $\phi_P = 120°$.

6.4.2 Polarisation Reconfigurability

Since this antenna is symmetrical, it is expected that the polarisation can be switched by changing the position of the conducting cavity wall without affecting its radiation pattern. Fig. 6.11 shows measured radiation patterns at 3 different polarisation states $\phi = 0°, \phi = 60°$ and $\phi = 120°$ for the case of resonance frequency $f = 1.57$ GHz, i.e. $\alpha = 180°$. The E-plane and H-plane are adjusted according to the polarisation state. It can be observed that the radiation patterns remain stable, within measurement uncertainty, when changing the linear polarisation direction. These patterns show antenna reconfigurability between various polarisation states.

6.4.3 Antenna Gain and Efficiency

The measured and simulated antenna realised gains (in dBi) at four resonance frequencies, corresponding to $\alpha = 240°, 180°, 120°$ and $60°$, are shown in Fig. 6.12a. The measurement results are in a reasonable agreement with the numerical simulation, with discrepancies within 1 dB. The simulated antenna efficiency is also shown at these states. It can be observed that the antenna has better than 50% efficiency when $f \geq 1.57$ GHz (or $\alpha \leq 180°$). The gain and efficiency for the antenna at $f = 1.00$ GHz (when $\alpha = 300°$) are only about

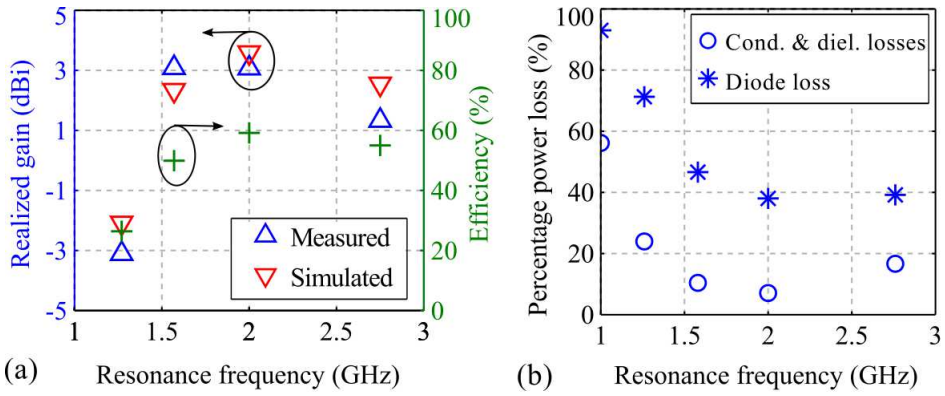

Figure 6.12. Gain and efficiency study. (a) Antenna realised gain (dBi) and simulated radiation efficiency.(b) Simulated percentage power loss for two cases: due to conductor and dielectric losses only, and due to loss from PIN diodes only.

-9 dB and 6%, respectively. These results restrict practical application of this state and are not included in Fig. 6.12a.

To comprehensively understand the source of losses in this type of antenna, we simulated power losses in two cases: (1) due to conductor and dielectric losses only ($R_{PIN} = 0$), and (2) due to loss from PIN diodes only (PEC and perfect dielectric). From the results in Fig. 6.12b, it is found that the degradation of efficiency comes mostly from the internal resistance of PIN diodes. As α increases, the resonance frequency decreases and there is larger current flowing through the PIN diodes, which decreases the antenna efficiency. At the other extreme, when α decreases, the resonance frequency increases and the radiating aperture decreases resulting in slightly lower antenna efficiency caused by higher conductor and dielectric loss in the cavity.

6.5 Conclusion

The operational principle and design of a polarisation- and frequency-reconfigurable antenna have been presented in this chapter. The key concept is to vary the position and length of the equivalent magnetic-current source. This type of antenna can be designed to switch its operating frequency and polarisation across a wide range of discrete values. The switching resolution increases with the number N of the switchable shorting vias used, but this number can be chosen at the design stage to satisfy the antenna's specifications.

For demonstration, an antenna that can be reconfigured to operate in six different polarisation states at five discrete frequencies has been fabricated and experimentally validated. Although the efficiency is a limitation for this type of antenna at the lower switchable frequencies, this limitation has been identified to be due mostly to the internal resistance of the tuning devices and can be further improved in the future.

Chapter 7

Reconfigurable Monopolar Antennas

TWO reconfigurable designs of low-profile monopolar antennas are proposed in this chapter. First, a reconfigurable antenna with independent control of two separate frequency tuning ranges is presented. The structure is based on the dual-band low-profile monopolar antenna shown in Chapter 4. The second design exploits the monopolar mode in addition to the conventional patch mode of a microstrip antenna to design a pattern- and frequency-reconfigurable antenna. In this design, the loading-stub technique proposed in Chapter 5 is utilised as tuning mechanism.

7.1 Introduction

As discussed in Chapter 4, the low-profile monopolar antennas have been investigated extensively due to their omnidirectional radiation patterns with vertical polarisation and compact configuration. For wideband design, further lowering the antenna height is extremely challenging as seen from many attempts in the literature listed in Table 4.1. By adding symmetrical radiating slots, a dual-band radiator can be designed (as presented in Section 4.3) with a significant reduction in the antenna height while maintaining the omnidirectional radiation patterns. Nevertheless, the bandwidth of each band becomes narrow and is still limited by the antenna height. With the aim of covering a wider frequency range, the first main part of this chapter proposes a reconfigurable design based on this structure. The antenna achieves two wide frequency tuning ranges with an even higher reduction in the antenna profile. Importantly, each frequency range can be tuned independently from each other.

Typically, low-profile monopolar antennas are designed with several shorting rods (or wires, conducting vias) at the edges of a patch, such as in [92–96, 98] or demonstrated in Chapter 4 (published in [99]). This configuration guarantees that the antennas are symmetrical and the radiation patterns are omnidirectional in the H-plane. However, as shown in the early literature [85–87], the monopolar mode can be excited with shorting wires or vias placed inside the patch cavity at the cost of slightly disturbed omnidirectional patterns. It is noticed that if these vias are placed along the symmetry line of the patch, they do not affect the conventional microstrip patch mode which radiates towards broadside. Based on this principle, Lee *et al.* [171] proposed a low-profile dual-band antenna with omnidirectional pattern at one band and broadside pattern at the other. The second main part of this chapter further develops this principle to design a frequency- and pattern-reconfigurable antenna. In this design, the resonance frequencies of two bands are tuned at the same time. As a result, there exists an overlapping frequency range where the antenna can switch its radiation pattern. The findings have been published in [111, 172].

7.2 Dual-band Reconfigurable Monopolar Antenna

As a matter of fact, dual-band reconfigurable antennas have been proposed previously in the literature. However, they have been designed to target different applications with

broadside radiation patterns [173–175], tunable polarisation [176] or for mobile phone in which radiation patterns can be largely frequency-dependent with unspecified polarisation [177–181]. Anagnostou *et al.* [182] proposed a reconfigurable antenna that can be switched among multi-band and single-band operations at different discrete frequencies. Recently, Kang *et al.* [183] designed a dual-band antenna with frequency-reconfigurability at a single band while the resonance frequency at the other band remains fixed using miniaturised substrate-integrated waveguide. Li *et al.* [184] demonstrated a dual-band design with different patterns at each band that can be switched ON or OFF but does not allow frequency tunability. For monopolar antennas, reconfigurable designs have only been proposed in [123] with only a single band tunability reported.

As demonstrated in Section 4.3, for monopolar antennas, dual-band operation can be achieved by the addition of radiating symmetrical slots. The parameter study in Fig. 4.21 indicates that the resonance frequency can be varied independently by changing the corresponding size of the radiation source (antenna edges or slots) when the slots' positions are fixed. This suggests that the resonance frequency at each band can be controlled independently with two separate sets of voltage-controlled tuning devices, e.g. varactors, applied at the source of radiation. In this section, the antenna tuning principle are explained and followed by a description of the bias circuit design and the experimental results.

7.2.1 Design and Operational Principle

The antenna structure first follows the dual-band design shown in Section 4.3 and Fig. 4.18. At this stage, the objective is to provide a tuning mechanism for each frequency band, which is discussed and shown as follows.

First, it is noted that in [123], the frequency of a low-profile monopolar antenna was varied using varactors loaded with symmetrical patch sectors distributed along the edge of the patch. These patch sectors were left open-circuited at their other end, similar to the rectangular-stub configuration proposed in Chapter 5. For the present design, since shorting rods are placed at the edges of the patch, the frequency-tunability is achieved by using varactors to connect the patch with these rods (Fig. 7.1–varactors C_1). The physical principle is to use varactors shorted at one end to vary the reactance loaded at the edges of

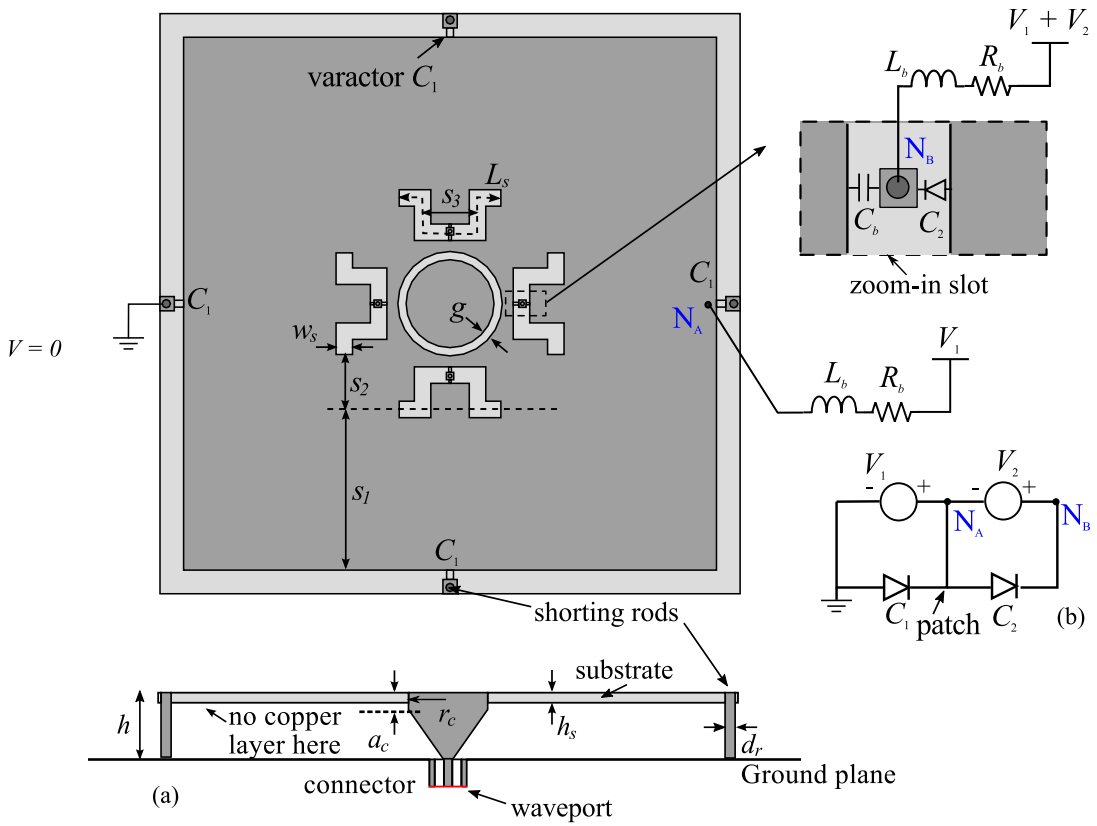

Figure 7.1. Design of the frequency-reconfigurable dual-band monopolar antenna. (a) Top view and side view of the antenna. Parameters are consistent with Fig. 4.18. Darker shaded areas are conductor while lighter shaded areas are the substrate. At nodes N_A and N_B, wires that go through the ground plane are used for connection to the bias circuit network located on the back side of the ground plane. (b) Diagram to connect the voltages for biasing the varactors (other components are ignored).

the patch. This variation of the reactance in turn changes the resonance frequency of the patch, and therefore alters the operation frequency f_1 in the lower band of the antenna.

For the upper band, the radiation originates from the symmetrical slots, thus, a technique aiming at tuning the resonance frequency of a slot can be applied [173, 174, 183]. Varactors are placed in the centre of the slots, with connections to the two slot sides (Fig. 7.1–Varactor C_2). Using a transmission line model for the slot, it can be shown that the resonance frequency of each slot, and thus the upper operation frequency f_2 of the antenna, can be varied with the capacitance of the loading varactor.

Although the resonance frequencies change with varying varactor capacitances, the radiating sources at resonances, i.e. the patch circumference apertures and the slots, do not change. Therefore, omnidirectional radiation patterns with vertical polarisation are maintained across both frequency tuning ranges.

7.2.2 Bias Circuit

In order to tune these two sets of varactors, a bias network that isolates DC and RF signals is necessary. For the case of C_1 that controls the lower resonance frequency f_1, the varactor connects the patch to the shorting rods which are soldered to the ground. Hence, there is no need for an extra capacitor to isolate the RF and DC signal. For the C_2, which controls the upper resonance frequency f_2, the varactors across the slots connects two sides of the same patch. Therefore, a blocking capacitor $C_b = 47$ pF is required to isolate the RF and DC signal (Fig. 7.1–zoom-in at a slot). To isolate RF currents from flowing into the bias circuit, a choke inductor $L_b = 330$ nH and blocking resistor $R_b = 1$ MΩ are used before connection to the DC bias voltages.

At this stage, three different DC voltage levels, including a DC ground, at different terminals of the varactors are required. These voltages are shown in Fig. 7.1: $V = 0$ V at the shorting rods that connects to the ground, V_1 at the patch (node N_A) and $V_1 + V_2$ at the copper pads located within the slots, i.e. the second terminal of varactor C_2 (node N_B). In this configuration, the varactors C_1 and C_2 are controlled independently by V_1 and V_2, respectively (Fig. 7.1b). The voltages V_1 and V_2 are provided at the back of the ground plane to minimise their effects on the antenna radiation.

7.2.3 Measurement Results

Based on the proposed design principle, a reconfigurable dual-band antenna has been optimised and fabricated targeting two frequency tuning ranges centred at about 0.9 GHz and 1.7 GHz. The optimised antenna parameters are shown in Table 7.1. Two sets of varactors are used, namely with type BB439 E6327 (Infineon Technology) and MA46H120 (MACOM Technical Solutions) with capacitance in range of $C_1 \in [5, 52]$ pF and $C_2 \in [0.15, 1.30]$ pF, respectively. The internal resistance of these varactors are

Table 7.1. Parameters of the frequency-reconfigurable dual-band antenna

Par.	Value (mm)	Par.	Value (mm)	Par.	Value (mm)
L	97	h	8	h_s	1.575
r_c	8	a_c	1.65	g	1.5
w_s	3	s_1	28.25	s_2	10
s_3	10	L_s	31	d_r	1.5

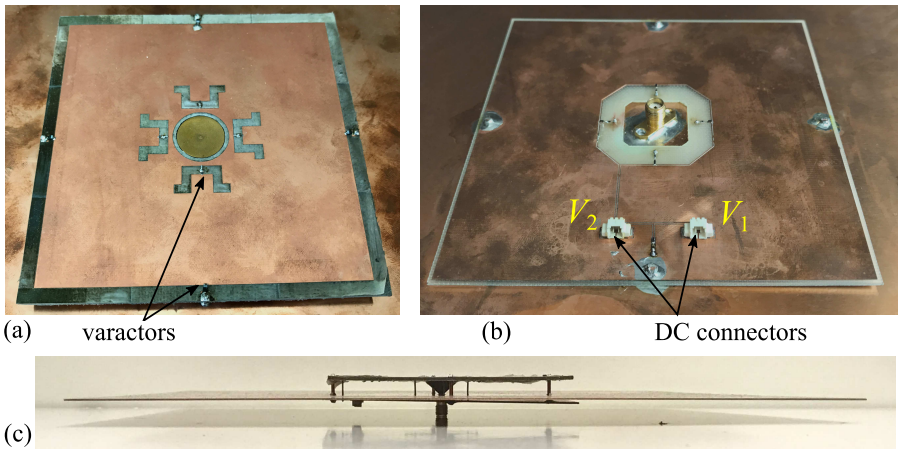

Figure 7.2. Photograph of the fabricated frequency-reconfigurable dual-band monopolar antenna. (a) top view; (b) bottom view with bias network (c) side view.

$R_1 = 0.4\,\Omega$ (estimated from datasheet) and $R_2 = 2\,\Omega$ (see Section 5.2.2). The antenna thickness $h = 8$ mm $= 0.021\lambda_{\text{min}}$ is chosen, where λ_{min} is the free-space wavelength at the minimum operating frequency $f_{\text{min}} = 0.76$ GHz. The ground plane size is kept as $280\times$ 280 mm^2. A photograph of the fabricated antenna with bias network is shown in Fig. 7.2.

Frequency Tuning Range

The simulated and measured reflection coefficients for different combinations of bias voltages (V_1, V_2) are shown in Figs. 7.3 and 7.4. In Fig. 7.3, the voltage V_1 is fixed at 0 V ($C_1 = 52$ pF) while V_2 is varied to tune the upper band resonance frequency f_2. In contrast, the lower band resonance frequency f_1 is tuned by varying V_1 and fixing V_2 (Fig. 7.4). Reasonable agreements between the simulation and measurement are obtained. Small shifts in the resonance frequencies are identified to come from the variation in the components'

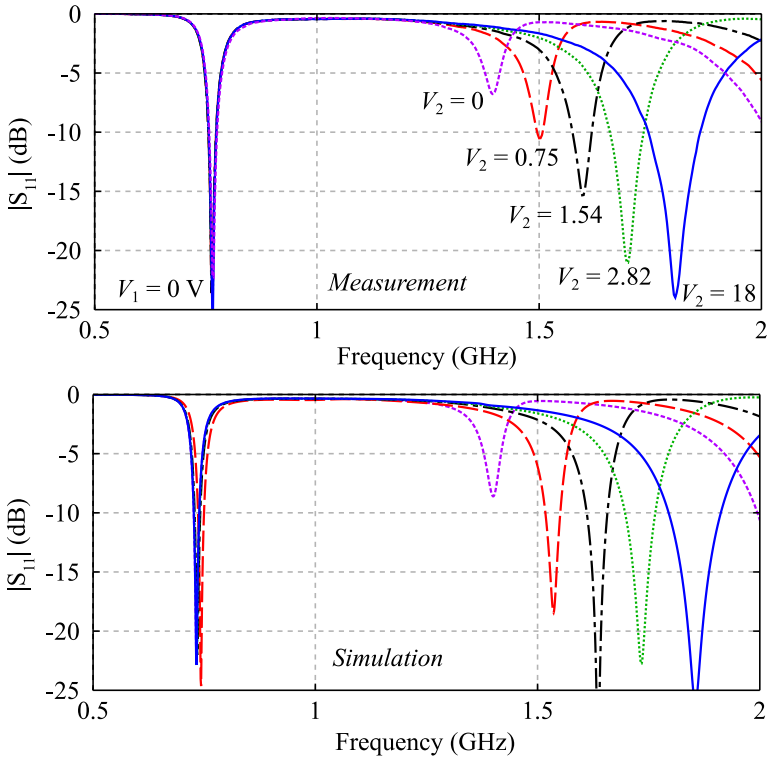

Figure 7.3. Reflection coefficients of the antenna for fixed V_1 and varying V_2. Measured results are shown at top and and simulated results are shown at bottom. The unit for the voltages is volts.

values, especially the parasitic inductance of the varactors, and the effect from the bias circuit, which can slightly change the impedance loaded at the antenna edges and the slots. Figures 7.3 and 7.4 confirm that the radiation of each band does not depend on each other and each resonance frequency can be tuned independently without affecting the other. The measured -10-dB frequency tuning ranges are $f_1 \in [0.76, 1.04]$ GHz, i.e. 31%, and $f_2 \in [1.50, 1.87]$ GHz, i.e. 22%.

Radiation Patterns

The normalised radiation patterns at different frequencies in the two tuning ranges are shown in Fig. 7.5. Very good agreement between simulation and measurement results is obtained for the co-polarisations. The antenna exhibits stable monopole-like radiation pattern with vertical polarisations at both frequency bands. The simulated cross-polarisation in E-plane is very small and not visible in these plots. The measured cross-polarisation

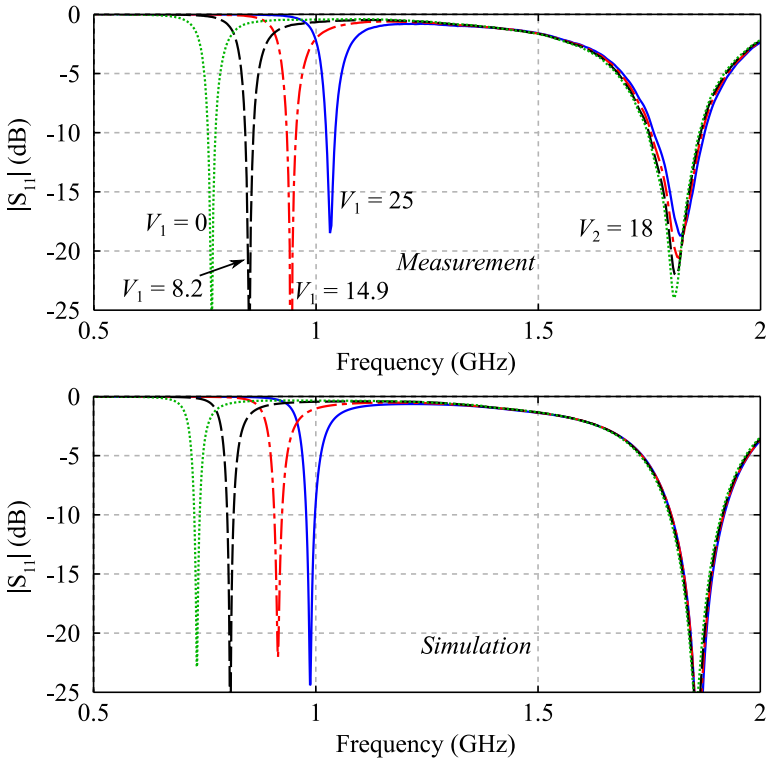

Figure 7.4. Reflection coefficients of the antenna for fixed V_2 and varying V_1. Measured results are shown at top and and simulated results are shown at bottom. The unit for the voltages is volts.

is larger but this result is mostly attributed to the imperfection of our anechoic chamber, which does not effectively absorb the cross-polarisations in the E-plane measurement at the low frequencies (due to inherent low-frequency limitations). This is confirmed by measurements in the H-plane where simulation and measurement results of cross-polarisations agree very well with each other, showing almost no cross-polarisation at $\phi = 0^\circ$ and 90°.

Antenna Gain and Efficiency

The simulated and measured antenna realised gain for both frequency bands are shown in Fig. 7.6. For the upper band, the antenna realised gain increases from 4 to 5.5 dBi when the resonance frequency is increased from 1.50 GHz to 1.87 GHz. For the lower band, the realised gain varies from -0.7 to 3.5 dBi when tuning the resonance frequency from 0.76 GHz to 1.04 GHz. At higher frequencies, the ground plane becomes effectively

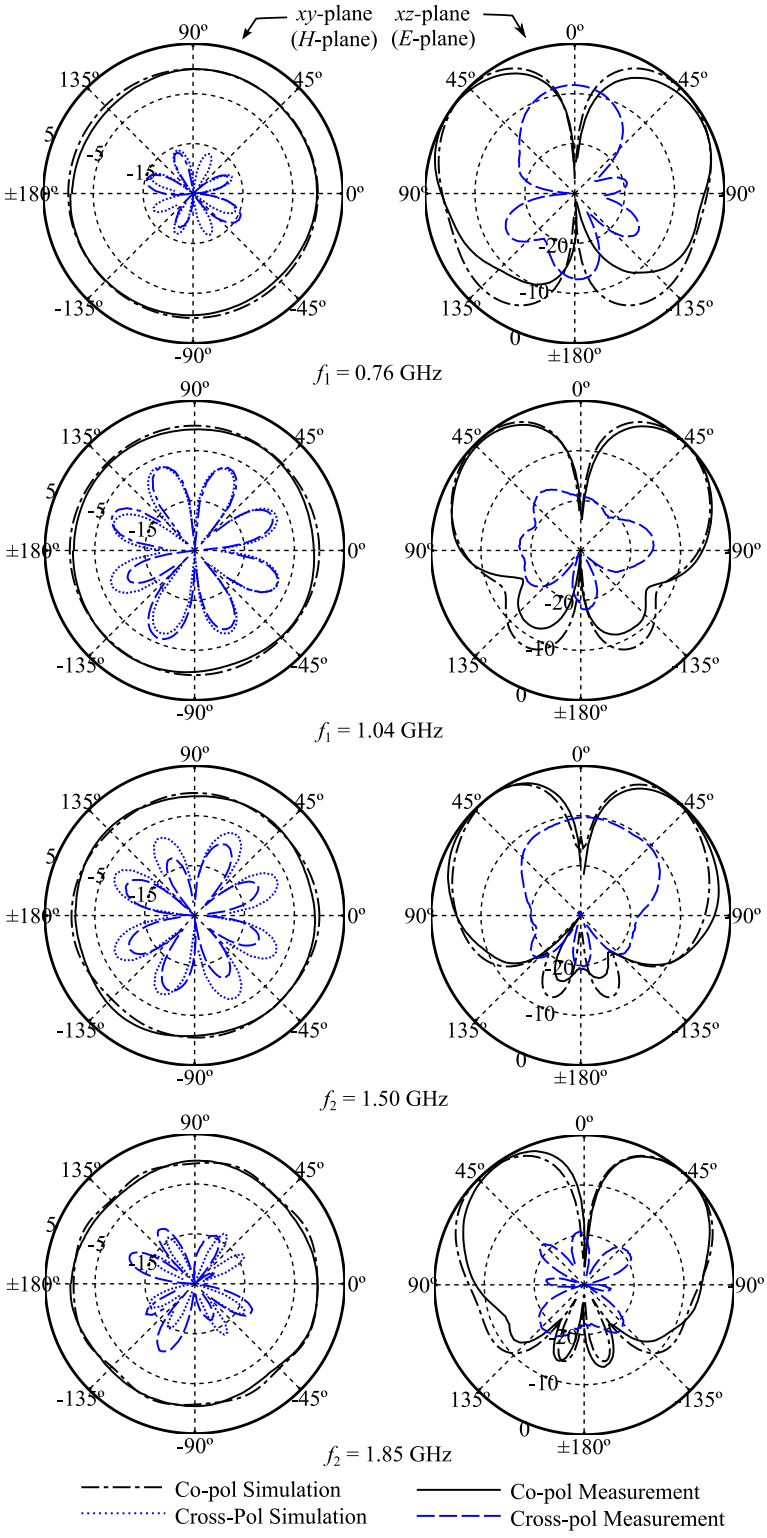

Figure 7.5. Radiation pattern results. Normalised radiation patterns of the reconfigurable dual-band antenna at different resonance frequencies across the tuning ranges.

larger, and thus the antenna pattern becomes more conical to the upper plane ($\theta > 0°$) and higher gain is obtained. At lower frequency, the antenna pattern resembles more that of an electric dipole (Fig. 7.5 for $f = 0.76$ GHz), and thus a lower gain is not unexpected. Furthermore, the higher variation in the measured antenna gain at the lower band is due to the imperfection of the anechoic chamber at lower frequency, which causes multiple path losses. This phenomenon was also observed in gain measurement of a wideband antenna (see Fig. 4.12).

The simulated antenna efficiency is also shown in Fig. 7.6. The antenna efficiency is above 60% in both frequency tuning ranges and generally increases with increasing frequency. For the dual-band antenna without reconfigurabilities (shown in Section 4.3), the antenna efficiency is almost 100% in both frequency bands. Therefore, lower antenna efficiency is mostly due to the internal resistances of the varactors. This detrimental effect is more severe at lower frequency in each tuning range due to the higher current flowing through the varactors. This lowering of antenna efficiency is expected and has been previously reported in numerous papers on frequency-reconfigurable antennas [105, 123, 175, 181]. The 100% antenna efficiency at 1.85 GHz is expected since at this stage, the capacitance reaches down to $C_2 = 0.15$ pF which is almost an open circuit and therefore almost no current flows through these varactors. Based on the measured and simulated gain results from Fig. 7.6, the practical antenna efficiency is estimated to be from 50% to 80% for the lower band and 55% to 100% for the upper band. Finally, various measurements, which are not shown here for brevity, also confirm that the antenna efficiency values at both bands are independent of each other

7.2.4 Summary of Reconfigurable Dual-Band Monopolar Antenna

In this section, the dual-band low-profile monopolar antenna proposed in Chapter 4 has been further developed with reconfigurability added to cover a larger operating frequency range. Two sets of varactor diodes were used to independently control the resonance frequencies of two bands. Measurement results show that the reconfigurable antenna achieves independent -10-dB-tuning ranges of 31% and 22% centred at about 0.9 GHz and 1.7 GHz, respectively. Stable omnidirectional patterns and vertical polarisation were achieved across both tuning ranges.

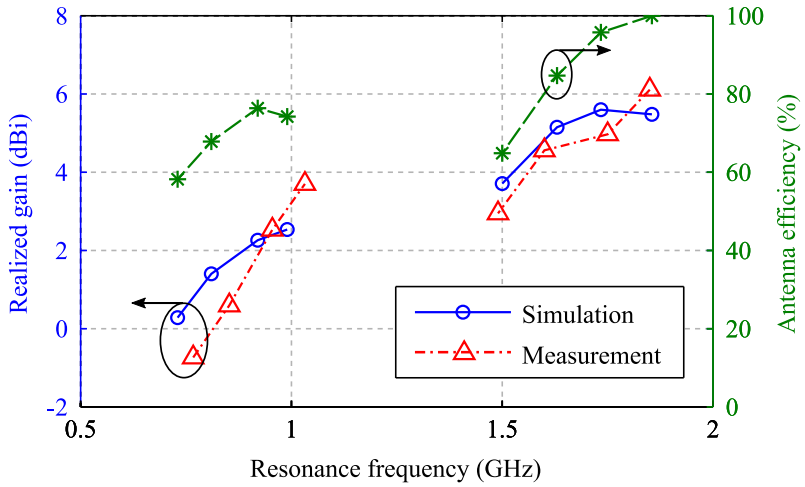

Figure 7.6. Realised gain and efficiency of the fabricated antenna across the two tuning ranges.

7.3 Frequency- and Pattern-Reconfigurable Antenna

This section proposes an antenna that can be reconfigured to operate with either broadside or monopole-like (null at broadside) radiation pattern in a relative continuous range of tuning frequency of more than 20%. Noteworthy is that only one DC bias voltage is required to control six varactors, divided into two groups to create the antenna tuning structure.

The section starts by explaining the antenna design and operational principle. Then a semi-analytical process for optimising the tuning frequency-range is presented. Finally, measurement results for various configurations are demonstrated as validation for the proposed antenna design concept.

7.3.1 Antenna Design and Operational Principle

Initially, the antenna consists of a square microstrip patch with a row of shorting via at its centre (Fig. 7.7a). This radiating structure is fed perpendicularly using a coaxial connector at position $(x, y) = (d_f, 0)$, the origin O being defined at the centre of the patch. By adding these shorting vias, two resonant modes at two distinct resonance frequencies can be excited simultaneously (Fig. 7.7b) [171]. At the regular TM^z_{100} mode resonance, the antenna radiates exactly as a conventional microstrip antenna with a broadside radiation

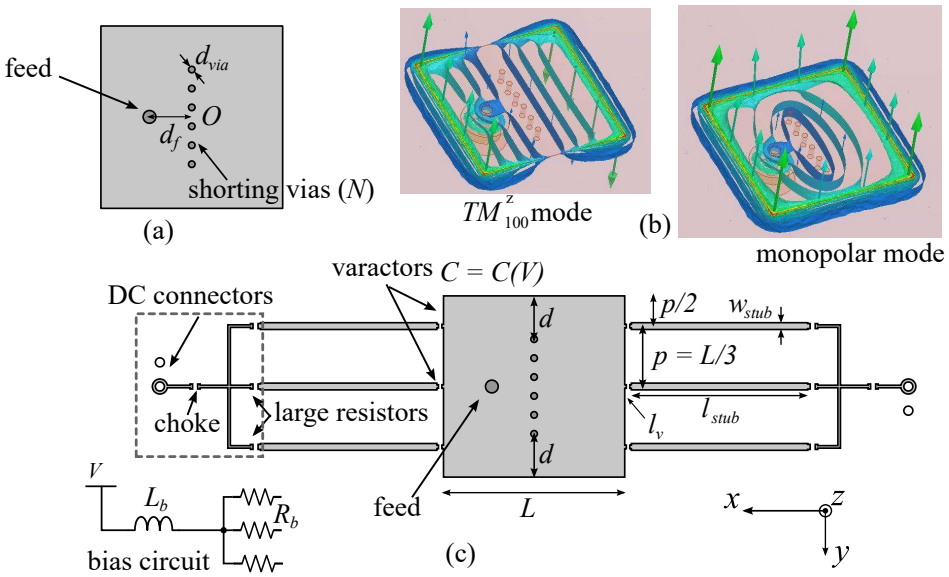

Figure 7.7. Antenna design and two resonant modes. (a) A patch antenna with N shorting vias at its centre and (b) simulated field distribution at the two first resonant modes. (c) A fully functional frequency- & pattern-reconfigurable patch antenna. The stubs are distributed evenly (with distance $p = L/3$) along two sides of the patch. The DC bias circuit for the varactors follows what presented in Chapter 5.

pattern. Because of the presence of the shorting vias at the centre line of the patch, the antenna also resonates in the monopolar mode. As discussed in Chapter 4, by using the field equivalence principle, the structure can be shown to be equivalent to a magnetic-current loop. Since these shorting vias are not symmetrical around the patch, the radiation pattern at this mode is not exactly omnidirectional; nevertheless, it will be shown later that it is close to omnidirectional to an acceptable degree.

The two resonance frequencies are then controlled and reconfigured by varying the reactance loaded at two opposed sides of the patch. In the design shown in Fig. 7.7c, the stub-loading technique proposed in Chapter 5 is utilised. As this method has already been discussed thoroughly, we focus here the reconfigurability in terms of both frequency and pattern for the proposed antenna. Figure 7.8 shows typical reflection coefficient responses for a particular structure at $C_{\min} = 0.149$ pF and $C_{\max} = 1.304$ pF. It can be observed that by increasing varactor capacitance, both resonance frequencies are decreased. We denote f_1 as the resonance frequency of the conventional TM^z_{100} mode and f_2 for that of the monopolar mode. Since the varactor allows continuous tuning, the antenna can be

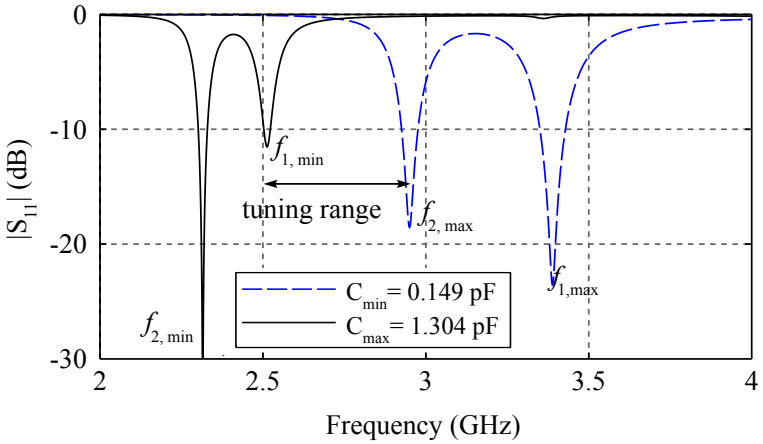

Figure 7.8. Antenna operational principle. Simulated reflection coefficient of a particular structure for $C_{min} = 0.149$ pF and $C_{max} = 1.304$ pF.

electronically reconfigured to operate with either radiation pattern in the frequency range $(f_{1,min}, f_{2,max})$, i.e. in the tuning range indicated in Fig. 7.8.

7.3.2 Antenna Analysis and Optimisation

In this section, the calculation of the resonance frequency for the conventional TM^z_{100} mode is briefly discussed first. Then the resonance frequency for the monopole mode is investigated empirically using a numerical simulation tool (Ansys HFSS). Based on these studies, an optimisation of the frequency tuning range for a given capacitance range is demonstrated.

Resonance frequency of the regular broadside TM^z_{100} mode

Provided that the radii of the shorting vias are very small, the resonance frequency for the conventional mode is almost the same as the resonance frequency of a single quarter-wave patch loaded with varactors and stubs (Fig. 7.9). The analysis of this antenna can be found in Section 5.3.2. The validation for the specific design presented in this chapter will be shown later in the optimisation result.

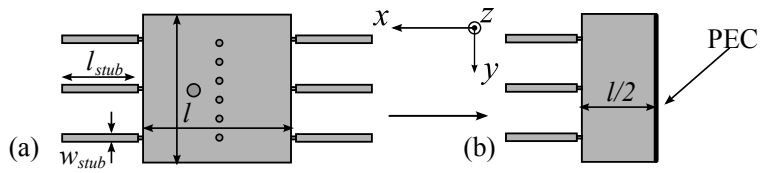

Figure 7.9. Step to analyse the antenna at the conventional mode. (a) The proposed antenna and (b) its equivalent quarter-wave patch to analyse to resonance frequency of the conventional TM^z_{100} mode.

Resonance frequency for the monopole mode

Because of the presence of shorting vias, the antenna also radiates in the monopolar mode (Fig. 7.7b). Figures 7.10 and 7.11 show the reflection coefficients when varying the number of shorting vias N and parameter d defined in Fig. 7.7c. As expected, the resonance frequency f_1 of the TM^z_{100} mode is not affected by these shorting vias. In contrast, increasing N or decreasing d causes the resonance frequency f_2 of the monopole mode to decrease. It can be observed from Fig. 7.10 that when f_2 is decreased by increasing d, the pattern at the monopole mode becomes more omnidirectional, which is explained by the higher isolation from the TM^z_{100} patch mode for larger frequency difference. However, the antenna matching becomes more difficult and the tuning range is also decreased (as mentioned, the tuning range is defined as the frequency range where the antenna can operate in either mode). Therefore, a trade-off has to be employed. In the proposed design, we choose f_2 such that the difference between the maximum and minimum gain for the omnidirectional pattern is less than 3 dB across the tuning range. Using numerical simulation tool, it is empirically found that this can be achieved if $f_2/f_1 \leq 0.85$ approximately.

Design Optimisation

As discussed in Section 7.3.1, the antenna can be reconfigured to operate at either radiating mode in a frequency tuning range of $(f_{1,\min}, f_{2,\max})$ where $f_{1,\min} = f_1(C_{\max})$ and $f_{2,\max} = f_2(C_{\min})$.

A typical design optimisation objective is to achieve a specified frequency tuning range for a given varactor capacitance range. For demonstration, in this design, we target a relative frequency tuning range $TR = 2(f_{2,\max} - f_{1,\min})/(f_{2,\max} + f_{1,\min})$ of 20% around a centre frequency of 3 GHz, i.e. $[2.7, 3.3]$ GHz for a chosen capacitance range $C \in [0.149, 1.304]$ pF.

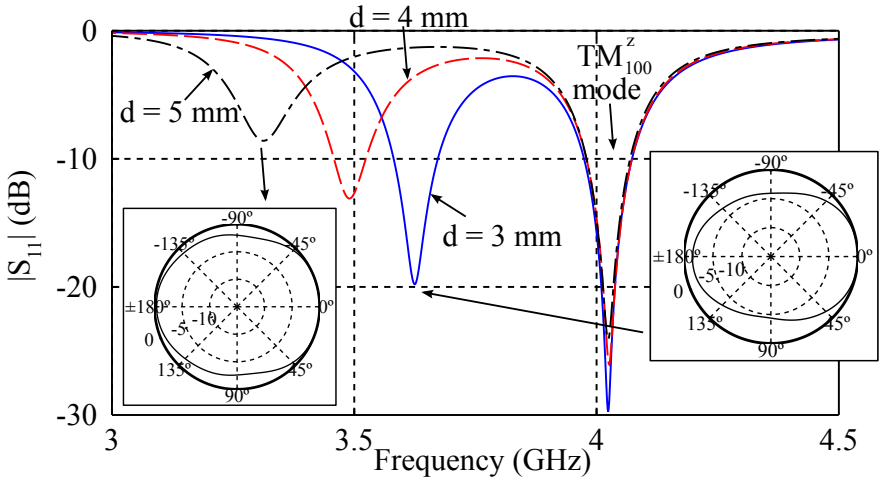

Figure 7.10. Effect of varying d. Simulated reflection coefficient of the antenna for different values of d (number of shorting vias $N = 6$). The insets are the simulated radiation pattern in xy-plane for the monopole mode.

The selected substrate is Rogers Duroid 5880 with relative permittivity $\epsilon_r = 2.2$ and thickness $h_s = 1.575$ mm.

Since an analytical solution for the resonance frequency for the conventional mode $f_1(C)$ is available, we only need to obtain an antenna dimension such that $f_1(C_{max}) = 2.7$ GHz and $f_1(C_{min}) = 3.3/0.85 \approx 3.9$ GHz (the value of 0.85 having been explained above). The optimisation follows then the procedure proposed in Section 5.2.3 to obtain the patch and stub size. The final optimised antenna dimensions are $L = 18$ mm, $l_{stub} = 17.51$ mm, $w_{stub} = 0.68$ mm and varactor gap length $l_v = 0.66$ mm. The simulated and analysed resonance frequencies of the antenna at the TM^z_{100} mode for different values of varactor capacitance C are shown in Fig. 7.12. Good agreement can be observed which again validates the analytical model proposed in Section 5.2.2. The higher simulated value of resonance frequency f_1 are mainly due to the finite size of shorting vias (diameter $d_{via} = 0.6$ mm), which slightly decreases the effective width of the quarter-wave patch (Fig. 7.9).

Next, the parameter d and number of shorting vias N are determined using numerical tool to obtain $f_{2,\max} \approx 0.85 f_{1,\max}$. Since the simulated $f_{1,\max} = 4.03$ GHz is slightly larger than its calculated value, i.e. 3.89 GHz (see Fig. 7.12), we choose $f_{2,\max} = 0.85 \times 4.03 \approx 3.45$ GHz, which slightly increases the frequency tuning range. In practice, a fine-tuning on the parameters to achieve an exact tuning range, e.g. $[2.7, 3.3]$ GHz may be required.

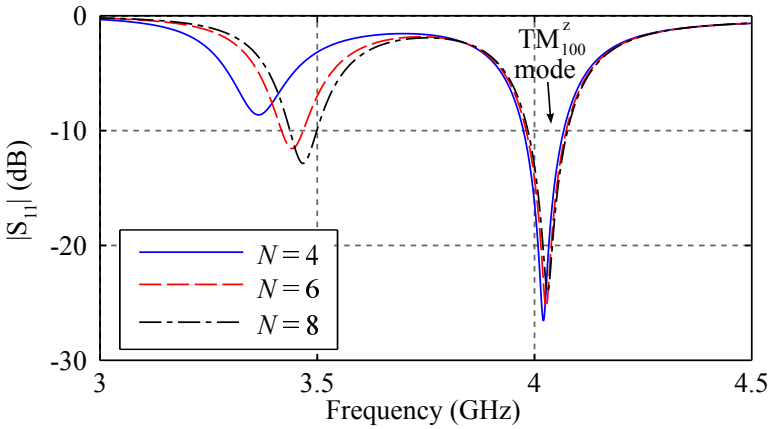

Figure 7.11. Effect of varying N. Simulated reflection coefficient of the antenna for different number of shorting vias N ($d = 4.3$ mm).

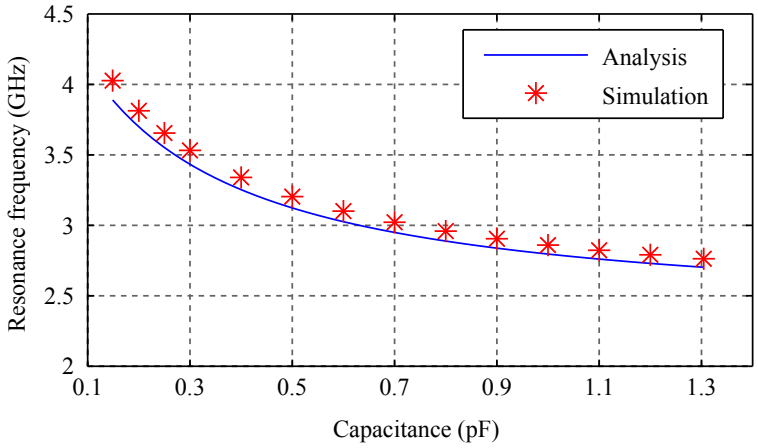

Figure 7.12. Validation of the conventional mode analysis and optimisation. Comparison of the results of semi-analytical calculations and full-wave simulations for the resonance frequency f_1 at the fundamental microstrip patch mode of the optimised antenna.

The final optimised parameters for shorting vias are $d = 4.3$ mm and $N = 6$. At this stage, the radiation patterns at the monopole mode are checked through full-wave simulations to verify that the difference between maximum and minimum simulated gain in xy-plane maintains below 3 dB across the tuning range. If this specification is not satisfied, one may need to decrease $f_{2,\max}$ which will slightly reduce the frequency tuning range. Finally, the feeding position $x = d_f$ is optimised through parametric simulations to achieve a satisfactory reflection coefficient in all antenna configurations.

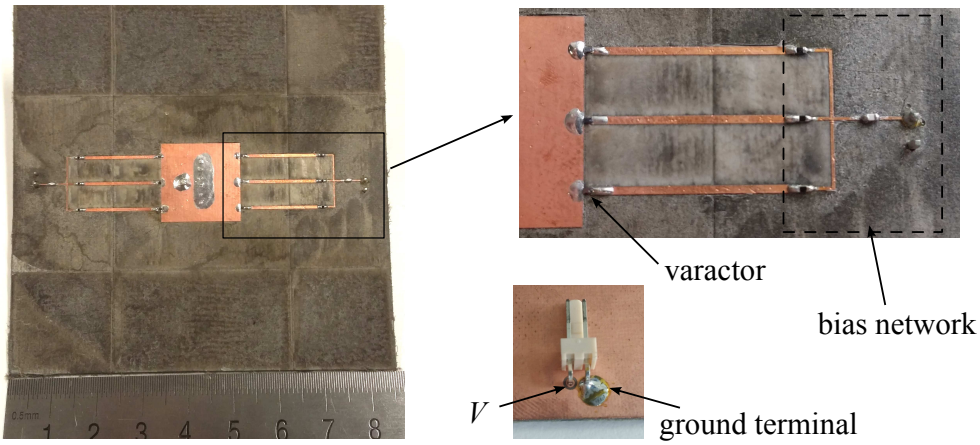

Figure 7.13. Photograph of the fabricated antenna. The detailed view of the bias network and DC connector on the back side of the substrate are shown on top right and bottom right, respectively.

7.3.3 Measurement Results

A photograph of the fabricated antenna optimised using the above process is shown in Fig. 7.13. The ground plane size is 85×85 mm^2. Results are presented in the following.

Reflection coefficient

The reflection coefficients for three different bias voltage configurations are shown in Fig. 7.14. A reasonable agreement between the simulation and measurement is obtained. The measured return loss at the monopole and TM^z_{100} resonance frequencies are always greater than 12.5 dB and 9.8 dB, respectively, across the whole tuning range from 2.68 GHz to 3.51 GHz. For a typical digital voltage range of [0, 5] V, the antenna still provides pattern reconfigurability from 2.68 GHz to 3.04 GHz, i.e. about 12%.

Radiation Patterns

The measured normalised radiation patterns at three different tuned frequencies f = 2.7 GHz, 3 GHz and 3.5 GHz in two pattern configurations are shown in Fig. 7.15. It can be observed that the patterns remain reasonably stable across the tuning range. The cross polarisation remains below -12 dB in all configurations. In the omnidirectional configuration, the differences between maximum and minimum measured gain in xy-plane

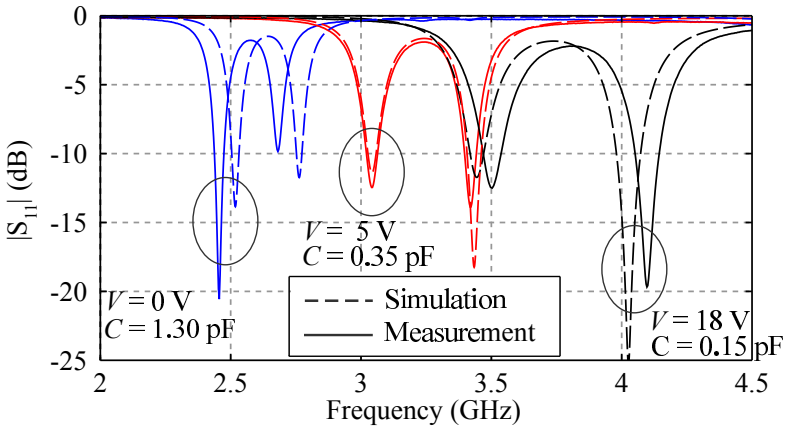

Figure 7.14. Simulated and measured reflection coefficient at different reverse bias voltages.

(the rightmost column) are 5.1 dB, 3.6 dB and 3.0 dB at $f = 2.7$ GHz, 3.0 GHz and 3.5 GHz, respectively. Higher values for these figures compared to simulation (where this difference remains below 3 dB) can be attributed to scattering effects from DC connector and testing equipment, e.g. antenna stand. It can be concluded from Fig. 7.14 and 7.15 that the antenna can be reconfigured to operate at either radiating mode over a frequency range of 2.68 GHz to 3.51 GHz, i.e. more than 20%, which covers the targeted frequency tuning range.

Antenna Gain and Efficiency

The antenna peak realised gains when operating at different modes across the tuning range are shown in Fig. 7.16. Good agreement between simulation and measurement is obtained with discrepancies generally less than 1 dB. The gain for the monopole mode is smaller than that for the broadside mode due its omnidirectionality. The simulated efficiency for the monopole mode and broadside mode increases from 51% to 94% and 45% to 76%, respectively, when the resonance frequency increases from 2.7 GHz to 3.5 GHz. From Fig. 7.16, it is estimated that the measured efficiency is from 58% to 74% for the monopole mode and from 40% to 82% for the broadside mode. The decrease in the antenna efficiency at lower frequency (lower bias voltage) is due to the higher loss in the internal resistance of the varactor. This phenomenon is expected due to higher current flow for higher varactor capacitance, which has been reported in many reconfigurable antennas in the literature [123, 133] and in previous chapters. This also explains that for a

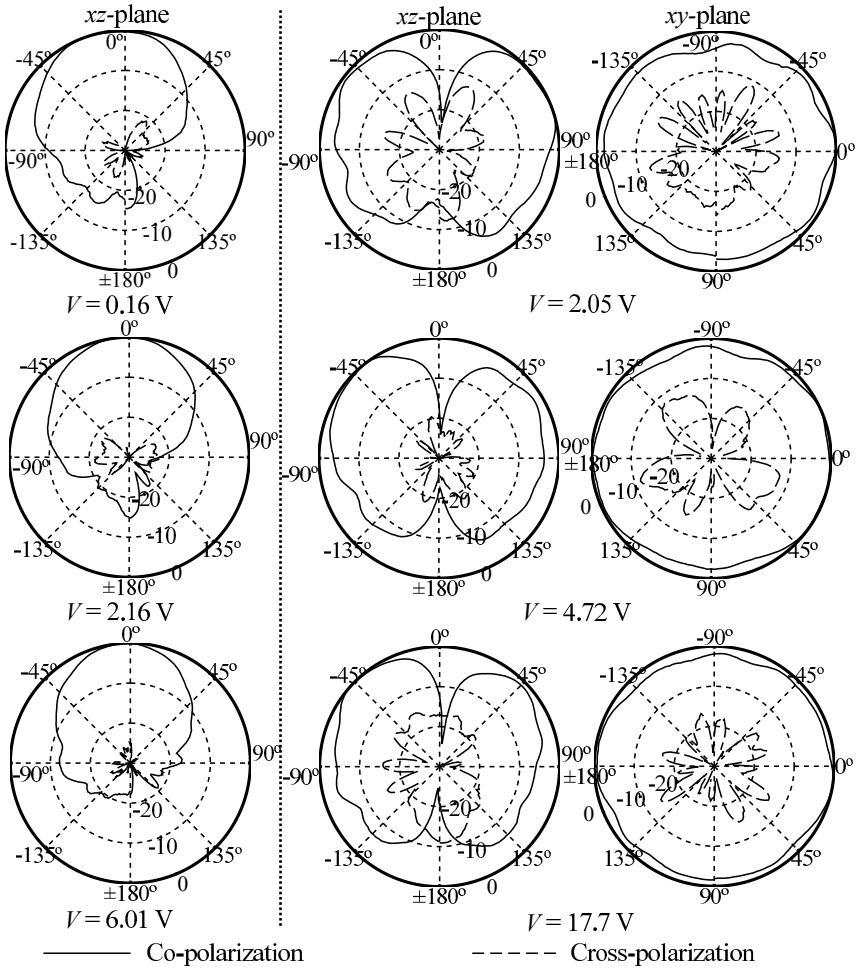

Figure 7.15. Radiation pattern and frequency reconfigurability demonstration. From top to bottom: normalised measured patterns at $f = 2.7, 3.0$ and 3.5 GHz. Left column: patterns in broadside configuration. Middle and right columns: patterns in monopole configuration. The corresponding reverse bias voltage is shown under the pattern.

given resonance frequency, generally the efficiency for broadside mode is lower than that of monopole mode due to higher required varactor capacitance (see Fig. 7.14).

7.3.4 Summary of Frequency- and Pattern-Reconfigurable Antenna

A frequency- and pattern-reconfigurable antenna has been proposed. The antenna can switch its operation between two distinct configurations, namely a microstrip patch

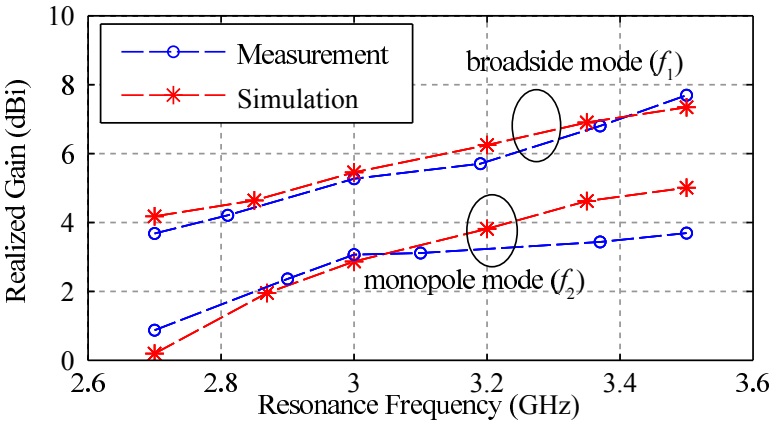

Figure 7.16. Peak realised gain of the antenna in two configurations.

broadside pattern or an omnidirectional monopolar pattern in a relative continuous frequency range of more than 20%, as demonstrated here from 2.68 GHz to 3.51 GHz. The antenna utilises varactors loaded with open-circuited stubs as its tuning mechanism. A design procedure based on a combination of a semi-analytical model and full-wave simulations has been demonstrated, which proved to be a convenient tool to optimise this type of antenna.

7.4 Conclusion

The original contributions of this chapter are two novel antenna designs, including a dual-band design with independent control of two frequency tuning ranges and a patch antenna that can switch its operation between omnidirectional pattern and broadside pattern across a continuous frequency range. The radiation principle can be explained conveniently using the field equivalence principle. Novel tuning techniques different from literature and those proposed earlier in this thesis (Chapter 5) have been utilised. The first dual-band design can be used when the design requirements target a very low antenna height profile and monopolar patterns in various frequencies at different bands. The second antenna might be suitable for integration into smart communication systems, especially when the pattern is required to be switched between uni-directional and omni-directional operation for example to enhance diversity.

Chapter 8

Thesis Conclusion

INSPIRED by the field equivalence principle and the concept of magnetic-current source, this thesis has proposed and investigated numerous antennas across a wide range of applications. The findings have been ordered into three major parts corresponding to three application themes, i.e. travelling-wave antennas, monopolar antennas and reconfigurable antennas. This last chapter summarises the original contributions of each part and proposes possible future work on the topic.

This chapter provides a summary of the thesis' original contributions, which spans three major parts. The general theme is planar or low-profile antennas that are built from equivalent magnetic-current sources. Different research directions based on the presented results are also proposed for future investigations.

8.1 Part I: Travelling-Wave Antennas

This part consists of Chapters 2 and 3, in which the design, analysis, optimisation and many aspects of the half-mode substrate-integrated waveguide (HMSIW) antennas have been studied. It is noted that the HMSIW antenna is equivalent to a magnetic-dipole.

8.1.1 Original Contributions

- As a first contribution in Chapter 2, the variational method has been used to calculate the propagation constant of various half-mode substrate-integrated waveguide (HMSIW) structures, including the truncated HMSIW with or without an infinite ground plane and the substrate-integrated waveguide (SIW) with a longitudinal slot. The dielectric and conductor losses of the HMSIW have been analysed to include their effect on the attenuation constant calculation. The impacts of these losses becomes crucial in the higher frequency range, e.g. for millimetre-wave operation. The method has also been applied to analyse the folded substrate-integrated waveguide (FSIW) (this later analysis is shown in the Appendix A as it is not directly related to the presented antennas). These contributions have been published in [18,36].
- A lossy transmission line model based on waveguide circuit theory for nonuniform continuous-source travelling-wave antennas (TWAs) has been proposed. Compared to the classical approach for this type of antennas, the proposed analysis has demonstrated a higher accuracy in the calculation of both aperture-field and far-field distributions. The inclusion of the feeding transition in the analysis with the aid of numerical simulation have also been shown. This consideration improves the accuracy of the analysis especially for wideband antennas where near-perfect matching is extremely difficult to achieve in a wide range of frequency. These contributions have been published in [16].

- Different aspects of the wideband tapered HMSIW antenna have been investigated next, including the near-field distribution and the effects of the feeding transition on the radiation patterns. It has been found that for this type of antenna, the radiation ripples in the broad beam pattern originate from the discontinuities at the feed. Based on this study, a novel transition for the integration of the HMSIW antennas into metallic structures has been proposed to minimise the radiation ripples. Furthermore, an optimisation process for this antenna targeting wideband operation and maximum gain towards broadside has been proposed. Ultimately, two millimetre-wave antennas integrated into a cylindrical pole or a flat metal surface have been presented and experimentally validated, showing a near-perfect magnetic-dipole pattern radiating into half free-space. These contributions have been published in [17, 18, 36].

- Based on the proposed semi-analytical model of nonuniform TWA, a technique for pattern synthesis in leaky-wave antenna (LWA) has been demonstrated. This method utilises global optimisation techniques to obtain the antenna dimensions directly from the pattern specifications. It is noted that the method becomes feasible due to the fast calculation of the antenna patterns obtained from the semi-analytical model. Compared to the classical approach utilising Fourier-transform pair of near- and far-field, the proposed method shows a higher flexibility in pattern synthesis and it does not require an independent control on the attenuation constant α and phase constant β. Two specific designs have been demonstrated as illustration of the method versatility, targeting a low sidelobe level and a wide null in the radiation patterns of the HMSIW LWA. These contributions have been published in [63, 185, 186].

- Finally, a framework for optimisation of wideband antennas including statistical reliability considerations has been proposed. Using predetermined tolerances of the manufacturing process, the analysis provides the failure probability of the considered antennas and characterise the influence of each antenna parameter. It has been shown that for wideband operation in the context of reliability, the safe margins for both reflection coefficient and bandwidth are the relevant optimising factors. As an illustration, a wideband tapered HMSIW antenna has been optimised to obtain a failure probability of less than 1%. These contributions have been published

in [55, 56] with the contributions shared equally among A. Kouassi and the author of this thesis.

8.1.2 Future Work

As shown in [17] and [186], for the highly tapered wideband antenna, most of the radiation occurs around a short effective aperture length (hence leading to broad-beam radiation pattern). This motivates a wideband monopulse design, in which two HMSIW antennas are arranged in such a way that the distance, relative to wavelength, between the two radiation sources at any frequency is constant. This guarantees that the difference-to-sum ratio in the monopulse antenna is constant across a wide frequency range.

The lossy transmission line model can also be investigated further for application in periodic structures. It is predicted that the model is still reasonably accurate when the period and the variation between two adjacent unit-cells are relatively small.

Reliability-aware optimisation can be further studied to apply the technique in different antenna whose properties are strongly affected by uncertainties such as wearable or flexible antennas.

8.2 Part II: Low-Profile Monopolar Antennas

This part has focused on different realisations of low-profile monopolar antennas and consists of Chapter 4. Using the field equivalence principle, this type of antenna can be shown to operate as a magnetic-current loop radiating on a ground plane. Therefore, the antenna radiation patterns resemble that of an electric monopole.

8.2.1 Original Contributions

- The first design is a wideband antenna with reduction in the antenna height while maintaining its planar size and omnidirectional patterns with vertical polarisation. This has been achieved by the introduction of symmetrical tapered slots on the patch. Two antenna realisations have been designed and fabricated, targeting the

integration onto vehicles, i.e. with a large flat ground plane, and onto helmets, i.e. with a curved ground plane. In the latter design, the helmet material has also been integrated into the design to reduce the antenna height seen from the top of the helmet. Moreover, the tapered nature of the curved ground plane can further reduce the antenna height. The final results have demonstrated that a curved-ground plane can yield patterns resembling more that of a dipole with slight improvement in its omnidirectional gain, i.e. towards the horizon. The contributions have been published in [99].

- The second design is a dual-band antenna with a significant reduction in antenna height. The technique of placing additional symmetrical slots has been adapted in this design to open another resonance band. The slot geometry is tailored to gain flexibility in choosing the second resonance frequency as well as optimising the impedance matching. A parameter study on key parameters and features of the antenna have been carried out. Based on this, a thorough design procedure has been proposed for the adaptation at different resonance frequencies. An antenna prototype has been fabricated with measurement results validating the design concept. This contribution here has been written as an article and submitted to a journal.

8.2.2 Future Work

The two antennas mentioned above have been designed targeting vehicle integration, i.e. tested with a large ground plane, as well as helmet applications, with a smaller curved ground surface. The future investigations should adapt the antenna design into a real vehicle and study the effects of the vehicle on the antenna performance. One possible direction is to create a shallow cavity and place the antenna inside. This might further reduce the antenna height (seen from the ground plane). In this case, the size of the cavity will be optimised to achieve satisfactory reflection coefficients.

8.3 Part III: Reconfigurable Antennas

This part consists of Chapters 5, 6 and 7, which are dedicated to reconfigurable antennas.

8.3.1 Original Contributions

- First, a frequency-reconfigurable antenna based on a stub-loaded HMSIW cavity has been proposed. This antenna has been studied thoroughly with an analytical model, allowing to accurately determine the resonance frequency. On that basis, an optimisation process to achieve a target tuning range for a given range of varactor capacitance has been developed. Since the antenna is equivalent to only one magnetic current radiating on a ground plane, it achieves highly stable radiation patterns and very low cross polarisation across a very large tuning range of 44%. The stub-loading technique also requires a simple bias circuit and allows independent control of each varactor. The proposed antenna shows a significant improvement in the radiation performance and reflection coefficient compared to other published reconfigurable antennas using similar structure or principle. The contributions have been published in [105, 107].

- The tuning principle and analytical model proposed for the stub-loaded HMSIW cavity has been extended to design a stub-loaded microstrip patch antenna with both frequency and polarisation reconfigurability. This antenna can be reconfigured to operate at either three linear polarisation (LP) states or two circular polarisation (CP) states in a continuous tuning range of about 40%. The antenna also exhibits stable broadside radiation patterns across the whole frequency range at different polarisation states. These contributions have been published in [106].

- A family of reconfigurable antennas using varactors loaded with rectangular stubs are summarised with further antenna examples based on a quarter-mode substrate-integrated waveguide (QMSIW) and a quarter-wave patch. These examples again validate the accuracy of the proposed analytical model. A folded-stub configuration has been proposed for antenna miniaturisation. For this family of reconfigurable antennas, the trade-off among antenna size, cross-polarisation level and efficiency has also been discussed. These contributions have been published in [108–110].

- A systematic approach to vary the operating frequency and linear polarisation direction of a circular cavity antenna has been proposed. The novel principle is to vary the length and position of the equivalent magnetic current. An antenna prototype has been designed and validated with measurement results. This particular

realisation can change the linear polarisation in six different angles and at five discrete frequencies. Importantly, based on the proposed principle, quasi-continuous frequency- and polarisation-reconfiguration is feasible using individual control of a large number of switching devices. The contributions have been published in [167].

- To further reduce the height of the low-profile monopolar antenna and cover a wider operating frequency range, a dual-band reconfigurable antenna with independent control of two frequency tuning ranges has been proposed. The principle is based on the fact that for the dual-band monopolar antenna discussed in Part II, the two resonance frequencies can be controlled independently by varying the length of the corresponding radiation source while fixing the slots' position. Different tuning techniques from literature were adapted in this antenna design. Measurement results show that the reconfigurable antenna achieves independent -10-dB-tuning ranges of 31% and 22% centred at about 0.9 GHz and 1.7 GHz, respectively. Stable omnidirectional patterns and vertical polarisation were achieved across both tuning ranges. The findings have been written and submitted to an IEEE journal and the manuscript is under reviewing process.

- Finally, the two radiating modes, including the conventional patch mode and monopolar mode, of a centred-shorted microstrip patch antenna have been utilised to design a frequency- and pattern-reconfigurable antenna. This centred-shorted microstrip antenna operates as a dual-band antenna with two distinct patterns at two frequencies. The principle is to simultaneously vary these two resonance frequencies by tuning a set of varactors. As a results, the antenna can switch its operation between two distinct configurations, namely a microstrip patch broadside pattern or an omnidirectional monopolar pattern in a continuous frequency range (more than 20% from 2.68 GHz to 3.51 GHz). The stub loading technique proposed previously in this major part has been used as tuning mechanism. The original contributions have been published in [111, 172].

8.3.2 Future Work

Several aspects of the reconfigurable antennas based on varactors and loading stubs can be further investigated. Firstly, increasing the number of tuning devices may not necessarily

increase the overall loss. This is because the RF current flowing through each varactor also decreases, which may in turn lower the loss. This effect can be investigated in future work to possibly enhance the antenna efficiency. Secondly, different techniques to improve the antenna tuning range can be explored.

In the polarisation- and frequency-reconfigurable design (Chapter 6), the PIN diodes can be switched to change the position of the current source. If this current source is directed by coupling elements placing around the cavity, beam-switching antenna can be designed. This concept has been investigated as a preliminary study in [187]. The future investigation is to realise this antenna with optimised coupling elements for highest gain and largest steering angle.

The stub-loading technique can be applied for the periodically loaded travelling-wave HMSIW antenna. Utilising the semi-analytical model and pattern synthesis method proposed in Chapter 2, the antenna can be rapidly optimised to change its main beam at a fixed frequency for a set of varactor configuration. This antenna also has the potential to switch into wideband broad-beam operation, as similar to the tapered HMSIW antenna's operation. In order to perform this, the analysis in Chapter 2 needs to be adapted for periodic structures and a bias circuit able to independently control a large number of varactors need to be designed. These are subjected to future work and investigations.

8.4 Concluding Statement

Finally, as a general conclusion to this thesis, I would like to emphasise again the importance and versatility of the field equivalence principle in the analysis of planar or low-profile antennas in the microwave and millimetre-wave regimes. Although numerous analytical and numerical techniques have been developed in the past, this classical principle has never lost its significance. It is an easy-to-use but remarkably effective tool to initially understand the antenna radiations' mechanism. Furthermore, the use of equivalent magnetic current has inspired and can open many novel antenna developments. Various analytical and semi-analytical models based on this common fundamental principle have been proposed, enabling rapid optimisations towards different targets.

Appendix A

Variational Analysis of Folded Substrate-Integrated Waveguide

AN ACCURATE numerical solution describing the propagation behaviour of two types of folded substrate-integrated waveguide (FSIW) is demonstrated in this appendix. The computation is based on a variational method which can be carried out efficiently by solving the stationary equation corresponding to each type of FSIW. The approach can be extended to solve various folded structures, i.e. with different gap positions, where the layers are made of substrates with different thicknesses and material properties. The result is an extension from the variational analysis of different types of half-mode substrate-integrated waveguide (HMSIW) presented in Chapter 2

A.1 Introduction

The folded substrate-integrated waveguide (FSIW) is typically used for structure miniaturisation in a trade-off of fabrication complexity as a mutli-layer structure [188,189]. This type of transmission line has been designed mostly in the two configurations depicted in Fig. A.1. The first configuration of FSIW exhibits a horizontal symmetry plane (type I, Fig. 1a). Its propagation characteristics has been investigated in [188] and utilised to design filters in [190]. The second configuration (type II, Fig. 1b) exhibits a vertical symmetry plane and has been proposed in [189].

The analysis of these multi-layer structures is not trivial. The solution in [188] uses an empirical factor for the equivalent capacitor at the junction between two layers of the waveguide, which is also utilised in [191]. In order to avoid this empirical factor, the variational method is employed to obtain the dispersion characteristics of the FSIW. The proposed technique is applied to solving the mentioned types of FSIW, but it also shows versatility in finding a solution for various parameters of the upper and lower layers of the waveguide. The results demonstrate the broad applicability of variational technique in solving the various modes propagating in different SIW structures while the calculation is kept simple without empirical parameters. The findings described in this appendix have been published in [36].

A.2 Variational Analysis of FSIW

Similarly to the analysis of the half-mode substrate-integrated waveguide (HMSIW) in Chapter 2, the via hole walls of the FSIW can be converted into equivalent solid perfect

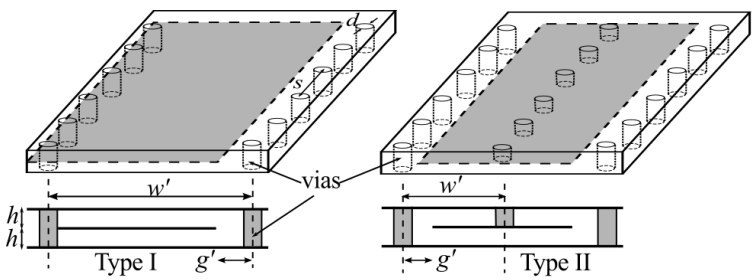

Figure A.1. Two types of FSIW (top is 3D-view and bottom is cross-section of each waveguide).

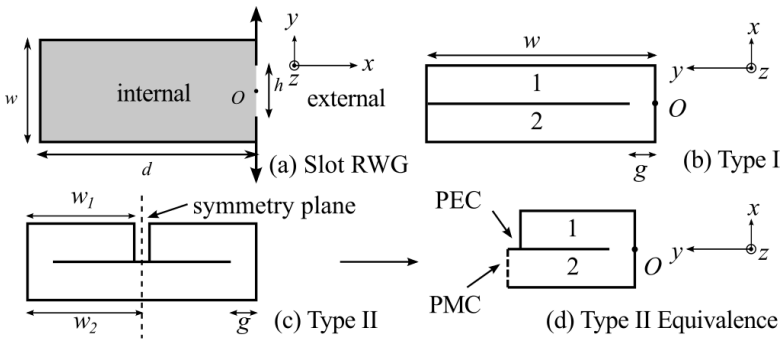

Figure A.2. Cross-section of slot and folded rectangular waveguides. (a) Slot rectangular waveguide and (b,c,d) equivalent folded rectangular waveguides of the FSIWs.

electric conductor (PEC) walls by using an empirical formula in [35]. The correction term Δ for the via-wall location can be expressed as

$$\Delta = \frac{d^2}{0.95s} \tag{A.1}$$

where s and d are the spacing and diameter of the vias, respectively (Fig. A.1) [35]. The FSIW is now converted into a folded rectangular waveguide (FRWG) with a solid wall as shown in Fig. A.2b and 2c. For the FSIW type I,

$$w = w' - \Delta;\ g = g' - \Delta/2. \tag{A.2}$$

It is noted that in the FSIW type II, there is an extra via hole wall in the middle of the top layer which results in different equivalent widths of the top and bottom layers

$$w_1 = w' - \Delta;\ w_2 = w - \Delta/2;\ g = g' - \Delta/2. \tag{A.3}$$

The FSIW is then divided into two regions 1 and 2, in analogy to the internal and external regions in the case of the slot rectangular waveguide. The variational analysis requires solving the stationary equation (2.2) shown in Chapter 2. This equation is rewritten here for the geometry of the FSIW shown in Fig. A.2

$$\Phi(\gamma) = \int_0^g \left[E_y({}^1H_z - {}^2H_z) + E_z({}^1H_y - {}^2H_y)\right] dy = 0, \tag{A.4}$$

Since in practical realisations the gap is small compared to the width of the waveguide, a reasonable assumption of the tangential field in this gap is $E_y = 1$ and $E_z = 0$. A

possible refinement of this assumption would involve introducing more terms of a Fourier expansion on the field distribution and then applying the Rayleight-Ritz method for a stationary equation [30]. However, it will be shown that the simple assumption ($E_y = 1, E_z = 0$) already provides very accurate results while keeping the analysis simple. The expression (A.4) is then reduced to

$$\Phi(\gamma) = \int_0^g ({}^1H_z - {}^2H_z)dy = 0. \tag{A.5}$$

The two types of FSIW are then analysed slightly differently.

A.2.1 Type I

As explained in Chapter 2, the magnetic field that fits the assumed electric field distribution in the slot is determined by the field equivalence principle. Since the structure is symmetrical along the plane $x = 0$, the equivalent magnetic currents $\mathbf{M} = \mathbf{E} \times \hat{\mathbf{n}}$ are opposite on the two sides of the gap. Consequently, the magnetic fields in region 1 and 2 have the same magnitude but opposite sign. Combining this consideration with (A.5), the propagation constant of an FSIW type I can be found by solving the equation

$$\int_0^g {}^1H_z(\gamma)dy = 0. \tag{A.6}$$

Following the detailed analysis with orthogonal mode expansion in a rectangular waveguide in [30], a closed-form expression for the integral of H_z can be calculated as

$$\begin{aligned}\int_0^g H_z dy \;=\; & \frac{j}{\omega\mu}\left[\frac{g^2 l_0}{w}\cot l_0 h\right. \\ & \left. +2\sum_{n=1}^{\infty}\sin^2\frac{n\pi g}{w}\cot l_n h\left(\frac{\ln w}{(n\pi)^2}+\frac{1}{w l_n}\right)\right]\end{aligned} \tag{A.7}$$

with

$$l_n = \sqrt{\epsilon_r k_0^2 + \gamma^2 - \left(\frac{n\pi}{w}\right)^2} \tag{A.8}$$

where $k_0 = \omega/c$ and ϵ_r is the relative permittivity of the substrate. Utilising this formula, the stationary equation can be efficiently solved by a iterative Newton's method. The first guessed root of Eq. (A.6) can be chosen as

$$\gamma_0 = \sqrt{\left(\frac{\pi}{2w}\right)^2 - \epsilon_r k_0^2} \tag{A.9}$$

by approximating the FSIW as a RWG with double width.

A.2.2 Type II

For the second configuration, which exhibits a vertical symmetry, the FSIW has an equivalent half-sized problem with a perfect magnetic conductor (PMC) wall in the middle as illustrated in Fig. A.2d. The waveguide is thus divided into two regions whose eigenfuntions are known analytically: Region 1 is similar to that of type I, whereas region 2 can be obtained through an appropriate adaptation on the boundary condition at the PMC. The expression for the integral of the magnetic field in region 2 is calculated as

$$\begin{aligned}\int_0^g H_z dy &= -\frac{j}{\omega\mu}\left[\sum_{n=0}^{\infty}\sin^2\frac{\pi(n+0.5)g}{w_2}\right. \\ &\times \left.\cot l_n' h\left(\frac{2\ln w_2}{[(n+0.5)\pi]^2}+\frac{1}{w_2 l_n'}\right)\right] \end{aligned} \tag{A.10}$$

with

$$l_n' = \sqrt{\epsilon_r k_0^2 + \gamma^2 - \left(\frac{(n+0.5)\pi}{w_2}\right)^2} \tag{A.11}$$

The stationary equation (A.5) is then solved by Newton's method, with similar first guessed root as in type I since the unfolded waveguide still has a total width of approximately $2w$.

It is worth mentioning that the stationary equation (A.5) has infinitely many roots corresponding to infinite number of propagation modes of the FSIW. By iteratively increasing the first guessed root, higher order mode propagation constants can also be obtained.

A.3 Analysis and Simulation Results

To verify the proposed method, the geometry of the FSIW in [188] is chosen as example with substrate permittivity $\epsilon_r = 2.65$, height $h = 0.8$ mm, via diameter $d = 0.9$ mm and via spacing $s = 1.2$ mm. For the FSIW type I, $w' = 8.12$ mm and for the FSIW type II, $w' = 4.06$ mm. The calculated and simulated results for various gap widths are shown in Fig. A.3. Satisfactory convergence is typically obtained for $n \leq 30$. The PEC-wall simulated results, i.e. for the equivalent FRWG, are obtained from 2D eigenmode port solution.

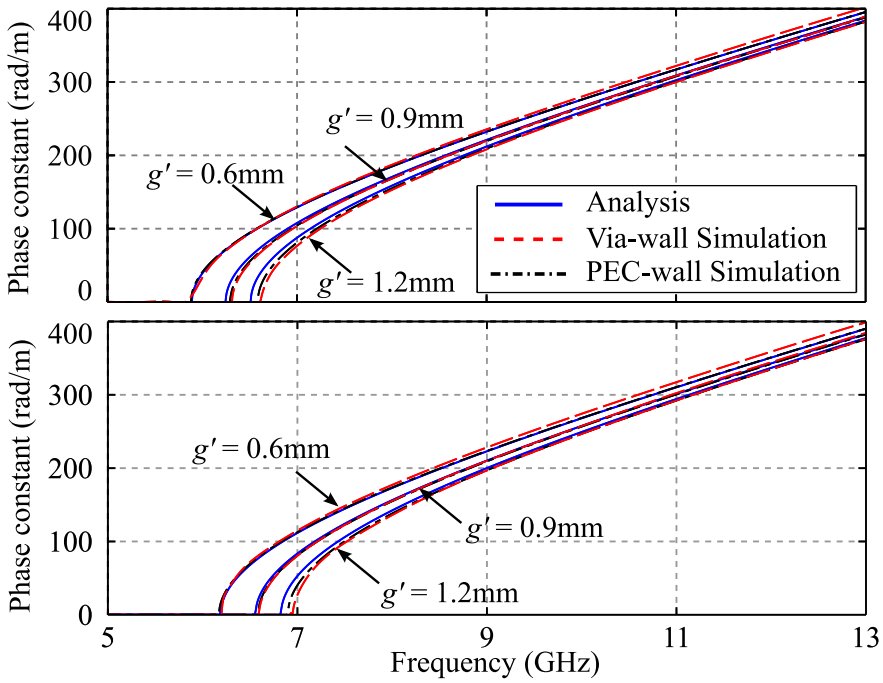

Figure A.3. Calculated and simulated phase constant of the FSIW type I (top) and type II (bottom). The legends are the same for both figures.

The via-wall results are obtained using the multi-line method [37] and the simulation of two FSIWs with different lengths. All simulations are carried out using Ansys HFSS. It can be observed that there is a very good agreement between analysis and simulation. Figure. A.3 also shows that when the gap is relatively small, the analysis almost yields an exact result (compared to PEC-wall simulation). This is because the assumed field distribution in the slot ($E_y = 1, E_z = 0$) becomes more accurate when decreasing the gap width g'. When g' increases, the analysis still gives a very good approximation on the phase constant. The error in cutoff frequency for the case $g' = 1.2$ mm of the FSIW type I is 1.52% while the analysis in [188] yields an error of 2.88%. Various numerical simulations and analyses show that the error in cutoff frequency when compared to PEC-wall simulation is less than 2% if $g/w < 0.12$ and $g/h < 2$. It is noted that in practice, g' should not be chosen very large otherwise the waveguide will approach a rectangular waveguide with the same width and the structure loses the miniaturisation advantage of the folded waveguide.

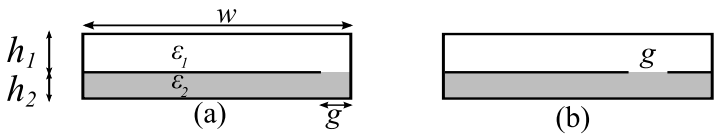

Figure A.4. Generalised FSIW type I that can be solved by the proposed method.

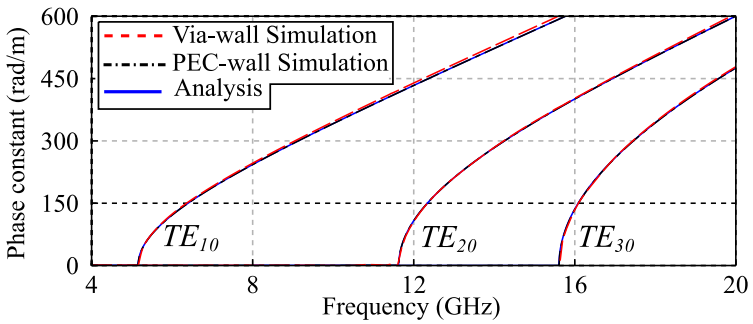

Figure A.5. Further results for the generalised FSIW type I. Phase constant for TE_{10}, TE_{20} and TE_{30} modes of the generalised FSIW type I (Fig.A.4a).

A.4 Further Application

Although the method does not yield an explicit formula for the propagation constant, it still allows for a fast computation and provides an alternative to [188], without requiring an empirical factor. The application of the proposed method can be extended for example to analyse the FSIW type I with two layers filled with different substrates (Fig. A.4a), or for the gap moved within the waveguide (Fig. A.4b). In general, the technique can solve any structure with two rectangular shapes joined by a small gap. For a brief verification, Fig. A.5a shows the results for three lowest order modes, i.e TE_{10}, TE_{20}, TE_{30} propagating in the FSIW in Fig. A.4a with $h_1 = 1.1$ mm, $h_2 = 0.5$ mm, $\epsilon_{r1} = 2.65$, $\epsilon_{r2} = 4$, $w' = 8.12$ mm and $g' = 0.6$ mm. Excellent agreement between analysis and simulation can be observed, which further demonstrates the wide range of applications of the analysis.

A.5 Conclusion

The application of a variational analysis for solving the dispersion characteristics of two types of FSIW has been demonstrated. The method is shown to yield reasonably accurate phase constant without an empirical factor for the solution of the equivalent FRWG.

A.5 Conclusion

Stationary equations in a closed-form have been given, which can be solved efficiently by Newton's method. The presented results for various configurations of folded rectangular waveguides and propagation modes demonstrate the broad applicability of the proposed method. The method presented here is an extension from the variational analysis of different variations of the HMSIW presented in Chapter 2.

Appendix B

Transmission Line Matrix Transformation

THIS appendix shows the formula for conversion between ABCD-matrix and S-parameters of the travelling-wave defined in Chapter 2. These conversions are used for the analysis of nonuniform continuous-source travelling-wave antennas presented also in Chapter 2

B.1 ABCD - S Parameter Conversion

The conversion between S-parameters (**S**) and ABCD-parameters can be carried through the impedance matrix **Z**. As demonstrated in [42], for a travelling-wave

$$\mathbf{S} = \mathbf{U}(\mathbf{Z}-\mathbf{Z}_0)(\mathbf{Z}+\mathbf{Z}_0)^{-1}\mathbf{U}^{-1}, \tag{B.1}$$

$$\mathbf{Z} = (\mathbf{I}-\mathbf{U}^{-1}\mathbf{S}\mathbf{U})^{-1}(\mathbf{I}+\mathbf{U}^{-1}\mathbf{S}\mathbf{U})\mathbf{Z}_0. \tag{B.2}$$

where $\mathbf{Z}_0$ is a diagonal matrix whose elements are the characteristic port impedances $Z_0^{(i)}$ (the superscript $i = 1, 2$ denotes the port number), **U** is a diagonal matrix whose elements are the normalised constant of the travelling-wave defined in equation (2.20). With the normalisation imposed in (2.21),

$$\mathbf{U} = \begin{bmatrix} \frac{\sqrt{Re(Z_0^{(1)})}}{|Z_0^{(1)}|} & 0 \\ 0 & \frac{\sqrt{Re(Z_0^{(2)})}}{|Z_0^{(2)}|} \end{bmatrix}. \tag{B.3}$$

The conversion between impedance matrix **Z** and ABCD-matrix **A** is well-known and can be derived easily from their definitions that relate the voltage and current between two ports,

$$\begin{aligned} \mathbf{Z} &= \frac{1}{C}\begin{bmatrix} A & (AD-BC) \\ 1 & D \end{bmatrix} \\ \mathbf{A} &= \frac{1}{Z_{21}}\begin{bmatrix} Z_{11} & (Z_{11}Z_{22}-Z_{12}Z_{21}) \\ 1 & Z_{22} \end{bmatrix}. \end{aligned} \tag{B.4}$$

Appendix C

Contour Search Algorithm

THIS appendix demonstrates the contour search algorithm used to obtain the probability curve in the reliability-aware optimisation of wideband antenna presented in Chapter 3.

C.1 The Algorithm

The stair-case search algorithm to obtain an approximation of the P_{f0}-curve is illustrated in Fig. C.1. The solid black curve is assumed to be the exact unknown P_{f0}-curve. As a feature of the search algorithm, the objective is to obtain (as many as possible) blue-rectangular points (Fig. C.1) which are as close as possible to the exact curve while keeping a failure probability $P_f < P_{f0}$. The search domain of the algorithm is defined as $[|S_{11}|_{tg\,start}\,,\ |S_{11}|_{tg\,end}]$ and $[\Delta_{BW\,start}\,,\ \Delta_{BW\,end}]$.

In order to get the maximum number of the $|S_{11}|_{tg}$ and Δ_{BW} values describing the P_{f0}-curve, the proposed algorithm is divided into two parts, starting from opposed corners of the search region. The first part is conducted in the part of the exact curve where the slope is greater than 1. In this part, the algorithm alternatively check $P_f \leq P_{f0}$ by increasing and decreasing Δ_{BW} by $\Delta_{BW\,step}$. When a satisfactory point is found, the algorithm increases the $|S_{11}|_{tg}$ and continues as before. Part II of the algorithm has the same general principle as Part I but gives priority to variation of $|S_{11}|_{tg}$ over Δ_{BW}. The algorithm in each part terminates when it reaches a point where ideally the slope of the exact curve is 1. Since the exact curve is unknown, this point can be estimated for example from Fig. 3.24a and 3.25a, which is defined at $\Delta_{BW\,lim}$ where $\Delta_{BW\,lim} \in [\Delta_{BW\,start}\,,\ \Delta_{BW\,end}]$.

At the beginning of the algorithm, the stepping parameters $|S_{11}|_{tg\,step}$ and $\Delta_{BW\,step}$, are set to relatively large values, namely -0.25 dB and 0.01 respectively, to quickly reach the region of interest. They are then reduced to -0.1 dB and 0.001, once the first occurrence of failure probability under 1% is reached. Table C.1 shows the algorithm parameters for the optimisation of Antenna I and II demonstrated in Chapter 3, Section 3.4.3.

It is worth mentioning that this proposed algorithm only serves as a simple solution to obtain a better approximation of the P_{f0}-curve, compared to a crude linear interpolation as shown in Fig. 3.24 and Fig. 3.25. In order to obtain a finer P_{f0}, one may include a mesh-adaptation algorithm, however, Figs. 3.26b and 3.27b suggests that a finer curve would not significantly improve the final optimised results.

Algorithm 1 P_{f0}-curve's determination

PART I: $|S_{11}|_{tg} \leftarrow |S_{11}|_{tg\,start}$, $\Delta_{BW} \leftarrow \Delta_{BW\,start}$
while $\Delta_{BW} \leq \Delta_{BW\,lim}$ **do**
  Initialise $P_{f\,old}$, $P_{f\,new}$
  while stop = 0 **do**
    Optimise antenna with $(|S_{11}|_{tg}, \Delta_{BW})$; Compute failure probability P_f; $P_{f\,new} \leftarrow P_f$
    if $P_{f\,new} \geq P_{f0}$ **then**
      Increase Δ_{BW}, $P_{f\,old} \leftarrow P_{f\,new}$
    else if $P_{f\,new} < P_{f0}$ & $P_{f\,old} < P_{f0}$ **then**
      Decrease Δ_{BW}, $P_{f\,old} \leftarrow P_{f\,new}$
    else
      stop $\leftarrow 1$
    end if
  end while
  Increase $|S_{11}|_{tg}$
end while

PART II: $|S_{11}|_{tg} \leftarrow |S_{11}|_{tg\,end}$, $\Delta_{BW} \leftarrow \Delta_{BW\,end}$
while $\Delta_{BW} > \Delta_{BW\,lim}$ **do**
  Initialise $P_{f\,old}$, $P_{f\,new}$
  while stop = 0 **do**
    Optimise antenna with $(|S_{11}|_{tg}, \Delta_{BW})$; Compute failure probability P_f; $P_{f\,new} \leftarrow P_f$
    if $P_{f\,new} \geq P_{f0}$ **then**
      Decrease $|S_{11}|_{tg}$, $P_{f\,old} \leftarrow P_{f\,new}$
    else if $P_{f\,new} < P_{f0}$ & $P_{f\,old} < P_{f0}$ **then**
      Increase $|S_{11}|_{tg}$, $P_{f\,old} \leftarrow P_{f\,new}$
    else
      stop $\leftarrow 1$
    end if
  end while
  Decrease Δ_{BW}
end while

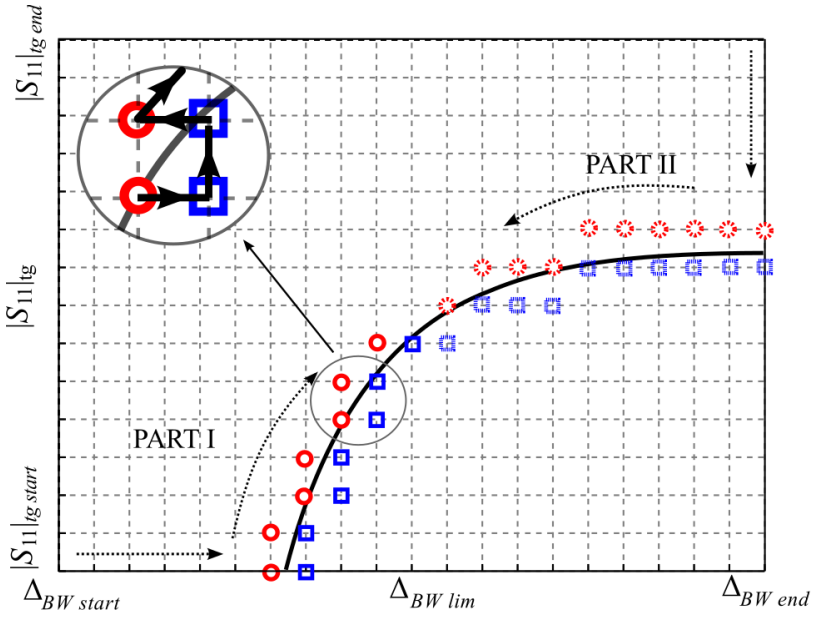

Figure C.1. Illustration of the algorithm to obtain an approximation of P_{f0}-curve.

Table C.1. Algorithm's parameters

	Antenna I	Antenna II
$\|S_{11}\|_{tg\ start}$ (dB)	-13	-13
$\|S_{11}\|_{tg\ end}$ (dB)	-11	-10
$\Delta_{BW\ start}$	0	0
$\Delta_{BW\ end}$	0.04	0.04
$\Delta_{BW\ lim}$	0.026	0.026

References

[1] R. F. Harrington, *Time-Harmonic Electromagnetic Fields*. New York: McGraw-Hill, 1961.

[2] C. Balanis, *Antenna Theory: Analysis and Design*, ser. Knovel library. Wiley, 2005.

[3] W. Hong, B. Liu, Y. Wang, Q. Lai, H. Tang, X. X. Yin, Y. D. Dong, Y. Zhang, and K. Wu, "Half mode substrate integrated waveguide: A new guided wave structure for microwave and millimeter wave application," in *Joint 31st International Infrared Millimeter Waves Conference/14th Int. Teraherz Electronic Conference, 2006. IRMMW-THz 2006.*, Sept. 2006, p. 219.

[4] J. Xu, W. Hong, H. Tang, Z. Kuai, and K. Wu, "Half-mode substrate integrated waveguide (HMSIW) leaky-wave antenna for millimeter-wave applications," *IEEE Antennas and Wireless Propagation Letters*, vol. 7, pp. 85 –88, 2008.

[5] G. M. Zelinski, G. Thiele, M. Hastriter, M. Havrilla, and A. Terzuoli, "Half width leaky wave antennas," *IET Microwaves, Antennas Propagation*, vol. 1, no. 2, pp. 341–348, 2007.

[6] D. K. Karmokar, K. P. Esselle, and T. S. Bird, "Wideband microstrip leaky-wave antennas with two symmetrical side beams for simultaneous dual-beam scanning," *IEEE Transactions on Antennas and Propagation*, vol. 64, no. 4, pp. 1262–1269, April 2016.

[7] Q. Lai, C. Fumeaux, and W. Hong, "Periodic leaky-wave antennas fed by a modified half-mode substrate integrated waveguide," *IET Microwaves, Antennas Propagation*, vol. 6, no. 5, pp. 594 –601, 2012.

[8] Q. H. Lai, W. Hong, Z. Q. Kuai, Y. S. Zhang, and K. Wu, "Half-mode substrate integrated waveguide transverse slot array antennas," *IEEE Transactions on Antennas and Propagation*, vol. 57, no. 4, pp. 1064 –1072, April 2009.

[9] R. Henry and M. Okoniewski, "A broadside-scanning half-mode substrate integrated waveguide periodic leaky-wave antenna," *Antennas and Wireless Propagation Letters, IEEE*, vol. 13, pp. 1429–1432, 2014.

[10] D. K. Karmokar and K. P. Esselle, "Periodic u-slot-loaded dual-band half-width microstrip leaky-wave antennas for forward and backward beam scanning," *IEEE Transactions on Antennas and Propagation*, vol. 63, no. 12, pp. 5372–5381, Dec 2015.

[11] Y. Dong and T. Itoh, "Composite right/left-handed substrate integrated waveguide and half mode substrate integrated waveguide leaky-wave structures," *IEEE Transactions on Antennas and Propagation*, vol. 59, no. 3, pp. 767–775, March 2011.

[12] A. Oliner, D. Jackson, and J. Volakis, "Antenna engineering handbook," *McGraw Hill*, 2007.

[13] N. Nguyen-Trong, T. Kaufmann, and C. Fumeaux, "A wideband omnidirectional horizontally polarized traveling-wave antenna based on half-mode substrate integrated waveguide," *IEEE Antennas and Wireless Propagation Letters*, vol. 12, pp. 682–685, 2013.

[14] ——, "Wideband transition from coaxial line to half-mode substrate integrated waveguide," in *2013 Asia-Pacific Microwave Conference Proceedings (APMC)*, Nov 2013, pp. 110–112.

[15] T. Tomofuji, H. Terada, S. Kawabata, K. Wakino, and T. Kitazawa, "Full-wave analysis and design of circular half-width microstrip leaky-wave antennas," *IEEE Transactions on Antennas and Propagation*, vol. 61, no. 8, pp. 3967–3975, 2013.

[16] N. Nguyen-Trong, L. Hall, and C. Fumeaux, "Transmission-line model of non-uniform leaky-wave antennas," *IEEE Trans. Antennas Propag.*, vol. PP, no. 99, pp. 1–1, 2016.

[17] N. Nguyen-Trong, T. Kaufmann, L. Hall, and C. Fumeaux, "Investigation of parasitic effects from feed and termination on the far-field pattern of leaky-wave antennas based on HMSIW," in *Antennas and Propagation Conference (LAPC), 2014 Loughborough*, Nov 2014, pp. 72–76.

[18] N. Nguyen-Trong, L. Hall, T. Kaufmann, and C. Fumeaux, "Wideband millimeter-wave antennas with magnetic-dipole patterns integrated in metallic structures," *IEEE Transactions on Antennas and Propagation*, vol. 64, no. 11, pp. 4877–4882, Nov 2016.

[19] Q. Lai, C. Fumeaux, W. Hong, and R. Vahldieck, "Characterization of the propagation properties of the half-mode substrate integrated waveguide," *IEEE Transactions on Microwave Theory and Techniques*, vol. 57, no. 8, pp. 1996 –2004, Aug. 2009.

[20] A. Martínez-Ros, J. Gómez-Tornero, F. Clemente-Fernández, and J. Monzó-Cabrera, "Microwave near-field focusing properties of width-tapered microstrip leaky-wave antenna," *IEEE Transactions on Antennas and Propagation*, vol. 61, no. 6, pp. 2981–2990, 2013.

[21] D. Karmokar, D. Thalakotuna, K. Esselle, L. Matekovits, and M. Heimlich, "Reconfigurable half-width microstrip leaky-wave antenna for fixed-frequency beam scanning," in *2013 7th European Conference on Antennas and Propagation (EuCAP)*, 2013, pp. 1314–1317.

[22] D. K. Karmokar, K. P. Esselle, and S. G. Hay, "Fixed-frequency beam steering of microstrip leaky-wave antennas using binary switches," *IEEE Trans. Antennas Propag.*, pp. 1–1, 2016.

[23] G. Thiele and D. Janning, "Conformal microstrip leaky wave antenna," Sep. 19 2006, US Patent 7,109,928.

[24] W. Menzel, "A new travelling-wave antenna in microstrip," in *Archiv fuer Elektronik und Uebertragungstechnik*, April 1979, pp. 137–140.

[25] A. Oliner and K. Lee, "Microstrip leaky wave strip antennas," in *Antennas and Propagation Society International Symposium, 1986*, vol. 24, June 1986, pp. 443–446.

[26] Y. Wang, W. Hong, Y. Dong, B. Liu, H. J. Tang, J. Chen, X. Yin, and K. Wu, "Half mode substrate integrated waveguide (hmsiw) bandpass filter," *IEEE Microwave and Wireless Components Letters*, vol. 17, no. 4, pp. 265–267, April 2007.

[27] Y. Cheng, W. Hong, and K. Wu, "Half mode substrate integrated waveguide (hmsiw) directional filter," *IEEE Microwave and Wireless Components Letters*, vol. 17, no. 7, pp. 504–506, July 2007.

[28] G. H. Zhai, W. Hong, K. Wu, J. X. Chen, P. Chen, J. Wei, and H. J. Tang, "Folded half mode substrate integrated waveguide 3 db coupler," *IEEE Microwave and Wireless Components Letters*, vol. 18, no. 8, pp. 512–514, Aug 2008.

[29] B. Liu, W. Hong, Y. Zhang, H. J. Tang, X. Yin, and K. Wu, "Half mode substrate integrated waveguide 180 degree 3-db directional couplers," *IEEE Transactions on Microwave Theory and Techniques*, vol. 55, no. 12, pp. 2586–2592, Dec 2007.

[30] V. Rumsey, "Traveling wave slot antennas," *Journal of Applied Physics*, vol. 24, no. 11, pp. 1358–1365, 1953.

[31] Y. J. Cheng, W. Hong, K. Wu, and Y. Fan, "Millimeter-wave substrate integrated waveguide long slot leaky-wave antennas and two-dimensional multibeam applications," *IEEE Transactions on Antennas and Propagation*, vol. 59, no. 1, pp. 40–47, Jan 2011.

[32] E. F. Kuester, R. Johnk, and D. Chang, "The thin-substrate approximation for reflection from the end of a slab-loaded parallel-plate waveguide with application to microstrip patch antennas," *IEEE Transactions on Antennas and Propagation*, vol. 30, no. 5, pp. 910–917, 1982.

[33] J. Liu, D. Jackson, and Y. Long, "Propagation wavenumbers for half- and full-width microstrip lines in the EH_1 mode," *IEEE Transactions on Microwave Theory and Techniques*, vol. 59, no. 12, pp. 3005–3012, Dec 2011.

[34] J. Liu, Y. Li, S. Zheng, and Y. Long, "Method of auxiliary sources for analyzing half-mode substrate integrated waveguide," *IEEE Antennas and Wireless Propagation Letters*, vol. 13, pp. 1043–1046, 2014.

[35] Y. Cassivi et al., "Dispersion characteristics of substrate integrated rectangular waveguide," *IEEE Microw. Wireless Compon. Lett.*, vol. 12, no. 9, pp. 333–335, 2002.

[36] N. Nguyen-Trong, T. Kaufmann, L. Hall, and C. Fumeaux, "Variational analysis of folded substrate-integrated waveguides," *IEEE Microwave and Wireless Components Letters*, vol. 25, no. 6, pp. 352–354, June 2015.

[37] R. B. Marks, "A multiline method of network analyzer calibration," *IEEE Transactions on Microwave Theory and Techniques*, vol. 39, no. 7, pp. 1205–1215, 1991.

[38] R. E. Collin, *Field Theory of Guided Waves*, ser. The IEEE Press Series on electromagnetic wave theory. Inst. of Electrical and Electronics Engineers, 1991.

[39] D. Deslandes and K. Wu, "Accurate modeling, wave mechanisms, and design considerations of a substrate integrated waveguide," *IEEE Trans. Microw. Theory Techn.*, vol. 54, no. 6, pp. 2516–2526, June 2006.

[40] C. Walter, *Traveling Wave Antennas*, ser. McGraw-Hill electronic science series. McGraw-Hill, 1965.

[41] J. Guo, Z. Li, J. Wang, M. Chen, and Z. Zhang, "Analysis and design of leaky-wave antenna with low SLL based on half-mode SIW structure," *International Journal of Antennas and Propagation*, vol. 2015, Ariticle ID 570693, 5 pages, 2015.

[42] R. B. Marks and D. F. Williams, "A general waveguide circuit theory," *Journal of Research - National Institute of Standards and Technology*, vol. 97, pp. 533–533, 1992.

[43] J. Liu, D. Jackson, and Y. Long, "Modal analysis of dielectric-filled rectangular waveguide with transverse slots," *IEEE Transactions on Antennas and Propagation*, vol. 59, no. 9, pp. 3194–3203, Sept 2011.

[44] ——, "Substrate integrated waveguide (SIW) leaky-wave antenna with transverse slots," *IEEE Transactions on Antennas and Propagation*, vol. 60, no. 1, pp. 20–29, Jan 2012.

[45] P. Burghignoli, F. Frezza, A. Galli, and G. Schettini, "Synthesis of broad-beam patterns through leaky-wave antennas with rectilinear geometry," *IEEE Antennas and Wireless Propagation Letters*, vol. 2, no. 1, pp. 136–139, 2003.

[46] J. L. Gomez-Tornero, A. T. Martinez, D. C. Rebenaque, M. Gugliemi, and A. Alvarez-Melcon, "Design of tapered leaky-wave antennas in hybrid waveguide-planar technology for millimeter waveband applications," *IEEE Transactions on Antennas and Propagation*, vol. 53, no. 8, pp. 2563–2577, Aug 2005.

[47] J. Liu, D. Jackson, Y. Li, C. Zhang, and Y. Long, "Investigations of SIW leaky-wave antenna for endfire-radiation with narrow beam and sidelobe suppression," *IEEE Trans. Antennas Propag.*, vol. 62, no. 9, pp. 4489–4497, Sept 2014.

[48] N. Nguyen-Trong, T. Kaufmann, and C. Fumeaux, "A semi-analytical solution of a tapered half-mode substrate-integrated waveguide with application to rapid antenna optimization," *IEEE Transactions on Antennas and Propagation*, vol. 62, no. 6, pp. 3189–3200, June 2014.

[49] F. Xu and K. Wu, "Guided-wave and leakage characteristics of substrate integrated waveguide," *IEEE Trans. Microw. Theory Techn.*, vol. 53, no. 1, pp. 66 – 73, Jan. 2005.

[50] N. Nguyen-Trong, T. Kaufmann, and C. Fumeaux, "Near-field characteristic of a wideband traveling-wave antenna based on a tapered half-mode substrate-integrated waveguide," in *2014 International Workshop on Antenna Technology (iWAT)*, Mar 2014, pp. 322–325.

[51] S. Podilchak, L. Matekovits, A. Freundorfer, Y. Antar, and M. Orefice, "Controlled leaky-wave radiation from a planar configuration of width-modulated microstrip lines," *IEEE Transactions on Antennas and Propagation*, vol. 61, no. 10, pp. 4957–4972, Oct 2013.

[52] A. Martinez-Ros, J. Gomez-Tornero, V. Losada, F. Mesa, and F. Medina, "Non-uniform sinusoidally modulated half-mode leaky-wave lines for near-field focusing pattern synthesis," *IEEE Transactions on Antennas and Propagation*, vol. 63, no. 3, pp. 1022–1031, March 2015.

[53] R. E. Collin, *Field Theory of Guided Waves*, ser. The IEEE Press Series on Electromagnetic Wave Theory. The Inst. of Electrical and Electronics Engineers, 1991.

[54] A. A. Oliner and D. R. Jackson, "Leaky-wave antennas," *Antenna Engineering Handbook*, vol. 4, 1993.

[55] A. Kouassi, N. Nguyen-Trong, T. Kaufmann, S. Lalléchère, P. Bonnet, and C. Fumeaux, "Reliability-aware optimization of a wideband antenna," *IEEE Trans. Antennas Propag.*, vol. 64, no. 2, pp. 450–460, Feb 2016.

[56] N. Nguyen-Trong, C. Fumeaux, A. Kouassi, S. Lalléchère, and P. Bonnet, "Reliability-aware optimization for the sidelobe level of leaky-wave antennas," in *2016 International Conference on Electromagnetics in Advanced Applications (ICEAA)*, Sept 2016, pp. 708–711.

[57] R. Poli, J. Kennedy, and T. Blackwell, "Particle swarm optimization," *Swarm Intelligence*, vol. 1, no. 1, pp. 33–57, 2007.

[58] R. L. Haupt, "An introduction to genetic algorithms for electromagnetics," *IEEE Antennas and Propagation Magazine*, vol. 37, no. 2, pp. 7–15, Apr 1995.

[59] R. Honey, "A flush-mounted leaky-wave antenna with predictable patterns," *IRE Transactions on Antennas and Propagation*, vol. 7, no. 4, pp. 320–329, October 1959.

[60] J. Gómez-Tornero, A. Martínez-Ros, and R. Verdú-Monedero, "FFT synthesis of radiation patterns with wide nulls using tapered leaky-wave antennas," *IEEE Antennas Wireless Propag. Lett.*, vol. 9, pp. 518–521, 2010.

[61] C. Caloz and T. Itoh, "Array factor approach of leaky-wave antennas and application to 1-d/2-d composite right/left-handed (crlh) structures," *IEEE Microwave and Wireless Components Letters*, vol. 14, no. 6, pp. 274–276, June 2004.

[62] R. Siragusa, E. Perret, P. Lemaitre-Auger, H. Van Nguyen, S. Tedjini, and C. Caloz, "A tapered CRLH interdigital/stub leaky-wave antenna with minimized sidelobe levels," *IEEE Antennas Wireless Propag. Lett.*, vol. 11, pp. 1214–1217, 2012.

[63] N. Nguyen-Trong, L. T. Hall, and C. Fumeaux, "Pattern synthesis with angular mask for leaky-wave antennas," in *2016 17th International Symposium on Antenna Technology and Applied Electromagnetics (ANTEM)*, July 2016, pp. 1–2.

[64] E. Garcia, "Electromagnetic compatibility uncertainty, risk, and margin management," *IEEE Transactions on Electromagnetic Compatibility*, vol. 52, no. 1, pp. 3–10, 2010.

[65] L. R. A. X. de Menezes, A. Ajayi, C. Christopoulos, P. Sewell, and G. A. Borges, "Efficient computation of stochastic electromagnetic problems using unscented transforms," *Science, Measurement Technology, IET*, vol. 2, no. 2, pp. 88–95, 2008.

[66] F. Boeykens, H. Rogier, and L. Vallozzi, "An efficient technique based on polynomial chaos to model the uncertainty in the resonance frequency of textile antennas due to bending," *IEEE Trans. Antennas Propag.*, vol. 62, no. 3, pp. 1253–1260, March 2014.

[67] M. Rossi, A. Dierck, H. Rogier, and D. Vande Ginste, "A stochastic framework for the variability analysis of textile antennas," *IEEE Transactions on Antennas and Propagation*, vol. 62, no. 12, pp. 6510–6514, Dec 2014.

[68] Y. Chen, Q. Zhang, A. Alomainy, P. Santi Anwar, and L. Huang, "Characterizing physically transient antennas," *IEEE Trans. Antennas Propag.*, vol. 63, no. 6, pp. 2421–2429, June 2015.

[69] N. Nikolova, J. Bandler, and M. Bakr, "Adjoint techniques for sensitivity analysis in high-frequency structure cad," *IEEE Transactions on Microwave Theory and Techniques*, vol. 52, no. 1, pp. 403–419, Jan 2004.

[70] H. Abdel-Malek and J. Bandler, "Yield optimization for arbitrary statistical distributions: Part I-theory," *IEEE Transactions on Circuits and Systems*, vol. 27, no. 4, pp. 245–253, Apr 1980.

[71] ——, "Yield optimization for arbitrary statistical distributions: Part II-implementation," *IEEE Transactions on Circuits and Systems*, vol. 27, no. 4, pp. 253–262, Apr 1980.

[72] J. Wojciechowski and J. Vlach, "Ellipsoidal method for design centering and yield estimation," *IEEE Transactions on Computer-Aided Design of Integrated Circuits and Systems*, vol. 12, no. 10, pp. 1570–1579, Oct 1993.

[73] S.-K. Au and J. L. Beck, "Estimation of small failure probabilities in high dimensions by subset simulation," *Probabilistic Engineering Mechanics*, vol. 16, no. 4, pp. 263 – 277, 2001.

[74] A. Kouassi, J.-M. Bourinet, S. Lalléchère, P. Bonnet, and M. Fogli, "Safety assessment of a transmission line with emc requirements," in *General Assembly and Scientific Symposium (URSI GASS), 2014 XXXIth URSI*, Aug 2014, pp. 1–4.

[75] O. Ditlevsen and H. Madsen, *Structural reliability methods*. John Wiley & Sons, 1996.

[76] D. Kroese, T. Taimre, and Z. Botev, *Handbook of Monte Carlo methods*. John Wiley & Sons, 2011.

[77] D. Kroese and D. Rubinstein, *Simulation and the Monte Carlo method*. John Wiley & Sons, 2008.

[78] M. Rosenblatt, "Remarks on a multivariate transformation," *The Annals of Mathematical Statistics*, vol. 23, no. 3, pp. 470–472, 1952.

[79] A. Nataf, "Détermination des distributions dont les marges sont données," *Comptes Rendus de l'Académie des Sciences*, vol. 225, no. 4, pp. 42 – 43, 1962.

[80] Rogers Corporation, Roger Ultram 2000 Series Datasheet. [Online]. Available: www.itee.uq.edu.au/etsg/system/storage/serve/2256/Mss0141.pdf

[81] E. T. Jaynes, "Information theory and statistical mechanics," *Phys. Rev.*, vol. 106, pp. 620–630, May 1957. [Online]. Available: http://link.aps.org/doi/10.1103/PhysRev.106.620

[82] J.-M. Bourinet, C. Mattrand, and V. Dubourg, "A review of recent features and improvements added to FERUM software," in *Proc. 10th International Conference on Structural Safety and Reliability (ICOSSAR 2009), Osaka, Japan, September 13–17, 2009*, H. Furuta, D. M. Frangopol, and M. Shinozuka, Eds. CRC Press, 2009.

[83] I. M. Sobol, "Sensitivity estimates for nonlinear mathematical models (in Russian)," *Mathematical Models*, vol. 2, pp. 112–118, 1990.

[84] A. Saltelli, M. Ratto, T. Andres, F. Campolongo, J. Cariboni, D. Gatelli, M. Saisana, and S. Tarantola, *Global Sensitivity Analysis: The Primer*. Wiley, 2008.

[85] E. W. Seeley, "An experimental study of the disk-loaded folded monopole," *IRE Transactions on Antennas and Propagation*, vol. 4, no. 1, pp. 27–28, Jan. 1956.

[86] C. Delaveaud, P. Leveque, and B. Jecko, "New kind of microstrip antenna: the monopolar wire-patch antenna," *Electronics Letters*, vol. 30, no. 1, pp. 1–2, Jan. 1994.

[87] R. Burberry and P. Foster, "(Comment) New kind of microstrip antenna: the monopolar wire patch antenna," *Electronics Letters*, vol. 30, no. 10, p. 745, May 1994.

[88] K.L. Lau and K.M. Luk, "A wide-band monopolar wire-patch antenna for indoor base station applications," *IEEE Antennas and Wireless Propagation Letters*, vol. 4, pp. 155–157, 2005.

[89] F. Yang, Y. Rahmat-Samii, and A. Kishk, "Low-profile patch-fed surface wave antenna with a monopole-like radiation pattern," *IET Microwaves, Antennas Propagation*, vol. 1, no. 1, pp. 261–266, February 2007.

[90] H. Nakano, H. Iwaoka, K. Morishita, and J. Yamauchi, "A wideband low-profile antenna composed of a conducting body of revolution and a shorted parasitic ring," *IEEE Transactions on Antennas and Propagation*, vol. 56, no. 4, pp. 1187–1192, April 2008.

[91] A. Elsherbini and K. Sarabandi, "Very low-profile top-loaded UWB coupled sectorial loops antenna," *IEEE Antennas and Wireless Propagation Letters*, vol. 10, pp. 800–803, 2011.

[92] N. Behdad, M. Li, and Y. Yusuf, "A very low-profile, omnidirectional, ultrawideband antenna," *IEEE Antennas and Wireless Propagation Letters*, vol. 12, pp. 280–283, 2013.

[93] J.-F. Zürcher, "Tripod omnidirectional low profile antenna: A vertically polarized antenna with 90% bandwidth," *Microwave Optical Technology Letter*, vol. 55, pp. 516–521, 2013.

[94] S. Abadi and N. Behdad, "An electrically small, vertically polarized ultrawideband antenna with monopole-like radiation characteristics," *IEEE Antennas and Wireless Propagation Letters*, vol. 13, pp. 742–745, 2014.

[95] M. Koohestani, J.-F. Zürcher, A. Moreira, and A. Skrivervik, "A novel, low-profile, vertically-polarized UWB antenna for WBAN," *IEEE Transactions on Antennas and Propagation*, vol. 62, no. 4, pp. 1888–1894, April 2014.

[96] K. Ghaemi and N. Behdad, "A low-profile, vertically polarized ultrawideband antenna with monopole-like radiation characteristics," *IEEE Transactions on Antennas and Propagation*, vol. 63, no. 8, pp. 3699–3705, Aug. 2015.

[97] A. Lai, K. Leong, and T. Itoh, "Infinite wavelength resonant antennas with monopolar radiation pattern based on periodic structures," *IEEE Transactions on Antennas and Propagation*, vol. 55, no. 3, pp. 868–876, March 2007.

[98] T. Kaufmann and C. Fumeaux, "Low-profile magnetic loop monopole antenna based on a square substrate-integrated cavity," *International Journal of Antennas and Propagation*, Volume 2015, Article ID 694385, 6 pages (2015).

[99] N. Nguyen-Trong, A. Piotrowski, T. Kaufmann, and C. Fumeaux, "Low-profile wideband monopolar UHF antennas for integration onto vehicles and helmets," *IEEE Transactions on Antennas and Propagation*, vol. 64, no. 6, pp. 2562–2568, June 2016.

[100] D. Herold, L. Griffiths, and T. Y. Fung, "Lightweight, high-bandwidth conformal antenna system for ballistic helmets," in *IEEE Military Communications Conference, MILCOM*, Oct 2007, pp. 1–6.

[101] T. Björninen and F. Yang, "Low-profile head-worn antenna with a monopole-like radiation pattern," *IEEE Antennas and Wireless Propagation Letters*, vol. PP, no. 99, pp. 1–1, 2015.

[102] S. Yang, C. Zhang, H. Pan, A. Fathy, and V. Nair, "Frequency-reconfigurable antennas for multiradio wireless platforms," *IEEE Microwave Magazine*, vol. 10, no. 1, pp. 66–83, February 2009.

[103] R. Haupt and M. Lanagan, "Reconfigurable antennas," *IEEE Antennas and Propagation Magazine*, vol. 55, no. 1, pp. 49–61, Feb 2013.

[104] Y. Guo, P.-Y. Qin, and T. Bird, "Reconfigurable antennas for wireless communications," in *2013 7th European Conference on Antennas and Propagation (EuCAP)*, April 2013, pp. 165–168.

[105] N. Nguyen-Trong, T. Kaufmann, L. Hall, and C. Fumeaux, "Analysis and design of a reconfigurable antenna based on half-mode substrate-integrated cavity," *IEEE Transactions on Antennas and Propagation*, vol. 63, no. 8, pp. 3345–3353, Aug. 2015.

[106] N. Nguyen-Trong, L. Hall, and C. Fumeaux, "A frequency- and polarization-reconfigurable stub-loaded microstrip patch antenna," *IEEE Trans. Antennas Propag.*, vol. 63, no. 11, pp. 5235–5240, Nov 2015.

[107] ——, "On the tuning range of a reconfigurable half-mode substrate-integrated cavity antenna," in *2015 International Symposium on Antennas and Propagation (ISAP)*, Nov 2015, pp. 1–4.

[108] ——, "A biasing technique for varactor-loaded reconfigurable antennas," in *2016 IEEE 2nd Australian Microwave Symposium (AMS)*, Feb 2016, pp. 23–24.

[109] ——, "Reconfigurable antennas based on stub-loaded substrate-integrated circuits," in *2016 10th European Conference on Antennas and Propagation (EuCAP)*, April 2016, pp. 1–4.

[110] ——, "A reconfigurable quarter-wave patch antenna employing a folded loading stub," in *2016 IEEE International Symposium on Antennas and Propagation (APSURSI)*, June 2016, pp. 831–832.

[111] N. Nguyen-Trong, L. T. Hall, and C. Fumeaux, "Impedance matching of a frequency- and pattern-reconfigurable antenna," in *2016 17th International Symposium on Antenna Technology and Applied Electromagnetics (ANTEM)*, July 2016, pp. 1–2.

[112] T. Kaufmann and C. Fumeaux, "Wearable textile half-mode substrate-integrated cavity antenna using embroidered vias," *IEEE Antennas and Wireless Propagation Letters*, vol. 12, pp. 805–808, 2013.

[113] S. Agneessens and H. Rogier, "Compact half diamond dual-band textile HMSIW on-body antenna," *IEEE Transactions on Antennas and Propagation*, vol. 62, no. 5, pp. 2374–2381, May 2014.

[114] C. Jin, R. Li, A. Alphones, and X. Bao, "Quarter-mode substrate integrated waveguide and its application to antennas design," *IEEE Transactions on Antennas and Propagation*, vol. 61, no. 6, pp. 2921–2928, June 2013.

[115] S. Agneessens, S. Lemey, T. Vervust, H. Rogier, "Wearable, small, and robust: the circular quarter-mode textile antenna," *IEEE Antennas and Wireless Propagation Letters*, in print (2015).

[116] S. Sam and S. Lim, "Compact frequency-reconfigurable half-mode substrate-integrated waveguide antenna," *IEEE Antennas and Wireless Propagation Letters*, vol. 12, pp. 951–954, 2013.

[117] H. Kang and S. Lim, "Electrically small dual-band reconfigurable complementary split-ring resonator (CSRR)-loaded eighth-mode substrate integrated waveguide (EMSIW) antenna," *IEEE Transactions on Antennas and Propagation*, vol. 62, no. 5, pp. 2368–2373, May 2014.

[118] L.-S. Wu, X.-L. Zhou, W.-Y. Yin, C.-T. Liu, L. Zhou, J.-F. Mao, and H.-L. Peng, "A new type of periodically loaded half-mode substrate integrated waveguide and its applications," *IEEE Transactions on Microwave Theory and Techniques*, vol. 58, no. 4, pp. 882–893, April 2010.

[119] MACOM Technology Solutions, MA46H120 Varactor Datasheet. [Online]. Available: http://cdn.macom.com/datasheets/MA46H120.pdf

[120] C. Luxey and J.-M. Laheurte, "Effect of reactive loading in microstrip leaky wave antennas," *Electronics Letters*, vol. 36, no. 15, pp. 1259–1260, 2000.

[121] K. M. Noujeim, "Wave propagation characteristics of a reactively loaded microstrip," in *IEEE MTT-S International Microwave Symposium Digest*, vol. 2, 2003, pp. 821–824.

[122] T. Jang and S. Lim, "Novel capacitor-loaded substrate-integrated-waveguide structure and its electronically controlled leaky-wave antenna application," *Electromagnetics*, vol. 34, no. 8, pp. 585–592, 2014.

[123] L. Ge and K.-M. Luk, "Frequency-reconfigurable low-profile circular monopolar patch antenna," *IEEE Transactions on Antennas and Propagation*, vol. 62, no. 7, pp. 3443–3449, July 2014.

[124] K. W. Eccleston, "Mode analysis of the corrugated substrate integrated waveguide," *IEEE Transactions on Microwave Theory and Techniques*, vol. 60, no. 10, pp. 3004–3012, 2012.

[125] F.-X. Liu, T. Kaufmann, Z. Xu, C. Fumeaux, "Wearable applications of quarter-wave patch and half-mode cavity antennas," *IEEE Antennas and Wireless Propagation Letters*, in print (2015).

[126] D. Deslandes and K. Wu, "Integrated microstrip and rectangular waveguide in planar form," *IEEE Microw. Wireless Compon. Lett.*, vol. 11, no. 2, pp. 68 –70, Feb. 2001.

[127] M. Kirschning, R. Jansen, and N. Koster, "Accurate model for open end effect of microstrip lines," *Electronics Letters*, vol. 17, no. 3, pp. 123–125, February 1981.

[128] R. E. Collin, *Foundations for microwave engineering*. John Wiley & Sons, 2007.

[129] M. Kirschning, R. Jansen, and N. Koster, "Measurement and computer-aided modeling of microstrip discontinuities by an improved resonator method," in *IEEE MTT-S International Microwave Symposium Digest*, May 1983, pp. 495–497.

[130] V. I. Cojocaru and T. Brazil, "A large-signal equivalent circuit model for hyperabrupt p-n junction varactor diodes," in *22nd European Microwave Conference*, vol. 2, Sept 1992, pp. 1115–1121.

[131] S. V. Hum and H. Y. Xiong, "Analysis and design of a differentially-fed frequency agile microstrip patch antenna," *IEEE Transactions on Antennas and Propagation*, vol. 58, no. 10, pp. 3122–3130, 2010.

[132] E. Palantei, D. V. Thiel, and S. O'Keefe, "Rectangular patch with parasitic folded dipoles: A reconfigurable antenna," in *International Workshop on Antenna Technology: Small Antennas and Novel Metamaterials, iWAT 2008.*, March 2008, pp. 251–254.

[133] P.-Y. Qin, Y. Guo, Y. Cai, E. Dutkiewicz, and C.-H. Liang, "A reconfigurable antenna with frequency and polarization agility," *IEEE Antennas and Wireless Propagation Letters*, vol. 10, pp. 1373–1376, 2011.

[134] S. F. Mahmoud, A. F. Sheta, M. A. Alkanhal and Z. Alhekail, "Analysis and design of compact wide tunable-band antenna based on reactively loaded patch," *Microw. Opt. Technol. Lett.*, vol. 54, pp. 884–888, 2012.

[135] M.-C. Tang, R. Ziolkowski, S. Xiao, M. Li, and J. Zhang, "Frequency-agile, efficient, near-field resonant parasitic monopole antenna," *IEEE Transactions on Antennas and Propagation*, vol. 62, no. 3, pp. 1479–1483, March 2014.

[136] A. Sheta and S. Mahmoud, "A widely tunable compact patch antenna," *IEEE Antennas and Wireless Propagation Letters*, vol. 7, pp. 40–42, 2008.

[137] S.-L. Yang, A. Kishk, and K.-F. Lee, "Frequency reconfigurable U-slot microstrip patch antenna," *IEEE Antennas and Wireless Propagation Letters*, vol. 7, pp. 127–129, 2008.

[138] J.-S. Row and T.-Y. Lin, "Frequency-reconfigurable coplanar patch antenna with conical radiation," *IEEE Antennas and Wireless Propagation Letters*, vol. 9, pp. 1088–1091, 2010.

[139] L. Feldner, C. Rodenbeck, C. Christodoulou, and N. Kinzie, "Electrically small frequency-agile PIFA-as-a-package for portable wireless devices," *IEEE Transactions on Antennas and Propagation*, vol. 55, no. 11, pp. 3310–3319, Nov 2007.

[140] H. AbuTarboush, R. Nilavalan, S. Cheung, K. Nasr, T. Peter, D. Budimir, and H. Al-Raweshidy, "A reconfigurable wideband and multiband antenna using dual-patch elements for compact wireless devices," *IEEE Transactions on Antennas and Propagation*, vol. 60, no. 1, pp. 36–43, Jan 2012.

[141] J.-S. Row and J.-F. Tsai, "Frequency-reconfigurable microstrip patch antennas with circular polarization," *IEEE Antennas and Wireless Propagation Letters*, vol. 13, pp. 1112–1115, 2014.

[142] M. Fries, M. Grani, and R. Vahldieck, "A reconfigurable slot antenna with switchable polarization," *IEEE Microwave and Wireless Components Letters*, vol. 13, no. 11, pp. 490–492, Nov 2003.

[143] N. Jin, F. Yang, and Y. Rahmat-Samii, "A novel patch antenna with switchable slot (PASS): dual-frequency operation with reversed circular polarizations," *IEEE Transactions on Antennas and Propagation*, vol. 54, no. 3, pp. 1031–1034, March 2006.

[144] C. Jung, M.-J. Lee, and F. De Flaviis, "Reconfigurable dual-band antenna with high frequency ratio (1.6:1) using MEMS switches," *Electronics Letters*, vol. 44, no. 2, pp. 76–77, January 2008.

[145] S.-Y. Lin, Y.-C. Lin, C.-Y. Li, and Y.-M. Lee, "Patch antenna with reconfigurable polarization," in *2011 Asia-Pacific Microwave Conference Proceedings (APMC)*, Dec 2011, pp. 634–637.

[146] J.-S. Row and C.-J. Shih, "Polarization-diversity ring slot antenna with frequency agility," *IEEE Transactions on Antennas and Propagation*, vol. 60, no. 8, pp. 3953–3957, Aug 2012.

[147] P.-F. Zhang, S.-Z. Liu, and S. Zhao, "A novel reconfigurable microstrip patch antenna with frequency and polarization diversities," *Microw. Opt. Technol. Lett.*, vol. 57, pp. 1494–1500, 2015.

[148] H. Gu, J. Wang, and L. Ge, "Circularly polarized patch antenna with frequency reconfiguration," *IEEE Antennas and Wireless Propagation Letters*, vol. 14, pp. 1770–1773, 2015.

[149] T. Korosec, P. Ritos, and M. Vidmar, "Varactor-tuned microstrip-patch antenna with frequency and polarisation agility," *Electronics Letters*, vol. 42, no. 18, pp. 1015–1016, Aug 2006.

[150] M. Haneishi and S. Yoshida, "A design method of circularly polarized rectangular microstrip antenna by one-point feed," *Electron. Comm. Jpn.*, vol. 64, pp. 46–54, 1981.

[151] K. R. Carver and J. Mink, "Microstrip antenna technology," *IEEE Transactions on Antennas and Propagation*, vol. 29, no. 1, pp. 2–24, Jan 1981.

[152] L. Huitema et al, "Frequency tunable antenna using a magneto-dielectric material for DVB-H application," *IEEE Trans. Antennas Propag.*, vol. 61, no. 9, pp. 4456–4466, Sept 2013.

[153] M. Memon and S. Lim, "Frequency-tunable compact antenna using quarter-mode substrate integrated waveguide," *IEEE Antennas and Wireless Propagation Letters*, vol. 14, pp. 1606–1609, 2015.

[154] J. Herd, M. Davidovitz, and H. Steyskal, "Reconfigurable microstrip antenna array geometry which utilizes micro-electro-mechanical system (MEMS) switches," Mar. 6 2001, US Patent 6,198,438.

[155] D. Rodrigo and L. Jofre, "Frequency and radiation pattern reconfigurability of a multi-size pixel antenna," vol. 60, no. 5, pp. 2219–2225, May 2012.

[156] D. Rodrigo, B. A. Cetiner, and L. Jofre, "Frequency, radiation pattern and polarization reconfigurable antenna using a parasitic pixel layer," *IEEE Trans. Antennas Propag.*, vol. 62, no. 6, pp. 3422–3427, June 2014.

[157] F. Yang and Y. Rahmat-Samii, "A reconfigurable patch antenna using switchable slots for circular polarization diversity," *IEEE Microw. Wireless Compon. Lett.*, vol. 12, no. 3, pp. 96–98, March 2002.

[158] X. Ding, R. Wang, Y. Q. Wen, B. Z. Wang, and D. E. Anagnostou, "A novel polarization reconfigurable antenna based on transmission line theory," in *2015 IEEE International Symposium on Antennas and Propagation USNC/URSI National Radio Science Meeting*, July 2015, pp. 2375–2376.

[159] S. Jain, S. Reddy, P. Ratna, and U. P. Verma, "Frequency and polarization reconfigurable antenna for airborne application," in *2015 International Symposium on Antennas and Propagation (ISAP)*, Nov 2015, pp. 1–4.

[160] M. S. Alam and A. M. Abbosh, "Beam-steerable planar antenna using circular disc and four pin-controlled tapered stubs for wimax and wlan applications," *IEEE Antennas Wireless Propag. Lett.*, vol. 15, pp. 980–983, 2016.

[161] ——, "Beam-steerable planar antenna using circular disc and four pin-controlled tapered stubs for wimax and wlan applications," *IEEE Antennas and Wireless Propagation Letters*, vol. 15, pp. 980–983, 2016.

[162] W. Lin and H. Wong, "Polarization reconfigurable wheel-shaped antenna with conical-beam radiation pattern," *IEEE Trans. Antennas Propag.*, vol. 63, no. 2, pp. 491–499, Feb 2015.

[163] ——, "Wideband circular polarization reconfigurable antenna," *IEEE Trans. Antennas Propag.*, vol. 63, no. 12, pp. 5938–5944, Dec 2015.

[164] Y. Cao, S. Cheung, and T. Yuk, "A simple planar polarization reconfigurable monopole antenna for GNSS/PCS," *IEEE Trans. Antennas Propag.*, vol. 63, no. 2, pp. 500–507, 2015.

[165] W. Lin and H. Wong, "Wideband 45° polarization reconfigurable aperture-fed patch antenna," in *2015 International Symposium on Antennas and Propagation (ISAP)*, Nov 2015, pp. 1–3.

[166] D. E. Anagnostou, M. T. Chryssomallis, B. D. Braaten, J. L. Ebel, and N. Sepúlveda, "Reconfigurable uwb antenna with RF-MEMS for on-demand WLAN rejection," *IEEE Transactions on Antennas and Propagation*, vol. 62, no. 2, pp. 602–608, Feb 2014.

[167] N. Nguyen-Trong, A. Piotrowski, L. Hall, and C. Fumeaux, "A frequency- and polarization-reconfigurable circular cavity antenna," *IEEE Antennas and Wireless Propagation Letters*, 2016, in print.

[168] P. S. Hall, E. Lee, C. Song, and R. Waterhouse, "Planar inverted-F antennas," *Printed antennas for wireless communications*, pp. 209–218, 2007.

[169] H. T. Chattha, Y. Huang, X. Zhu, and Y. Lu, "An empirical equation for predicting the resonant frequency of planar inverted-F antennas," *IEEE Antennas Wireless Propag. Lett.*, vol. 8, pp. 856–860, 2009.

[170] MACOM Technology Solutions, MADP-042XX5 PIN Diode Datasheet. [Online]. Available: cdn.macom.com/datasheets/MADP-042XX5.pdf

[171] E. Lee, P. Hall, and P. Gardner, "Compact dual-band dual-polarisation microstrip patch antenna," *Electron. Lett.*, vol. 35, no. 13, pp. 1034–1036, June 1999.

[172] N. Nguyen-Trong, L. Hall, and C. Fumeaux, "A frequency- and pattern-reconfigurable center-shorted microtrip antenna," *IEEE Antennas Wireless Propag. Lett.*, 2016, in print.

[173] N. Behdad and K. Sarabandi, "A varactor-tuned dual-band slot antenna," *IEEE Transactions on Antennas and Propagation*, vol. 54, no. 2, pp. 401–408, Feb. 2006.

[174] ——, "Dual-band reconfigurable antenna with a very wide tunability range," *IEEE Transactions on Antennas and Propagation*, vol. 54, no. 2, pp. 409–416, Feb. 2006.

[175] L. Ge, M. Li, J. Wang, and H. Gu, "Unidirectional dual-band stacked patch antenna with independent frequency reconfiguration," *IEEE Antennas and Wireless Propagation Letters*, 2016, in print.

[176] P. Y. Qin, Y. J. Guo, and C. Ding, "A dual-band polarization reconfigurable antenna for WLAN systems," *IEEE Transactions on Antennas and Propagation*, vol. 61, no. 11, pp. 5706–5713, Nov. 2013.

[177] N. C. Karmakar, "Shorting strap tunable stacked patch PIFA," *IEEE Transactions on Antennas and Propagation*, vol. 52, no. 11, pp. 2877–2884, Nov. 2004.

[178] Z. H. Hu, C. T. P. Song, J. Kelly, P. S. Hall, and P. Gardner, "Wide tunable dual-band reconfigurable antenna," *Electronics Letters*, vol. 45, no. 22, pp. 1109–1110, October 2009.

[179] A. F. Sheta and M. A. Alkanhal, "Compact dual-band tunable microstrip antenna for gsm/dcs-1800 applications," *IET Microwaves, Antennas Propagation*, vol. 2, no. 3, pp. 274–280, April 2008.

[180] M. Komulainen, M. Berg, H. Jantunen, E. T. Salonen, and C. Free, "A frequency tuning method for a planar inverted-f antenna," *IEEE Transactions on Antennas and Propagation*, vol. 56, no. 4, pp. 944–950, April 2008.

[181] B. Avser and G. M. Rebeiz, "Tunable dual-band antennas for 0.7–1.1-GHz and 1.7–2.3-GHz carrier aggregation systems," *IEEE Transactions on Antennas and Propagation*, vol. 63, no. 4, pp. 1498–1504, April 2015.

[182] D. Anagnostou, G. Zheng, I. Papapolymerou, and C. Christodoulou, "Reconfigurable multifrequency antenna with rf-mems switches," Sep. 15 2009, US Patent 7,589,674.

[183] H. Kang and S. Lim, "Electrically small dual-band reconfigurable complementary split-ring resonator (CSRR)-loaded eighth-mode substrate integrated waveguide (EMSIW) antenna," *IEEE Transactions on Antennas and Propagation*, vol. 62, no. 5, pp. 2368–2373, May 2014.

[184] P. K. Li, Z. H. Shao, Q. Wang, and Y. J. Cheng, "Frequency- and pattern-reconfigurable antenna for multistandard wireless applications," *IEEE Antennas and Wireless Propagation Letters*, vol. 14, pp. 333–336, 2015.

[185] N. Nguyen-Trong, T. Kaufmann, L. Hall, and C. Fumeaux, "Optimization of leaky-wave antennas based on non-uniform hmsiw," in *2015 IEEE MTT-S International Conference on Numerical Electromagnetic and Multiphysics Modeling and Optimization (NEMO)*, Aug 2015, pp. 1–4.

[186] N. Nguyen-Trong, L. Hall, and C. Fumeaux, "Transmission-line model of nonuniform leaky-wave antennas," *IEEE Trans. Antennas Propag.*, vol. 64, no. 3, pp. 883–893, March 2016.

[187] N. Nguyen-Trong, A. Piotrowski, L. Hall, and C. Fumeaux, "Concept of a beam-steerable cavity-fed antenna with magnetic-dipole coupling elements," in *2017 European Conference on Antennas and Propagation (EuCAP))*, 2017, accepted.

[188] W. Che et al., "Analysis and experiments of compact folded substrate-integrated waveguide," *IEEE Trans. Microw. Theory Techn.*, vol. 56, no. 1, pp. 88–93, Jan 2008.

[189] N. Grigoropoulos and P. Young, "Compact folded waveguides," in *Microw. Conf., 2004. 34th European*, vol. 2, Oct 2004, pp. 973–976.

[190] R. Wang et al., "Compact folded substrate integrated waveguide cavities and bandpass filter," *Progress In Electromagnetics Research*, vol. 84, pp. 135–147, 2008.

[191] W. Che et al., "Investigations on propagation and the band broadening effect of ridged rectangular waveguide integrated in a multilayer dielectric substrate," *IET Microw., Antennas Propag.*, vol. 4, no. 6, pp. 674–684, June 2010.

List of Acronyms

BOR Body of Revolution

CP Circular Polarisation

EMSIW Eighth-Mode Substrate-Integrated Waveguide

FSIW Folded Substrate-Integrated Waveguide

GA Genetic Algorithm

GSM Global System for Mobile Communication

HMSIW Half-Mode Substrate-Integrated Waveguide

LHCP Left-Hand Circular Polarisation

LP Linear Polarisation

LWA Leaky-Wave Antenna

MEMS MicroElectroMechanical System

PDF Probability Distribution Function

PEC Perfect Electric Conductor

PMC Perfect Magnetic Conductor

PSO Particle Swarm Optimisation

QMSIW Quarter-Mode Substrate-Integrated Waveguide

RF Radio Frequency

RHCP Right-Hand Circular Polarisation

SIW Substrate-Integrated Waveguide

TRM Transverse Resonance Method

TWA Travelling-Wave Antenna

UTL Uniform Transmission Line

UWB Ultrawideband

VSWR Voltage Standing Wave Ratio

Biography

Nghia Nguyen-Trong was born in Daklak, Vietnam, in 1990. He received the Bachelor's degree (first class Hons.) in electrical and electronic engineering from the University of Adelaide, SA, Australia, in 2013. He started his Ph.D. degree at the Adelaide Applied Electromagnetic Group, University of Adelaide in 2014. His research interests include applications based on substrate-integrated waveguide technology. He is currently working with different types and aspects of leaky-wave antennas, monopolar antennas and reconfigurable antennas. He is the first author of more than 20 IEEE Journals and Conference papers.

Before coming to Australia, Mr. Nguyen-Trong received the First Prize for competing in the Mathematical Olympiad for Vietnamese University Students in 2009 and perfect score in the University Entrance Exam to win a scholarship from Vietnam Ministry of Education and Training. During his undergraduate, he was the recipient of the scholarship from the IEEE MTT-s in 2012 (worldwide), the South Australia Governor's International Student of the Year Award in 2012 (State Award), the IEEE Australia MTT/AP Chapters Travel Grant and the first prize for IEEE Australian Council Paper Contest (nationwide) in 2013. Based on his academic achievement, he received numerous Awards from the School of EEE, the University Medal and the Adelaide Graduate Research Scholarship in 2014. During his postgraduate study, he received the Best Student Paper Award at the 2014 iWAT Conference, the First Prize in the Student Paper Competition at the 2015 IEEE MTT-S NEMO Conference, Best Student Paper Presentation at Australian Symposium on Antennas (ASA) 2017, the Travel Grant of the 2016 ICEAA & IEEE AWPC Conference, the IEEE SA-Chapter Travel Grant and the Simon Rockliff Award. He has served as reviewer in the *IEEE Transactions on Antennas and Propagations* and in the 2015 ISAP Conference. He is a student member of the Institute of Electrical and Electronics Engineers.

Nghia Nguyen-Trong
nghia.nguyentrong@adelaide.edu.au